Understanding the Impact of Confinement on Ionomer Thin Film Transport Properties

By
Meron Tesfaye

A dissertation submitted in partial fulfillment of the

requirements for the degree of

Doctor of Philosophy

in

Chemical Engineering

in the

Graduate Division

of the

University of California, Berkeley

Committee members:

Dr. Adam Z. Weber, Co-chair
Professor Bryan D. McCloskey, Co-chair
Professor Clayton J. Radke
Professor Andrew M. Minor

Spring 2019

Abstract

Existing state-of-the-art electrochemical devices like polymer-electrolyte fuel cells (PEFCs) and other growing applications like separation membranes, protective coatings, photonics, nanocomposites, and microelectronics utilize polymers of thicknesses less than 100 nm. These thin and ultra-thin polymer films provide ease of processing, application-specific tunable properties, and reduction in material cost. Nano-confined polymer thin films, however, often display surface and thickness-dependent behavior that results in deviation from well-characterized bulk properties. As a result, they pose significant challenges to predictability, optimization, and performance. In PEFCs, thin film ion-conducting polymers (ionomers) of thickness < 100 nm serve as functional binder in the catalyst layers (CLs), aiding proton conduction and extending the reaction zone of the CL porous electrode. Unfortunately, these same ionomer thin films contribute to large proton- and gas-transport losses in PEFCs, thereby considerably limiting commercialization of affordable, low precious-metal catalyst-loaded fuel cells. Remediation of this phenomenon requires fundamental understanding of thin film behavior near interfaces and surfaces and quantification of an ionomer's thickness-dependent properties. Furthermore, design improvements circumventing the losses aforementioned will require establishment of correlations between tunable variables and ionomer thin-film properties under a range of operating conditions. This dissertation aims to carry this out in three interconnected ways. First, model systems are used to develop fundamental understanding of dimensional swellability and thermal relaxation of ionomer thin films proximal to supports and dynamic interfaces that mimic phenomena in CLs. Second, ionomer thin film structure-property relationships are established through exploring and exploiting ionomer counterion identity and thickness variation. Third, properties like ionomer thin-film gas transport are quantified as a function of thickness to create a direct link between losses observed in the CL to local alterations in thin-film properties.

Understanding pairwise interactions between gas/ionomer thin film, ionomer/substrate, and gas/substrate are critical for decoupling the impact of substrate and interface from intrinsic ionomer thin-film properties driven by a finite-size effect. Swelling and thermal relaxation of ionomer thin films on different supports are explored in Chapters 2 and 3 to provide meaningful insights that may also occur at interfaces in the electrode. Swelling behavior, morphology, and mechanical properties of ionomer thin films (~50 nm) spin coated onto the platinum (Pt) support were exposed to both H_2 and Air as experimental systems that mimic anode and cathode CLs and their Pt/ionomer system. Findings indicate lower uptake, increased densification of ionomer matrix, and increased rate in relative humidity-induced aging in a reducing environment as compared to an oxidizing and/or inert environment. Intrinsic mobility of ionomer chains anchored by strong interaction with substrate were additionally explored via thermal relaxation. The change in thermal transition temperature is a key marker of stiffness and polymer-chain mobility and has direct implications on ease of water and gas transport through polymer films. An increase in thermal transition temperature in ionomers supported on silicon (Si/SiO_2) is observed with decrease in thickness. Thermal relaxation dynamics observed result from the positive effect of increased chain mobility at the free surface and the hindered motion at the strongly interacting substrate interface. Monitoring of swellability in alternative gas-environment experiments demonstrated that substrate/ionomer interface can dictate water distribution through the thin film. Absent a dynamic interface and hydration, anchoring of ionomer chains at the substrate interface creates a distributed degree of chain mobility across the thickness that is overpowered by the influence of substrate interaction with further reduction in thickness.

Water uptake and chain mobility findings from these model systems have implications that translate to ion conductivity and gas transport in PEFCs. This correlation is established through structure-property relationships, notably altering cation as a proxy of tuning the nature of ionomer with no additional synthesis as explored in Chapter 4. Alteration of intermolecular forces in the conventional, proton conducting, acid-form ionomer was conducted via exchange with metal cations. Water-uptake capacity, mechanical property, and thermal transition were explored for these exchange ionomers. For monovalent cations with varying cation size and Lewis acid strength, water content showed an inverse relationship with the former and direct relationship with the latter. Hydration is reduced by the increase in mechanical strength upon cation exchange, which is a result of solvation and thermodynamic energy equilibrium in the ionomer matrix. Similar insight was gained for thermal expansivity; an increase in thermal transition temperature was observed in cation exchanged ionomers with a minimal dependence on ionomer thickness. Upon confinement, the interplay between chain mobility at the free surface and near the substrate is dominated by internal hindered motion of ionomer chains tethered to the strong cation. Findings also provide awareness to the impact of ionic contamination in operating PEFCs.

Lastly, links from property measurements in well-defined model systems to real PEFC performance metrics must be established. In this work, quantification of ionomer gas-transport property is carried out in three separate methods to account for variable pertinent conditions for operation (temperature, humidity, and potential). Constant-volume-permeation method showed that unsupported films under dry concentration gradients demonstrated a slight increase in gas permeability with reduction in thickness. However, this data suffered from various sources of inaccuracies due to the fragile nature of thin films under high concentration gradients. Oxygen permeation via luminescent quenching method overcomes this challenge by employing supported thin film system that maintains integrity of thin films during experiment. Additionally, humidity- and potential-dependent microelectrode method was also utilized. Both methods reflect an order of magnitude reduction in gas permeability for thin films of thickness 260 to 440 nm relative to the bulk ionomer membrane counterparts. However, more work is needed to ensure confidence in these findings and explore wide range of thicknesses under variable conditions essential to PEFC CLs.

Electrodes in electrochemical devices are somewhat of a black box with minimal direct insights and predictions. Improved understanding of confinement related performance losses at surfaces and interfaces can help expand ionomer thin-film functionality and affordability of energy-conversion devices by providing critical design metrics and research directions. It is therefore essential to employ model systems and investigate properties of ionomer thin films with perturbations similar to those in operating devices. Such insights are not only useful for PEFCs, but also extend fundamental insights into thin functional polymer films employed in various applications.

To my incredible family whose character inspires me,

To my home country, Ethiopia whose people, history, and very essence fuels me,

To my great Comforter in Heaven, whose relentless pursuit after me is the sole reason for who I am and where I today and every day.

Acknowledgement

It has truly taken a village to raise this graduate study into a PhD. I was blessed to have so many wells to draw from along this journey. So many people have inspired me, supported me, educated me, comforted me, invested in me, validated me, trained me, encouraged me, listened to me, empowered me, and helped me expand and grow beyond what I thought I was capable of and beyond the journey of graduate school or the doctorate degree. But above all, all my praises go to God; I have no reason to boast except in the Lord. Thank you so much for allowing this journey to be finished in the way that it did. Your continued presence in my life has restored my self-image, reorganized my priorities, my relationships with people, and my perspective on graduate school, knowledge, science and research.

I am grateful for Dr. Rahilla Tarfa for guiding my immigrant journey, sparking my love of research and my pursuit of graduate school, and for being an amazing example of brilliance and grit. Rat, thanks for introducing me to the TheRead; my days in lab were filled laughing and nodding along their furious thoughts. Thank you to Era Teshale who even until a few months ago wouldn't let me quit graduate school. She always understands, she predicts my depression and helps me manage my anxiety. She has taught me there is no failure, no amount of shame or struggle that renders me irredeemable. Thank you to my chosen sister, Betselot Teklu who despite being Catholic will go to an Orthodox church to pray for me. Her brilliance and internal knowledge of justice has always inspired me to do better, to work harder, and be open minded. Betsi, thank you for being there for me. Thank you Dolly, Rahel, Dockmias, Abraham, Abinet and Woubzi thank you for believing in me when I didn't believe in myself.

Thank you to Adrian Bitton, my mentor from a distance, my example of beauty, strength and leadership. Your authenticity and intentional care for me in my last year as an undergraduate and throughout graduate school has meant everything to me. Thank you to PLC council of 2013, Evan, Dave and Sean; your letters of support were my lifeline for the first two years of graduate school. Thank you to Dr. Craig Slack who through his own PhD journey demonstrated to me that a doctorate is a degree but the practice and relationships with those in the disciple are worth more. Thank you to LaToya Tools for investing in my spiritual growth, for introducing me to praise flagging and The Way despite my hesitance. I wouldn't have survived the past few years of graduate school without either. Thank you to Kim Flom whose prayer for me and my life is equivalent to my own mother. Thank you for providing me a family away from home, for being an advocate, a trustee, and a friend in so many wonderful ways. Thank you for allowing me to enter your wonderfully cultivated spiritual and professional networks. Thank you to Tomas, Valerie, Heidi, Shion, and so many in Veritas; thank you for your friendship and journeying this work-faith life with me. Thank you to Dr. Faheemah Mustafaa. Your wholesome and affirming energy, your love of writing and people has sincerely helped me finish writing my dissertation. Thank you for arriving in my life at the right time and for being a companion in my pursuit for more of God.

Thank you to my roommates Ashia and Valencia. Thank you for being examples of black excellence. Thank you for giving me the space to exist as my full self in this predominantly white and at times joy-sucking institution. Thanks to Michelle Liu, my roommate and fellow companion in this CBE graduate life. Thank you to future Dr. Adrian K. Davey, whose presence in my life in this last year has been a true blessing. To my DEI co-rebels, Anthony, Sarah and Helen, your care and friendship in the last 8 months has restored my soul. Thank you to Andrew Crothers, whose friendship has followed me to Berkeley, all the way from undergrad REU in St. Louis. Your

brilliance and self-discipline inspire me. Thank you, Adriana, Margaret, Efrem, Pete, Sarah, Anamika, and Julie; your friendship has enriched the last 6 years of my life. Thank you, Doug, for being so wonderfully weird, funny and making the office a joyful place to be in. Thank you to everyone in the ECG group; I could not have chosen a better group to foster my growth both as person and as a researcher.

Thank you to my advisor, Dr. Adam Weber. I am beyond grateful for your patience, your care for my wellbeing beyond research, and for accepting me in to the group with my full-self and motivations. Thank you for always being open to hear my feedback, and for bringing insightful, smart and caring folks into our research group. Thank you to Prof. Bryan McCloskey for always being willing to discuss research and for being pivotal in helping me navigate my first year. I am so grateful to have had Dr. Ahmet Kusoglu as my unofficial advisor and mentor. Thank for cultivating my image making, paper writing and data synthesis skills and process. Your high standards, work ethic, passion for teaching and care for fairness has transformed my own habits and has guided my career path. Thank you so much to Prof. Kelsey Hatzel, Prof. Rohini Bala Chandran, Prof. Iyrna Zenyuk and Dr. Nemanja Danilovic for being brilliant, sincere, and honest examples, mentors, guides and advocates for me.

So much love to my brother Mussie for consistently reconfiguring my distorted self-image and doing it so lovingly. Your energy and unconditional support have always been the ignition behind my pursuit of engineering. Thank you for consistently reminding me that I am valued more than my external achievements and awards. Thank you Seli, for being a wonderful example of vulnerability, care, independence, and clarity all in one. Thank you, Messi, for allowing our sisterhood to grow into friendship; you are amazing. Thank you Fani for always reminding me that God is in control. Thank you Zele, for brining me to the US and for being so exceptionally smart that I always have a high standard of excellence to strive for in-house. Thank you, Feke, Neftu, Eske, Mesfin, Sitoti, Mattu, Abi for being a blessing and source of comfort and support in my life. Thank you so much mom. Your continual prayer upholds me, your upright character is an example for me, and your inability to quit runs within me. I am grateful for you.

Table of Contents

List of Figures

List of Tables

1. The Critical Role of Ionomer Thin films in Fuel Cells

1.1. Brief Overview

A growing rise in extreme weather events, increase in ocean acidity, and shrinking of glacial landmass are few of the several indicators of the Earth's unsustainable rise in temperature.[1] Understanding the inevitability of the dire consequences without additional action, 195 nations have pushed climate change agenda to the global stage, reaching an agreement to limit global temperature rise by 2ºC above the pre-industrial average (Paris 2015, COP21).[2] Although much remains to be accomplished to meet this target, clean-energy momentum has been decoupled from reflexive response to climate change to market driven, competitive landscape. Emission reduction has just become one of the factors critical for good business.[3] This is even more true for energy-conversion and -storage technologies that are already contributing to the fight against climate change by increasing energy-conversion efficiency and minimizing emissions.[4] More specifically, clean transportation holds the key for reducing transportation-related emissions that are expected to rise with the almost tripling of passenger cars by 2050.[5] Hydrogen-powered clean vehicles present a low-carbon option by offering long range per tank, zero emission, fast refueling speed, low maintenance cost, higher efficiency, and fuel security.[5] For these reasons, hydrogen-powered fuel-cell vehicles are the main focus of this dissertation. Critical to their widespread application are transport losses that occur at high current densities required for optimal transportation end use. These losses occur at the electrode triple-phase region, where electrons from the carbon support meet with protons and gas transported through the ion-conducting thin polymeric coating at the precious-metal platinum interface. This work is conducted to understand and mitigate these transport losses:

- by exploring the platinum/ion-conducting polymer interface under various gaseous and humidified conditions,
- by examining ion-conducting polymer relaxation properties near interfaces under various tuning parameters, and
- by developing different methodologies that can capture and correlate these losses to functionalities observed outside of the fuel cell.

1.2. Introduction to Fuel Cells and Electrochemical Devices

The core utility of electrochemical devices relies on the spatially separated reactive surfaces (anode and cathode) that catalyze balanced reactions. This geometry creates an electrochemical potential gradient that is balanced by the external circuit that selectively transmits electrons, and the electrolyte that provides electroneutrality and ion-conduction pathways for mobile ions generated at the electrode while electrically insulating electrodes. Conventionally, the task of the electrolyte is achieved using dissolved salts or acid-containing liquid electrolytes (e.g., sulfuric acid in a lead-acid battery). However, vast commercialization of electrochemical devices with minimal losses and safety concerns have propelled solid polymer electrolytes to the forefront of electrochemical device design. Although ion mobility in solid polymer electrolytes is significantly reduced relative to their liquid analogues as a result of reduced degree of dissociation and steric effects of the polymer matrix host, in many electrochemical applications their advantages far outweigh these drawbacks. Solid polymer electrolytes (ionomers) offer flexibility in cell and electrode design, reduce weight and cost, expand range of operating temperature by increasing

decomposition temperature, minimize possibility of leaks and reactant crossover, and improve cell robustness and shock resistance due to their all solid-state architecture.[6,7] As a result of these gains, electrochemical devices employing solid electrolytes have infiltrated all aspects of the 21st century human activity and life.[8] Energy storage devices like Li-ion battery cells are utilized in everyday consumer goods like cellphones and laptops. Various energy-storage and -conversion devices are emerging to meet short and long-term distributed and centralized energy needs more efficiently and in manners that minimize negative impacts on the environment. Redox flow batteries are enhancing the expansion of renewable energy like solar and wind by providing grid balance and storage to these intermittent resources.[4] Large stationary fuel cells are making energy utilization more efficient by supplying combined heat and power and making backup and distributed energy more affordable.[9] Nowadays, automotive transportation is also employing electrochemical devices to tackle transportation-caused air pollution, greenhouse gas emission, and introduce automation technology.[10,11] Electrolyzers and solar-to-fuel conversion devices are bringing innovation to classical chemical processes and fuel production and transforming economies at a large scale.[4,12,13] Additionally, issues of water shortage and fresh-water contamination impacting millions of low-income people in the world are also being addressed by electrochemical processes.[14] Continued expansion of energy production and storage via electrochemical technologies is an inevitable future as Nobel laureate scientist Friedrich Ostawald predicted in 1894.[15]

1.2.1. Introduction to Polymer Electrolyte Fuel Cells (PEFCs)

The fuel cell, a critical electrochemical energy-conversion device utilized today, dates its fundamental origin to the early 1840's.[15] Its current form as polymer-electrolyte fuel cell (PEFC), utilizing a solid polymer electrolyte is a more recent development dating to 1950's.[15] PEFCs have gained significant notoriety in the past decade thanks to their unique fuel conversion and electric efficiency as high as 60%, combined heat and power efficiency as high as 90%, and zero energy-production emission.[16] In PEFCs, the exothermic, but spatially segregated, reaction of oxygen (O_2 or Air) and hydrogen (H_2) gas to form water and generate power(Equation 3). Pure H_2 gas is fed through the porous gas diffusion medium (DM) as shown in Figure 1-1 and undergoes hydrogen oxidation reaction (HOR) at the anodic catalyst layer (Equation 1). These catalyst layers (CLs) are critical microporous components consisting of 2 to 5 nm platinum (Pt) nanoparticles supported on 20 to 30 nm primary carbon(C) particles bound with 2 to 70 nm thin-film ionomer coating.[17–19] The protons released from HOR travel through the bulk ion-conducting polymer (proton-exchange membrane, PEM) to the cathode forcing electrons to travel through the external circuit and do work. At the cathode CL, O_2 gas (or air), protons (from the ionomer), and electrons (from the carbon) react on the surface of Pt via oxygen-reduction reaction (ORR) to form water (Equation 2). The produced water moves through the DM to the O_2 flow field to be removed.[20] CLs are deposited on both sides of the bulk ionomer electrolytes to form a membrane-electrode assembly (MEA). (See components of a basic PEFC in Figure 1-1). Low-temperature PEFCs commonly operate at 50 to 80ºC at less than 5 atm pressure and provide power density ~1 W/cm^2 at 40 to 70% voltage efficiency.[21]

HOR:	$H_2(g) \rightarrow 2H^+ + 2e^-$	(1)
ORR:	$4H^+ + 4e^- + O_2(g) \rightarrow 2H_2O(l)$	(2)
Overall:	$2H_2(g) + O_2(g) \rightarrow 2H_2O(l)$	(3)

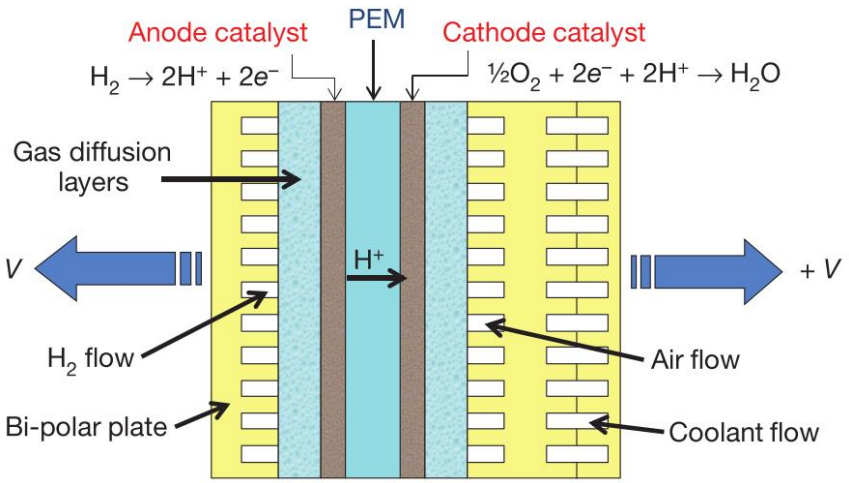

Figure 1-1: Polymer electrolyte fuel cell (PEFC) components of single unit. Reprinted by permission from Springer *Nature* Debe,[22] Copyright 2012.

The electrode on each side of the MEA is a three-dimensional structure composed of carbon (C)-supported Pt catalyst, ion-conducting polymer (ionomer) functional binder, and porosity with a total thickness of ~5 to 25 μm.[18,19,23] When Pt nanoparticles are deposited on the C support, Pt's Galvani potential raises the electronic density and lowers the Fermi level to accelerate Pt's electrocatalytic activity.[24–26] Therefore, the stability and accessibility of the C support is critical to the electron conductivity and performance of the PEFC. The fine carbon nanoparticles allow for close to 100% accessible active Pt surface area.[24] Reaction in the electrode occurs at the Pt surface where gas, electrons, and ions meet. This is commonly referred to as the triple-phase boundary although the reaction probably occurs more along a two-phase contact line. To execute these reactions at a fast turnover rate while ensuring high utilization of the Pt electrode has to be very small (2.2 to 4.5 nm nanoparticle) with high surface area (62 to 120 m^2/g Pt as measured by CO chemisorption) and well dispersed in the electrode. Other alternatives to the current C-supported Pt nanoparticle structure are explored later in this chapter. Current state-of-the-art PEFCs rated for typical 90 kW,1W/cm^2 MEA have 4.5g anode CL and 18g cathode CL total Pt loading.[27] The 4x or more difference in CL Pt loading is explained by the variation in ORR and HOR kinetics. To bind the Pt/C electrocatalyst, an ionomer loading on the order of 40 to 60 v-% (30 to 50 wt-%) is used.[28,29] Ideal performance has been observed to be at ionomer to carbon (I/C) ratio of 0.3 to 0.4 resulting in ionomer thickness distributions that range from 2 to 70 nm.[30] The rest of the electrode is composed of gas pores that allow gas and water to be shuttled in and out of the CL. This porous electrode is fabricated using an electrode ink (composed of ionomer, Pt/C, and solvents) followed by various coating and drying techniques that dictate its microstructure.[31] Resultant of the complex ink composition and solution processing is the formation of electrode agglomerates that are non-uniformly distributed within the bulk electrode.[18,32] Consequently, variation in accessibility electrocatalytic sites is experienced due to the existence of primary (small) and secondary (large) pores in the electrode.[18] These anodic and cathodic electrodes are then pressed on each side of the PEM (to compose the MEA) and supported by DM and bipolar plates that provide electrode mechanical support, facilitate species transport, and serve to transfer current.

1.2.2. Drivers of PEFC Adoption and Commercialization

The promise of high efficiency, low CO_2 emission, and potential independence from traditional sources of energy make PEFCs highly desirable energy conversion device. In just the recent past few years (2014 thru 2016) companies worldwide have shipped ~370 MW of fuel-cell power in transportation alone; almost 60% percent of that was shipped in year 2016 demonstrating the exponential growth trend of fuel cells in energy supply and transportation sector.[33,34] Despite this fact, PEFC proliferation in the energy landscape still lags. Adoption barriers can be grouped into technological and institutional barriers. Institutional barriers include key economic drivers like material suppliers, domestic manufacturing structure, and fuel supply and delivery infrastructure. These also involve codes and standards and factors affecting public's ease of adoption or technology awareness.[35] Despite PEFCs continued struggle for recognition, progress is actively being made to provide incentives, introduce policies, and set targets in Japan, US, Europe, and UK.[5] A notable boost in public awareness occurred with the advertising campaign of Toyota Mirai and Honda Clarity in 2015 and 2016, respectively.[33] Other highlights contributing to shift this barrier include effort from state governments and private actors including, but not limited to, increased adoption of more than 2780 PEFC cars and buses, deployment of 11,600 PEFC powered forklifts (some delivery vans also), and expansion of 70 H_2 refueling stations especially in California just in 2018 alone.[5,34,36,37]

Technological barriers, on the other hand, include PEFC cost and lifetime concerns and fuel production and storage costs and capacity needs that remain unmet. Major cost of PEFCs is due to (1) the rare and expensive precious-metal based electrocatalyst, (2) the large performance losses that remain unmitigated and (3) durability concerns that limit the longevity of these devices. Much has been done and is currently underway to minimize Pt group metal (PGM) loading in PEFC electrodes. Cost competitiveness with conventional internal combustion engines will require a stretch goal of < 6 g total loading per vehicle (compare to ~23 g PGM loading of state-of-the-art).[38] The U.S. Department of Energy (DOE) has a target goal to decrease the cost of an automotive PEFC from $55/kW to $30/kW at high manufacturing volumes with an increase in durability from ~3900 to >5000 h and less than 20% performance degradation over its lifetime.[18,19] Current estimates of stack cost, assuming a 500k car production per year, show 50% of cost stack cost stemming from Pt loading at the cathode. This cost can successively be reduced with a drop in Pt loading. However, without global market strategies that facilitate high economies of scale even ~5g PGM loading will not result in major stack cost reduction.[19] Therefore, it is necessary to (1) make R&D efforts to move away from conventional Pt/C electrocatalyst, (2) minimize losses in the electrode to improve Pt utilization, and (3) reduce the cost of the rest of the PEFC components and establishment of infrastructure. The first is a topic of discussion in section 1.4.1. The second is conducted as part of this dissertation by exploring the origins of transport resistances at the confined ionomer/Pt/C interface; it is discussed further in section 1.4.3. (3) requires reduction in cost of bipolar plates, PEM membranes, and H_2 production and delivery; it involves new, low-weight, low-cost material pathways, manufacturing methods, and economies of scale that are outside the scope of this dissertation. However, it is with this broad contextual perspective that we approach our view towards improving design and optimizing performance of PEFCs, especially as we narrowly focus on ionomers.

1.3. Introduction to Ion-Conducting Polymers (Ionomers)

Central to the operation of PEFCs and other electrochemical devices are solid polymer electrolytes that selectively conduct ions and inhibit electrons. Ionomers are simply polymers containing single or multiple ionic groups. Different from highly charged polyelectrolytes, ionomers only contain ~15 mol % ionic group as calculated from the number of backbone atoms or repeat units where they are attached.[39] Ionomers are also insoluble in polar solvents (like water) at room temperature but can be neutralized by presence of counterions.[40] Early industrial and academic research interest in ionomers dates back to the mid-1960's when property changes of neutralized polymers were observed to be altered by the presence of different counterions.[41] Properties in ionomers are, therefore, governed both by ionic interaction and polymer-chain aggregation and the thermodynamic energy balance of these seemingly disparate phases especially in the presence of solvents.[41] Desired qualities of a high performing ionomer membrane in electrochemical devices are (1) selective ion transport, (2) no electrical conductivity, (2) high counterion mobility, (3) high chemical stability, (4) high mechanical stability, (5) low fuel species crossover (low gas and liquid permeability) and (6) ease of processing.[15]

Depending on the specific application, ionomers transport different counterions. Optimal transport of ions of interest through a polymer electrolyte is dictated by concentration of ion, size of counterion, solvation of counterion, and anion-counterion interaction.[42] The concentration of ions (counterions) in an ionomer can be quantified by the ion-exchange capacity (IEC, mequiv/g). The main route of ion transport is solvent mediated and through the hydrophilic-phase, ionic network embedded in the polymer matrix. As a result, varying the IEC of the ionomer membrane can control both its solvent uptake and conductivity. Increasing conductivity by increasing ion content (increasing IEC) in the ionomer must always be balanced by other aspects of ionomer that may decrease as a result. High IEC can increase swellability and ionic-network pathways, but will also compromise mechanical integrity and possibly durability of the ionomer.[43] Optimizing these desired ionomer qualities for specific application/device and developing ionomer design criteria have been the focus of research over the past three decades.

1.3.1. Common Architecture of Ionomers in Electrochemical Devices

Basic requirements and aspects pertaining to the physical, chemical and mechanical makeup of ionomers is shared among many electrochemical devices (including PEFCs). Common ionomer architecture is composed of an (1) inert polymer backbone that is populated with (2) side chains containing the (3) ionic group of interest. Altering the chemical and physical structure of these three building blocks can tune an ionomer's desired property, resulting in optimal performance in an electrochemical application.

The chemical nature and structure of the backbone of the ionomer is critical for providing thermal, mechanical, and chemical stability, thereby influencing ionomer lifetime and its degradation mechanism. Many ionomers considered for PEFC application have so far been perfluorinated or hydrocarbon based. Although the thermal and chemical stability of linear perfluorinated-backbone ionomers have been the benchmark for a long time, hydrocarbon-based ionomers are promising low cost, safe, and tunable chemical-synthesis pathways for emerging ionomers.[15,44] Hydrocarbon-based ionomers usually contain monomers based on sulfonated aromatic polymers, e.g, polyphenylenes, polyketones, polysulfones, and polyethers.[44,45] Sulfonated hydrocarbon-driven ionomers allow tailoring of length and block distribution of the precursors resulting in better microphase hydrophobic backbone/hydrophilic sidechain copolymer

separation that results in well-connected ionic channels.[44,46,47] However, these same ionomers suffer from low oxidative(chemical) stability compared to their perfluorinated counterparts due to their aliphatic character.[44] Addition of imide group to aromatic ionomer backbones tends to turn this trend around as observed with six-membered polyimide ionomers demonstrating relatively high thermal stability, high mechanical strength, good film-forming ability, low gas permeability, and superior chemical resistance.[44,48] Incorporating aromatics, nitrogen atoms, and phosphorus to the molecular architecture of polyphosphazene ionomer backbone has shown low fuel crossover and ease in processing with tunable side-chain attachment synthesis scheme.[15,44] Despite polyphosphazene's high performing metrics, it still suffers from failure in mechanical integrity especially upon hydration, limiting its use in highly hydrated electrochemical devices like direct methanol and polymer electrolyte fuel cells.[44] The improvement in a given property alone is not sufficient to provide maximal performance. Performance Maximization of ionomers requires optimization on multiple fronts of ionomer design.

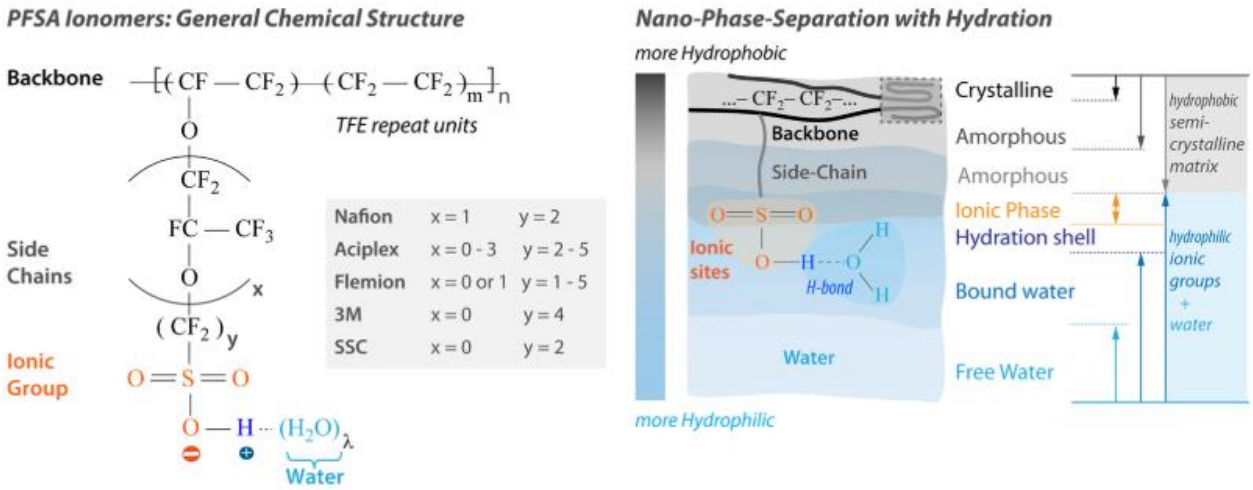

Figure 1-2: General chemical formula for the PFSA ionomers of various side-chain length and key chemical structural parameters governing their phase-separated morphology. Image adapted with permission from Kusoglu and Weber, [43] Copyright 2017 American Chemical Society.

Aside from ionomer backbone, the chemical nature of the side-chain is another lever of ionomer design that can be modulated for desired function. As one of the most commonly employed ionomers in PEFCs, perfluorosulfonic-acid ionomers (PFSA) are prime examples for examining side-chain effects. PFSAs are composed of random copolymer of tetrafluoroethylene (TFE) backbone sequence (~87 mol % at 0.91 IEC) with a perfluorinated vinyl ether comonomer and a pendant side chain of sulfonic acid moeity.[43,44] See Figure 1-2. Incompatibility of the ionic group with the non-polar TFE backbone results in nanophase separated morphology where ionic domains (hydrophilic) are distributed in the TFE matrix (hydrophobic). This physiochemical structure of PFSAs results in high conductivity and good chemical, physical, and mechanical stability making them ideal candidates for PEFCs and related electrochemical applications. When fully hydrated, PFSAs demonstrate conductivities as high as 0.1 S/cm, while enduring mechanical swelling strain of added water molecules of up to 40% by volume.[43,49] However, improving the conductivity of these ionomers at low relative humidity (e.g. during start/stop of car operation) and degradation concerns (due to the oxidative nature of the PEFC environment) remain challenges.

One pathway that has been pursued to modify PFSA for improved performance is altering side-chain length and chemistry to produce short side-chain ionomers (like 3M and Aquivion, see Figure 1-2). Reduction in side-chain length increases IEC by reducing the amount of polymer per acid (ion carrying) site and increasing conductivity compared to the benchmark long side-chain PFSA, Nafion.[50,51] Altering side-chain length and chemistry can also impact backbone/side-chain interaction resulting in changes ionomer aggregation, backbone and side-chain stiffness, and ultimately impacting ionic channel networks.[43] Reduction in side-chain length and especially the removal of the flexible ether bond increases side-chain stiffness and IEC, and has been shown to improve Pt electrode/ionomer interface and ionomer phase separation even under dry conditions.[52] As previously stated, increasing IEC has to be balanced with maintaining or improving mechanical integrity and minimizing dissolution upon exposure to solvent.[43] Additional performance gains via side-chain modification have also been accomplished by keeping the main components of PFSA and attaching imide groups and aromatic moieties.[53,54] These side-chain chemistries result in multi-acid side-chain ionomers, like perfluoroimide acids and Ortho Bis Acid, with increased proton concentration (higher IEC), resulting in improved ionomer ion transport.[53] Additionally, the differentiation between types of protons near imide, aromatic, and sulfonic-acid groups corresponds to water retention, especially at low humidification. Low acidity protons attached to aromatic sulfonic-acid groups exhibit significantly lower conductivity relative to perfluorinated imide acid groups, which are considered to be stronger Brønsted acids.[55]

The remaining lever that can be used to alter ionomer architecture is the nature of ionic group commonly found tethered to the pendant sidechain. In an anhydrous system like that of solid-state Li-ion battery, ions in solid-state electrolytes use the non-polar polymer matrix as their mode of mobility. As such, long-range polymer segmental mobility is key to raising conductivity in these ionomers. Conversely, in almost all PEFCs, water is present as product and/or reactant. As such, the mode of ion (usually OH^- and H^+) conduction has an alternative pathway of transport where ions are shuttled through water domains via vehicular or hopping mechanisms. As a result of this critical role of water in PEFCs, water management is necessary for optimal transport. Other electrochemical systems like flow batteries, chloroalkai process, water electrolyzers, and water desalination via electrodialysis require transport of other counter ions of interest such as Na^+, K^+, Ca^{2+}, Zn^{2+}, etc.[48,56] In a hydrated operation, the water content of the ionomer strongly depends on the nature of cations present in the membrane. More hydrated ions, those with high hydration number and smaller solvation size, remain mostly dissociated in the water channel and can be shuttled through the water network.[57] Those with low hydration and strong association with fixed anion charges in the membrane are hindered in their transport. Mobility of these ions is hindered by their own size and charge density; Cs ion would have a lower overall diffusion coefficient, because of its larger mean-free path in diffusing through the polymer, compared to sodium ion. Specific interaction with different parts of the ionomer also impact the ease by which cation moves.[56,58] One consequence of this is a change in stiffness and physical crosslinking due to the presence of strongly ionic monovalent or divalent cations.[59–61] Although strong association of cations with polymer sidechains improves thermal and mechanical stability, it impedes ionomer phase separation and ion diffusivity. Therefore, understanding the nature of cation is critical for understanding the ionomer's properties and performance.

1.3.2. Chemical Structure and Morphology of Perfluorosulfonic Acid Ionomers

The bottom-up approach of altering the chemical nature of the backbone, side-chain, and ionic-group chemistry cannot be detangled from the morphological effects that molecular assembly of

ionomer chains has on property and function. Central to performance of ionomers and embedded in their natural selective transport is their morphology and nano-phase separated structure. In hydrated systems, like that found in PEFCs, ionomer hydration and solvation of ionic groups in water molecules is in constant balance with the hydrophobic polymer matrix that sustains the overall integrity of the membrane.[62] Such morphology also dictates water and gas transport in ionomers, where phase separation is correlated with ionomer-chain aggregation size and hydrophilic network and available free volume for gas permeation.[58] Tunable nanostructures that control the extent of hydration and transport pathways can be designed via synthesis or processing techniques for well-ordered ionomers like sulfonated block or graft co-polymers. However, for disordered copolymers like PFSA, the extent of hydration is preparation-dependent (i.e. pre-treatment, cation contamination) and stimuli driven (i.e., humidity, temperature, and solvent). Nonetheless, various researchers have proposed morphological descriptions of PFSAs in different conditions that can explain the relationship between ionomer nanostructure and resultant property observed experimentally.[39,40,43,44,58,63–65] The physical structure of benchmark PFSA, Nafion®, has been probed by various imaging techniques including Small Angle X-ray Scattering (SAXS), Small Angle Neutron Scattering (SANS), Quasielastic Neutron Scattering (QENS), and Transmission Electron Microscopy (TEM). Figure 1-3 shows two morphological depictions of structure and a cryo-TEM 3-D image of Nafion. One of the oldest morphological descriptions from Yeager et al. concluded Nafion to be a three-phase system consisting of a TFE crystalline backbone (A region in Figure 1-3a), inhomogeneous amorphous matrix phase (B region) consisting of pendant side-chain, and ionic-cluster containing end groups, counterions, and water (C region).[66,67] The volume fractions of these regions can alter transport pathways, e.g., water and ion transport are mainly through polar ionic pathways, while gas dissolution is dominant in non-polar regions of the ionomer.[58] Figure 1-3b shows morphological features of Nafion proposed from SAXS and USAXS (Ultra Small Angle X-ray Scattering) observations. Elongated rods with local features of 3 to 5 nm separation between ionic groups were reported along with long rod-like aggregates of 80 nm.[40] These rods were proposed to be bundled into large isotropic aggregates using SAXS information.[40] More recently, Allen et al. showed a first 3-D direct-imaging via cryo TEM tomography (Figure 1-3c). The structure reveals a locally flat interconnected channel-type network where hydrophilic (yellow phase) domains ~3.5 to 5 nm (dry to hydrated membrane) diameter were observed that change from spherical to locally flat upon hydration.[64] Although PFSAs are random copolymers, morphological visualizations highlight hydration-dependent phase-separated structure and network that ultimately impacts properties. Other ionomers like block copolymers and graft copolymers also show similar relationship where, for instance, increases in phase separation between ionic and non-ionic domain result in ion-conductivity enhancment.[48,68]

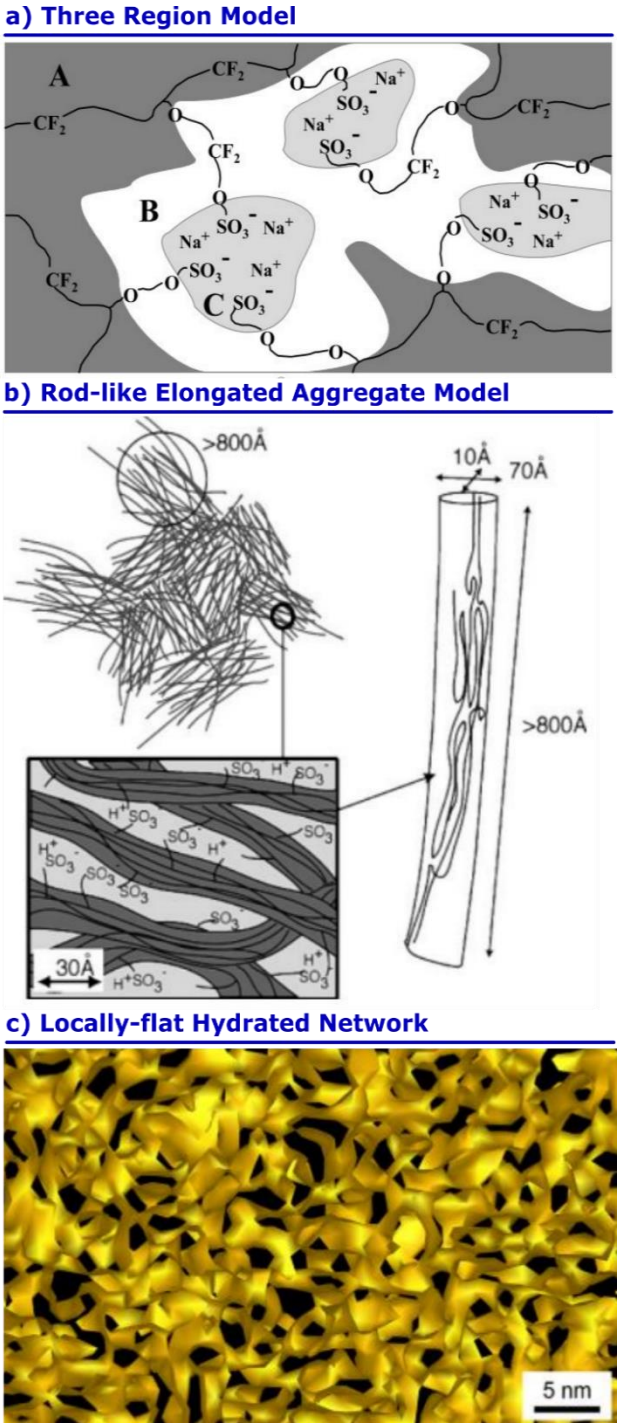

Figure 1-3: PFSA ionomer (Nafion) morphology: (a) Proposed three region model. Reprinted with permission from Yeager et al.[58] *J. Electrochem. Soc*., 128, 1880 (1981). Copyright 1981, The Electrochemical Society. (b) Proposed elongated polymeric aggregates (cylindrical or ribbon-like aggregates) Reprinted with permission from John Wiley and Sons *Fuel Cells* Gebel et al.[40] Copyright 2005 (c) 3-D reconstruction of the frozen- hydrated as-cast Nafion membrane from transmission electron microscopy (TEM).[64] Image reprinted with permission from Allen et al.[64] Copyright 2015 American Chemical Society.

1.4. Performance Challenges and Limitations in PEFCs

As previously noted in section 1.2.2, mitigating losses experienced by PEFCs is critical to their widespread adoption and commercialization. A PEFC experiences various losses upon polarization (extraction of energy from the system) that reduce its usable energy (equation 3). These are commonly referred to as overpotentials. Losses in a typical PEFC can be grouped into: kinetic, ohmic, and mass-transport losses and are shown in Figure 1-4.[20] Kinetic losses are associated with the turnover rate and reactivity of species on the catalytic surfaces. The rate of reaction of HOR >> ORR on Pt surfaces (three orders of magnitude faster). Thus ORR results in the largest overall loss of around 0.3 V at low current densities.[69–71] Research focusing on catalytic surface structure and nature to minimize these losses is key to fast tracking PEFCs into mainstream use. The second type of losses, ohmic losses, are prevalent at moderate current densities and scale linearly with current density. These are due to electronic contact resistances between the flow-fields and DM as well as hindered ion conductivity through the PEM separator.[20,71] At this point the cell performance becomes limited by the number of protons required to be shuttled to the catalytic site and potential varies linearly with current density. At high current densities, losses are overwhelmed by mass-transport resistances. Reactants are depleted expediently and voltage rapidly drops as the supply of reactant reaching the catalytic site is limited. This loss usually occurs between 0.6 V window which is the critical operating window for car and stationary operation.[19] This high current density regime is also necessary for fast start/stop activity, as well as high acceleration or large power withdrawal. Even during low overall current density performance, local high current densities are likely to be present. Additionally, this is where performance and cost optimization face their largest strain; with decreasing Pt loading, required for low-cost fuel cells, lower cell voltage output is experienced at higher local current density.[27]

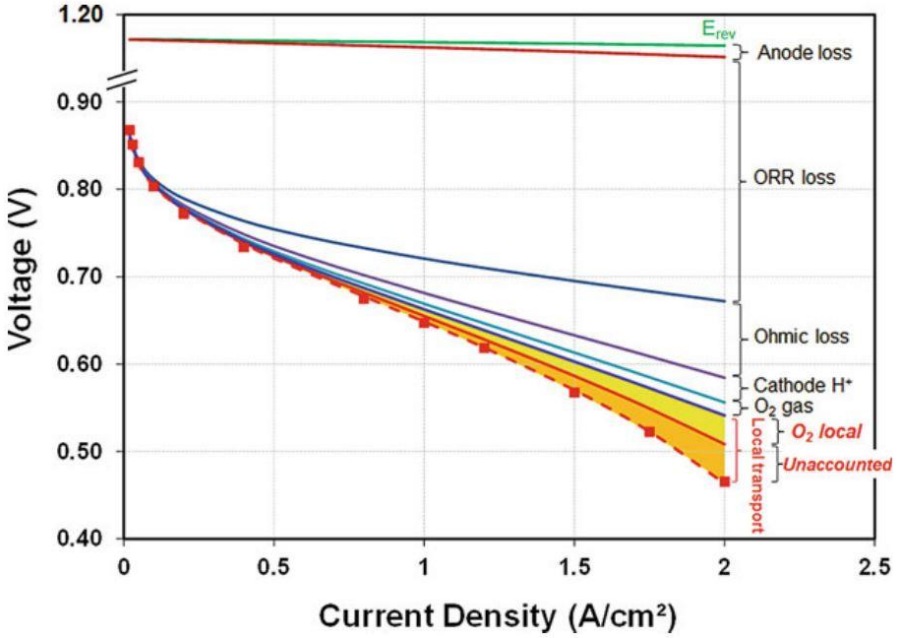

Figure 1-4: Polarization curve of low-Pt loaded PEFC showing voltage loss terms in a low-Pt PEMFC operated under differential cell conditions operated at H_2/air, 150 kPa, 80°C, and 100% RH. The symbols represent the experimental data. Reprinted with permission from Springer *Nature* Kongkanand et al.,[19] Copyright 2018.

1.4.1. Progress and Challenges to Addressing Kinetic Limitations in PEFCs

An active catalytic site is a highly dynamic interface that encounters multiple species (gas, protons, electrons, and water). Therefore, minimizing losses at this interface requires activity maximization and improvement of accessibility to this interface. Research efforts have been focused on designing new catalyst structures such as Pt-alloys, Pt-shell non-precious core geometries, non-precious metal catalysts, nano frames, nano cylinders, and nanostructure thin film (NSTF). Figure 1-5 shows specific activity improvement of some of these electrocatalysts compared to the conventional benchmarks, i.e., polycrystalline Pt and Pt/C. These new geometries have shown 3 to 20x activity improvements relative to the traditional Pt electrocacatalyst.[17,21,27,71] Significant improvements to specific ORR activity has been achieved for Pt alloyed with base metals such as Fe, V, Co, Ni, Mn, Cr, and Ti.[23,71,72] Reasons for observed increase in activity are still under debate but include preferential Pt crystal orientation as a result of co-alloy, improvement of the Pt-Pt inter-atomic distance facilitating O-O bond cleaving, and lattice strain to downshift Pt's d-band center with alloying critical for improved O adsorption process.[21,71,73,74] A Pt-shell non-precious core consisting of Au, Ni, Pd, Co, or Cu have also reported performance improvements of a factor of 10 relative to polycrystalline Pt.[22,27,73] This concept was also extended to the current Pt/C structure to produce C-supported Pt_3Co nanoparticles that have shown kinetic-rate increases of up to a factor of ~3, especially after heat treatment.[22,73] A notable standout of electrode structures that have significant extended surface area and ORR activity improvement of 5 to 10x are nanostructure thin films (NSTF) and mesostructured thin films (MSTF).[22,75] NSTFs are composed of thin film of Pt alloy coated on individual single crystalline 0.5 to 1 μm long whiskers of an perylene red organic compound.[22,27,76] (See Figure 1-5) Advantages of these nanostructures stem from their electrically non-conductive whiskers, their low susceptibility to electro-oxidative corrosion, and the semi-continuous bulk Pt-like characteristics in this microstructure.[27,75,76] However, widespread deployment of such a structure requires efficient fabrication methods that can translate electrodes from the laboratory into MEA that can be manufactured at a large scale which is yet to be accomplished. Additionally, introduction of ionomer thin film for improved proton conductivity that has resulted in unexpected ionomer-coating-dependent mass-transport limitation in these NSTF electrodes.[19,76] Pursuit of non-PGM electrodes are also being considered. Non-precious metal electrocatalysts containing metal oxides doped with C and nitrogen are reaching notable turnover rates and lifetimes.[73,77] However, their power density and durability at high current density is not sufficient for widespread application.[77] Despite the high activities of these new electrocatalysts commonly reported from rotating-disk electrode studies, performance metrics are still unable to translate directly to MEAs. The heterogeneous structure and complex environment of a PEFC electrode is a major hurdle limiting the incorporation of these electrocatalysts into existing electrode structure. Deployment of these alternative electrocatalysts into PEFCs also has to involve efforts to ensure unimpeded accessibility to catalytic sites in the current state-of-the-art PEFC electrodes.

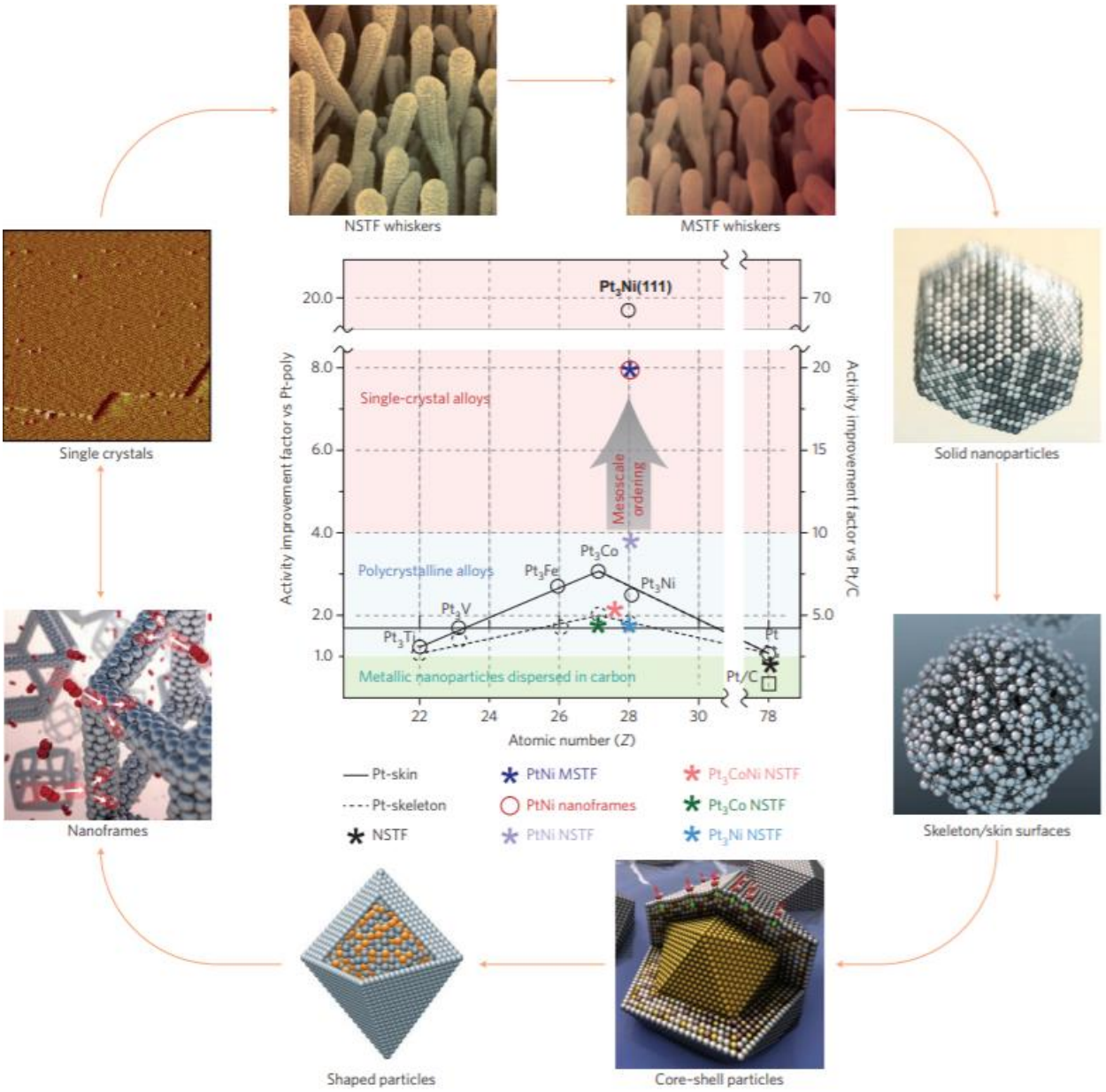

Figure 1-5: Electrocatalyst structures and materials under development and their activity for Oxygen Reduction Reaction (ORR) relative to conventional polycrystalline Pt and Pt/C structure. Reprinted by permission from Springer *Nature* Stamenkovic et al.[21] Copyright 2016.

To date, the dominant path for electrode-structure optimization has occurred through variations in the electrode-ink preparation, i.e., varying carbon support types, ionomer/carbon (I/C) ratio, Pt loading, and solvent type and content.[31,78] Solvents utilized to prepare these electrode dispersions dictate the C/ionomer, ionomer/Pt, and Pt/C interactions even prior to electrode formation. Effects of solvents like isopropyl alcohol, water, N-Methyl-2-Pyrrolidone, and Dimethyl sulfoxide have been explored in ink state as well as in electrode form.[78–80] Ionomer ionic and non-ionic segment chain confirmation can be impacted by the solvent pH, electrostatic effects, viscosity, surface tension, dielectric constant, and solubility parameter.[31,81,82] Final ionomer film formation, morphology, and performance, therefore, depends on the various binary interactions.[17,78] Varying

accessibility of the C support in the electrode can also impact electrode activity by supporting uncoated Pt, which is thought to have improved activity due to uninhibited access to gas and electrons. Carbon supports are manufactured from petroleum-driven aromatic residue oils or via thermal decomposition of acetylene and range from porous to solid.[2626,38] Most popular carbon supports employed are moderate-surface-area solid carbon supports with good corrosion resistance like Vulcan (solid) and high-surface-area porous supports suitable for Pt deposition like Ketjenblack (porous).[38] Figure 1-6 shows schematics of components and interfaces of of PEFC CL at different length scales. The key component of the electrode interface and the main focus of this work is ionomer thin film and the dynamic Pt/ionomer interface. Optimizing performance of electrode interface in PEFC requires maximization of proton conductivity to and from Pt active sites while minimizing ionomer thickness for high gas and water transport. The challenges and limitations are discussed in the following section.

1.4.2. Performance Defining Phenomenon in Nanometer Thin Films and Interfaces

Two (micrometer-thin) electrodes pressed against a solid electrolyte PEM make up the essential core of PEFC energy-conversion system. However, this seemingly simple structure contains many interfaces at different length scales that are critical for power generation. Figure 1-6 shows a schematic of the various components of PEFC at a range of length scales. Key exchanges, interactions, and reactions occur at the nanometer length electrode interface that define performance at the system level. The focus of this work revolves around this critical interface. Due to the CLs relatively small thickness and heterogeneous nature, identifying the source of mass-transport resistances from limiting-current results lacks precision.[83] Transport resistance in the CL occurs due to minimized accessibility to active sites and species (H^+, electrons, and gas). Accessibility to H^+ in the CL results from impeded ion transport through the ionomer thin film. This could be due to ionomer morphological variation that result in reduced proton mobility in-plane, due to surface water distribution, or reduction in overall water content in ionomer thin film.[84] Accessibility to electrons has to do with C support; porosity and pore geometry of the C inside the CL can impact gas-transport resistance. High-surface-area C supports have numerous primary pores and allow Pt nanoparticles to be deposited inside nanometer pore space.[85,86] As a result of this structure, there is increasing amount of uncoated active Pt sites, increase in electroactive surface, and increase in H^+ shuttled via condensed water without requiring diffusion through an ionomer thin-film coating.[86] Accessibility of gas has to do with a resistive coating on Pt and available Pt active site. The latter resistance is associated with access to Pt sites that can be limited due to Pt oxidation and ionomer sulfate adsorption at the Pt active surface.[87,88] The former resistance is commonly assigned to the total sum of resistance at the Pt/ionomer interface, through the ionomer thin film, and at the ionomer/pore(gas) interface.[19,27,89] A clear delineation and quantification of the contribution of each source of resistance requires in-depth understanding of the impact of ionomer confinement at near-free (air/gas) surfaces and solid interfaces.

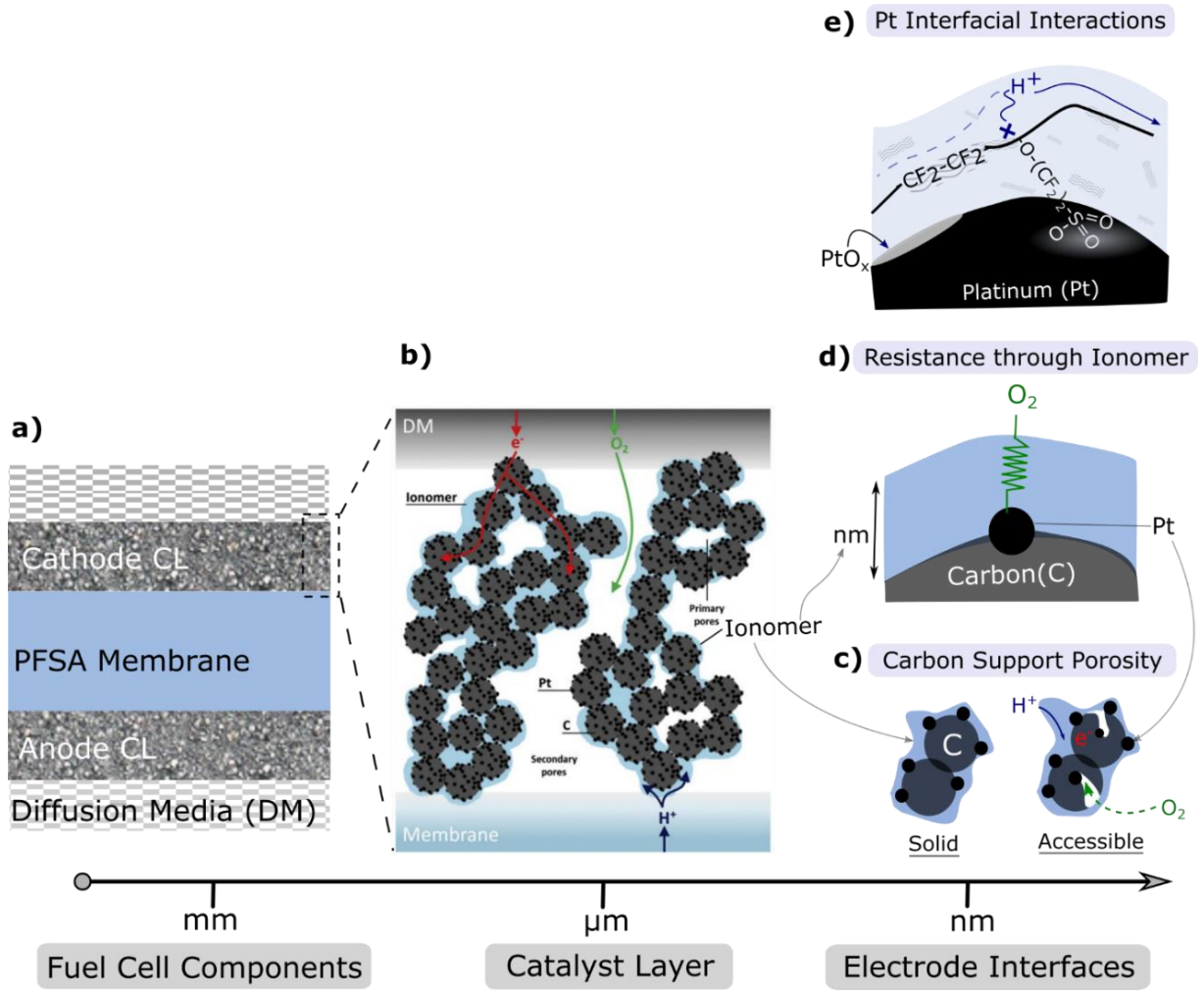

Figure 1-6: Schematic of fuel cell components at different length scales. Catalyst layer schematic reprinted from *J. Power Sources*, 344, Cetinbas, F. C.; Ahluwalia, R. K.; Kariuki, N.; De Andrade, V.; Fongalland, D.; Smith, L.; Sharman, J.; Ferreira, P.; Rasouli, S.; Myers, D. J., Hybrid Approach Combining Multiple Characterization Techniques and Simulations for Microstructural Analysis of Proton Exchange Membrane Fuel Cell Electrodes, 62–73, Copyright (2017), with permission from Elsevier.

1.4.3. Proton Conductivity and Gas-Transport Losses in PEFC Electrodes

The ionomer binder in the CL is critical to create a well-bonded and connected electrode-membrane interface and allow optimal transport of H^+, gas, and water to/from the catalytic sites. In CLs, recast thin-film ionomers of thicknesses < 100 nm aid proton conduction and extend the reaction zone of the CL.[90] As catalyst binders, ionomer thin films at the Pt surface have slightly different requirements and challenges relative to bulk PEM ionomer electrolytes. An ideal thin film exhibits (1) fast gas/species transport, (2) good connective interface with catalytic site, (3) compatibility with electrolyte and catalyst support for ease of casting, (4) ability to withstand highly oxidative environment (5) high ion conductivity, (6) high mechanical, thermal, and chemical stability, and (7) ease of processability during ink casting. The later three are requirements shared with bulk PEM electrolyte and reasons for employment of PFSA ionomers both as electrode binder and solid electrolyte separator. The former four are unique to the ionomer in the electrode and a case for separating ionomer design for CL and membrane separators.

Additionally, the first two requirements are key bottlenecks for CL performance in PEFCs as they contribute 60 to 80% of total mass-transport losses.[91–94] Several investigators have provided significant insight into these losses in CLs, with *operando* studies employing MEAs with varying Pt and ionomer loading. In doing so, they identified an unknown source of mass-transport resistance, which is a lumped sum of local resistances comprising the gas/ionomer and Pt/ionomer interfaces as well as resistance to transport through the ionomer.[19,89,93,95–98] Figure 1-7 shows these local resistance increases with a decrease in Pt loading. However, a clear quantification of the contribution each source of resistance is lacking. Concurrently, voltage loss in electrodes is also experienced due to loss in proton conductivity, especially at low relative humidity (RH). Recent CL studies have reported through-plane proton conductivity as low as two orders of magnitude lower than bulk PEM at ~35% RH and low ionomer/C ratio.[85,99,100] These CLs contained an average ionomer thickness ~2 nm reflecting the impact of ionomer confinement on critical performance metrics. Findings also reported ionomer/C ratio dependent loss in water content of CL, indicating impact of ionomer thickness on performance.[85,101] Although these findings shed light on the reduction in transport property experienced in an operating PEFC, sources of loss in gas and ion transport remain highly coupled with the nature of the nanometer thin-ionomer film and the heterogeneous structure of the CL. Understanding the impact of confinement, thickness, surfaces, and interfaces on ionomer thin film ion and gas-transport properties in an isolated manner can elucidate the sources of losses in the PEFC and expand the ionomer's functionality in PEFCs as well as other solid-state energy devices.

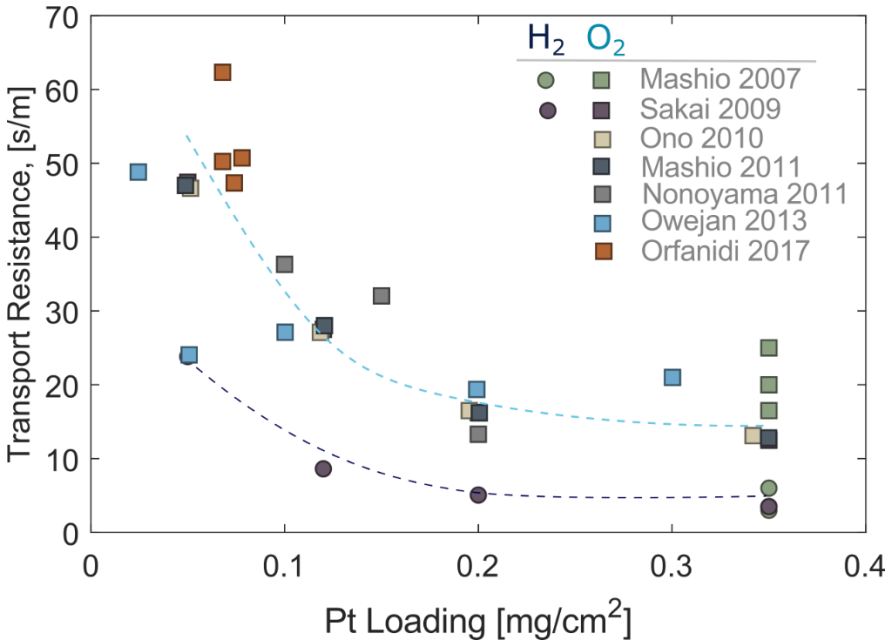

Figure 1-7: Unexplained, pressure independent transport resistance as a function of Pt loading at 80ºC near 100% relative humidity(RH) from refs.[30,93,95,96,98,102,103]

1.5. Confinement Effects in Thin Film Polymers and Ionomers

The need for minimizing material waste, rising interest in microelectronics, and use of polymers in electronic devices, coatings, displays, sensors, optical equipment, and electrochemical devices results in accelerated use of nanometer thin-film polymers.[104] The definition of what is

traditionally termed 'bulk' polymer is referring to >10 μm thick, commercially available polymers whose intrinsic property has not demonstrated any thickness dependence. However, thickness-dependent behavior in polymer films has been observed for thicknesses ranging from several micrometers to nanometer thin films. These are commonly referred to as thin film and ultra-thin-film ionomers (see schematic in Figure 1-8). The general term describing the overall phenomenon that results in thickness-dependent property as polymer-film thickness approaches its characteristic polymer-chain length is termed confinement. Confinement describes a unique state of polymer when the polymer chains are far from their equilibrated state, and experiencing high strain, friction or adhesion imposed by processing conditions. As such, thin and ultra-thin film polymers prepared by various casting methods commonly on different supports demonstrate property deviations from their bulk counterparts.[105] Confinement effects in thin polymer films can be induced due to polymer/surface interaction, polymer/free-surface interaction, and finite-size effects.[106] Confined polymer thin films therefore exhibit properties that are influenced by entropic effects that depend on polymer chain density and distribution, nature of interaction with substrate (positive, negative, neutral), characteristic molecular lengths (like radius of gyration, cooperative chain length), and nature of polymer and chain entanglement.[107,108] Since many or all of these parameters are present in a polymer thin film, perturbations can result in unexplainable responses that deviate from the bulk.

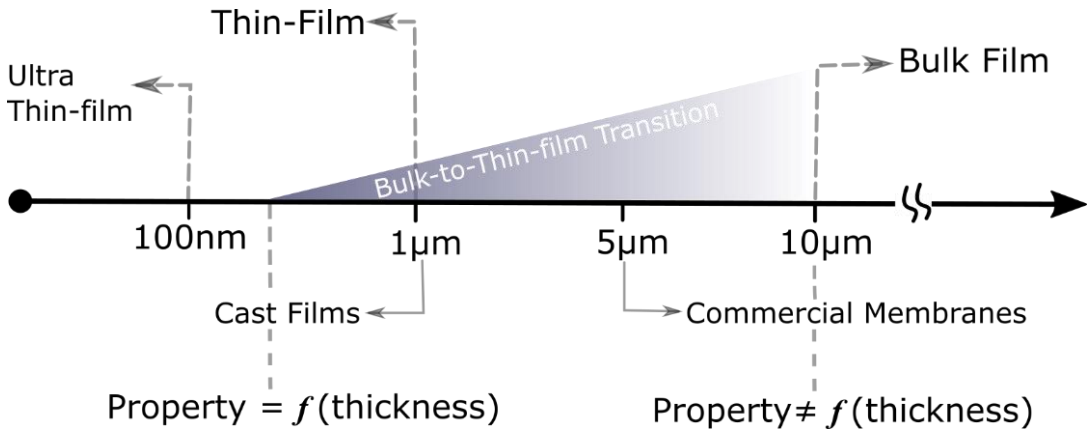

Figure 1-8: Approximate thickness regimes and labels indicating when intrinsic property becomes thickness dependent.

Probes aimed at understanding these dynamic properties of thin-film polymers have started to take center stage after two and half decades.[109] Evidence of confinement on thin-film polymer properties and structure has been studied via spectroscopic ellipsometry (SE),[110–117] X-ray reflectivity (XR),[118,119] Brillouin light scattering (BLS),[120,121] second harmonic generation (SHG),[122] nano-indentation,[123] fluorescence techniques,[112,113,122,124–126] atomic force microscopy (AFM),[127,128] Fourier transform infrared spectroscopy (FT-IR),[115] cantilever beam bending,[129,130] capacitive scanning dilatometry[131], dielectric spectroscopy[131,132], positron lifetime spectroscopy (PAL), and gas permeability[133,134] starting in the late 1990's. Examination of thin films have focused on three main aspects: (1) intrinsic changes to polymer thin-film property due to finite-size effects, (2) pinning and polymer chain/substrate interaction for substrate supported thin films, and (3) changes to chain mobility and relaxation near free surface interface for both free-standing and supported thin films. Finite-size effects in thin-film polymers arise as polymer thickness approaches cooperative length in the polymer. As a result, polymer dynamics and properties that

involve cooperation are effectively altered in thin-film polymers relative to their bulk form.[106] Finite-size effects can alter relaxation dynamics, mechanical properties, glass-transition temperature, ageing and relaxation property, and polymer density. Confinement to dimensions on the order of few radii of gyration of the polymer has been shown to change chain dimensions parallel to surfaces.[135] Chain confirmation and configurations observed with scattering techniques indicate elongated in-plane persistent length in polystyrene thin films.[136] Increase in viscoelasticity and entanglement has also been reported for ultra-thin polyphenylmethysiloxane polymers confined to mica supports.[137] Due to confinement physical ageing, a phenomenological approach towards some equilibrated state for inherent in the naturally non-equilibrated glassy polymers, is expected to result in a drift in measured property as a function of time and is accelerated in thin-film polymers.[133,138]

Proximity to free (vacuum/air) and rigid (substrate/interface) surfaces also impacts packing distribution, morphology and orientation as well as relaxation dynamics in thin-film polymers. Using substrate supported polymer thin films, Virgiliis et al. demonstrated that near-free surfaces experience ease in hydrogen bonding and reduced polymer-chain sterics, and are associated with enhanced mobility of chains while reduced mobility and restricted dynamics are observed near supported surfaces.[139] Experimentally, employing X-ray reflectivity, Reiter demonstrated polystyrene films supported on a glass substrate have a density distribution that decreases with increasing distance from substrate.[140] Such a distribution is argued to increase mobility near-free surfaces.[141] Relaxation dynamics observed using dye molecular probes and atomistic molecular simulations have also reported similar differences in mobility near substrate and free surfaces.[142–144] Priestley and co-workers demonstrated impeded relaxation (factor of 2 to 15x), in poly(methyl methacrylate) (PMMA) polymers near the substrate with influence that spanned more than 100 nm into the film interior.[144] Frank et al. used small-molecule-tagging experimental techniques to capture reduced polymer thin-film chain self-diffusion of polystyrene with reduction in thickness; a drop in bulk polymer self-diffusion coefficient began ~150 nm.[145] These examples denote that deviation from bulk properties starts to take place at thicknesses greater than cooperative length scales, which points to the critical role of substrate and free-interface interactions.[120,146] The interaction with substrate and free surface has also resulted in conflicting results that are compounded by other factors like nature of the polymer/substrate interaction and molecular-weight effects. That is, near free surfaces low molecular-weight polymers show increased mobility whereas high molecular weight polymers demonstrate no significant change.[145,147] However, at solid surfaces positive, negative, and neutral interactions between polymer/substrate dictate the resultant change in properties of thin films from bulk properties. Attractive interactions between polymer and substrate increase the glass-transition temperature and mechanical properties. Negative/neutral interaction are dominated by free-surface effects that result in the opposite trends. Thin-film PMMA supported on silicon supports with a native oxide reportedly increase glass-transition temperature, and modulus especially at the immediate vicinity of the substrate due to enhanced hydrogen bonding.[110,148–150] Alternatively, weakening interaction via non-interacting, hydrophobic or brush or grafting techniques results in variations that depend on processing conditions, wettability of substrate, and degree of polymer-chain adsorption at the interface.[110,124,132,135,146,151–153]

Similar phenomena can be expected for ionomer thin films found in the CL. There is growing evidence of change in structure and property ionomers confined to thin film (< 1 μm) and ultra-thin film (< 100 nm) thicknesses that are highly influenced by processing and operating conditions. At these thicknesses, ionomers are approaching the elongated ionomer rod length or the same order

of magnitude as ionomer coils and therefore highly sensitive to interfaces. Although some consensus has been built around the effect of confinement on thin-film homopolymers; ionomer thin film literature mainly focusing on PFSA shows scattered and at times contradictory results.[17,19,84] This is mainly due to the fact that there is variability in processing solvents, casting methodology, post-film formation heat treatment, and variation in storage and test environmental conditions.[84] The hygroscopic nature of ionomers also adds complexity to these phenomena. Both structure and properties are changing due the presence of water.

Current studies of ionomer thin films show evidence for deviation of ionomer thin-film properties from that of bulk. The molecular origin of this deviation is largely speculative and remains unknown. Notably, reduction in ionomer thin-film conductivity by 2/3rd to 1/7th of bulk ionomer has been reported with experiments employing ionomer thin films coated on planar electrodes.[154–157] Activation energy of conductivity was also observed to increase by a factor of 3 from the bulk ionomer, reflecting the increased limitation in proton mobility experienced in thin films.[158,159] Water uptake and transport has also been shown to be dramatically impacted by confinement to thicknesses < 100 nm.[43,84,160] Reduction in swelling dimension of ionomer thin films supported on various substrates has been reported for thicknesses < 1 μm.[161–164] Eastman et al. demonstrated reduction of through-plane water diffusion coefficient from bulk values. A rapid loss by orders of magnitude in water diffusion coefficient was observed for thicknesses beginning ~200 nm.[165] An increase in modulus upon confinement has also been shown by a few researchers.[130,166,167] Observed property changes are highly correlated with substrate impacts, thickness, and morphological changes in ionomer thin films.[164,168] For instance, loss of crystallinity in spin-cast thin-film ionomers and localization of crystallites near the substrate caused by annealing has been invoked to explain impeded proton diffusion near the electrode/ionomer interface.[155,160,169] Spectroscopic studies looking at ionomer orientation on different supports report greater parallel structural alignment near metallic surfaces, which has been shown to impact activation energy of proton transport.[156,170] Substrate-dependent morphological changes like increased anisotropic parallel orientation on Pt and loss in phase separation with thickness have also been reported from scattering studies.[43,84] Exploring, understanding, and correlating structural and molecular origins of ionomer thin films with their thickness-dependent property is the goal of this work. In this study, model ionomer/substrate systems are utilized to characterize ionomer thin-film behavior.

1.6. Use of Model Systems to Probe Thin-Film Ionomers and Interfaces

CL ionomer thin-film performance metrics like gas transport and proton conductivity are strongly correlated to ionomer processing, chemistry, and structure. Transmission electron microscopy (TEM) images of actual electrodes show variable distribution of ionomer on the surfaces of both Pt and C particles.[171] As already noted, the electrode structure is complex with variable C-support porosity and non-uniform Pt-site distributions. The interface is further made complex by operating conditions (like temperature, humidity, and potential) that impact the surfaces in different ways and by operation events like start/stop cycles as well as continual withdrawal of power for extended periods of time. Additionally, the CL electrode interface is a high kinetic and transport traffic site where multiple species (water, gas, protons, and electrons) are shuttled at varying rates and routes. Therefore, detangling the impact of one component, condition, or factor from the observed performance is a challenging task. Model systems of ionomer-coated substrates offer elementary units that can progressively build to resemble the

complex structure of CL electrodes and interfaces (see Figure 1-9). Model systems allow for improved control of operating conditions, surface variability, ionomer chemistry, gaseous environment, reactions, etc. In such controlled scenarios, the impact of the multitudes of factors and species conveying through the interface can be detangled from the fundamental underlying dynamics that result in a given performance in the electrode. Prime model systems employed in this dissertation are ionomer thin films coated on silicon (Si/SiO_2) substrates. Such model systems also allow translation of technique and understandings between non-ionic polymer thin films examined in the polymer thin-film community to ionomer thin film exploration studies that remain largely unexplored. Introduction of factors pertinent to PEFC electrode interfaces can be accomplished by using additional substrates (Pt, C, Au), alternating substrate identity (interdigitated electrodes), inducing potential gradients (using planar or disk electrodes), exposing to gaseous environments (oxidizing, reducing and inert gases), and varying ionomer thickness (using coating techniques) and chemistry (Nafion, 3M, multiple IEC). It must be noted that model systems can never truly represent the complex structure and activity that an electrode or even a single Pt site may experience. Bulk planar surface (like continuous polycrystalline Pt substrate) does not adequately describe the highly rough interface the ionomer thin film binder experiences in a real CL. Additionally bulk planar surfaces also limit observed phenomenon (like gas diffusion, volume expansivity) in only one dimension perpendicular from the substrate, while real thin films in the CL have activities that need to be captured in all three dimensions. In model systems multi-dimensional, multi-species and multi-interface interactions are forsaken for a focused glimpse into single measurable properties under well-defined constraints. Therefore, it is not necessary for model systems to capture all phenomena, rather critical that they elucidate the influence of a single factors with direct observable properties that can accurately be captured. This makes model systems ideal in providing tunable variables and surface specific parameters that are critical for systems scale modeling and design optimization.

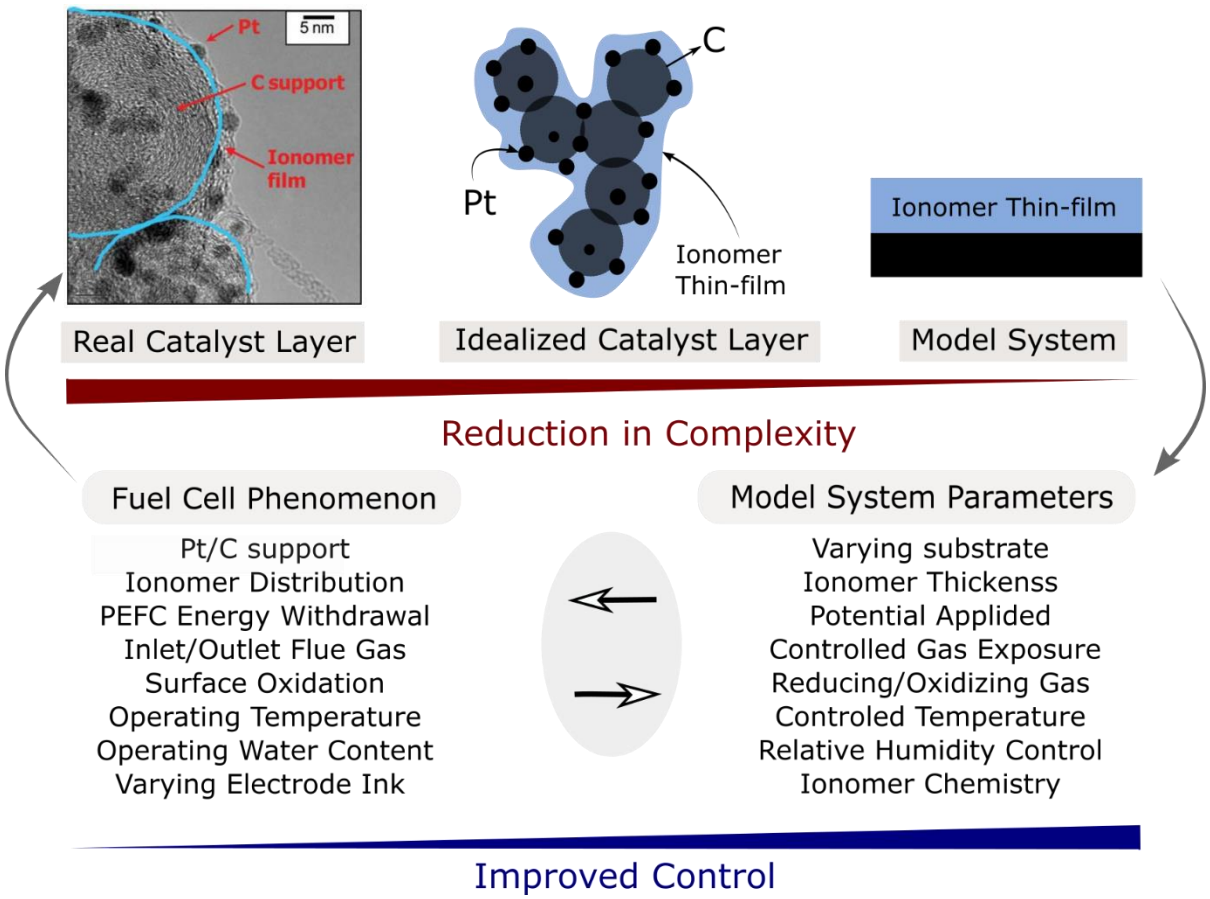

Figure 1-9: Role of model systems as a way of simplifying complexity and improving control of highly complex, heterogeneous system like catalyst layers.

1.7. Overall Research Objectives and Chapter Outline

This study aims to understand the impact of confinement, substrate, and surface interaction on the properties and performance of ionomer thin films employed in PEFC electrodes. This work aims to answer critical questions around the impact of nanometer thin-ionomer films like:

- How does confinement alter ionomer structure and transport properties?
- Does confinement explain the transport limitations observed in PEFC CLs?
- What tunable parameters control confinement effects and deviations of properties from that of bulk behavior?
- What lessons can we draw about designing ionomer systems that induce favorable thin-film ionomer behavior?
- How can ionomer thin-film interactions be controlled to optimize performance and stability?

In pursuit of answering these questions, the following chapters discuss details of explored parameters and insights gained as a result.

Chapter 2: Ionomer thin film-coated Pt surfaces can serve as model systems providing a focused glimpse into the heterogeneous dynamics and complex interfaces of the catalyst layer. Water-vapor sorption dynamics of dispersion-cast Nafion thin films under reducing (H_2), oxidizing (Air), and inert (Ar, N_2) environments are investigated to understand the Pt/ionomer interaction in

both the anode and cathode catalyst layers. Findings in this chapter indicate decreased swelling, increased densification of ionomer matrix, and increased humidity-induced aging rates in reducing environment as compared to oxidizing and inert environments. Observed phenomenon are related to underlying Pt/gas interaction dictating Pt/ionomer behavior.

Chapter 3: This chapter highlights the effects of confinement and interface-dependent interactions of ionomer thin films by exploring thin-film thermal-transition temperature. Change in thermal-transition temperature in polymers is an indicator for chain relaxation and mobility with implications on properties like gas transport. Results point to an interplay between increased chain mobility at the free surface and hindered motion near the rigid substrate interface, which is amplified upon further confinement. Understanding the molecular/morphological origins of relaxation dynamics, therefore, can help establish bottom-up approaches for designing polymers with desired structure-function relationships.

Chapter 4: This chapter extends the fundamental insights from bulk PFSA membranes to thin-film ionomers coating the electrocatalyst. Although both thin-film ionomers and bulk membranes are sourced from the same polymer, confinement and finite-size effects in thin films point towards deviation of thin-film ionomer behavior from bulk membrane, as discussed in Chapter 1. As such, local impacts of co-alloy leaching and cation contamination in thin ionomer films requires additional attention. Impact of cations on thin-film ionomers so far remains unexplored with few studies focused on the impact of transition-metal cations limiting fundamental understanding to specific cations. In this work, water uptake and morphology of ionomer thin films of thickness 20 to 200 nm are investigated as a function of different cation doping amounts. Metal-cation exchanged ionomers demonstrate strong ionic association in the ionomer, making the intramolecular forces within the matrix dominate over the forces present at the ionomer/substrate interface.

Chapter 5: Local gas-transport limitation attributed to the ionomer thin film in the catalyst layer is a major deterrent to widespread commercialization of PEFCs. Thus far, measurements of ionomer thin-film gas-transport parameters have involved several *in-situ* techniques. This chapter discusses gas permeability of bulk ionomers, parameters that control their properties, and extends the main insights gained to ionomer thin films. To that effort, three different methods aimed at capturing ionomer thin-film gas permeability are surveyed. By combining these methodologies with Chapters 2 thru 4, new understanding of confinement effects on gas transport is gained.

Chapter 6: The final chapter in this dissertation contextualizes the work with greater research and development needed for the advancement of PEFCs. It also provides a summary of findings and future directions relevant to the development and optimization of materials for solid-state energy-conversion devices.

1.8. References

(1) Rankoana, S. A. Human Perception of Climate Change. Weather 2018, 73 (11), 367–370.

(2) Schleussner, C. F.; Rogelj, J.; Schaeffer, M.; Lissner, T.; Licker, R.; Fischer, E. M.; Knutti, R.; Levermann, A.; Frieler, K.; Hare, W. Science and Policy Characteristics of the Paris Agreement Temperature Goal. Nat. Clim. Chang. 2016, 6 (9), 827–835.

(3) Obama, B. The Irreversible Momentum of Clean Energy. Science (80-.). 2017, 355 (6321), 126–129.
(4) Badwal, S. P. S.; Giddey, S. S.; Munnings, C.; Bhatt, A. I.; Hollenkamp, A. F. Emerging Electrochemical Energy Conversion and Storage Technologies. Front. Chem. 2014, 2 (September), 1–28.
(5) Staffell, I.; Scamman, D.; Abad, A. V.; Balcombe, P.; Dodds, P. E.; Ekins, P.; Shah, N.; Ward, K. R. The Role and Status of Hydrogen and Fuel Cells across the Global Energy System. Energy Environ. Sci. 2019.
(6) Tenhaeff, W. E.; Yu, X.; Hong, K.; Perry, K. A.; Dudney, N. J. Ionic Transport Across Interfaces of Solid Glass and Polymer Electrolytes for Lithium Ion Batteries. J. Electrochem. Soc. 2011, 158 (10), A1143.
(7) Steele, B. C.; Heinzel, A. Materials for Fuel-Cell Technologies. Nature 2001, 414 (6861), 345–352.
(8) Pereira, E. C.; Cuesta, A. A Personal Perspective on the Role of Electrochemical Science and Technology in Solving the Challenges Faced by Modern Societies. J. Electroanal. Chem. 2016, 780, 355–359.
(9) Mekhilef, S.; Saidur, R.; Safari, A. Comparative Study of Different Fuel Cell Technologies. Renew. Sustain. Energy Rev. 2012, 16, 981–989.
(10) Mathias, M. F.; Makharia, R.; Gasteiger, H. A.; Conley, J. J.; Fuller, T. J.; Gittleman, C. J.; Kocha, S. S.; Miller, D. P.; Mittelsteadt, C. K.; Xie, T.; et al. Two Fuel Cell Cars In Every Garage ? Electrochem. Soc. Interface 2005.
(11) Jones, Philip B; Levy, J.; Bosco, J.; Howat, J.; Van Alst, John W; Schwartz, L. The Future of Transportation Electrification: Utility, Industry and Consumer Perspectives; 2018.
(12) Greenblatt, J. B.; Miller, D. J.; Ager, J. W.; Houle, F. A.; Sharp, I. D. The Technical and Energetic Challenges of Separating (Photo)Electrochemical Carbon Dioxide Reduction Products. Joule 2018, 2 (3), 381–420.
(13) Botte, G. G. Electrochemical Manufacturing in the Chemical Industry. Electrochem. Soc. Interface 2014, 23 (3), 49–55.
(14) Anderson, M. A.; Cudero, A. L.; Palma, J. Capacitive Deionization as an Electrochemical Means of Saving Energy and Delivering Clean Water. Comparison to Present Desalination Practices: Will It Compete? Electrochim. Acta 2010, 55 (12), 3845–3856.
(15) Page, K. A.; Rowe, B. W. An Overview of Polymer Electrolyte Membranes for Fuel Cell Applications. ACS Symp. Ser. 2012, 1096, 147–164.
(16) Peighambardoust, S. J.; Rowshanzamir, S.; Amjadi, M. Review of the Proton Exchange Membranes for Fuel Cell Applications; Elsevier Ltd, 2010; Vol. 35.
(17) Karan, K. PEFC Catalyst Layer: Recent Advances in Materials, Microstructural Characterization, and Modeling. Curr. Opin. Electrochem. 2017, 5 (1), 27–35.
(18) Cetinbas, F. C.; Ahluwalia, R. K.; Kariuki, N.; De Andrade, V.; Fongalland, D.; Smith, L.; Sharman, J.; Ferreira, P.; Rasouli, S.; Myers, D. J. Hybrid Approach Combining Multiple Characterization Techniques and Simulations for Microstructural Analysis of Proton Exchange Membrane Fuel Cell Electrodes. J. Power Sources 2017, 344, 62–73.
(19) Kongkanand, A.; Gu, W.; Mathias, M. F. Proton-Exchange Membrane Fuel Cells with Low-Pt Content. In Encyclopedia of Sustainability Science and Technology; 2018.
(20) Weber, A. Z.; Newman, J. Transport in Polymer-Electrolyte Membranes. J. Electrochem. Soc. 2003, 150 (7), A1008.

(21) Stamenkovic, V. R.; Strmcnik, D.; Lopes, P. P.; Markovic, N. M. Energy and Fuels from Electrochemical Interfaces. Nat. Mater. 2016, 16 (1), 57–69.
(22) Debe, M. K. Electrocatalyst Approaches and Challenges for Automotive Fuel Cells. Nature 2012, 486 (7401), 43–51.
(23) Ralph, T. R.; Hogarth, M. P. Catalysis for Low Temperature Fuel Cells PART I: THE CATHODE CHALLENGES. Platin. Met. Rev. 2002, 46 (1), 3–14.
(24) Auer, E.; Freund, A.; Pietsch, J.; Tacke, T. Carbons as Supports for Industrial Precious Metal Catalysts. Appl. Catal. A Gen. 1998, 173 (2), 259–271.
(25) Vedrine, J. C. .; Dufaux, M. ; Naccache, C.; Imelik, B. ; X-Ray Photoelectron Spectroscopy Study of Pd and Pt Ions in Type Y-Zeolite. Faraday Trans 1978, No. X, 440–449.
(26) Yu, X.; Ye, S. I Recent Advances in Activity and Durability Enhancement of Pt/C Catalytic Cathode in PEMFC. Part I. Physico-Chemical and Electronic Interaction between Pt and Carbon Support, and Activity Enhancement of Pt/C Catalyst. J. Power Sources 2007, 172 (1), 133–144.
(27) Kongkanand, A.; Mathias, M. F. The Priority and Challenge of High-Power Performance of Low- Platinum Proton-Exchange Membrane Fuel Cells. J. Phys. Chem. Lett. 2016, 7, 1127–1137.
(28) Zhao, X.; Li, W.; Fu, Y.; Manthiram, A. Influence of Ionomer Content on the Proton Conduction and Oxygen Transport in the Carbon-Supported Catalyst Layers in DMFC. Int. J. Hydrogen Energy 2012, 37 (12), 9845–9852.
(29) Andersen, S. M.; Grahl-Madsen, L. Interface Contribution to the Electrode Performance of Proton Exchange Membrane Fuel Cells - Impact of the Ionomer. Int. J. Hydrogen Energy 2016, 41 (3), 1892–1901.
(30) Orfanidi, A.; Madkikar, P.; El-Sayed, H. A.; Harzer, G. S.; Kratky, T.; Gasteiger, H. A. The Key to High Performance Low Pt Loaded Electrodes. J. Electrochem. Soc. 2017, 164 (4), F418–F426.
(31) Hatzell, K. B.; Dixit, M. B.; Berlinger, S. A.; Weber, A. Z. Understanding Inks for Porous-Electrode Formation. J. Mater. Chem. A 2017, 5 (39), 20527–20533.
(32) Padgett, E.; Andrejevic, N.; Liu, Z.; Kongkanand, A.; Gu, W.; Moriyama, K.; Jiang, Y.; Kumaraguru, S.; Moylan, T. E.; Kukreja, R.; et al. Connecting Fuel Cell Catalyst Nanostructure and Accessibility Using Quantitative Cryo-STEM Tomography. J. ofThe Electrochem. Soc. 2018, 165 (3).
(33) Hart, David; Lehner, Franz; Rose, Robert; Lewis , Jonathan; Klippenstein, M. The Fuel Cell Industry Review 2015; 2015.
(34) Council, H. How Hydrogen Empowers the Energy Transition; 2017.
(35) Satyapal, S. Hydrogen & Fuel Cells Program Overview. In DOE Annual Merit Review; 2011.
(36) Martin, C. FedEx Rolls Out First Hydrogen-Fueled Delivery Van in New York. Bloomberg. 2018.
(37) Curtin, S.; Gangi, J. State of the States: Fuel Cells in America 2016. U.S. Dep. Energy 2016, No. November, 1–46.
(38) Yarlagadda, V.; Carpenter, M. K. .; Moylan, T. E. .; Kukreja, Ratandeep Singh; Koestner, R.; Gu, W.; Thompson, L.; Kongkanand, A. Boosting Fuel Cell Performance with Accessible Carbon Mesopores. ACS Energy Lett. 2018, 3, 618–621.
(39) Loppinet, B.; Gebel, G.; Williams, C. E. Small-Angle Scattering Study of Perfluorosulfonated Ionomer Solutions. J. Phys. Chem. B 1997, 101 (10), 1884–1892.

(40) Gebel, G.; Diat, O. Neutron and X-Ray Scattering: Suitable Tools for Studying Ionomer Membranes. Fuel Cells 2005, 5 (2), 261–276.
(41) Schlick, S. Ionomers: Characterization, Theory, and Applications; 1996.
(42) Liu, W.; Janik, M. J.; Colby, R. H. First Principles Design of Ionomers for Facile Ion Transport. In Polymers for energy storage and delivery: polyelectrolytes for batteries and fuel cells; American Chemical Society, 2012; pp 19–44.
(43) Kusoglu, A.; Weber, A. Z. New Insights into Perfluorinated Sulfonic-Acid Ionomers. Chem. Rev. 2017, 117, 987–1104.
(44) Hickner, M. A.; Ghassemi, H.; Kim, Y. S.; Einsla, B. R.; McGrath, J. E. Alternative Polymer Systems for Proton Exchange Membranes (PEMs). Chem. Rev. 2004, 104 (10), 4587–4611.
(45) Higashihara, T.; Matsumoto, K.; Ueda, M. Sulfonated Aromatic Hydrocarbon Polymers as Proton Exchange Membranes for Fuel Cells. Polymer (Guildf). 2009, 50 (23), 5341–5357.
(46) Miller, A. D.; Gervais, M.; Krishnamurthy, J.; Dyers, L.; Zhu, X.; Potrekar, R.; Fei, X.; Weber, A.; Kerr, J. B. Polymer Materials for Charge Transfer in Energy Devices. ACS Symp. Ser. 2012, 1096, 165–174.
(47) Kim, Y. S.; Pivovar, B. S. Moving Beyond Mass-Based Parameters for Conductivity Analysis of Sulfonated Polymers. Annu. Rev. Chem. Biomol. Eng. 2010, 1 (1), 123–148.
(48) Hickner, M. A. Ion-Containing Polymers: New Energy & Clean Water. Mater. Today 2010, 13 (5), 34–41.
(49) Hinatsu, J. T. Water Uptake of Perfluorosulfonic Acid Membranes from Liquid Water and Water Vapor. J. Electrochem. Soc. 1994, 141 (6), 1493.
(50) Kreuer, K. D.; Schuster, M.; Obliers, B.; Diat, O.; Traub, U.; Fuchs, a.; Klock, U.; Paddison, S. J.; Maier, J. Short-Side-Chain Proton Conducting Perfluorosulfonic Acid Ionomers: Why They Perform Better in PEM Fuel Cells. J. Power Sources 2008, 178 (2), 499–509.
(51) Tsou, Yu-Min; Kimble, M. C.; White, R. E. . Hydrogen Diffusion, Solubility and Water Uptake in SSC and Perflorocarbon Membra. J. Electrochem Soc. 1992, 139 (7), 1913–1917.
(52) Park, Y. C.; Kakinuma, K.; Uchida, H.; Watanabe, M.; Uchida, M. Effects of Short-Side-Chain Perfluorosulfonic Acid Ionomers as Binders on the Performance of Low Pt Loading Fuel Cell Cathodes. J. Power Sources 2015, 275, 384–391.
(53) Schaberg, Mark S.; Abulu, J.E.; Haugen, G.M.; Emery, M. A.; O'Conner, S. J.; Xiong, P.N.; Hamrock, S. J. New Multi Acid Side-Chain Ionomers for Proton Exchange Membrane Fuel Cells. ECS Trans. 2010, 33 (1), 627–633.
(54) Appleby, A. J.; Vellev, O. A.; Lehelloco, J. G.; Parthasarthy, A.; Srinivasan, S.; Desmarteau, D. . D.; Gillette, M. S.; Ghosh, J. K. Polymeric Perfluoro Bis-Sulfonimides As Possible Fuel-Cell Electrolytes. J. Electrochem. Soc. 1993, 140 (1), 109–111.
(55) Hamrock, S. J.; Yandrasits, M. a. Proton Exchange Membranes for Fuel Cell Applications. J. Macromol. Sci. Part C 2006, 46 (3), 219–244.
(56) Bolintineanu, D. S.; Stevens, M. J.; Frischknecht, A. L. Influence of Cation Type on Ionic Aggregates in Precise Ionomers. Macromolecules 2013, 46 (13), 5381–5392.
(57) Okada, T. Ion and Water Transport Characteristics in Membranes for Polymer Electrolyte Fuel Cells Containing H+ and Ca 2+ Cations. J. Electrochem. Soc. 1997, 144 (8), 2744.
(58) Yeager, H. L.; Steck, A. Cation and Water Diffusion in Nafion Ion Exchange Membranes: Influence of Polymer Structure. J. Electrochem. Soc. 1981, 128 (9), 1880.

(59) Shi, S.; Weber, A. Z.; Kusoglu, A. Structure-Transport Relationship of Perfluorosulfonic-Acid Membranes in Different Cationic Forms. Electrochim. Acta 2016, 220, 517–528.
(60) Fan, Y.; Tongren, D.; Cornelius, C. J. The Role of a Metal Ion within Nafion upon Its Physical and Gas Transport Properties. Eur. Polym. J. 2014, 50, 271–278.
(61) Lage, L. G.; Delgado, P. G.; Kawano, Y. Thermal Stability and Decomposition of Nafion Membrane with Different Cations Using High-Resolution Thermogravimetry. J. Therm. Anal. Calorim. 2004, 75, 521–530.
(62) Kusoglu, A.; Santare, M. H.; Karlsson, A. M.; Cleghorn, S.; Johnson, W. B. Micromechanics Model Based on the Nanostructure of PFSA Membranes. J. Polym. Sci. Part B Polym. Phys. 2008, 46 (22), 2404–2417.
(63) Gebel, G.; Aldebert, P.; Pineri, M. Structure and Related Properties of Solution-Cast Perfluorosulfonated Ionomer Films. Macromolecules 1987, 20 (6), 1425–1428.
(64) Allen, F. I.; Comolli, L. R.; Kusoglu, A.; Modestino, M. A.; Minor, A. M.; Weber, A. Z. Morphology of Hydrated As-Cast Na Fi on Revealed through Cryo Electron Tomography. ACS Macro Lett. 2015, 4.
(65) Yang, Y.; Holdcroft, S. Synthetic Strategies for Controlling the Morphology of Proton Conducting Polymer Membranes. Fuel Cells 2005, 5 (2), 171–186.
(66) Tant, M. R.; Darst, K. P.; Lee, K. D.; Martin, C. W. Structure and Properties of Short-Side-Chain Perfluorosulfonate Ionomers. ACS Symp. Ser. 1989, 395, 370–400.
(67) Roche, E. J.; Pineri, M.; Duplessix, R.; Levelut, a M. Small-Angle Scattering Studies of Nafion Membranes. J. Polym. Sci. Polym. Phys. Ed. 1981, 19 (1), 1–11.
(68) Park, M. J.; Hong, J.; Kim, S. Y. Role of Nanostructures in Polymer Electrolytes for Energy Storage and Delivery. In ACS Symposium Series 1096; Polymers for Energy Storage and Delivery: Polyelectrolytes for Batteries and Fuel Cells; 2012; pp 129–146.
(69) Yousfi-Steiner, N.; Moçotéguy, P.; Candusso, D.; Hissel, D. A Review on Polymer Electrolyte Membrane Fuel Cell Catalyst Degradation and Starvation Issues: Causes, Consequences and Diagnostic for Mitigation. J. Power Sources 2009, 194 (1), 130–145.
(70) Zecevic, S. K.; Wainright, J. S.; Litt, M. H.; Gojkovic, S. L.; Savinell, R. F. Kinetics of 02 Reduction on a Pt Electrode Covered with a Thin Film of Solid Polymer Electrolyte. J. Electrochem. Soc. J. Am. Chem. Soc. Chem. Phys. Carbon, P. A. Thrower, Ed. Langmuir This J. J. Power Sources This J. Sci. 1997, 144 (264), 2973–2982.
(71) Gasteiger, H. A.; Kocha, S. S.; Sompalli, B.; Wagner, F. T. Activity Benchmarks and Requirements for Pt, Pt-Alloy, and Non-Pt Oxygen Reduction Catalysts for PEMFCs. Appl. Catal. B Environ. 2005, 56, 9–35.
(72) Mathias, M. F.; Makharia, R.; Gasteiger, H. a.; Conley, J. J.; Fuller, T. J.; Gittleman, C. J.; Kocha, S. S.; Miller, D. P.; Mittelsteadt, C. K.; Xie, T.; et al. Two Fuel Cell Cars in Every Garage? Electrochem. Soc. Interface 2005, 14, 24–35.
(73) Gröger, O.; Gasteiger, H. A.; Suchsland, J.-P. Review—Electromobility: Batteries or Fuel Cells? J. Electrochem. Soc. 2015, 162 (14), A2605–A2622.
(74) Rao, M. L. B.; Damjanovic, A.; Bockris, J. O. Oxygen Adsorption Related to the Unpaired D-Electrons in Transition Metals. J. Phys. Chem. 1963, 67 (11), 2508–2509.
(75) Debe, M. K.; Schmoeckel, A. K.; Vernstrom, G. D.; Atanasoski, R. High Voltage Stability of Nanostructured Thin Film Catalysts for PEM Fuel Cells. J. Power Sources 2006, 161 (2), 1002–1011.

(76) Kongkanand, A.; Owejan, J. E.; Moose, S.; Dioguardi, M.; Biradar, M.; Makharia, R. Development of Dispersed-Catalyst/NSTF Hybrid Electrode. J. Electrochem. Soc. 2012, 159 (11), F676–F682.
(77) Jaouen, F.; Proietti, E.; Lefèvre, M.; Chenitz, R.; Dodelet, J. P.; Wu, G.; Chung, H. T.; Johnston, C. M.; Zelenay, P. Recent Advances in Non-Precious Metal Catalysis for Oxygen-Reduction Reaction in Polymer Electrolyte Fuel Cells. Energy Environ. Sci. 2011, 4 (1), 114–130.
(78) Kim, T. H.; Yi, J. Y.; Jung, C. Y.; Jeong, E.; Yi, S. C. Solvent Effect on the Nafion Agglomerate Morphology in the Catalyst Layer of the Proton Exchange Membrane Fuel Cells. Int. J. Hydrogen Energy 2017, 42, 478–485.
(79) Kim, Y. S.; Welch, C. F.; Hjelm, R. P.; Mack, N. H.; Labouriau, A.; Orler, E. B. Origin of Toughness in Dispersion-Cast Nafion Membranes. Macromolecules 2015, 48 (7), 2161–2172.
(80) Kim, Y. S.; Welch, C. F.; Mack, N. H.; Hjelm, R. P.; Orler, E. B.; Hawley, M. E.; Lee, K. S.; Yim, S.-D.; Johnston, C. M. Highly Durable Fuel Cell Electrodes Based on Ionomers Dispersed in Glycerol. Phys. Chem. Chem. Phys. 2014, 16 (13), 5927–5932.
(81) Berlinger, S. A. .; Dagan, N. .; McCloskey, B. D. .; Weber, A. Z. . The Effect of PH on Fuel-Cell Catalyst-Layer Inks. ECS Trans. 2018, 86 (13), 133–140.
(82) Berlinger, S. A.; McCloskey, B. D.; Weber, A. Z. Inherent Acidity of Perfluorosulfonic Acid Ionomer Dispersions and Implications for Ink Aggregation. J. Phys. Chem. B 2018, 122 (31), 7790–7796.
(83) Parthasarthy, A.; Srinivasan, S.; Appleby, A. J.; Martin, C. R. Electrode-Kinetics of Oxygen Reduction at Carbon-Supported and Unsupported Platinum Microcrystallite Nafion(R) Interfaces. J. Electroanal. Chem. 1992, 339, 101–121.
(84) Beuscher, U. Experimental Method to Determine the Mass Transport Resistance of a Polymer Electrolyte Fuel Cell. J. Electrochem. Soc. 2006, 153 (9), A1788.
(85) Suzuki, T.; Kudo, K.; Morimoto, Y. Model for Investigation of Oxygen Transport Limitation in a Polymer Electrolyte Fuel Cell. J. Power Sources 2013, 222, 379–389.
(86) Ono;, Y.; Mashio, T.; Takaichi, S.; Ohma, A.; Kanesaka, H.; Shinohara, K. The Analysis of Performance Loss with Low Platinum Loaded Cathode Catalyst Layers. Electrochim. Acta 2010, 28 (27), 69–78.
(87) Kudo, K.; Jinnouchi, R.; Morimoto, Y. Humidity and Temperature Dependences of Oxygen Transport Resistance of Nafion Thin Film on Platinum Electrode. Electrochim. Acta 2016, 209, 682–690.
(88) Weber, A. Z.; Kusoglu, A. Unexplained Transport Resistances for Low-Loaded Fuel-Cell Catalyst Layers. J. Mater. Chem. A 2014, 2 (c), 17207–17211.
(89) Nonoyama, N.; Okazaki, S.; Weber, A. Z.; Ikogi, Y.; Yoshida, T. Analysis of Oxygen-Transport Diffusion Resistance in Proton-Exchange-Membrane Fuel Cells. J. Electrochem. Soc. 2011, 158 (4), B416–B423.
(90) Sakai, K.; Sato, K. ; Mashio, T.; Ohma, A.; Yamaguchi, K.; Shinohara, K. Analysis of Reactant Gas Transport in Catalyst Layers ; Effect of Pt-Loadings. Trans. E C S Soc. Electrochem. 2009, 25 (1), 1193–1201.
(91) Mashio, T.; Iden, H.; Ohma, A.; Shinohara, K. Local Gas Transport in Catalyst Layers of PEM Fuel Cell. J. Electroanal. Chem. 2017, 790.
(92) Owejan, J. P.; Owejan, J. E.; Gu, W. Impact of Platinum Loading and Catalyst Layer Structure on PEMFC Performance. J. Electrochem. Soc. 2013, 160 (8), 824–833.

(93) Iden, H.; Sato, K.; Ohma, A.; Shinohara, K. Relationship among Microstructure, Ionomer Property and Proton Transport in Pseudo Catalyst Layers. J. Electrochem. Soc. 2011, 158 (8), B987.
(94) Liu, Y.; Murphy, M. W.; Baker, D. R.; Gu, W.; Ji, C.; Jorne, J.; Gasteiger, H. A. Proton Conduction and Oxygen Reduction Kinetics in PEM Fuel Cell Cathodes: Effects of Ionomer-to-Carbon Ratio and Relative Humidity. J. Electrochem. Soc. 2009, 156 (8), B970.
(95) Ji, C.; Gasteiger, H. A.; Liu, Y.; Jorne, J.; Gu, W. Effects of Catalyst Carbon Support on Proton Conduction and Cathode Performance in PEM Fuel Cells. J. Electrochem. Soc. 2011, 158 (6), B614.
(96) Kusoglu, A.; Kwong, A.; Clark, K. T.; Gunterman, H. P.; Weber, A. Z. Water Uptake of Fuel-Cell Catalyst Layers. J. Electrochem. Soc. 2012, 159, 530–535.
(97) Mashio, T.; Ohma, A.; Yamamoto, S.; Shinohara, K. Analysis of Reactant Gas Transport in a Catalyst Layer. ECS Trans. 2007, 11 (1), 529–540.
(98) Mashio, T.; Iden, H.; Ohma, A.; Tokumasu, T. Modeling of Local Gas Transport in Catalyst Layers of PEM Fuel Cells. J. Electroanal. Chem. 2017, 790, 27–39.
(99) Darling, R. A Comparison of Models for Transport Resistance in Fuel-Cell Catalyst Layers. J. ofThe Electrochem. Soc. 2018, 165.
(100) Kusoglu, A. Ionomer Thin Films in PEM Fuel Cells. In Encyclopedia of Sustainability Science and Technology; Meyers, R., Ed.; Springer, New York, NY, 2018.
(101) Iden, H.; Mashio, T.; Ohma, A. Gas Transport inside and Outside Carbon Supports of Catalyst Layers for PEM Fuel Cells. J. Electroanal. Chem. 2013, 708, 87–94.
(102) Liu, Y.; Mathias, M.; Zhang, J. Measurement of Platinum Oxide Coverage in a Proton Exchange Membrane Fuel Cell. Electrochem. Solid-State Lett. 2010, 13, B1.
(103) Masuda, T.; Sonsudin, F.; Singh, P. R.; Naohara, H.; Uosaki, K. Potential-Dependent Adsorption and Desorption of Perfluorosulfonated Ionomer on a Platinum Electrode Surface Probed by Electrochemical Quartz Crystal Microbalance and Atomic Force Microscopy. J. Phys. Chem. C 2013, 117 (30), 15704–15709.
(104) Brauman, J. I.; Szuromi, P. Thin Films. Science (80). 1996, 273 (5277), 855.
(105) Frank, C. W.; Rao, V.; Despotopoulou, M. M.; Pease, R. F. W.; Hinsberg, W. D.; Miller, R. D.; Rabolt, J. F. Structure in Thin and Ultrathin Spin-Cast Polymer Films. Science (80). 1996, 273 (5277), 912–915.
(106) Alcoutlabi, M.; McKenna, G. B. Effects of Confinement on Material Behaviour at the Nanometre Size Scale. J. Phys. Condens. Matter 2005, 17 (15), R461–R524.
(107) Tsui, O. K. C. Anomalous Dynamics of Polymer Films. In Polymer Thin Films; World Scientific Publishing Co Pte Ltd, 2008; pp 267–294.
(108) Vogt, B. D. Mechanical and Viscoelastic Properties of Confined Amorphous Polymers. J. Polym. Sci. Part B Polym. Phys. 2018, 56, 9–30.
(109) Roth, C. B.; Dutcher, J. R. Glass Transition and Chain Mobility in Thin Polymer Films. J. Electroanal. Chem. 2005, 584, 13–22.
(110) Keddie, J. L.; Jones, R. A. L.; Cory, R. A. Size-Dependent Depression of the Glass Transition Temperature in Polymer Films. Europhys. Lett. 1994, 27 (1), 59–64.
(111) Kawana, S.; Jones, R. a L. Effect of Physical Ageing in Thin Glassy Polymer Films. Eur. Phys. J. E. Soft Matter 2003, 10 (3), 223–230.

(112) Askar, S.; Torkelson, J. M. Stiffness of Thin, Supported Polystyrene Films: Free-Surface, Substrate, and Confinement Effects Characterized via Self-Referencing Fluorescence. Polym. (United Kingdom) 2016, 99, 417–426.
(113) Kim, S.; Hewlett, S. A.; Roth, C. B.; Torkelson, J. M. Confinement Effects on Glass Transition Temperature, Transition Breadth, and Expansivity: Comparison of Ellipsometry and Fluorescence Measurements on Polystyrene Films. Eur. Phys. J. E 2009, 30 (1), 83–92.
(114) Pye, J. E.; Roth, C. B. Above, below, and in-between the Two Glass Transitions of Ultrathin Free-Standing Polystyrene Films: Thermal Expansion Coefficient and Physical Aging. J. Polym. Sci. Part B Polym. Phys. 2015, 53 (1), 64–75.
(115) Grohens, Y.; Hamon, L.; Reiter, G.; Soldera, A.; Holl, Y. Some Relevant Parameters Affecting the Glass Transition of Supported Ultra-Thin Polymer Films. Eur. Phys. J. E 2002, 8 (2), 217–224.
(116) Dalnoki-Veress, K.; Forrest, J. a; Murray, C.; Gigault, C.; Dutcher, J. R. Molecular Weight Dependence of Reductions in the Glass Transition Temperature of Thin, Freely Standing Polymer Films. Phys. Rev. E 2001, 63 (3), 031801-1–10.
(117) Pye, J. E.; Rohald, K. A.; Baker, E. A.; Roth, C. B. Physical Aging in Ultrathin Polystyrene Films: Evidence of a Gradient in Dynamics at the Free Surface and Its Connection to the Glass Transition Temperature Reductions. Macromolecules 2010, 43 (19), 8296–8303.
(118) Orts, W. J. .; Van Zanten, J. H. .; Wu, W.; Satija, S. K. Observation of Temperature Dependent Thicknesses in Ultrathin Polystyrene Films on Silicon. Phys. Rev. Lett. 1993, 71 (6).
(119) Prucker, O.; Christian, S.; Bock, H.; Rühe, J.; Frank, C. W.; Knoll, W. Glass Transition in Ultrathin Polymer Films of Different Molecular Architecture. Macromol. Chem. Phys. 1998, 199, 1435–1444.
(120) Forrest, J. a; DalnokiVeress, K.; Stevens, J. R.; Dutcher, J. R. Effect of Free Surfaces on the Glass Transition Temperature of Thin Polymer Films. Phys. Rev. Lett. 1996, 77 (111), 2002–2005.
(121) Mattsson, J.; Forrest, J. A.; Börjesson, L. Quantifying Glass Transition Behavior in Ultrathin Free-Standing Polymer Films. Phys. Rev. E 2000, 62 (4), 5187–5200.
(122) Hall, D. B.; Miller, R. D.; Torkelson, J. M. Molecular Probe Techniques for Studying Diffusion and Relaxation in Thin and Ultrathin Polymer Films. J Polym Sci B Polym Phys 1997, 35, 2795–2802.
(123) Harry D. Rowland, William P. King, John B. Pethica, G. L. W. C. Molecular Confinement Accelerates Deformation of Entangled Polymers During Squeeze Flow. Science (80-.). 2008, 322, 720–724.
(124) Priestley, R. D.; Mundra, M. K.; Barnett, N. J.; Broadbelt, L. J.; Torkelson, J. M. Effects of Nanoscale Confinement and Interfaces on the Glass Transition Temperatures of a Series of Poly(n-Methacrylate) Films. Aust. J. Chem. 2007, 60 (10), 765–771.
(125) Shundo, Atsuomi; Okada, Yohei; Ito, Fuyuki; Takana, K. Fluorescence Behavior of Dyes in Thin Films of Various Polymers. Macromolecules 2012, 45, 329–355.
(126) Burroughs, M. J.; Napolitano, S.; Cangialosi, D.; Priestley, R. D. Direct Measurement of Glass Transition Temperature in Exposed and Buried Adsorbed Polymer Nanolayers. Macromolecules 2016, 49 (12), 4647–4655.
(127) Fakhraai, Z; Forrest, J. A.. Measuring the Surface Dynamics of Glassy Polymers. Science (80). 2008, 318.

(128) O'Connell, P. A.; McKenna, G. B. Rheological Measurements of the Thermoviscoelastic Response of Ultrathin Polymer Films. Science (80). 2005, 307, 1760–1763.
(129) Frieberg, B. R.; Page, K. A.; Graybill, J. R.; Walker, M. L.; Stafford, C. M.; Stafford, G. R.; Soles, C. L. Mechanical Response of Thermally Annealed Nafion Thin Films. ACS Appl. Mater. Interfaces 2016, 8 (48), 33240–33249.
(130) Page, K. A.; Shin, J. W.; Eastman, S. A.; Rowe, B. W.; Kim, S.; Kusoglu, A.; Yager, K. G.; Stafford, G. R. In Situ Method for Measuring the Mechanical Properties of Nafion Thin Films during Hydration Cycles. ACS Appl. Mater. Interfaces 2015, 7 (32), 17874–17883.
(131) Yin, H.; Cangialosi, D.; Schönhals, A. Glass Transition and Segmental Dynamics in Thin Supported Polystyrene Films: The Role of Molecular Weight and Annealing. Thermochim. Acta 2013, 566, 186–192.
(132) Napolitano, S.; Wübbenhorst, M. The Lifetime of the Deviations from Bulk Behaviour in Polymers Confined at the Nanoscale. Nat. Commun. 2011, 2 (1).
(133) Huang, Y.; Paul, D. R. Physical Aging of Thin Glassy Polymer Films Monitored by Gas Permeability. Polymer (Guildf). 2004, 45 (25), 8377–8393.
(134) Rowe, B. W.; Freeman, B. D.; Paul, D. R. Physical Aging of Ultrathin Glassy Polymer Films Tracked by Gas Permeability. Polymer (Guildf). 2009, 50 (23), 5565–5575.
(135) Russell, T. P.; Chai, Y. 50th Anniversary Perspective: Putting the Squeeze on Polymers: A Perspective on Polymer Thin Films and Interfaces. Macromolecules 2017, 50 (12), 4597–4609.
(136) Brûlet, A.; Boué, F.; Menelle, A.; Cotton, J. P. Conformation of Polystyrene Chain in Ultrathin Films Obtained by Spin Coating. Macromolecules 2000, 33 (3), 997–1001.
(137) Hu, H.-W.; Granick, S. Visoelastic Dynamics of Confined Polymer Melts. Science (80-.). 1992, 258, 1339–1342.
(138) Huang, Y.; Paul, D. R. Effect of Film Thickness on the Gas-Permeation Characteristics of Glassy Polymer Membranes. Ind. Eng. Chem. Res. 2007, 46 (8), 2342–2347.
(139) De Virgiliis, A.; Milchev, A.; Rostiashvili, V. G.; Vilgis, T. a. Structure and Dynamics of a Polymer Melt at an Attractive Surface. Eur. Phys. J. E. Soft Matter 2012, 35 (97), 1–11.
(140) Reiter, G. Mobility of Polymers in Films Thinner than Their Unperturbed Size. Europhys. Lett. 1993, 23 (8), 579–584.
(141) Wu, W. -l; Orts, W. J.; Van Zanten, J. H.; Fanconi, B. M. Density Profile of Spin Cast Polymethylmethacrylate Thin Films. J. Polym. Sci. Part B Polym. Phys. 1994, 32 (15), 2475–2480.
(142) Ch Daoulas, K.; Harmandaris, V. A.; Mavrantzas, V. G. Detailed Atomistic Simulation of a Polymer Melt/Solid Interface: Structure, Density, and Conformation of a Thin Film of Polyethylene Melt Adsorbed on Graphite.
(143) Rittigstein, P.; Priestley, R. D.; Broadbelt, L. J.; Torkelson, J. M. Model Polymer Nanocomposites Provide an Understanding of Confinement Effects in Real Nanocomposites. Nat. Mater. 2007, 6 (4), 278–282.
(144) Priestley, R. D.; Ellison, C. J.; Broadbelt, L. J.; Torkelson, J. M. Structural Relaxation of Polymer Glasses at Surfaces, Interfaces, and in Between. Science 2005, 309 (5733), 456–459.
(145) Frank, B.; Gast, A. P.; Russell, T. P.; Brown, H. R.; Hawker, C. Polymer Mobility in Thin Films. Macromolecules 1996, 29 (20), 6531–6534.
(146) Napolitano, S.; Glynos, E.; Tito, N. B. Glass Transition of Polymers in Bulk, Confined Geometries, and near Interfaces. Reports Prog. Phys. 2017, 80 (3), 1–51.

(147) Tanaka, K.; Taura, A.; Ge, S. R.; Takahara, A.; Kajiyama, T. Molecular Weight Dependence of Surface Dynamic Viscoelastic Properties for the Monodisperse Polystyrene Film. Macromolecules 1996, 29 (8), 3040–3042.
(148) Chung, P. C.; Glynos, E.; Green, P. F. The Elastic Mechanical Response of Supported Thin Polymer Films. Langmuir 2014, 30 (50), 15200–15205.
(149) Watcharotone, S.; Wood, C. D.; Friedrich, R.; Chen, X.; Qiao, R.; Putz, K.; Brinson, L. C. Interfacial and Substrate Effects on Local Elastic Properties of Polymers Using Coupled Experiments and Modeling of Nanoindentation. Adv. Eng. Mater. 2011, 13 (5), 400–404.
(150) Inoue, R.; Nakamura, M.; Matsui, K.; Kanaya, T.; Nishida, K.; Hino, M. Distribution of Glass Transition Temperature in Multilayered Poly(Methyl Methacrylate) Thin Film Supported on a Si Substrate as Studied by Neutron Reflectivity. Phys. Rev. E 2013, 88.
(151) Napolitano, S.; Sferrazza, M. How Irreversible Adsorption Affects Interfacial Properties of Polymers. Adv. Colloid Interface Sci. 2017, 247, 172–177.
(152) Housmans, C.; Sferrazza, M.; Napolitano, S. Kinetics of Irreversible Chain Adsorption. Macromolecules 2014, 47.
(153) Evans, C. M.; Deng, H.; Jager, W. F.; Torkelson, J. M. Fragility Is a Key Parameter in Determining the Magnitude of T G-Confinement Effects in Polymer Films. Macromolecules 2013, 46 (15), 6091–6103.
(154) Chen, D.; Kongkanand, A.; Jorne, J. Proton Conduction and Oxygen Diffusion in Ultra-Thin Nafion Films in PEM Fuel Cell: How Thin? J. Electrochem. Soc. 2019, 166 (2), F24–F33.
(155) Modestino, M. A.; Paul, D. K.; Dishari, S.; Petrina, S. A.; Allen, F. I.; Hickner, M. A.; Karan, K.; Segalman, R. A.; Weber, A. Z. Self-Assembly and Transport Limitations in Con Fi Ned Na Fi on Films. Macromolecules 2013, 46, 867−873.
(156) Ono, Y.; Nagao, Y. Interfacial Structure and Proton Conductivity of Nafion at the Pt-Deposited Surface. Langmuir 2016, 32, 352–358.
(157) Paul, D. K.; McCreery, R.; Karan, K. Proton Transport Property in Supported Nafion Nanothin Films by Electrochemical Impedance Spectroscopy. J. Electrochem. Soc. 2014, 161 (14), F1395–F1402.
(158) Siroma, Z.; Kakitsubo, R.; Fujiwara, N.; Ioroi, T.; Yamazaki, S.; Yasuda, K. Depression of Proton Conductivity in Recast Nafion® Film Measured on Flat Substrate. J. Power Sources 2009, 189 (2), 994–998.
(159) Siroma, Z.; Ioroi, T.; Fujiwara, N.; Yasuda, K. Proton Conductivity along Interface in Thin Cast Film of Nafion. Electrochem. commun. 2002, 4, 143–145.
(160) Kusoglu, A.; Dursch, T. J.; Weber, A. Z. Nanostructure/Swelling Relationships of Bulk and Thin-Film PFSA Ionomers. Adv. Funct. Mater. 2016, 26, 4961–4975.
(161) Nadermann, N. K.; Davis, E. M.; Page, K. A.; Stafford, C. M.; Chan, E. P. Using Indentation to Quantify Transport Properties of Nanophase-Segregated Polymer Thin Films. Adv. Mater. 2015, 27 (33), 4924–4930.
(162) Dishari, S. K.; Hickner, M. a. Antiplasticization and Water Uptake of Nafion Thin Films. ACS Macro Lett. 2012, 1 (2), 291–295.
(163) Abuin, G. C.; Cecilia Fuertes, M.; Corti, H. R. Substrate Effect on the Swelling and Water Sorption of Nafion Nanomembranes. J. Memb. Sci. 2013, 428, 507–515.
(164) Kusoglu, A.; Kushner, D.; Paul, D. K.; Karan, K.; Hickner, M. a.; Weber, A. Z. Impact of Substrate and Processing on Confi Nement of Nafi on Thin Films. Adv. Funct. Mater. 2014, 24 (30), 4763–4774.

(165) Eastman, S. A.; Kim, S.; Page, K. A.; Rowe, B. W.; Kang, S.; Soles, C. L.; Yager, K. G. Effect of Confinement on Structure, Water Solubility, and Water Transport in Nafion Thin Films. Macromolecules 2012, 45, 7920–7930.
(166) Page, K. A. .; Kusoglu, A.; Stafford, C. M. .; Kim, S.; Kline, R. J.; Weber, A. Z. . Confinement-Driven Increase in Ionomer Thin-Film Modulus. Nano Lett. 2014, 14, 2299–2304.
(167) Tesfaye, M.; MacDonald, A. N.; Dudenas, P. J.; Kusoglu, A.; Weber, A. Z. Exploring Substrate/Ionomer Interaction under Oxidizing and Reducing Environments. Electrochem. commun. 2018, 87, 86–90.
(168) Paul, D. K.; Shim, H. K. K.; Giorgi, J. B.; Karan, K. Thickness Dependence of Thermally Induced Changes in Surface and Bulk Properties of Nafion ® Nanofilms. J. Polym. Sci. Part B Polym. Phys. 2016, 54 (13), 1267–1277.
(169) Paul, D. K.; Karan, K.; Docoslis, A.; Giorgi, J. B.; Pearce, J. Characteristics of Self-Assembled Ultrathin Nafion Films. Macromolecules 2013, 46.
(170) Nagao, Y. Proton-Conductivity Enhancement in Polymer Thin Films. Langmuir 2017, 33, 12547–12558.
(171) More, K. L.; Allard, L.; Meyer, H. Microstructural Characterization of PEM Fuel Cell Materials. In DOE Hydrogen Program Annual Merit Review Proceedings; 2005.

2. Substrate/Ionomer Interaction Under Oxidizing and Reducing Environments

2.1. Introduction to the Dynamic Ionomer/Platinum (Pt) Interface

As discussed in Chapter 1, polymer electrolyte fuel cells (PEFCs) are composed of two diffusion mediums (DMs), two catalyst layers (CLs) separated by a selective, hydrogen-ion conducting polymer electrolyte membrane. CLs (anode and cathode) are microporous components consisting of 2-10 nm platinum (Pt) nanoparticles supported on 20-75 nm carbon (C) particles bound with coverage of a thin coating of ion-conducting polymer (ionomer).[1,2] Oxidation and reduction reactions are catalyzed at CLs via the consumption of hydrogen and oxygen gas and produce water.[3] Unfortunately, the local reaction site at the cathode CL where gas (O_2), ions (H^+), and electrons meet on the Pt catalyst interface has very sluggish reaction rate and remains unoptimized and poorly understood.[1,4,5] Mitigation of this underperformance requires high kinetic activity catalyst, and a catalytic interface with unobstructed Pt sites for gas adsorption, fast proton and gas transport through the ionomer thin film, and good Pt/C contact for abundant access to electrons. However, real catalysts are far from this idealized nature required for optimal performance. Figure 2-1 shows high definition transmission electron microscope (TEM) images of real CLs.[6–9] In real CLs, there is a variable distribution of ionomer on the surfaces of Pt particles and C particles (Fig. 2-1b). Additionally, accessibility to the C support could be limited due to internal porosity and blockage by water, non-uniform distribution of Pt sites (Fig 2-1c), and non-optimized continuity of the ionomer layer and gas flow networks (See Figure 2-1a). Non-idealities in the CL are further complicated with additional operational factors including start/stop cycles, continuous withdrawal of power for extended period of time, humidity, temperature and voltage cycling. As a result of the complex heterogeneous structure and high activity traffic, real CLs have vulnerabilities that result in non-optimal power output or lifetime.

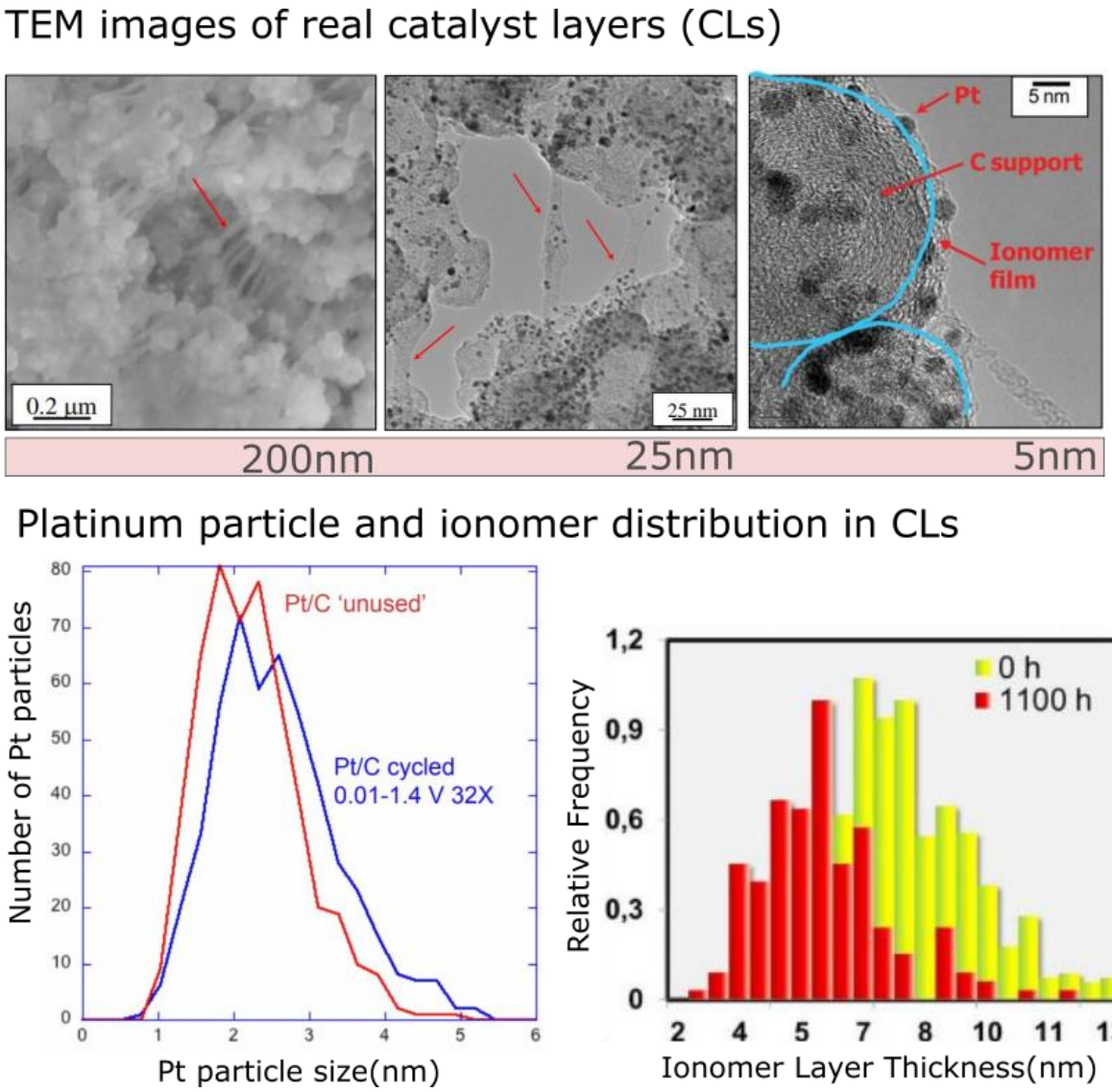

Figure 2-1: (Top) Heterogeneous structure of real catalyst layer containing Platinum (Pt) nanoparticles supported on carbon covered by ionomer thin film visualized by high resolution transmission electron microscope from ref.[7] (Bottom) Particle distribution of platinum in the catalyst layer (left) ionomer thickness distribution in the catalyst layer. (right) Variability with voltage cycling at 60% relative humidity from ref.[6–9] Reprinted with permission from Morawietz et al.[8] *J. Electrochem. Soc.*, 165 (2018). Copyright 2018. The Electrochemical Society.

Limitations in optimal CL output can be grouped into two general categories i.e. performance losses and degradation. Degradation concerns in PEFC electrodes commonly unfold when a cell is utilized under operating conditions repeatedly and continuously. They are commonly evaluated under accelerated stress tests that involve humidity and voltage cycling and hold. Degradation losses eventually overwhelm the electrode resulting in considerable reduction in efficiency, utilization and maybe even cell death. Divergently, performance losses in the electrode are related to normal or side electrochemical reactions and phenomenon that result in reduction in theoretical energy withdrawal. Therefore, these losses are usually (but not always) present in cell from onset. Some examples of performance losses in CL include sluggish oxidation reaction kinetics, high

local transport resistances, reduction in proton conductivity, Pt surface oxidation, [10–15] flooding of electroactive sites, and Pt sulfonate adsorption.[16–18] Degradation, on the other hand, pertains to any chemical or mechanical mechanisms that result in loss of integrity of component or dramatic loss in operation performance. Examples include Pt detachment and dissolution, C corrosion, fuel starvation, membrane contamination and pinhole formation, degradation due to temperature fluctuation and failure in other supporting components.[19–21] Degradation and performance losses in CLs are not mutually exclusive. Some performance losses like flooding of electroactive sites can enhance the rate of Pt detachment causing significant reduction in power withdrawn. Therefore, even as we investigate local Pt/ionomer interactions in this chapter, property changes as a function of humidity cycling and alternating gaseous environment can provide insight into the interrelated nature of performance loss in ionomer and degradation in the CL.

The Pt/ionomer interface has already been identified as a significant contributor to mass-transport related performance losses in the CL (See Chapter 1).[5,22] Notably, Pt/ionomer local interfacial resistances are caused by morphological and structural changes and partial electrochemical deactivation of the Pt surface.[23–26] Furthermore, researchers have shown the existence of oxide coverage and side-chain sulfonate group adsorption on the Pt surface that can result in reduced activity and increase transport resistance at the Pt/ionomer interface.[13,16–18,27] It is well known that Pt nanoparticles can undergo electrochemical oxidation during potential cycling.[11,15,28–30] In-situ particle-distribution characterization techniques combining electrochemical cells with anomalous small angle X-ray scattering (ASAXS) and small angle X-ray scattering (SAXS) have documented particle-size growth of 1 nm attributed to anodic oxide shells forming around Pt particles in the CL.[31,32] Although the mechanism and nature of Pt-oxide is not completely clarified, these findings are supported by several studies of oxidation of noble metal electrodes.[33–36] Performance of electrochemically active surfaces in the CL are highly coupled with the oxidation of Pt. Surface oxidation of Pt can further hamper the already sluggish oxygen reduction reaction kinetics at the cathode.[12,13,27] Pt surface oxidation has also been linked with catalyst degradation mechanisms.[37] Binding of ionomer film to the Pt catalyst has also been shown to be impacted by oxide formation on Pt nanoparticles.[29]

Parallel to the ever changing Pt interface, surface- and interface-dependent ionomer thin film behavior and performance can be impacted.[38,39] Dynamic transition of structure and orientation of ionomer in the presence of Pt bare and oxide layer has been postulated as a real phenomenon that occurs during cycling.[27] Using a large, flat, bulk, substrate Borges et al. showed surface-ionomer interaction impacts thin film morphology and structure.[40] To add to that, Ono et al. have demonstrated the impact of substrate on thin film Nafion ionomer conductivity.[41] However, this possible picture could change as a result of experiencing a dynamic reducing and oxidizing environment, which has not been explored. Full comprehension of the impact of dynamic Pt surface on the effects of gas, water and ion transport is necessary for CL design and improved performance. It is in that spirit that this chapter examines the impact of surface oxidation on thin film ionomer behavior and properties.

Ionomer thin films cast onto a Pt surface can serve as model systems providing a focused glimpse into the heterogeneous dynamics and complex interfaces of the catalyst layer. A bulk, continuous polycrystalline Pt surface does not fully describe Pt nanoparticle phenomena that are present in real CLs of PEFC. [42,43] However, ionomer thin-film coated Pt can still elucidate surface specific interactions that can impact ionomer property and morphology. Although the impact of Pt substrate on ionomer performance has been shown, efforts to clarify the source of this impact have at times been contradictory, [27,41] especially in elucidating the role of water on oxidized and

unoxidized Pt surfaces.[44,45] Additionally, the extent of ionomer impact due to the Pt surface as it experiences oxidation and reduction during operation has not been explored, especially as CLs function in oxidizing and reducing potentials and environments. In this study, water-vapor sorption dynamics of dispersion-cast Nafion thin films under reducing (H_2), oxidizing (Air), and inert (Ar, N_2) environments are investigated to understand the Pt/ionomer interaction in both the anode and cathode catalyst layers.

2.2. Materials and Experimental Methods

2.2.1. Substrate Preparation and Characterization

Substrates used in this study were Silicon (Si 100 n-type), gold (Au) and platinum (Pt) wafers. Pt and Au wafers were made by automatic deposition of titanium (2 to 5 nm) as an adhesion layer, followed by Pt or Au (~60 nm) sputtering on Si substrate at 2 nm/s via electron-beam physical-vapor deposition. Wafers were cut up into 1/2-inch squares before cleaning with distilled water and then twice with isopropyl alcohol (IPA) followed by nitrogen drying after each rinse. Rinsed Pt wafers were additionally cleaned with plasma using Argon (Ar) gas (83-90 sccm) for six minutes using a Harrick Plasma PDC-001 operating at a 10.5 W medium RF power.

Substrates surface energy was characterized in this study mainly via Goniometer. Presence of Pt surface oxide (PtO_x) was investigated via X-ray photoelectron spectroscopy (XPS). Uncoated Pt substrate interaction with different gas atmosphere (H_2, N_2, O_2) was also explored via frequency shift using Quartz Crystal Microbalance (QCM). Goniometers provide highly focused droplet images that can be analyzed using software packages to determine droplet properties such as contact angle, surface tension, and volume. A Ramé-Hart goniometer was used to take pictures of 50µL water droplets that were deposited on substrates (Si, Pt, Au). Drop-Image software was used to control the deposition of water and to take images. Contact angle measurements were analyzed by fitting the Young-Laplace equation to an image of a droplet using low-bond axisymmetric drop shape analysis (LBADSA) method; this method is rigorous and accurate even for low contact angle droplets.[46] ImageJ, image analyzer combined with LBADSA method was used to extract manually the contact angle. The contact angle of each side of the droplet was measured 3 times and averaged to find the representative contact angle.

To understand the surface composition chemistry of Pt supports, XPS spectra were acquired on a Kratos Axis Ultra DLD X-ray photoelectron spectrometer using a monochromatic Al Kα source operating at 150W. Substrates were mounted using conductive double-sided tape and no use of charge neutralization was necessary. All XPS data were collected at the Joint Center for Artificial Photosynthesis, a Department of Energy scientific hub for solar to fuel energy conversion. Data analysis and quantification were performed using CasaXPS software. Sensitivity factors provided by the manufacturer were utilized. A 70% Gaussian/30% Lorentzian line shape was utilized in the curve-fit of the spectra.

QCM is technique utilized to detect mass variations per quartz crystal surface area (full QCM details can be found in Appendix B). Clean and bare Pt coated quartz crystals were placed into the QCM holder and the loaded QCM holder was exposed to dry and humidified gas of pure H_2, O_2, and N_2 in a sealed chamber. All gases used in this study were >99.9% pure and obtained from Praxair. Shifts in frequency upon interaction of Pt coated quartz crystal substrate with gaseous environment was detected and findings are discussed later in section 2.3.

2.2.2. Ionomer Thin Film Preparation

A stock solution of 5wt% Nafion (1100EW from Sigma Aldrich) was diluted in IPA to 1wt% and stirred overnight on a stir plate for at least 12 hours. The solution was then filtered using a Millex-SV 5.0µm filter unit with a syringe to remove any large particulates and aggregates. Filtered solution was then degassed for 21 minutes using a 5510 Branson Ultrasonic to remove trapped air bubbles and ensure good dispersion of polymer in the IPA/water solvent. 350 µl of solution were deposited on wafers via spin-coating at 1000rpm for 1minute (Laurell WS-650-23B model) to obtain Nafion thin films of thickness 50nm. Samples were then annealed in a Binder vacuum oven at 150°C for 1 hour. To minimize ageing effects, water uptake measurements were done immediately (within 20mins) after removal of samples from vacuum oven.

2.2.3. Water Uptake Measurement via Spectroscopic Ellipsometry

Annealed Nafion thin film samples cast on Pt and Si were exposed to humidified gas at ambient temperature. Humidified gas was supplied to the environmental cell containing the sample by combining dry and saturated gas with varying ratios to match the set point relative humidity. Humidity was measured and logged right outside of the environmental cell via Omega RH sensor (Omega). The change in thickness of the thin film was monitored in-situ using spectroscopic ellipsometry (J. A. Woollam). Ellipsometry measures the changes in polarized light reflected from the substrate-supported ionomer thin films by capturing the change in wave amplitude (Ψ) and phase shift (Δ) caused by constructive interference of light. A multi-layered model is constructed to fit Ψ and Δ data and calculate the sample's index of refraction as a function of wavelength (See detailed description in Appendix A). As a transparent polymer film, the Nafion thin film layer was modeled by the Cauchy equation with two fitting constants. Model fits demonstrated good agreement with a mean squared error (MSE) maintained below 2×10^{-3} for dry conditions and 3.5×10^{-3} for samples partially saturated with water vapor. To create a consistent water-uptake history, all measurements were preceded with a dry to saturated hour-long step. Figure 2-2 shows humidity protocol used and thickness change with time. The thin films were allowed to equilibrate for 30 min and final thickness (L_{RH}) was calculated from the average of the last 10 min. The change in swelling is calculated relative to the dry thickness (L_o) as

$$\text{Change in Thickness (\%)} = 100 \times \frac{L_{RH}-L_o}{L_o} \quad (1)$$

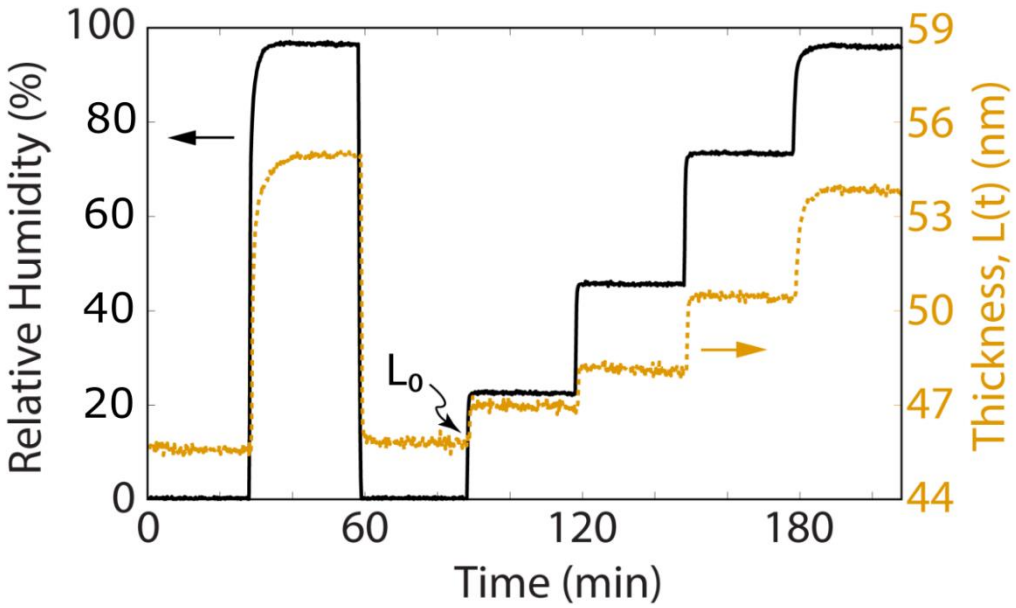

Figure 2-2: Humidity protocol used for water uptake measurement and change in thickness over time. Initial hour-long dry and saturated step is used to create consistent history. In-situ thickness as a function of time is given by $\boldsymbol{L(t)}$. Final thickness ($\boldsymbol{L_{RH}}$) was calculated from the average of the last 10 min. The change in swelling is calculated relative to the dry thickness ($\boldsymbol{L_o}$)

2.2.4. Grazing Incidence Small Angle X-ray Scattering (GISAXS) Measurement

Pt-supported Nafion thin films were placed into an in-house built environmental chamber with X-ray transparent Kapton windows as described in Ref [26]. The sample was equilibrated in dry H_2 and N_2 gas at room temperature, and GISAXS patterns were collected after multiple purges for 5 to 10 minutes in each gas. GISAXS patterns were collected at varying incidence angles (α_i) above the critical angle (α_c) for Nafion ($\alpha_c = 0.2^o$) but below that for Pt ($\alpha_c = 0.2^o$). All X-ray scattering experiments were performed in beamline 7.3.3 of the Advanced Light Source (ALS) at Lawrence Berkeley National Laboratory (LBNL). Sample to detector distance was approximately 1.8 m and 25 cm for the GISAXS and GIWAXS configurations, respectively. Exposure time for the collected images was 20 s. The X-ray energy applied was 10keV, with a monochromator energy resolution E/dE of 100. Patterns were acquired with a 2D Dectris Pilatus 1M CCD detector (172 µm × 172 µm pixel size).

2.2.5. Thin Film Ionomer Mechanical Property Measurement

For mechanical property measurements,[1] Nafion thin films (100 nm) prepared on Pt-coated thin Si-cantilever wafer (105µm thickness by approximately 0.5 cm x 4 cm). The coated sample was clamped in an environmental cell that allowed for humidified gas feeds. Constrained swelling caused by the presence of the substrate results in a compressive force, which bends the thin Si cantilever. Using a laser array reflected off the backside of the sample, the change in curvature of the substrate is measured. Using Stoney's thin film equation the stress-thickness $\sigma_f t_f$ can be calculated via

[1] Mechanical property measurements were conducted in collaboration with Peter J. Dudenas (PhD candidate, Chemical and Biomolecular Engineering, University of California, Berkeley)

$$\Delta F_c = \frac{E_s h_s^2 \Delta\kappa}{6(1-\nu_s)} = \sigma_f t_f \quad (2)$$

where E_s, ν_s, $\Delta\kappa$ and h_s are the Young's modulus, Poisson's ratio, change in curvature, and thickness of the substrate, respectively.[47] The measured cantilever force (ΔF_c) is equal to the average biaxial stress of the Nafion film (σ_f) multiplied by its thickness (t_f). A full description of the method can be found in ref. [48] Ellipsometry gives the strain (equation 1) under the same conditions. From these two experiments, stress-strain curves are generated. Integrating the area under the curve gives the deformation energy of the sample.

2.3. Dynamic Interaction of Platinum (Pt) Substrate with Gaseous Environment

The thin film ionomer binder in the catalyst layer sees various surfaces including Pt, C and their different oxidation states either upon potential cycling or degradation. As such, it is critical to observe how these surfaces behave separate from their ionomer coating counterparts. For the Pt surface, its oxidation state is of interest due to different environmental and potential operating conditions as mentioned above. Pathways to surface oxidation of Pt can be grouped into two: electrochemical and thermo-chemical (See Figure 2-3).[49] Electrochemical oxidation of Pt, as shown in Figure 2-3 (top), involves low-potential half-monolayer formation as a result of water molecule discharge, followed by continued monolayer growth, eventually leading to formation of platinum oxide lattice as a result of place exchange at the Pt interface at high potential.[33,34,36,49] Such surface oxide is formed during PEFC operation and can affect available surface area for electrochemical reaction. Thermo-chemical oxidation of Pt surface, on the other hand (shown in Figure 2-3 bottom), occurs due to interstitial sites and defects in the Pt lattice that allow for progressive coordination of oxygen into the Pt surface[49–51]. Thermo-chemical oxidation is facilitated by external temperature, pressure, and presence of water. Exposure to ambient gaseous environment and water vapor can build an unstable thermo-chemically passivated layer on the bulk Pt substrate used in this study. Ar plasma treatment, utilized here, has been demonstrated as one way to remove this platinum oxide (PtO_x) as well as any organic remnants from as deposited on the Pt surface.[52] Extended and harsher exposure to Ar plasma was avoided to prevent change in roughness of the Pt surface.

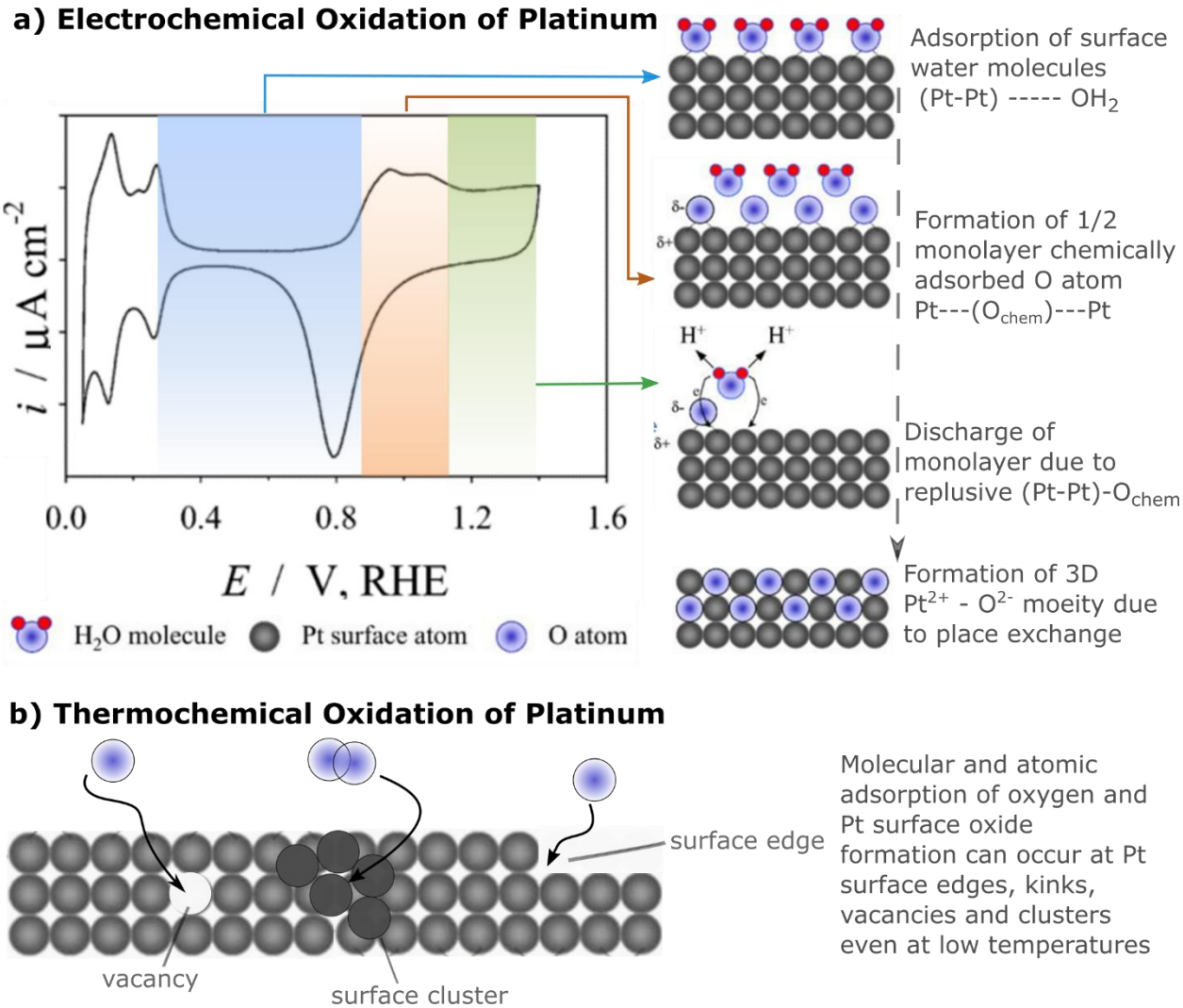

Figure 2-3: Oxidative pathways of Platinum (Pt) surface. (a) Electrochemical oxidation of Pt. (b) Thermo-chemical oxidation of Pt surface. Schematics inspired in part by ref [33,49,53].

The chemical nature of Pt surfaces as deposited and cleaned was compared to Pt surfaces treated with Ar plasma and evaluated using X-ray photoelectron spectroscopy (XPS) and contact angle (via Goniometer) as shown in Figure 2-4. XPS spectra and contact angle of Pt surfaces after different treatments is compared against other substrates (Si, Au). Si is one of the oldest and most commonly employed substrates in polymer thin film research. It is an ideal substrate because it is cheap, easy to clean, stable, easy for surface characterization, modification or chemistry and widely available. Most reference studies in exploring ionomer thin films use Si. However, ionomer-Pt metal interactions are of interest to real PEFC systems.[54] In this work, to gain a more comprehensive understanding, examinations of Pt surfaces are compared against Si as well as Au supports to leverage the vast amount of literature and understanding in the polymer thin film field as well as to expand the understanding of metal-ionomer interactions by employing a more stable metal substrate i.e. Au.

Figure 2-4a & b show XPS spectra of a plasma treated and non-treated Pt substrate. Limited effect of plasma applied on surface roughness was verified with Atomic Force Microscopy topography (Figure 2-4c). Figure 2-4d shows plasma treatment significantly reduces the contact

angle of surfaces by a factor of four. This is equivalent to the contact angle observed for a standard clean Si surface. Almost all Si surfaces are commonly covered by a 1-3nm of native silicon oxide (SiO_2) surface. Therefore, Si substrates here are referred to as Si/SiO_2 surface. XPS is an ideal tool for investigating surface oxidation due to its surface limited (10nm depth of penetration) sensitivity. There are indicators for presence of PtO_x via XPS: Pt spectra indicating various oxidative states of Pt and Oxygen spectra indicating the nature of various oxides at the surface. XPS Pt 4f spectra (Figure 2-4a) of both plasma treated and non-treated samples revealed the presence of Pt oxide indicating that a stable oxide layer had already formed during substrate preparation and remained despite plasma treatment. However, the O1s peaks in Figure 2-4b showed a slight shift from higher binding energy of organic chemical state (531.5-533 eV) for non-plasma treated surfaces to a lower binding energy with a more pronounced shoulder indicating PtO_x chemical state (529 – 530eV).[55] These results indicate that the plasma treatment employed here contributed significantly in the removal of organics from the Pt surface but did not remove existing surface PtO_x. Therefore, the improved contact angle from the baseline (non-treated case) is a reflection of removal of organics and associated oxides and not a reflection of the removal of PtO_x.

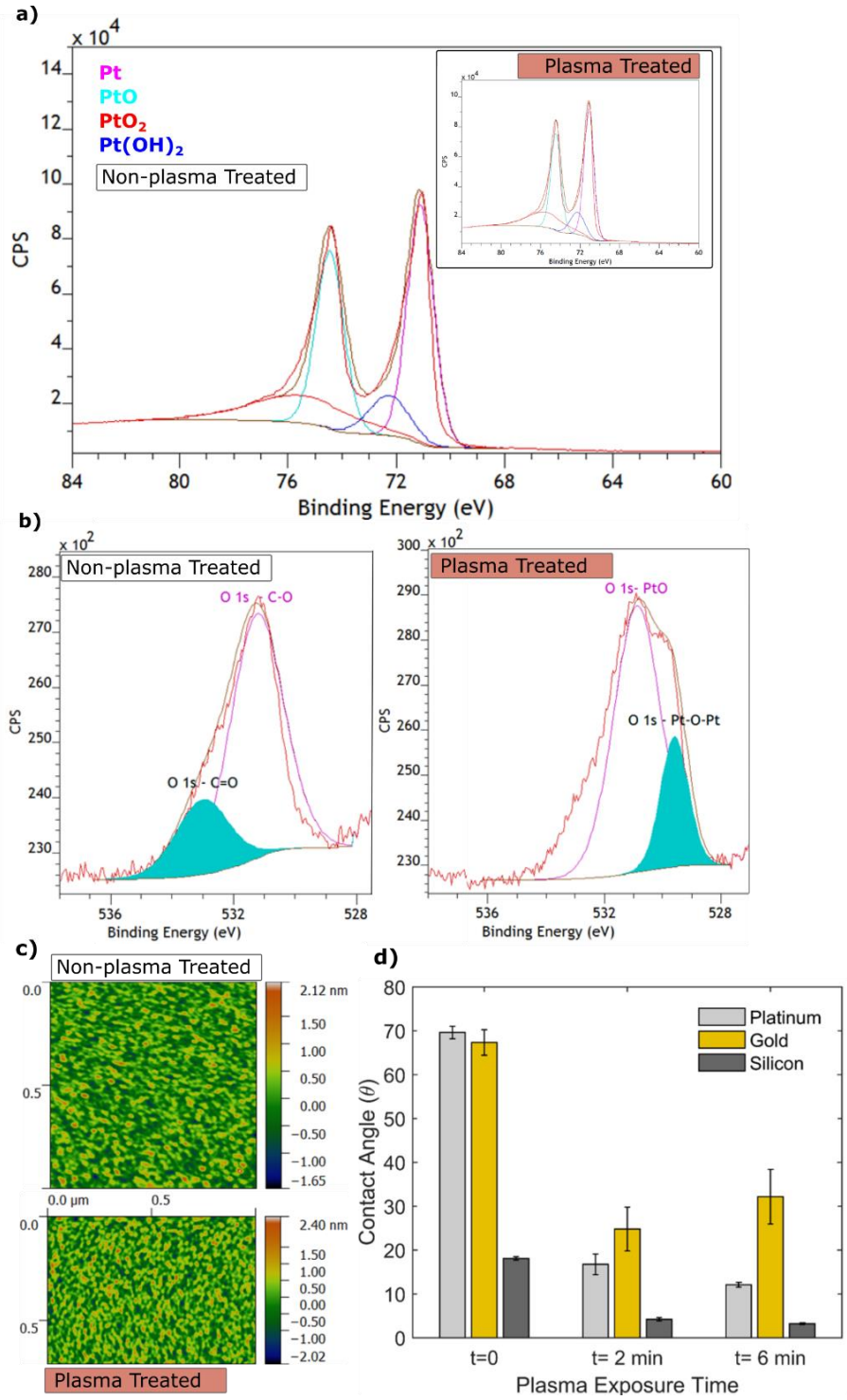

Figure 2-4: Effect of plasma treatment on platinum (Pt) substrate characterized by XPS (a & b), AFM(c) and contact angle (d). (a) XPS 4f Pt spectra of non-plasma treated Pt substrate show similar PtO_x as plasma treated Pt substrate (inset). (b) XPS O 1s spectra shows organic peaks that are not present in plasma treated substrates. (c) AFM images show roughness of plasma treatment remains unaffected compared to non-plasma treated substrate (RMS = 0.42 - 0.52). (d) Contact angle changes with different time exposure to plasma treatment.

To understand the interaction of Pt surface with gaseous environments, a Pt-coated quartz crystal was exposed to reducing (H_2), oxidizing (O_2), and inert (N_2) gaseous environments. Figure 2-5a show change in frequency of Pt QCM during dry gas exposure to H_2, O_2 and N_2. Both O_2 and N_2 exhibit an increase in crystal frequency implying mass loss due to removal of surface dust, organics, contaminants, and moisture during the positive flow of dry gas over the bare quartz crystal. However, upon exposure to H_2, Pt coated quartz crystal shows a reduction in frequency indicating mass gain due to H_2 adsorption on Pt QCM crystal surface. Same Pt quartz crystals were then exposed to water vapor saturated H_2 and O_2 gas for 3 hours continuously at ambient room temperature and pressure. Figure 2-5b shows mass of surface adsorbed water detected on bare Pt QCM over the time span of exposure. Change in frequency during saturated gas sorption was converted to mass using Sauerbrey equation (See Appendix B for details). Mass of water adsorbed in H_2 environment is five-fold of that in O_2. Differences in water adsorption under oxidizing and reducing environment has to do with gas-substrate interaction and the resultant nature of surface hydrophobicity/hydrophilicity.

From findings in Figure 2-4 it is clear that Pt substrates utilized in this study exist with some surface oxidation as they are stored in ambient room conditions. The oxidized surface continues to grow with continued exposure to an oxidizing environment via thermo-chemical surface oxidation. Alternatively, weakly formed oxides on Pt surface have been shown to be reduced and saturated with dissociated atomic hydrogen during H_2 exposure; a phenomenon that has been reported experimentally and computationally [43,56–58]. This is consistent with the phenomenon directly observed on the bare Pt-coated crystal in QCM in Figure 2-5a. Adsorbed hydrogen reduces the solid-surface free energy,[56] resulting in a more hydrophilic but non-polar Pt/H interface compared with that of oxidized Pt represented. This relatively greater affinity for water on Pt/H interface is consistent with greater water sorption detected by bare Pt coated QCM crystals exposed to saturated H_2 and O_2 gases in Figure 2-5b.

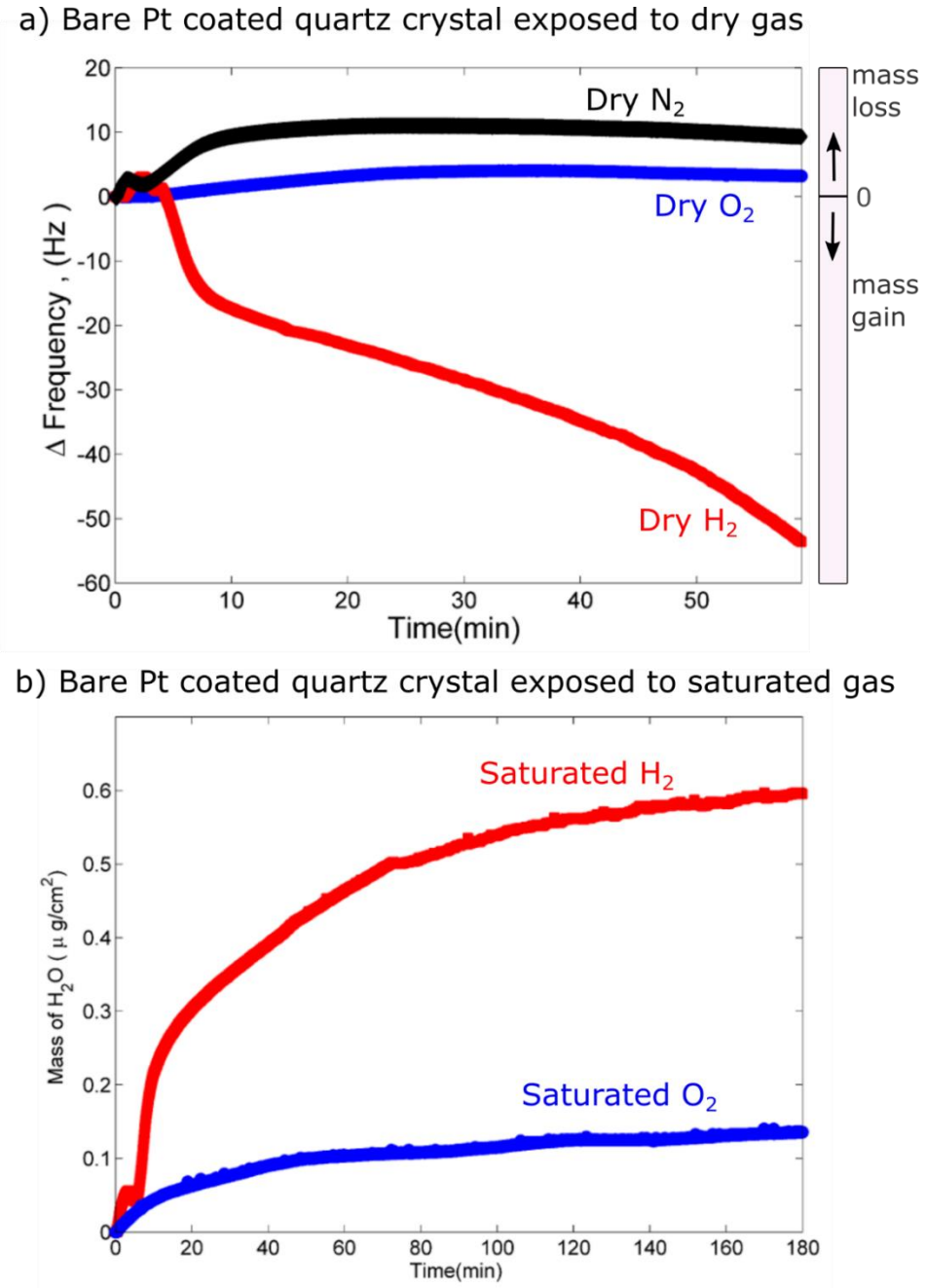

Figure 2-5: (a) Change in frequency of bare platinum (Pt) coated quartz crystal under dry H_2, O_2 and N_2 gas exposure. Positive shift associated with mass loss of crystal due to moisture and organic particulates removal. Negative shift is associated with mass gain due to gas adsorption on to Pt crystal. (b) Change in mass of Pt coated quartz crystal during saturated H_2, O_2 gas exposure.

2.4. Impact of Gas/Substrate Interaction on Ionomer Thin Film Water Uptake

Comparison of different humidified gas feeds on the ionomer thin film (~50nm) swelling on Pt and Si/SiO_2 support is shown in Figure 2-6. Swelling values measured here are between those reported by Kusoglu et al. [26] and Murthia et al. [45]. Differences are believed to be due to variation in sample preparation, thickness, substrate history, and ageing effects prior to measurements. The

results demonstrate a depression in swelling for ionomer thin films exposed to an environment of H_2 on both ionomer thin films cast on Pt and Si/SiO_2.

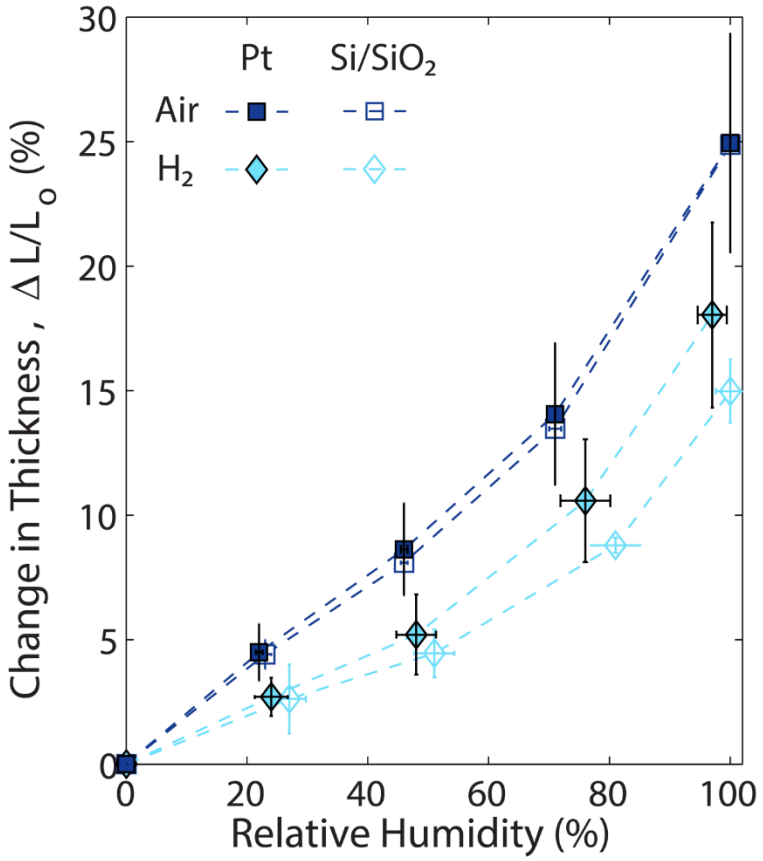

Figure 2-6: Water-vapor sorption dynamics of spin-cast Nafion thin films (50 nm) on Pt substrate (a) and Silicon (Si/SiO_2) (b) under H_2 (diamond) and Air (square) gas environments as a function of relative humidity.

Changes in ionomer thin film swelling under reducing and oxidizing environments were also monitored for morphological changes associated with substrate/ionomer interaction with gaseous environment. Change in structure of Nafion thin film coated on Pt substrate was tracked by GISAXS during exposure to dry H_2 and N_2 gases at varying incidence angles as shown in Figure 2-7. Scattered intensity is experienced when X-rays travel through a material elastically striking electrons within the material. Specific repeated features and structural arrangements with in the material show electron density contrast that appears as scattering at unique positions and incident angle. When the incident angle (α_i) of the X-ray beam is below the critical angle (α_c) of the polymer film, total external reflection occurs and scattering is surface sensitive, penetrating a few nanometers into the film.[59] See Figure 2-7. Above α_c of the film, the X-ray beam penetrates through the entire polymer film and scattering from the paracrystalline Pt surface. Figure 2-7, shows the absence of any scattering intensity in N_2 until the paracrystalline peak appears at α_i = 0.16. For H_2 appearance in scattering intensity does not happen until α_i = 0.18 in a H_2 environment, indicating an increase in the polymer's critical angle. Above this α_c, broad semi-circle halo dome is observed indicating an ionomer peak (at q_{peak} = 2 to 2.5 nm^{-1}) in both H_2 and N_2, signifying the phase-separated nanostructure with a correlation length of $2\pi/q_{peak}$ = 2.5 to 3 nm as expected for

this ionomer. α_c is a function of chemical structure and material density. Therefore, the positive shift in α_c indicates restructuring of the ionomer during exposure to H_2, including possible rearrangement of the hydrogen bonding of sidechains near the Pt/H interface, resulting in a more effectively packed, dense, hydrophobic ionomer structure.

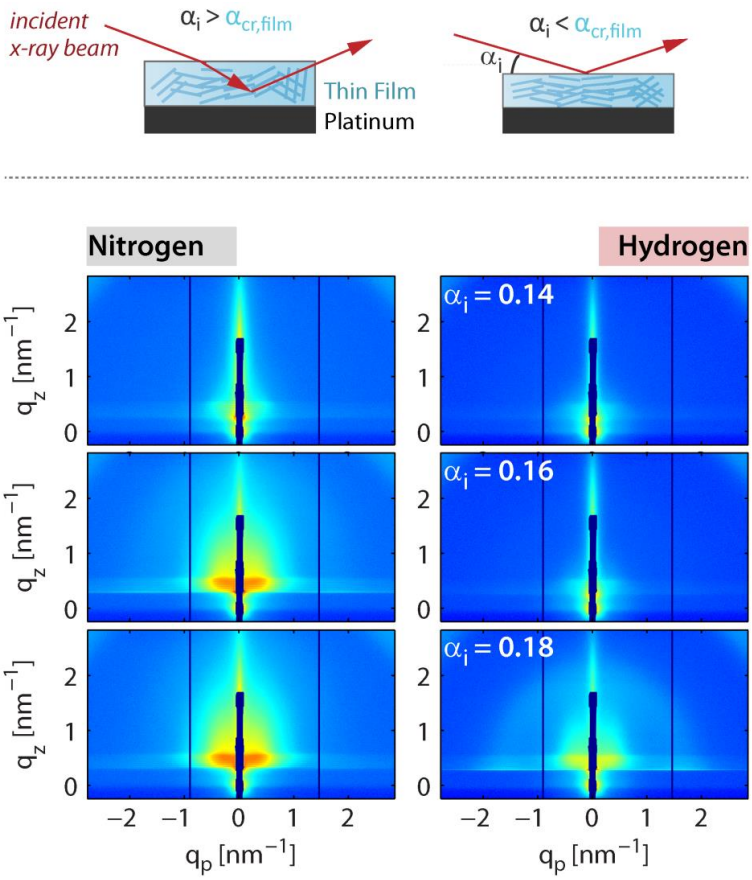

Figure 2-7: 2D Grazing Incidence Small Angle X-ray Scattering (GISAXS) pattern of Pt-supported Nafion thin films (50 nm) equilibrated in dry N_2 and H_2 gas. The Pt paracrystalline peak is visible at $\boldsymbol{\alpha_i \geq 0.16}$ in N_2 environment, while in H_2 environment the peak is only visible at $\boldsymbol{\alpha_i \geq 0.18}$.

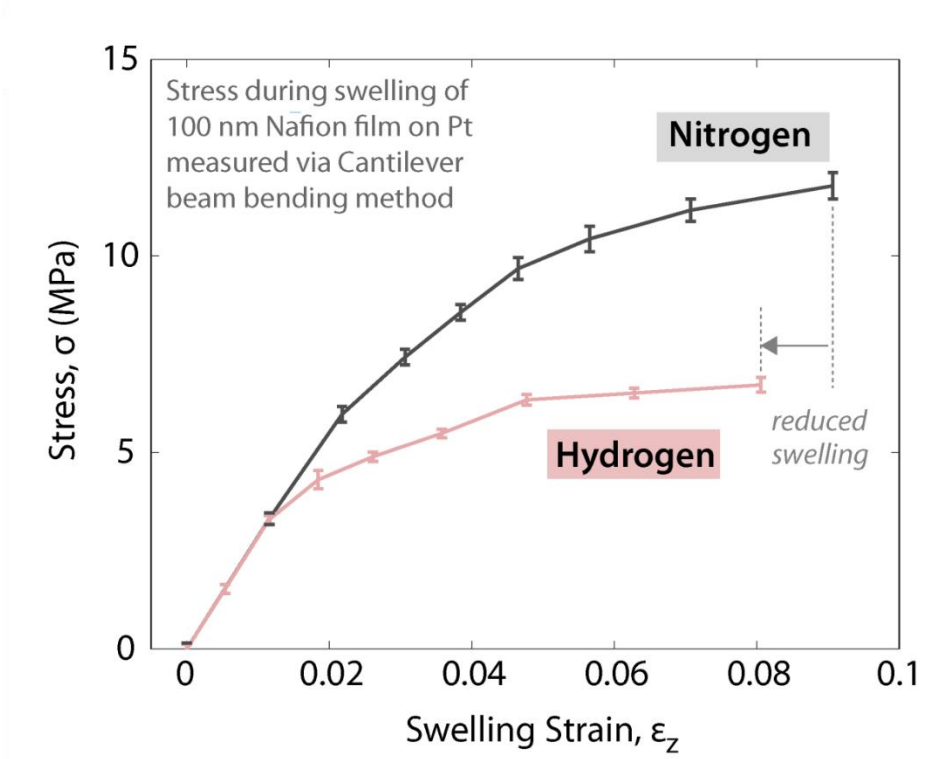

Figure 2-8: Stress-strain curves in both hydrogen and nitrogen environments. The nitrogen sample shows a larger area under the curve, indicating a higher deformation energy.

The mechanical response of substrate-supported ionomer thin films exposed to humidified H_2 and N_2 provides yet further evidence to the more hydrophilic but weakly interacting interface induced by H_2. Stress-strain curves produced from the cantilever-beam bending and ellipsometry measurements were used to calculate the deformation energy of these thin films in H_2 and N_2 (see Figure 2-8). Integrating the area under the curve to a strain value of 0.08 yields a deformation energy. The higher the energy, the more resistance to deformation the material exhibits. In other materials, stress-strain curves are carried out to the point of material failure and the area under the curve is known as 'toughness'.[60] Here, without reaching failure, area under the curve is interpreted as the energy generated during material deformation. The average deformation energy was found to be lower in H_2 than N_2 (539 versus 680 kJ/m^3), which is consistent with the greater hydrophilicity at the Pt/H interface creating a water-rich layer (see schematic Figure 2-9), thereby resulting in a reduced translation of ionomer deformation onto the substrate.

The findings in Figure 2-6 through Figure 2-8 are consequence of changes at the ionomer/Pt interface induced by the gas/Pt interaction. As noted in section 2.3 in a thermo-chemically oxidized Pt surface, exposure to an oxidative gaseous environment like air will enlarge oxidized metal islands on the Pt surface, while exposure to a reducing environment like H_2 can reduce the unstable passivated surface even under ambient conditions. [49–51,61] Thus, the ionomer thin film experiences different forces in the two environments: polar forces induced by the negatively charged oxygen atoms on an oxidized Pt surface, and the comparatively more hydrophilic but nonpolar Pt/H interface induced via the reducing environment. The balance in these forces yields different water uptake of the thin films as depicted in Figure 2-6. The Pt/H interface exhibits enhanced hydrophilicity and nonpolar Pt-H bond promotes non-polar interface that lacks strong electrostatic interactions. As a result, the ionomer possibly restructures to maximize hydrophilic sidechains

towards the Pt/H interface, where water molecules are likely to gather thereby creating a dense region of hydrophobic ionomer away from the interface. In such a scenario, with sidechains trussed close to the hydrophilic Pt/H interface, the ionomer behaves like a higher equivalent-weight ionomer and demonstrates lower water uptake. On the other hand, the negatively charged oxygen atoms on an oxidized Pt surface, which, while comparatively less hydrophilic, induce a strong polar dipole and enhance electrostatic interactions between hydronium ions and sulfonic-acid moieties. These interactions enhance the overall effective water uptake within the ionomer. This scenario is consistent with the greater effective water uptake calculated by He and coworkers in an ionomer on an oxidized Pt compared to an unoxidized Pt nanoparticle surface via molecular-dynamics simulations.[30] Similar to the Pt scenario under ambient conditions, growth of native oxide layer expected on a Si substrate. Continued layer-by-layer growth of SiO_2, however, requires presence of both water and oxygen. [62,63] Although reduction of oxide layer is not occurring under H_2 environment on Si/SiO_2 support, oxide formation is actively being facilitated under humidified air. Overall water uptake in the ionomer is heightened by strong electrostatic interactions with negatively charged oxygen atoms on SiO_2 resulting in more stabilized hydronium and sulfonic-acid groups similar to that seen on Pt-oxide.

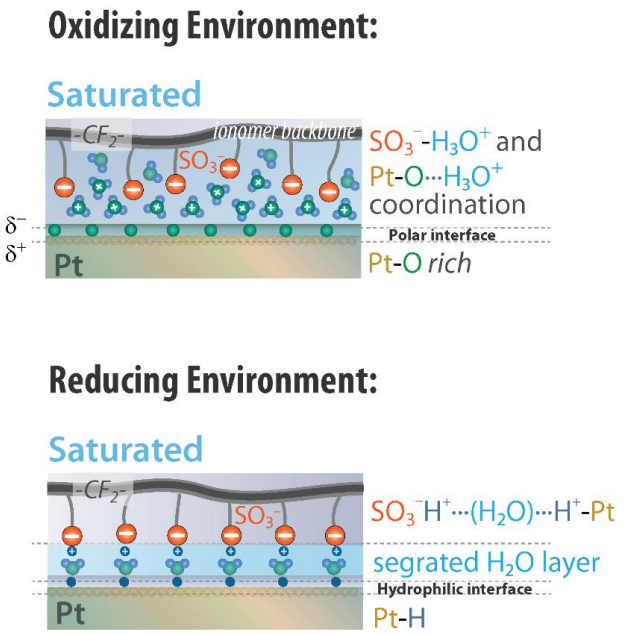

Figure 2-9: Schematic of platinum (Pt)/ionomer thin film interface in oxidizing and reducing environments.

2.5. Impact of Humidity Cycling on Ionomer Thin Film Water Uptake

The reversibility and persistence of the impact of the gaseous environment on ionomer swelling was explored using relative humidity (RH) cycling with alternating inert and reducing gas feeds. In-situ thickness change was monitored over three cycles: first, thin films were exposed to solvent history setting RH cycle of dry to 96% RH gas exposure (Cycle 0), then, the same gas was used to bring the thin film back to dry condition and RH was stepped (Cycle 1). Finally, the gas type was switched as the film went down to dry conditions and back up in humidity once again (Cycle 2). Figure 2-10 and Table 2-1 give the RH cycle protocol applied and combination of gases used for analysis.

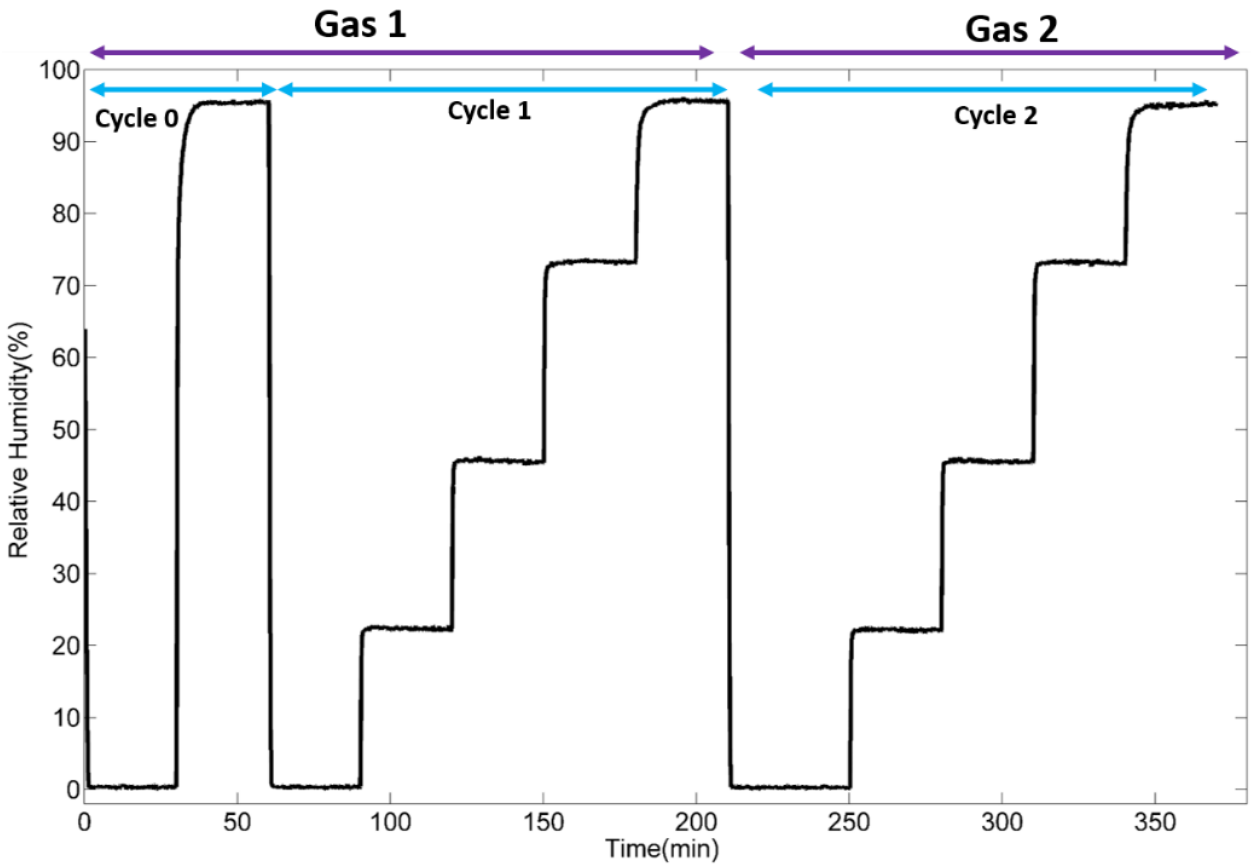

Figure 2-10: Humidity protocol used for relative humidity cycling experiment. In-situ monitoring of thickness was conducted both in different gases and as a function of changing relative humidity.

Table 2-1: Different combination of inert and reducing gas scenarios applied during relative humidity cycling protocol.

Scenario	Cycle 0	Cycle 1	Cycle 2
Case I	Ar		Ar
Case II	H_2		H_2
Case III	H_2		Ar
Case IV	Ar		H_2

Slightly different from the analysis in Figure 2-2, with each case, the reference dry thickness (L_{dry}) was set to the equilibrated dry thickness at ~0% RH in Cycle 0 and the reference saturated thickness (L_{sat}) was set to saturated RH thickness in Cycle 0; therefore Cycles 1 and 2 are compared against Cycle 0.

Figure 2-11a shows the change in dry thickness during RH cycling in each gas combination. RH cycling in an inert gas environment (Ar→ Ar→ Ar) maintains the dry ionomer initial condition. However, cycling in H_2 only (H_2→H_2 →H_2) and H_2 then Ar (H_2→H_2 →Ar) introduces a continual increase in 'dry' thickness with cycling. Swelling in Ar then H_2 (Ar→Ar→H_2) cycling demonstrates a large relative shift in 'dry' thickness immediately after H_2 exposure. These findings confirm the formation of hydrophilic, water-rich interface under conditions that facilitate Pt/H interface as already suggested in section 2.4.

Figure 2-11b shows swelling under saturated (96% RH) conditions during cycling for each gas combination. The thickness change in humid inert gas environment (Ar→Ar→Ar) is maintained despite the repeated tension and relaxation (swelling and de-swelling) introduced by changes in RH. However, RH cycling in both H_2 only (H_2→H_2 →H_2) and H_2 then Ar (H_2→H_2 →Ar) reduces maximum water-uptake capacity, at about the same rate, as indicated by the slope. The impact of the reducing environment not only reduces ionomer uptake successively upon cycling, but does so to a greater extent than an inert environment. Switching the order of H_2 then Ar (H_2→H_2 →Ar) to cycling in Ar then H_2 (Ar→Ar →H_2) exhibits a reduction in swelling under saturated conditions at a rate that is between that of H_2-only and Ar-only environments; confirming the impact of the H_2 environment on the effective water content of ionomer (as discussed in section 2.4).

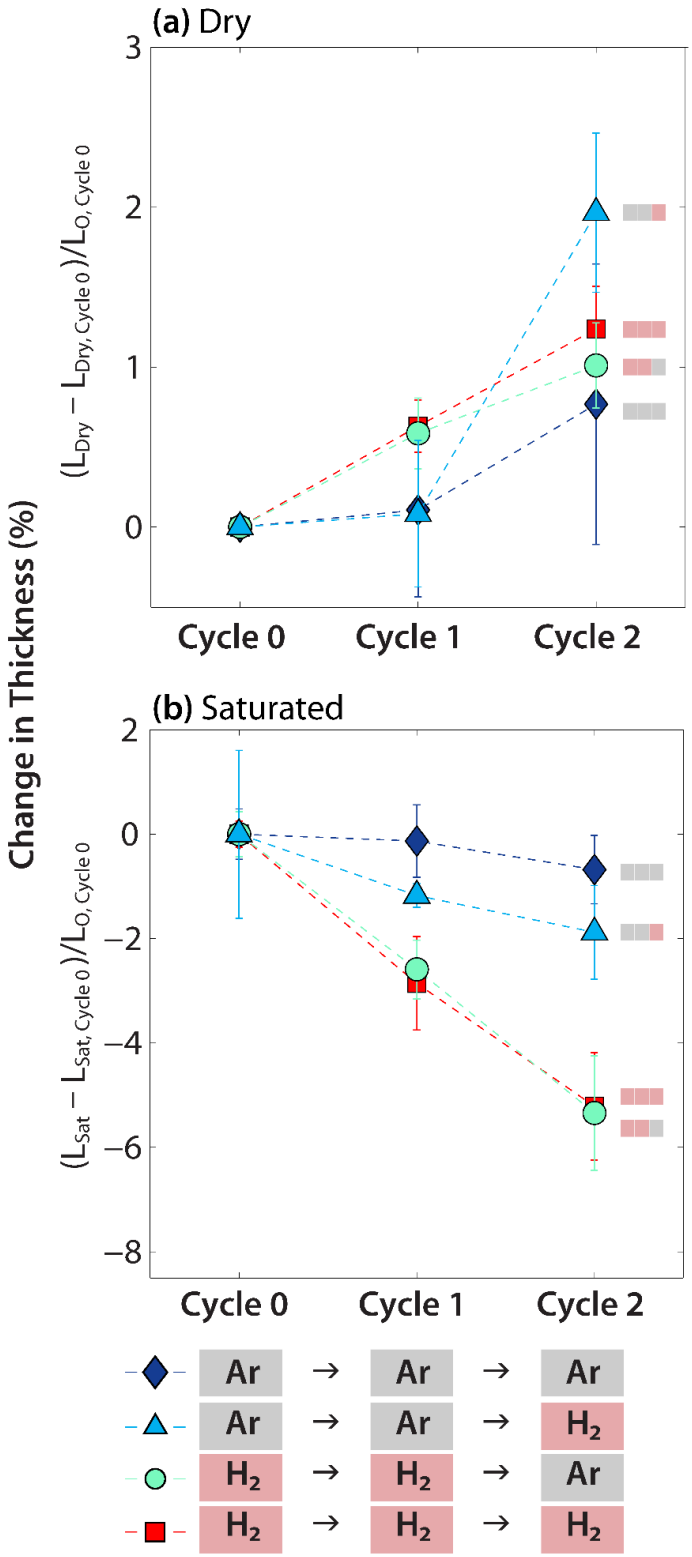

Figure 2-11: Relative humidity cycling of Pt-supported Nafion thin films (50 nm) with alternating inert and reducing gas. Comparison of Cycle 1 in gas 1 and Cycle 2 in alternative gas 2. (a) Dry change in thickness and (b) Saturated (96% RH) thickness change relative to dry thickness in Cycle 0 exposed to gas 1.

2.6. Summary

Despite being the least understood component, the gas/ionomer/Pt interface in the catalyst layer bears the utmost duty for PEFC performance. Thus, there is need for greater understanding

of pairwise interaction between gas/ionomer, ionomer/Pt, and gas/Pt interfaces to reduce critical transport losses and improve electrode design. To that effect, this chapter focused on how the gas/Pt interaction impacts the Pt surface and thus the ionomer thin film morphology and properties. Unexpectedly, a reduced water uptake was observed for ionomer thin films exposed to a reducing environment, H_2, relative to an oxidizing environment, Air. Increased densification in dry conditions, decreased deformation energy, and continual reduction in effective water uptake (measured via swelling) in the ionomer during cycling were observed under H_2. Such morphological changes are closely coupled to the ionomer thin film's transport properties.[64] These observations demonstrate the coupled impact of gas/substrate and ionomer/substrate interactions that can influence ionomer behavior. Therefore, there is a need for increased electrode-specific investigations and perhaps separate ionomer design for anode and cathode catalyst layers. The impact of electronic potential going from oxidation to reduction potentials can also affect the surface state identity and thus the morphology of the ionomer thin film, which is discussed in further chapters of this thesis. Furthermore, the existence of a water-rich phase at the Pt/ionomer interface in a reducing environment can impact surface conductivity significantly, which may not occur in an oxidizing environment. The findings herein also indicate heightened vulnerability to delamination of ultra-thin ionomer films in the anode or perhaps during electrolysis or possibly anodic potentials due to increased water-layer thickness with cycling and reduced deformation energy.

2.7. References

(1) Karan, K. PEFC Catalyst Layer: Recent Advances in Materials, Microstructural Characterization, and Modeling. Curr. Opin. Electrochem. 2017, 5 (1), 27–35.

(2) Cetinbas, F. C.; Ahluwalia, R. K.; Kariuki, N.; De Andrade, V.; Fongalland, D.; Smith, L.; Sharman, J.; Ferreira, P.; Rasouli, S.; Myers, D. J. Hybrid Approach Combining Multiple Characterization Techniques and Simulations for Microstructural Analysis of Proton Exchange Membrane Fuel Cell Electrodes. J. Power Sources 2017, 344, 62–73.

(3) Weber, A. Z.; Newman, J. Transport in Polymer-Electrolyte Membranes. J. Electrochem. Soc. 2003, 150 (7), A1008.

(4) Kongkanand, A.; Gu, W.; Mathias, M. F. Proton-Exchange Membrane Fuel Cells with Low-Pt Content. In Encyclopedia of Sustainability Science and Technology; 2018.

(5) Kongkanand, A.; Mathias, M. F. The Priority and Challenge of High-Power Performance of Low- Platinum Proton-Exchange Membrane Fuel Cells. J. Phys. Chem. Lett. 2016, 7, 1127–1137.

(6) Morawietz, T.; Handl, M.; Oldani, C.; Gazdzicki, P.; Hunger, J.; Wilhelm, F.; Blake, J.; Friedrich, K. A.; Hiesgen, R. High-Resolution Analysis of Ionomer Loss in Catalytic Layers after Operation. J. Electrochem. Soc. 2018, 165 (6), F3139–F3147.

(7) Moore, K. L. ; Reeves, K. S. . Microstructural Characterization Of PEM Fuel Cell MEAs. In DOE Hydrogen Program Annual Merit Review Proceedings; 2005.

(8) Mukherjee, P. P.; Kang, Q.; Wang, C. Y. Pore-Scale Modeling of Two-Phase Transport in Polymer Electrolyte Fuel Cells - Progress and Perspective. Energy Environ. Sci. 2010, 4 (2), 346–369.

(9) Moore, K. L. ; Reeves, S.; Blom, D. Microstructural Characterization of PEM Fuel Cell MEAs. In Department of Energy(DOE) Annual Merit Review Proceedings; 2007.

(10) Xu, H.; Kunz, R.; Fenton, J. M. Investigation of Platinum Oxidation in PEM Fuel Cells at

Various Relative Humidities. Electrochem. Solid-State Lett. 2007, 10 (1), B1.
(11) Redmond, E. L.; Setzler, B. P.; Alamgir, F. M.; Fuller, T. F. Elucidating the Oxide Growth Mechanism on Platinum at the Cathode in PEM Fuel Cells. Phys. Chem. Chem. Phys. 2014, 16 (11), 5301–5311.
(12) Kongkanand, A.; Ziegelbauer, J. M. Surface Platinum Electrooxidation in the Presence of Oxygen. J. Phys. Chem. C 2012, 116 (5), 3684–3693.
(13) Subramanian, N. P.; Greszler, T. A.; Zhang, J.; Gu, W.; Makharia, R. Pt-Oxide Coverage-Dependent Oxygen Reduction Reaction (ORR) Kinetics. J. Electrochem. Soc. 2012, 159 (5), 531–540.
(14) Furuya, Y.; Mashio, T.; Ohma, A.; Dale, N.; Oshihara, K.; Jerkiewicz, G. Surface Oxide Growth on Platinum Electrode in Aqueous Trifluoromethanesulfonic Acid. J. Chem. Phys. J. Chem. Phys. 2014, 141 (141), 164705–164705.
(15) Liu, Y.; Mathias, M.; Zhang, J. Measurement of Platinum Oxide Coverage in a Proton Exchange Membrane Fuel Cell. Electrochem. Solid-State Lett. 2010, 13, B1.
(16) Yagi, I.; Inokuma, K.; Kimijima, K.; Notsu, H. Molecular Structure of Buried Perfluorosulfonated Ionomer/Pt Interface Probed by Vibrational Sum Frequency Generation Spectroscopy. J. Phys. Chem. C 2014, 118, 26182–26190.
(17) Masuda, T.; Sonsudin, F.; Singh, P. R.; Naohara, H.; Uosaki, K. Potential-Dependent Adsorption and Desorption of Per Fl Uorosulfonated Ionomer on a Platinum Electrode Surface Probed by Electrochemical Quartz Crystal Microbalance and Atomic Force Microscopy. J. Phys. Chem. C 2013, 117 (30), 15704–15709.
(18) Kodama, K.; Motobayashi, K.; Shinohara, A.; Hasegawa, N.; Kudo, K.; Jinnouchi, R.; Osawa, M.; Morimoto, Y. Effect of the Side-Chain Structure of Perfluoro-Sulfonic Acid Ionomers on the Oxygen Reduction Reaction on the Surface of Pt. ACS Catal. 2018, 8, 694–700.
(19) Wu, J.; Yuan, X. Z.; Martin, J. J.; Wang, H.; Zhang, J.; Shen, J.; Wu, S.; Merida, W. A Review of PEM Fuel Cell Durability: Degradation Mechanisms and Mitigation Strategies. J. Power Sources 2008, 184 (1), 104–119.
(20) Yousfi-Steiner, N.; Moçotéguy, P.; Candusso, D.; Hissel, D. A Review on Polymer Electrolyte Membrane Fuel Cell Catalyst Degradation and Starvation Issues: Causes, Consequences and Diagnostic for Mitigation. J. Power Sources 2009, 194 (1), 130–145.
(21) Yu, X.; Ye, S. II Recent Advances in Activity and Durability Enhancement of Pt/C Catalytic Cathode in PEMFC. Part II: Degradation Mechanism and Durability Enhancement of Carbon Supported Platinum Catalyst. J. Power Sources 2007, 172 (1), 145–154.
(22) Beuscher, U. Experimental Method to Determine the Mass Transport Resistance of a Polymer Electrolyte Fuel Cell. J. Electrochem. Soc. 2006, 153 (9), 1788–1793.
(23) Weber, A. Z.; Kusoglu, A. Unexplained Transport Resistances for Low-Loaded Fuel-Cell Catalyst Layers. J. Mater. Chem. A 2014, 2 (c), 17207–17211.
(24) Jinnouchi, R.; Kudo, K.; Kitano, N.; Morimoto, Y. Molecular Dynamics Simulations on O2 Permeation through Nafion Ionomer on Platinum Surface. Electrochim. Acta 2016, 188, 767–776.
(25) Ohira, A.; Kuroda, S.; Mohamedz, H. F. M.; Tavernier, B. Effect of Interface on Surface Morphology and Proton Conduction of Polymer Electrolyte Thin Films. Phys. Chem. Chem. Phys. 2013, 15, 11494–11500.
(26) Kusoglu, A.; Kushner, D.; Paul, D. K.; Karan, K.; Hickner, M. a.; Weber, A. Z. Impact of Substrate and Processing on Confi Nement of Nafi on Thin Films. Adv. Funct. Mater. 2014,

24 (30), 4763–4774.
(27) Chlistunoff, J.; Pivovar, B. Effects of Ionomer Morphology on Oxygen Reduction on Pt. J. Electrochem. Soc. 2015, 162 (8), F890–F900.
(28) Yu, X.; Ye, S. I Recent Advances in Activity and Durability Enhancement of Pt/C Catalytic Cathode in PEMFC. Part I. Physico-Chemical and Electronic Interaction between Pt and Carbon Support, and Activity Enhancement of Pt/C Catalyst. J. Power Sources 2007, 172 (1), 133–144.
(29) He, Q.; Joy, D. C.; Keffer, D. J. Impact of Oxidation on Nanoparticle Adhesion to Carbon Substrates. RSC Adv. 2013, 3 (36), 15792.
(30) He, Q.; Suraweera, N. S.; Joy, D. C.; Keffer, D. J. Structure of the Ionomer Film in Catalyst Layers of Proton Exchange Membrane Fuel Cells. J. Phys. Chem. C 2013, 117 (48), 25305–25316.
(31) Haubold, H.-G.; Wang, X. H.; Goerigk, G.; Schilling, W. In Situ Anomalous Small-Angle X-Ray Scattering Investigation of Carbon-Supported Eleetroeatalysts. J. Appl. Cryst 1997, 30, 653–658.
(32) Smith, M. C.; Gilbert, J. A.; Mawdsley, J. R.; Nke Seifert, S.; Myers, D. J. In Situ Small-Angle X-Ray Scattering Observation of Pt Catalyst Particle Growth During Potential Cycling. J. AM. CHEM. SOC. 2008, 130, 8112–8113.
(33) Jerkiewicz, G.; Vatankhah, G.; Lessard, J.; Soriaga, M. P.; Park, Y. S. Surface-Oxide Growth at Platinum Electrodes in Aqueous H2SO 4 Reexamination of Its Mechanism through Combined Cyclic-Voltammetry, Electrochemical Quartz-Crystal Nanobalance, and Auger Electron Spectroscopy Measurements. Electrochim. Acta 2004, 49 (9–10), 1451–1459.
(34) Shibata, S.; Sumino, M. P. Kinetics and Mechanism of Reduction of Oxides Film on Smooth Platinum Electrodes with Hydrogen. Electrochim. Acta 1975, 20, 739–746.
(35) Conway, B. E. Electrochemical At Noble Metals Oxide Film Formation As a Surface-Chemical Process. Prog. Surf. Sci. 1995, 49 (95), 331–452.
(36) Conway, B. E.; Jerkiewicz, G. Surface Orientation Dependence of Oxide Film Growth at Platinum Single Crystals. J. Electroanal. Chem. 1992, 339 (1–2), 123–146.
(37) Topalov, A. a.; Cherevko, S.; Zeradjanin, A. R.; Meier, J. C.; Katsounaros, I.; Mayrhofer, K. J. J. Towards a Comprehensive Understanding of Platinum Dissolution in Acidic Media. Chem. Sci. 2014, 5 (2), 631.
(38) Kusoglu, A.; Kwong, A.; Clark, K. T.; Gunterman, H. P.; Weber, A. Z. Water Uptake of Fuel-Cell Catalyst Layers. J. Electrochem. Soc. 2012, 159, 530–535.
(39) Kusoglu, A.; Weber, A. Z. New Insights into Perfluorinated Sulfonic-Acid Ionomers. Chem. Rev. 2017, 117, 987–1104.
(40) Damasceno Borges, D.; Gebel, G.; Franco, A. a.; Malek, K.; Mossa, S. Morphology of Supported Polymer Electrolyte Ultrathin Films: A Numerical Study. J. Phys. Chem. C 2015, 119 (2), 1201–1216.
(41) Ono, Y.; Nagao, Y. Interfacial Structure and Proton Conductivity of Nafion at the Pt-Deposited Surface. Langmuir 2016, 32, 352–358.
(42) Gasteiger, H. A.; Kocha, S. S.; Sompalli, B.; Wagner, F. T. Activity Benchmarks and Requirements for Pt, Pt-Alloy, and Non-Pt Oxygen Reduction Catalysts for PEMFCs. Appl. Catal. B Environ. 2005, 56, 9–35.
(43) Gai, L.; Shin, Y. K.; Raju, M.; Van Duin, A. C. T.; Raman, S. Atomistic Adsorption of Oxygen and Hydrogen on Platinum Catalysts by Hybrid Grand Canonical Monte

Carlo/Reactive Molecular Dynamics. J. Phys. Chem. C 2016, 120 (18), 9780–9793.
(44) Wood, D. L.; Chlistunoff, J.; Majewski, J.; Borup, R. L. Nafion Structural Phenomena at Platinum and Carbon Interfaces. J. Am. Chem. Soc. 2009, 131 (50), 18096–18104.
(45) Murthia, V.S., Dura, J.A, Satijab , S., Majkrzakb, C. F. Water Uptake and Interfacial Structural Changes of Thin Film Nafion ® Membranes Measured by Neutron Reflectivity for PEM Fuel Cells. Trans. E C S Soc. Electrochem. 2008, 16 (2), 1471–1485.
(46) Staldera, A. F. .; Melchior, T.; Müller, M. ; Sage, D.; Blu, T.; Unser, M. Low-Bond Axisymmetric Drop Shape Analysis for Surface Tension and Contact Angle Measurements of Sessile Drops. Colloids Surfaces A Physicochem. Eng. Asp. 2010, 364 (1–3), 72–81.
(47) Stoney, G. G. The Tension of Metallic Films Deposited by Electrolysis Author (s): G . Gerald Stoney Source : Proceedings of the Royal Society of London . Series A , Containing Papers of a Published by : Royal Society Stable URL : Http://Www.Jstor.Org/Stable/92886 Acc. In Proceedings of the Royal Society of London series A, Containing Papers of a Mathematical and Physical Character; 1909; Vol. 82, pp 172–175.
(48) Page, K. A.; Shin, J. W.; Eastman, S. A.; Rowe, B. W.; Kim, S.; Kusoglu, A.; Yager, K. G.; Stafford, G. R. In Situ Method for Measuring the Mechanical Properties of Nafion Thin Films during Hydration Cycles. ACS Appl. Mater. Interfaces 2015, 7 (32), 17874–17883.
(49) Luo, H.; Park, S.; Yeung, H.; Chan, H.; Weaver, M. J. Surface Oxidation of Platinum-Group Transition Metals in Ambient Gaseous Environments: Role of Electrochemical versus Chemical Pathways. J. Phys. Chem. B 2000, 104, 8250–8258.
(50) Gland, J. L.; Korchak, V. N. THE ADSORPTION OF OXYGEN ON A STEPPED PLATINUM SINGLE CRYSTAL SURFACE. Surf. Sci. 1978, 75, 733–750.
(51) Gland, J. L. Molecular and Atomic Adsorption of Oxygen on the Pt(111) and Pt(S)-12(111) × (111) Surfaces. Surf. Sci. 1980, 93 (2–3), 487–514.
(52) Li, Z.; Beck, P.; Ohlberg, D. A. A.; Stewart, D. R.; Williams, R. S. Surface Properties of Platinum Thin Films as a Function of Plasma Treatment Conditions. Surf. Sci. 2003, 529 (3), 410–418.
(53) Gland, J. L. Molecular and Atomic Adsorption of Oxygen on the Pt(111) and Pt(S)-12(111) ?? (111) Surfaces. Surf. Sci. 1980, 93 (2–3), 487–514.
(54) Paul, D. K.; Karan, K.; Docoslis, A.; Giorgi, J. B.; Pearce, J. Characteristics of Self-Assembled Ultrathin Nafion Films. Macromolecules 2013, 46.
(55) Mohamed, H. F. M.; Kuroda, S.; Kobayashi, Y.; Oshima, N.; Suzuki, R.; Ohira, A. Possible Presence of Hydrophilic SO 3 H Nanoclusters on the Surface of Dry Ultrathin Nafion s Films: A Positron Annihilation Study. Phys. Chem. Chem. Phys 2013, 15, 1518–1525.
(56) Shi, Q.; Sun, R. Adsorption Manners of Hydrogen on Pt(100), (110) and (111) Surfaces at High Coverage. Comput. Theor. Chem. 2017, 1106, 43–49.
(57) Baldwin, V. H.; Hudson, J. B. Coadsorption of Hydrogen and Carbon Monoxide on (111) Pt. J. Vac. Sci. Technol. 1971, 8 (1), 49–52.
(58) Christmann, K.; Ertl, G.; Pignet, T. Adsorption of Hydrogen on a Pt(111) Surface. Surf. Sci. 1976, 54 (2), 365–392.
(59) Muller-Buschbaum, P. A Basic Introduction to Grazing Incidence Small Angle X-Ray Scattering. In Applications of Synchrotron Light to Scattering and Diffraction in Materials and Life Sciences.; 2009; Vol. 776, pp 61–89.
(60) Hiemenz, P. C. .; Lodge, T. P. . Polymer Chemistry; CRC Press, 2007.
(61) McCabe, R. W.; Wong, C.; Woo, H. S. The Passivating Oxidation of Platinum. J. Catal. 1988, 114 (2), 354–367.

(62) Morita, M.; Ohmi, E.; Hasegawa, E.; Kawakami, M.; Suma, K. Control Factor of Native Oxide Growth on Silicon in Air or in Ultra Pure Water. Appl. Phys. Lett. 1989, 55 (6), 562–564.
(63) Morita, M.; Ohmi, T.; Hasegawa, E.; Kawakami, M.; Ohwada, M. Growth of Native Oxide on a Silicon Surface. J. Appl. Phys. 1990, 68 (3), 1272–1281.
(64) Kusoglu, A.; Dursch, T. J.; Weber, A. Z. Nanostructure/Swelling Relationships of Bulk and Thin film PFSA Ionomers. Adv. Funct. Mater. 2016, 26, 4961–4975.

3. On Thermal Relaxation of Ionomer Thin Films and Gas Transport

3.1. Relationship Between Thermal Transitions and Gas Transport in Polymers

Though polymers are macromolecules comprised of thousands of atoms and covalent bonds in varying coordination, they have characteristic properties that define them. Transition temperature is one example. Thermal transitions of polymers are associated with thermodynamic phase transitions from one phase into another. Since polymers contain both amorphous and crystalline phases, their phase transition is usually reflected in change in slope, discontinuity or continuity of the first partial derivative with respect to temperature of a given continuous state function (e.g. chemical potential, volume or enthalpy).[1] For an amorphous or semi-crystalline polymer, the temperature at which change in slope as of a state function occurs is referred to as thermal transition. Transition temperature reflects the energy required for molecular rotation and motion of polymer segments, thus, it is highly sensitive to structure.[1] One of the most commonly utilized types of thermal transition is glassy to rubbery transition, which is referred to as the glass transition temperature (T_g). Polymers in glassy state are thought to be rigid and solid-like, whereas polymers in a rubbery state are flexible and behave liquid-like. Glassy polymers are commonly utilized at temperatures below their T_g, and therefore are not in a state of thermodynamic equilibrium. T_g is considered to be a characteristic thermodynamic transition temperature, but is also kinetically controlled. This means that the thermally induced relaxation phenomenon dependens on time and rate of heating, and can be altered via processing conditions. When a polymer is cooled below its melting temperature, a super-cooled liquid is obtained. As the temperature is reduced, the rate of cooperative intermolecular rearrangement is significantly slowed compared to the timescale of the experiment. The polymer viscosity increases as the T_g is approached, and the number of energy minimum configurational states is greatly reduced.[2] This transition temperature, therefore, has implications for physical properties that affect performance such as the modulus, specific heat capacity, thermal expansion coefficient, and gas-transport properties.

Two physical polymer-membrane properties of interest associated with T_g are mechanical strength and gas-transport properties. Gas transport through dense polymers involves dissolution of gas/membrane interface followed by a diffusional transport process, which is driven by a chemical-potential gradient through the membrane and available free-volume in the polymer.[3] The accessible free volume represents a distribution of transient void spaces resulting from the molecular and morphological arrangements of polymer chains. Therefore, available free volume for gas transport is a function of penetrant gas size and type as well as the chemical and physical nature of the polymer. For glassy, rigid polymers, accessible free volume is restricted by prohibited rotation of polymer segments. Low chain agility in glassy polymers decreases diffusive transport. However, with increase in temperature towards T_g and transition into the rubbery state of polymer, accessible free volume significantly increases the mobility of polymer chains, thereby improving transport rates by orders of magnitude.[3] Similar phenomenological dynamics can be extended to mechanical properties. Mechanical properties are critical indicators for structural stability, thermo-mechanical impact resistance, and withstanding chemical-mechanical stressors and degradation during processing and operation. Near characteristic phase-transition temperatures, viscoelastic dynamics in polymers is influenced by chain aggregation size, crystallinity and stiffness.[4] This change in dynamics near characteristic temperatures results in temperature-dependent segmental mobilities that dictate deformation and mechanical properties like modulus, stress-strain response,

and expansivity. Experimentally, mechanical properties of polymers are controlled by varying the chemical nature, molecular coordination, and processing conditions. Examples include varying molecular weight to control brittle strength, incorporating ether linkages for improved chain flexibility and rotation, and varying processing temperature to induce varying crystallinity.[4] From such a vantage point, mechanical properties and gas-transport behavior are, therefore, interrelated as the mobility of polymer chains and crystallinity control accessible local sites for dissolution and diffusion of gas through polymers. Understanding the molecular/morphological origins of relaxation dynamics, therefore, can establish bottom-up approaches for designing polymers with desired structure-function relationships. It is with this lens that this chapter examines thermal transitions in perfluorosulfonic ionomer (PFSI).

3.2. Thermal Transitions and Relaxation of Bulk Perfluorosulfonic Ionomer

In this chapter, the general term PFSI is used and represents both the acidic form perfluorosulfonic acid (PFSA) discussed in pervious chapters and other cation exchanged perfluorosulfonic ionomers. The random copolymer nature of PFSI results in significant differences in relaxation behavior from homopolymers. Relaxation dynamics further complicated by the tethered ionic end groups (Figure 3-1). One key difference is that using T_g as a single marker for PFSI relaxation behavior, as is frequently utilized for neutral homopolymers, is not an adequate descriptor for observed mechanical and relaxation behaviors. Additionally, PFSIs have multiple thermal transitions (T_T) whose nature and source is long-debated.[5–8] PFSIs' antipodal composition of hydrophobic tetrafluoroethylene backbone and hydrophilic perfluorovinyl ether side chains containing an ionic end group $–SO_3H$ results in nano-phase separated, complex ionic structures that possess four thermal transitions (γ, β', β, α).[9,10] (See schematic in Figure 3-1) T_γ (–100 to –80°C) occurs due to local short-range motion in the backbone $-CF_2-$ chains independent of counterion type (SO_3-M).[5,7] β' and β relaxation have been attributed to ether side-chain motion and main-chain motion in PFSI network, respectively.[7,11] T_β relaxation is considered equivalent to the T_g in classical glassy polymers, which marks the onset of transition from glassy (brittle) to rubbery (viscous) behavior.[8] For PFSI in H^+ form, β relaxations have been reported to be around –60 to 23 ºC.[9] However, exchanging H^+ with different counterions (M^+) results in distinct dynamic-mechanical analysis peaks for the ether side-chain $T_{\beta'}$ (near –20 to –30 °C) and ionomer matrix, T_β (around 130-170 °C).[6,7] The final thermal transition, α-relaxation, T_α (87-120 °C in H^+ form and 210-240 °C in various M^+ form),[8,12,13] is attributed to relaxation of the clustered ionic domains scattered within the nonpolar ionomer matrix. Although the T_T are discussed here as discrete, small-scale chain motion local relaxations, they can still influence gas transport by impacting segmental mobility, molecular packing, and available free-volume, independently as well as in a coupled manner as exemplified in other polymers.[14,15]

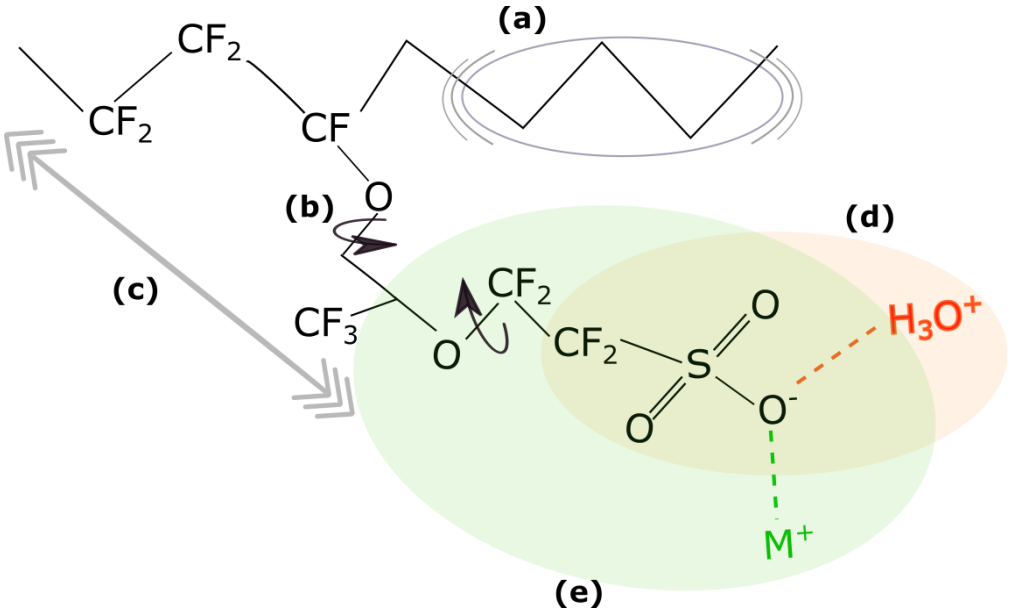

Figure 3-1: Schematic of possible PFSI physiochemical origins of molecular motions and relaxation modes observed at different temperatures. (a) γ-relaxation refer to local backbone vibrations; (b) β'-relaxation refer to sidechain rotation and motion; (c) β-relaxation are due to main-chain long-range mobility; (d) &(e) α-relaxation of ionic end-group mobility with varying spheres of influence for (d) T_α in proton form or (e) T_α in different metal cation type; has larger sphere of influence due to strong ionic association with sulfonic acid group.

For PFSIs used in electrochemical devices, characteristic transition temperatures are critical for understanding relaxation dynamics, mechanical integrity, and gas transport useful for defining optimal operating conditions and explaining failures. In bulk PFSI (thickness typically >10 μm), EW (equivalent weight), and side-chain length and chemistry dictate polymeric packing, torsional movement, and chain relaxation required for gas adsorption, solubility, and permeation.[14,16–18] In thin film (thickness < 100 nm), temperature driven structural relaxation phenomenon and behavior in PFSIs is additionally influenced by local interfaces and finite size effects of confined ionomer films as discussed below.[19,20]

3.3. Thermal Transition in Thin and Ultra-Thin Perfluorosulfonic Ionomer Films

Use of nanometer-scale polymer films has accelerated coating-application technology, gas-separation systems, and energy-conversion devices by reducing cost and material waste.[21–23] However, deviation of thin film polymers from measured bulk physical property adds significant uncertainty to their utility.[24–27] As polymer film thickness approaches the molecular length scale, the influence of local surface and interface effects are amplified, resulting in thin film structure non-uniformity, stability differences, and variations in dynamics compared to bulk behavior.[23,28–30] As previously discussed in Chapter 1, such is the case for ion-conducting polymer (ionomer) thin films employed in polymer-electrolyte fuel cells (PEFCs) and related technologies.[31–35] Studies focusing on nano-confined PFSI ionomers have demonstrated the effect of thickness and substrate on morphology and domain orientation that alter an ionomer's proton conductivity on carbon and platinum surfaces.[36–39] In addition, changes in ionomer ion-exchange capacity (inverse of EW), variability in processing conditions, and differences in surface wettability and interaction

have already been proven to impact mechanical properties and water-uptake capacity of ionomer thin films.[39–45] Following these trends, it is reasonable to presuppose similar nano-confinement effects on relaxation dynamics and gas permeability to explain the aforementioned inferred PFSI thin film gas-transport limitations.[46] However, a direct correlation of gas transport to confinement-driven parameters in ionomer thin films has yet to be established. Utilizing T_T as characteristic thermodynamic transition of structural relaxation, this study aims to develop understanding of confinement-driven changes in T_T of PFSIs (Nafion and 3M) in the 30 to 250°C range as a proxy for chain mobility and packing impacting critical properties like gas permeability. Spectroscopic ellipsometry technique of substrate-supported ionomer thin films characterizes local changes in mobility and evaluates the dependence of T_T on electrostatic network via metal counterion exchange (Na^+, Li^+, Cs^+).

3.4. Materials and Experimental Methods

3.4.1. Substrate Preparation

Substrates used in this study were silicon (Si 100 n-type). Wafers were cut into 1/2-inch squares before cleaning by rinsing with water and then twice with isopropyl alcohol (IPA) with nitrogen drying after each rinse.

3.4.2. Ionomer Thin film Preparation

H^+ form Thin film Sample Preparation: Commercially available Nafion resin (5wt%) from Sigma Aldrich and manufacturer provided 3M PFSA resin (25wt%) were used as stock solutions. EW of Nafion resin solutions were 1100 g/mol, while 3M resins of EW 825 and 725 g/mol (IEC = 0.91, 1.21, 1.38 meq/g respectively) were used. Stock solutions were diluted (0.4 wt.% to 3.6 wt.% ionomer) to result in desired film thickness. Diluted solutions were filtered (Millex-SV 2-5.0µm, EMD Millipore Corporation) to remove contaminants or large aggregates, sonicated for 20 min (5510 Branson Ultrasonic) to ensure thorough dispersion, and allowed to equilibrate for at least 24 hours prior to casting. Solutions were spun cast on Si substrates at variable speeds of 500 to 3000 rpm for 1 minute (Laurell WS-650-23B model) to obtain the desired film thickness. The resultant spin-cast thin film was annealed to remove residual solvents in vacuum oven at 150 ºC for 1 hour (Binder) and immediately removed. These un-exchanged thin PFSI films are referred to as 'H^+' form thin films.

M^+ form Thin film Sample Preparation: Spin-cast, annealed samples were immersed in 0.5 M solution of their respective sulfate salts (Na_2SO_4, Cs_2SO_4, Li_2SO_4) for 5.5 hrs. Exchanged thin PFSI films are referred to as 'M^+' form thin films depending on type of cation exchanged. Re-exchanged samples are those that were turned back to cast 'H^+' form by immersing cation exchanged samples in 0.5 M H_2SO_4 for 5 hrs.

3.4.3. Ionomer Thin Film Thermal Expansion via Heated-Cell Ellipsometry

In this work, in-situ temperature-induced thickness change (thickness expansivity) was measured using a variable-angle spectroscopic ellipsometer (VASE) M-2000D Model from J. A. Woollam (Expanded details on spectroscopic ellipsometer are found in Appendix 1). Cast and annealed samples were immediately removed into ambient conditions to ensure an initial trapped amorphous state. A slow cooling and heating rate of 1°C/min was applied to ensure that the thickness change was properly observed. A low-flow dry nitrogen environment was applied during

heating and cooling to facilitate removal of adsorbed water, as well as to prevent water reabsorption from the surrounding environment. By working in the spectral range of 400 to 1000 nm at a single incident angle of 70º, the ionomer thin film thickness supported on Si wafer was accurately captured. A two-layer model (Si, SiO_2 and Cauchy material) was constructed as the optical system. The optical model shows presence of SiO_2 layers of 1 to 4 nm in thickness. Model-fit mean-squared error ranged from $1.5\sim16\times10^{-3}$. It is critical to note that thickness and refractive index values are strongly correlated in ellipsometry, particularly for thinner films.

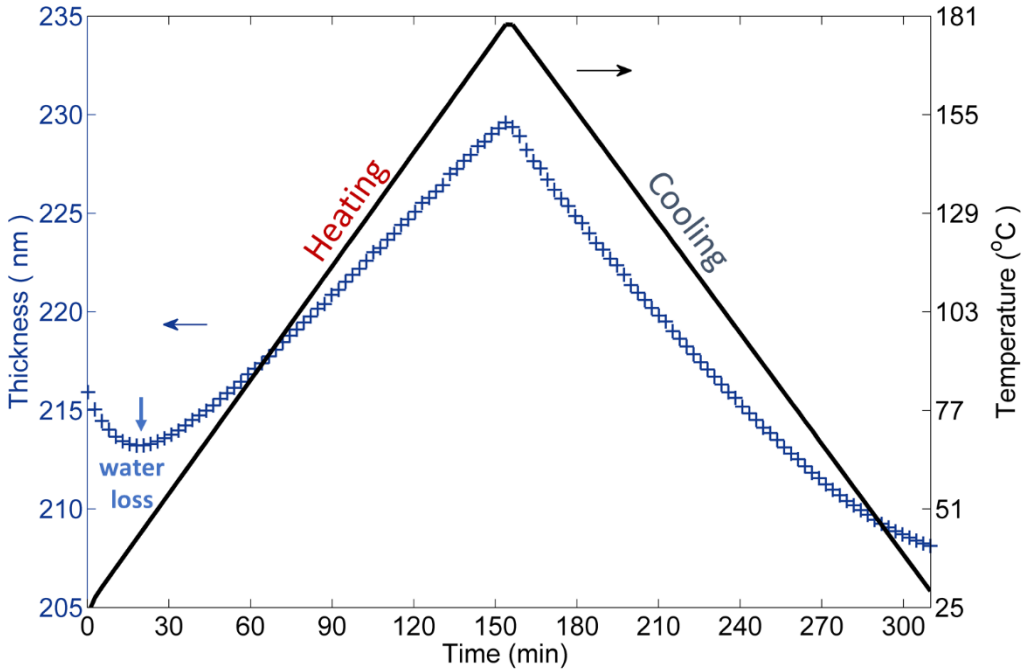

Figure 3-2: Example of heating protocol applied to PFSI thin film samples supported on Si/SiO_2 substrate.

3.5. Characterization of Ionomer Thin Film Transition Temperature

T_T in thin film polymers can be obtained via volume expansion,[47] segmental mobility,[48] and viscoelasticity[49] tracking techniques. Heated-cell ellipsometry is commonly employed to monitor transition temperature via one-dimensional thickness changes. Figure 3-2 shows heating protocol applied and expansive and depressive thickness response of a Nafion ionomer thin film as monitored in-situ via heated-cell experiments. Initial depression in thickness during heating in Figure 3-2 is associated with residual water loss from the film, which is thickness dependent (see Figure 3-3b). Expansion dynamics during the first heating cycle is highly influenced by processing history. Therefore, transition temperatures were evaluated using data acquired during the cooling protocol. Second heating was also explored, but changes in thickness during the first cooling and second heating remained very similar (see Figure 3-3a).

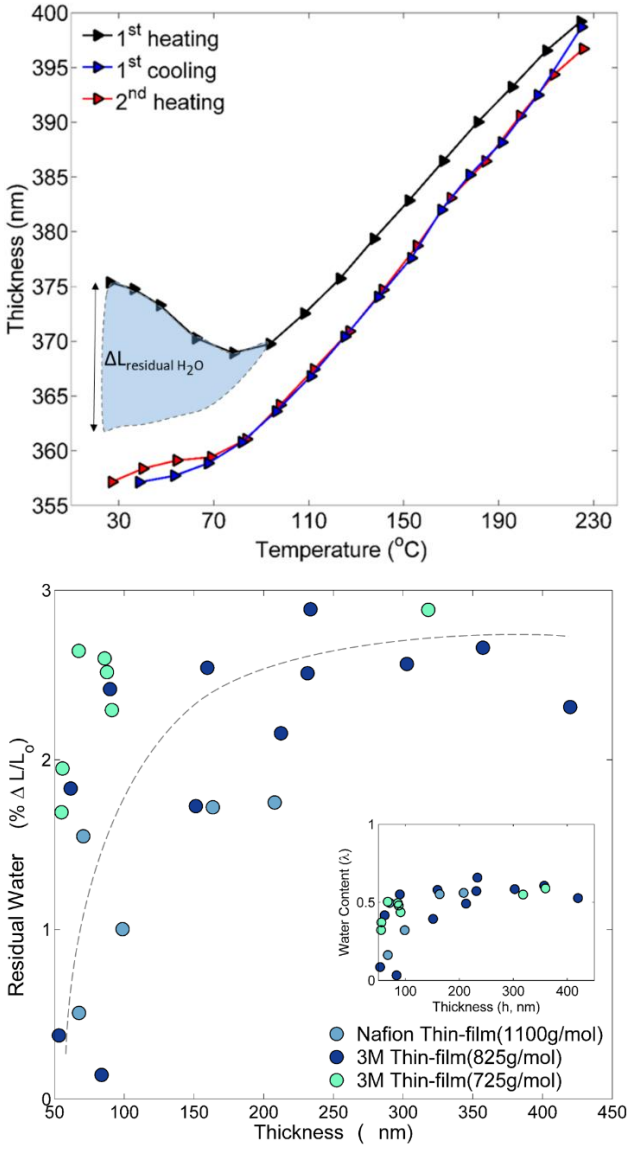

Figure 3-3: (a) Example of heat-cool-heat protocol initially applied PFSI thin film samples. Water loss is observed during first heating. First cooling and second heating show similar expansion dynamics. (b) Residual water loss from ionomer thin films during first heating.

Figure 3-4 shows the normalized thickness profile of Nafion thin films in acid (H^+) and cationic (Li^+, Na^+ and Cs^+) forms obtained via in-situ heated-cell ellipsometry. Linear thermal-expansion coefficients (α_L) in pre- and post-transition temperature regimes are calculated via

$$\alpha_L = \frac{1}{L_o}\frac{\Delta L}{\Delta T} \quad (1)$$

where L_o is the ambient, dry thickness at the end of the run and ΔL and ΔT represent change in thickness and temperature, respectively. Figure 3-6 shows T_T and pre- and post- α_L of PFSI-H^+ as a function of thickness, extracted from similar measurements shown in Figure 3-4.

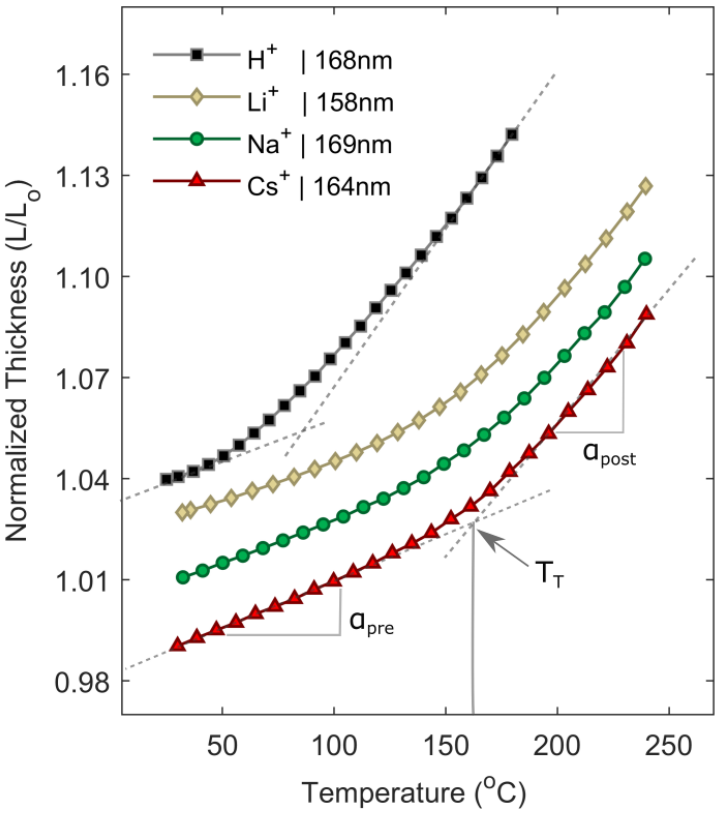

Figure 3-4: Change in normalized thickness (L/L_o) of Nafion (1100 EW) thin films with respect to dry thickness (L_o) during cooling used for calculating transition temperature (T_T) and pre- and post-transition expansion rate (α_{pre} and α_{post}). Curves are offset in the y-axis for improved visibility.

Reversibility of ion-exchange process was ensured by re-exchanging select Na^+ PFSI ionomer samples back to H^+ form and monitoring expansion rate (see Figure 3-5). Expansion trends were reproduceable.

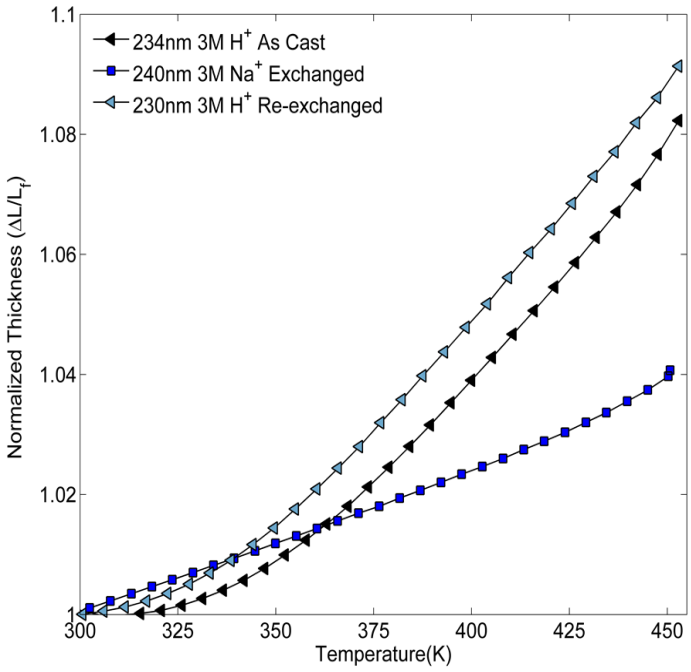

Figure 3-5: Expansion of pristine (as cast) PFSI-H^+ ionomer thin film cast on Si substrate compared to exchanged (PFSI-Na^+) and re-exchanged (re-PFSI-H^+) thin films. Expansion in PFSI-Na^+ is reversible upon re-exchange to acid form.

3.6. Impact of Confinement on Ionomer Thin Films Thermal Transition

Given a system of confined ionomer thin film supported on a solid substrate, with a significantly small thermal expansion rate, differential expansion is expected to be detected only in the ionomer layer and perpendicular to the support. Therefore, for an equivalent comparison, the anisotropic, 1-dimensional thin film expansion, α_L, is compared to the isotropic, 3-dimensional volumetric thermal-expansion coefficient, α_V, of bulk PFSI obtained from the average bulk linear expansion coefficient, where $\alpha_V \approx 3 \cdot \alpha_{L,bulk}$ from ref.[50,51] (See Figure 3-6) Both thin film T_T and α_L demonstrate no significant correlation with PFSI EW. This is counter to the reported increase in T_T of ion-containing systems with increase in ion content (decrease in EW) reported by Yeo et. al.[52] However, as also discussed in the same paper, impact on transition temperature is observed as a result of varying water content and crystallinity in the bulk system. In the thin film ionomer scenario, it is expected that the ionomer is amorphous and contains no bound water within the T_T evaluation window (first cooling stage). The relative difference between pre- and post-expansion rate and range of T_T observed for thin film PFSI-H^+ indicates that T_T is likely T_α. The T_T of thin film ionomers >100 nm in Figure 3-6a are lower than T_α of cast bulk Nafion in H^+ form (~87 °C),[9,53] and an increase in T_T with decreasing thickness is observed with some data variability. α_{pre} remains somewhat constant while α_{post} decreases with decreasing thickness (Figure 3-6b), consistent with the raised T_T evaluated. Thermal transition and subsequent relaxation behavior in thin film polymers is governed by chain conformation change upon confinement, polymer dynamics at the free-surface/polymer, and substrate/polymer interfacial interactions.[54] It is well documented that polymer chains adsorbed at attractive interfaces induce changes in orientation and local packing that results in a decreasing polymer density distribution away from the surface.[55,56] Spatially opposite to the polymer/substrate interface, the free-surface/polymer interface has unhindered

mobility and enhanced configurational freedom, thereby improving long-range motions and lowering T_T.[57–59] High wettability and low surface energy of the Si/SiO_2 support results in favorable adsorption of the PFSI-H^+ side-chain moieties,[39,60,61] pining ionomer chains and increasing local packing near the ionomer/substrate interface in dry conditions. Consequently, PFSI-H^+ thin films have significantly restricted chain mobility below T_T, as is reflected by the low α_{pre} as illustrated in the schematics in Figure 3-6. As the temperature exceeds T_T, entropically-frozen ionomer chains gain enough thermal energy to break electrostatic interactions between PFSI-H^+ side-chains and substrate, thereby relaxing the substrate-imposed constraints and resulting in an α_{post} similar to bulk PFSI. With a further decrease in thickness, the relative contribution of substrate interaction is amplified, resulting in a positive shift in T_T.

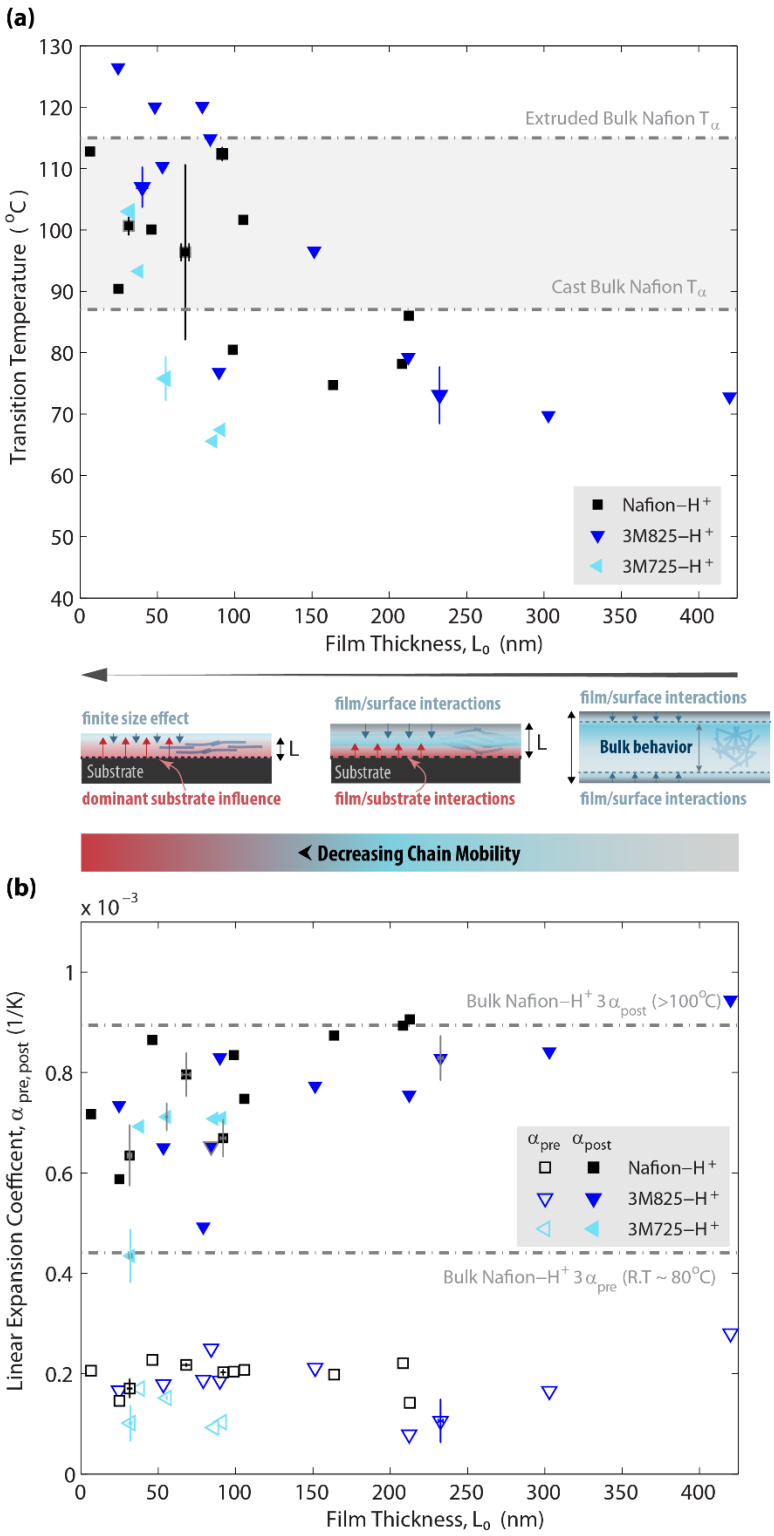

Figure 3-6: (a) Transition temperature and (b) Linear expansion coefficient, α_{pre} and α_{post}, of thin film PFSI-H^+ cast on Si/SiO_2 substrate compared to bulk Nafion linear expansion from Ref. [51]

3.7. Impact of Metal Cation on Ionomer Thin film Thermal Transition

Figure 3-7 shows T_T, α_{pre}, and α_{post} of ionomer thin films in Li^+, Na^+ and Cs^+ forms as well as bulk film. Both α_{pre} and α_{post} are similar to the expansion rates observed in bulk Nafion around the β transition.[51] Here, unlike the PFSI-H^+ for which T_T was assigned to the α transition, the T_T for PFSI-M^+ is attributed to the β transition due to (1) only a single T_T observed for PFSI-M^+ thin films and (2) the large positive shift (> 100 ºC) expected in both T_α and T_β with neutralization, as reported extensively in bulk PFSI literature.[5,8,11,52] PFSI-M^+ exhibits very small deviation from bulk T_β in the range of film thicknesses explored, contrary to PFSI-H^+ (Figure 3-7a). Table 3-1 compares PFSI T_α and T_β reported in literature with substrate-supported thin film PFSI T_T measured in this study. It is readily evident that the nature of the counterion (H^+ vs. M^+) can significantly alter relaxation behavior (α to β) causing a break in slope at high temperatures for strongly interacting, electrostatic network present in PFSI-M^+. Similar molecular origins have been shown for thermal and mechanical relaxation of bulk PFSI neutralized with various counterions.[8,52] Systematic spectroscopic and x-ray scattering studies correlating relaxations with morphological origins are required to confirm the speculated nature of T_T measured in PFSI-H^+ and PFSI-M^+ as T_α and T_β respectively.

Table 3-1: Comparison of T_T for bulk and thin film PFSI in different forms.

	T_β	T_α	Ref.
PFSI-H^+ (Bulk)	−20 to −30°C	87 to 115 ºC	[6–12]
PFSI-M^+ (Bulk)	130 to 170°C	210 to 240 °C	
PFSI-H^+ (Thin film)			
>100nm	T_T not observed.	70 to 85 °C	This work.
<100nm		70 to 130 °C	
PFSI-M^+ (Thin film)			
>100nm	140 to 170°C	T_T not observed.	This work.
<100nm	140 to 170°C		

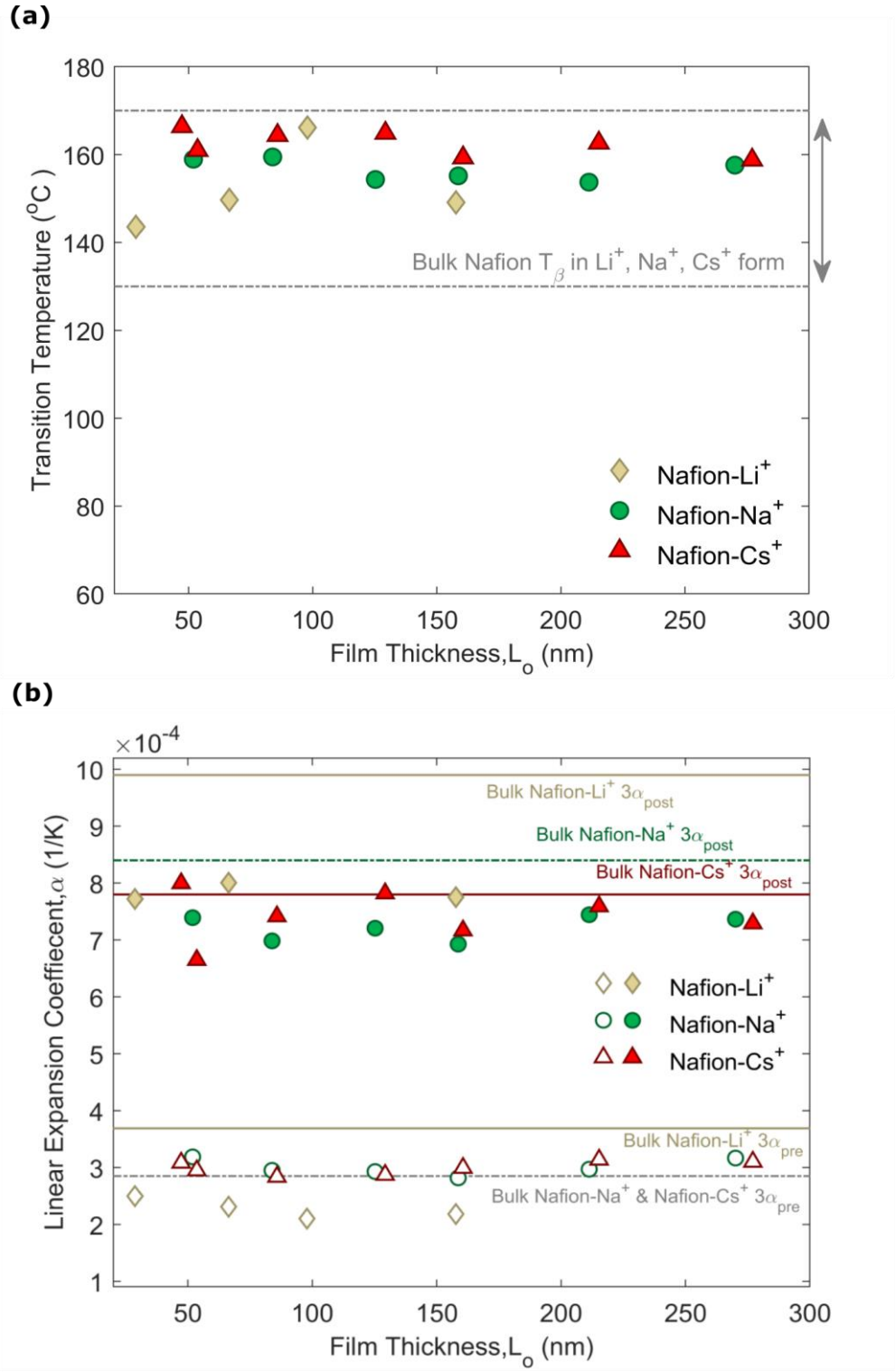

Figure 3-7: (a) Transition temperature of thin film PFSI-Li^+, PFSI-Na^+ and PFSI-Cs^+ form (b) Linear expansion coefficient, α_{pre} and α_{post}, of thin film PFSI-Li^+, PFSI-Na^+ and PFSI-Cs^+ cast on Si/SiO_2 substrate, compared to bulk Nafion linear expansion from Ref. [51]

3.8. Effect of Confinement and Counterion on Thin film Relaxation and Transport

Figure 3-6 and Figure 3-7 point to two pathways towards controlling ionomer relaxation dynamics, i.e. confining ionomer thin films to the nanometer scale, and addition of metal counterions. Together they portray a complementary view of relaxation dynamics in PFSI thin films. High mobility near the free-surface/ionomer interface reduces T_T of PFSI-H^+ thin films >100 nm relative to bulk as represented schematically in Figure 3-6. As ionomer chains tether to a solid structure and finite-size effects set in, mobility is restricted and expansion is unidirectional and anisotropic relative to the 3-dimensional expansion observed in bulk. T_T of PFSI-H^+ thin film, confined to thicknesses below 100nm, increases due to amplified impact of substrate interaction, likely through strong hydrogen bonding between the substrate and PFSI-H^+. Similar phenomenon impacting ionomer chain-end groups increases the thermal transition temperature in the presence of metal cation. Addition of metal cations increases the strength of electrostatic network in the PFSI-M^+ matrix increasing physical crosslinks, resulting in reduced conformational relaxation and subsequent increase in T_T, as depicted in Figure 3-8. Presumably, strong ion-polymer intermolecular interactions in PFSI-M^+ dominate (almost point of nullifying) the PFSI-H^+ substrate/ionomer interactions upon confinement such that T_T, α_{pre}, and α_{post} are similar to bulk PFSI-M^+ values regardless of film thickness.

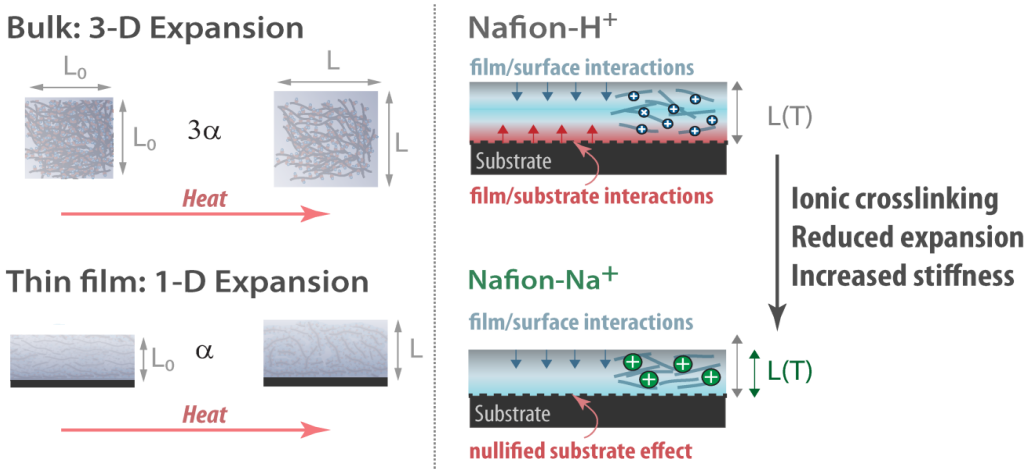

Figure 3-8: Illustration summarizing effect of confinement and counterion in ionomer thin film thermal relaxation. (on left) Comparative volumetric expansion of PFSI in bulk vs. thin film. (on right) Ionomer thin film expansion in acid form (H^+) vs. cation (Na^+) form.

This is the first time that spectroscopic ellipsometry is employed to evaluate thermal transitions in PFSI. Findings in this chapter confirm the strong influence of substrate and free surface upon confinement witnessed in neutralized polymer thin films.[23,28,57,62] Increasing T_T with confinement and presence of large univalent counterions point towards increased ionomer chain stiffness that could result in reduced gas permeability (see illustrations in Figure 3-1, Figure 3-6, Figure 3-8). In agreement with our findings, a study focusing on Cs^+ and Pt^{2+} ion-exchanged Nafion by Mohamed et al. showed greater free-volume thermal expansion in H^+ form.[63] The study also revealed chain stiffening-induced reduction in gas permeation with counterion exchange despite the higher free-volume measured. Confinement and counterion-induced chain stiffening has been observed with rise in modulus relative to bulk PFSI.[13,42,64,65] Although the polymer thickness at which the confinement effect commences does not always directly correlate with T_T deviations from the bulk value, the trend is in accord with the trends in moduli of various thin film

polymers.[26,66] Similarly, confined (<100 nm) and cation-exchanged PFSI impeded chain mobility and increased stiffness induced by substrate interactions and by physical ionic crosslinks, as evidenced by their higher T_T. Ionomer chain crosslinking is the stiffening of ionomer chain as a result of more rigid bond with counterion i.e. ionic bond between metal cation end group with side-chain of ionomer. Increased stiffness and low chain mobility can result in reduced gas permeability. Figure 3-9 shows this relationship between ionomer thin film chain mobility with gas permeability utilizing data obtained from electrode diagnostics[33] and microelectrode investigations.[34] T_T of a representative electrode ionomer thin film thickness of 46 nm was utilized to capture ionomer chain mobility at a given operating temperature (T_T -T); chain mobility increases with as T approaches T_T. Despite the fact that impact of water on ionomer chain mobility was not explored here, Figure 3-9 shows a strong relationship between reduction in ionomer chain mobility and decrease in ionomer thin film oxygen permeability.

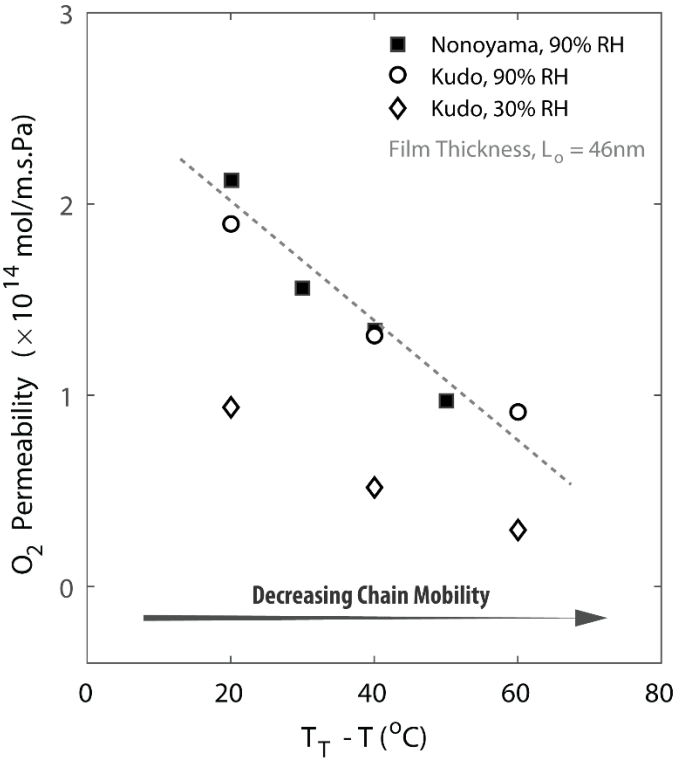

Figure 3-9: Nafion thin film oxygen permeability from catalyst layer resistance[13] and microelectrode measurements[34] as a function of PFSI-H^+ thin film (46 nm) mobility represented by T_T-T.

3.9. Summary

PFSI thin films in energy-conversion devices have limitations in functionality attributed to confinement-driven and surface-dependent interactions. This study highlights the effects of confinement and interface-dependent interactions of PFSI thin films by exploring thin film thermal transition temperature (T_T). Change in T_T in polymers is an indicator for chain relaxation and mobility with implications on properties like gas permeation. This work demonstrates an increase in T_T with decreasing PFSI film thickness in acid (H^+) form (from 70 to 130°C for 400 to 10 nm, respectively). In metal cation (M^+) exchanged PFSIs, T_T remained constant with thickness. These

results point to an interplay between increased chain mobility at the free surface and hindered motion near the rigid substrate interface, which is amplified upon further confinement. This balance is additionally impacted by ionomer intermolecular forces, as strong electrostatic networks within the PFSI-M^+ matrix raises T_T above the mainly hydrogen bonded PFSI-H^+ ionomer. For expanded insights, complementary methods tracking change in ionomer density as a function of ionomer thickness are needed to elucidate effect of confinement on ionomer chain packing. Additional synergistic surface characterization techniques like nano-indentation and techniques that can probe molecular fluctuations like broadband dielectric spectroscopy can further explore confinement-induced changes in ionomer properties. Such studies can expand this work to elucidate confinement-driven changes to gas transport under real device operating conditions, especially in the presence of water. Overall, findings in this chapter signify the interplay between the surface and electrostatic interactions controlling the thermal transitions in confined ionomer films, which could be harnessed to understand and tune ionomers' gas-transport properties and functionality in porous electrodes of electrochemical energy-conversion devices.

3.10. References

(1) van Krevelen, D. W. Chapter 6 Transition Temperatures. In Properties of Polymers; 2009.
(2) Hill, A. J.; Tant, M. R. The Structure and Properties of Glassy Polymers. In American Chemical Society; 1999; Vol. 710, pp 1–20.
(3) Yampolskii, Y.; Pinnau, I.; Freeman, B. D. Transport of Gases and Vapors in Glassy and Rubbery Polymers. In Materials Science of Membranes for Gas and Vapor Separation; 2006; pp 1–48.
(4) van Krevelen, D. W. Chapter 13: Mechanical Properties of Solid Polymers. In Properties of Polymers; 2009.
(5) Osborn, S. J.; Hassan, M. K.; Divoux, G. M.; Rhoades, D. W.; Mauritz, K. a.; Moore, R. B. Glass Transition Temperature of Perfluorosulfonic Acid Ionomers. Macromolecules 2007, 40 (10), 3886–3890.
(6) Matos, B. R.; Dresch, M. A.; Santiago, E. I.; Linardi, M.; de Florio, D. Z.; Fonseca, F. C. Nafion -Relaxation Dependence on Temperature and Relative Humidity Studied by Dielectric Spectroscopy. J. Electrochem. Soc. 2012, 160 (1), F43–F48.
(7) Kyu, T.; Hashiyama, M.; Eisenberg, A. Dynamic Mechanical Studies of Partially Ionized and Neutralized Nafion Polymers. Can. J. Chem. 1983, 61, 680–687.
(8) Page, K. A.; Cable, K. M.; Moore, R. B. Molecular Origins of the Thermal Transitions and Dynamic Mechanical Relaxations in Perfluorosulfonate Ionomers. Macromolecules 2005, 38 (15), 6472–6484.
(9) Kusoglu, A.; Weber, A. Z. New Insights into Perfluorinated Sulfonic-Acid Ionomers. Chem. Rev. 2017, 117, 987–1104.
(10) Mauritz, K. a; Moore, R. B. State of Understanding of Nafion. Chem. Rev. 2004, 104 (10), 4535–4585.
(11) Page, K. A.; Landis, F. A.; Phillips, A. K.; Moore, R. B. SAXS Analysis of the Thermal Relaxation of Anisotropic Morphologies in Oriented Nafion Membranes. Macromolecules 2006, 39 (11), 3939–3946.
(12) Fan, Y.; Tongren, D.; Cornelius, C. J. The Role of a Metal Ion within Nafion upon Its Physical and Gas Transport Properties. Eur. Polym. J. 2014, 50, 271–278.
(13) Shi, S.; Weber, A. Z.; Kusoglu, A. Structure-Transport Relationship of Perfluorosulfonic-

Acid Membranes in Different Cationic Forms. Electrochim. Acta 2016, 220, 517–528.
(14) Yampolskii, Y.; Pinnau, I.; Freeman, B. D. Materials Science of Membranes for Gas and Vapor Separation; 2006.
(15) Pixton, M. R.; Paul, D. R.; Yampol'skii, Y. Relationships between Structure and Transport Properties for Polymers with Aromatic Backbones. In Polymeric Gas Separation Membranes; CRC Press: Boca Raton, FL, 1994; pp 83–154.
(16) Shimizu, R.; Park, Y.-C.; Kakinuma, K.; Iiyama, A.; Uchida, M. Effects of Both Oxygen Permeability and Ion Exchange Capacity for Cathode Ionomers on the Performance and Durability of Polymer Electrolyte Fuel Cells. J. Electrochem. Soc. 2018, 165 (6), F3063–F3071.
(17) Mohamed, H. F. M.; Ito, K.; Kobayashi, Y.; Takimoto, N.; Takeoka, Y.; Ohira, A. Free Volume and Permeabilities of O2 and H2 in Nafion Membranes for Polymer Electrolyte Fuel Cells. Polymer (Guildf). 2008, 49 (13–14), 3091–3097.
(18) Buchi, F. N.; Wakizoe, M.; Srinivasan, S. Microelectrocle Investigation of Oxygen Permeation in Perfluorinatecl Proton Exchange Membranes with Different Equivalent Weights. J. Electrochem Soc. 1996, 143 (3), 927–932.
(19) Keddie, J. L.; Jones, R. A. L.; Cory, R. A. Size-Dependent Depression of the Glass Transition Temperature in Polymer Films. Europhys. Lett. 1994, 27 (1), 59–64.
(20) Frank, B.; Gast, A. P.; Russell, T. P.; Brown, H. R.; Hawker, C. Polymer Mobility in Thin Films. Macromolecules 1996, 29 (20), 6531–6534.
(21) Brauman, J. I.; Szuromi, P. Thin Films. Science (80-.). 1996, 273 (5277), 855.
(22) C. W. Frank, V. Rao, M. M. Despotopoulou, R. F. W. Pease, W. D. Hinsberg, R. D. M. and J. F. R. Structure in Thin and Ultrathin Spin-Cast Polymer Films. Science (80-.). 1996, 273.
(23) Alcoutlabi, M.; McKenna, G. B. Effects of Confinement on Material Behaviour at the Nanometre Size Scale. J. Phys. Condens. Matter 2005, 17 (15), R461–R524.
(24) Rowe, B. W.; Freeman, B. D.; Paul, D. R. Physical Aging of Ultrathin Glassy Polymer Films Tracked by Gas Permeability. Polymer (Guildf). 2009, 50 (23), 5565–5575.
(25) Rittigstein, P.; Priestley, R. D.; Broadbelt, L. J.; Torkelson, J. M. Model Polymer Nanocomposites Provide an Understanding of Confinement Effects in Real Nanocomposites. Nat. Mater. 2007, 6 (4), 278–282.
(26) Torres, J. M.; Stafford, C. M.; Vogt, B. D. Elastic Modulus of Amorphous Polymer Thin Films: Relationship to the Glass Transition Temperature. ACS Nano 2009, 3 (9), 2677–2685.
(27) Harry D. Rowland, William P. King, John B. Pethica, G. L. W. C. Molecular Confinement Accelerates Deformation of Entangled Polymers During Squeeze Flow. Science (80-.). 2008, 322, 720–724.
(28) Russell, T. P.; Chai, Y. 50th Anniversary Perspective: Putting the Squeeze on Polymers: A Perspective on Polymer Thin Films and Interfaces. Macromolecules 2017, 50 (12), 4597–4609.
(29) Napolitano, S.; Glynos, E.; Tito, N. B. Glass Transition of Polymers in Bulk, Confined Geometries, and near Interfaces. Reports Prog. Phys. 2017, 80 (3), 1–51.
(30) Askar, S.; Torkelson, J. M. Stiffness of Thin, Supported Polystyrene Films: Free-Surface, Substrate, and Confinement Effects Characterized via Self-Referencing Fluorescence. Polym. (United Kingdom) 2016, 99, 417–426.
(31) Gottesfeld, S., Raistrick, I. D., Srinivasan, S. Oxygen Reduction Kinetics on a Platinum RDE Coated with a Recast Nafion Film. J. Electrochem. Soc. 1987, 134 (6), 1455–1462.

(32) Parthasarthy, A.; Srinivasan, S.; Appleby, A. J.; Martin, C. R. Electrode-Kinetics of Oxygen Reduction at Carbon-Supported and Unsupported Platinum Microcrystallite Nafion(R) Interfaces. J. Electroanal. Chem. 1992, 339 (1–2), 101–121.
(33) Nonoyama, N.; Okazaki, S.; Weber, A. Z.; Ikogi, Y.; Yoshida, T. Analysis of Oxygen-Transport Diffusion Resistance in Proton-Exchange-Membrane Fuel Cells. J. Electrochem. Soc. 2011, 158 (4), B416–B423.
(34) Kudo, K.; Jinnouchi, R.; Morimoto, Y. Humidity and Temperature Dependences of Oxygen Transport Resistance of Nafion Thin Film on Platinum Electrode. Electrochim. Acta 2016, 209, 682–690.
(35) Suzuki, T.; Kudo, K.; Morimoto, Y. Model for Investigation of Oxygen Transport Limitation in a Polymer Electrolyte Fuel Cell. J. Power Sources 2013, 222, 379–389.
(36) Ohira, A.; Kuroda, S.; Mohamedz, H. F. M.; Tavernier, B. Effect of Interface on Surface Morphology and Proton Conduction of Polymer Electrolyte Thin Films. Phys. Chem. Chem. Phys. 2013, 15, 11494–11500.
(37) Kusoglu, A.; Kushner, D.; Paul, D. K.; Karan, K.; Hickner, M. a.; Weber, A. Z. Impact of Substrate and Processing on Confi Nement of Nafi on Thin Films. Adv. Funct. Mater. 2014, 24 (30), 4763–4774.
(38) Nagao, Y. Proton-Conductivity Enhancement in Polymer Thin Films. Langmuir 2017, 33 (44), 12547–12558.
(39) DeCaluwe, S. C.; Kienzle, P. A.; Bhargava, P.; Baker, A. M.; Dura, J. A. Phase Segregation of Sulfonate Groups in Nafion Interface Lamellae, Quantified via Neutron Reflectometry Fitting Techniques for Multi-Layered Structures. Soft Matter 2014, 10 (31), 5763–5776.
(40) Kusoglu, A.; Dursch, T. J.; Weber, A. Z. Nanostructure/Swelling Relationships of Bulk and Thin film PFSA Ionomers. Adv. Funct. Mater. 2016, 26, 4961–4975.
(41) Frieberg, B. R.; Page, K. A.; Graybill, J. R.; Walker, M. L.; Stafford, C. M.; Stafford, G. R.; Soles, C. L. Mechanical Response of Thermally Annealed Nafion Thin Films. ACS Appl. Mater. Interfaces 2016, 8 (48), 33240–33249.
(42) Page, K. A. .; Kusoglu, A.; Stafford, C. M. .; Kim, S.; Kline, R. J.; Weber, A. Z. . Confinement-Driven Increase in Ionomer Thin film Modulus. Nano Lett. 2014, 14, 2299–2304.
(43) Paul, D. K.; Shim, H. K. K.; Giorgi, J. B.; Karan, K. Thickness Dependence of Thermally Induced Changes in Surface and Bulk Properties of Nafion ® Nanofilms. J. Polym. Sci. Part B Polym. Phys. 2016, 54 (13), 1267–1277.
(44) Tesfaye, M.; MacDonald, A. N.; Dudenas, P. J.; Kusoglu, A.; Weber, A. Z. Exploring Substrate/Ionomer Interaction under Oxidizing and Reducing Environments. Electrochem. commun. 2018, 87, 86–90.
(45) DeCaluwe, S. C.; Baker, A. M.; Bhargava, P.; Fischer, J. E.; Dura, J. A. Structure-Property Relationships at Nafion Thin film Interfaces: Thickness Effects on Hydration and Anisotropic Ion Transport. Nano Energy 2018, 46, 91–100.
(46) Weber, A. Z.; Kusoglu, A. Unexplained Transport Resistances for Low-Loaded Fuel-Cell Catalyst Layers. J. Mater. Chem. A 2014, 2 (c), 17207–17211.
(47) Dalnoki-Veress, K.; Forrest, J. a; Murray, C.; Gigault, C.; Dutcher, J. R. Molecular Weight Dependence of Reductions in the Glass Transition Temperature of Thin, Freely Standing Polymer Films. Phys. Rev. E 2001, 63 (3), 031801-1–10.
(48) Hall, D. B.; Miller, R. D.; Torkelson, J. M. Molecular Probe Techniques for Studying Diffusion and Relaxation in Thin and Ultrathin Polymer Films. J Polym Sci B Polym Phys

1997, 35, 2795–2802.
(49) Buenviaje, C.; Dinelli, F.; Overney, R. M. Glass Transition Measurements of Ultrathin Polystyrene Films. In Techniques; 2000; Vol. 77, pp 1–18.
(50) Ho, C. Y.; Taylor, R. E. Thermal Expansion of Solids, Vol. 4.; ASM International, 1998.
(51) Takamatsu, T.; Eisenberg, a. Density and Expansion Coefficients of Nafion. J. App. Poly. Sci. 1979, 24, 2221–2235.
(52) Yeo, S. C.; Eisenberg, A. Physical Properties and Supermolecular Structure of Perfluorinated Ion-containing (Nafion) Polymers. J. Appl. Polym. Sci. 1977, 21 (4), 875–898.
(53) Schaberg, Mark S.; Abulu, J.E.; Haugen, G.M.; Emery, M. A.; O'Conner, S. J.; Xiong, P.N.; Hamrock, S. J. New Multi Acid Side-Chain Ionomers for Proton Exchange Membrane Fuel Cells. ECS Trans. 2010, 33 (1), 627–633.
(54) Hammerschmidt, J. A.; Gladfelter, W. L.; Haugstad, G. Probing Polymer Viscoelastic Relaxations with Temperature-Controlled Friction Force Microscopy. Macromolecules 1999, 32 (10), 3360–3367.
(55) De Virgiliis, A.; Milchev, A.; Rostiashvili, V. G.; Vilgis, T. a. Structure and Dynamics of a Polymer Melt at an Attractive Surface. Eur. Phys. J. E. Soft Matter 2012, 35 (97), 1–11.
(56) Pham, J. Q.; Green, P. F. The Glass Transition of Thin Film Polymer/Polymer Blends: Interfacial Interactions and Confinement. J. Chem. Phys. 2002, 116 (13), 5801–5806.
(57) Priestley, R. D.; Ellison, C. J.; Broadbelt, L. J.; Torkelson, J. M. Structural Relaxation of Polymer Glasses at Surfaces, Interfaces, and in Between. Science 2005, 309 (5733), 456–459.
(58) Burroughs, M. J.; Napolitano, S.; Cangialosi, D.; Priestley, R. D. Direct Measurement of Glass Transition Temperature in Exposed and Buried Adsorbed Polymer Nanolayers. Macromolecules 2016, 49 (12), 4647–4655.
(59) Paeng, K.; Swallen, S. F.; Ediger, M. D. Direct Measurement of Molecular Motion in Freestanding Polystyrene Thin Films. J. Am. Chem. Soc. 2011, 133 (22), 8444–8447.
(60) Ruhe, J.; Novotny, V.; Clarke, T.; Street, G. B. Ultrathin Perfluoropolyether Films---Influence of Anchoring and Mobility of Polymers on the Tribological Properties. J. Tribol. 1996, 118 (3), 663–668.
(61) Rühe, J. G. V. J. T. G. B., Blackman, G., Novotny, V. J., Clarke, T., Street, G. B., & Kuan, S. Terminal Attachment of Perfluorinated Polymers to Solid Surfaces. J. Appl. Polym. Sci. 1994, 53 (6), 825–836.
(62) Priestley, R. D.; Mundra, M. K.; Barnett, N. J.; Broadbelt, L. J.; Torkelson, J. M. Effects of Nanoscale Confinement and Interfaces on the Glass Transition Temperatures of a Series of Poly(n-Methacrylate) Films. Aust. J. Chem. 2007, 60 (10), 765–771.
(63) Mohamed, H. F. M.; Kobayashi, Y.; Kuroda, C. S.; Ohira, A. Free Volume and Gas Permeation in Ion-Exchanged Forms of the Nafion® Membrane. J. Phys. Conf. Ser. 2010, 225, 1–8.
(64) Albe, N. D.; Bas, C.; Reymond, L.; Dane, A.; Rossinot, E.; Flandin, L. Key Counter Ion Parameters Governing Polluted Nafion Membrane Properties. J. Polym. Sci. Part B Polym. Phys. 2009, 47 (14), 1381–1392.
(65) Page, K. A.; Shin, J. W.; Eastman, S. A.; Rowe, B. W.; Kim, S.; Kusoglu, A.; Yager, K. G.; Stafford, G. R. In Situ Method for Measuring the Mechanical Properties of Nafion Thin Films during Hydration Cycles. ACS Appl. Mater. Interfaces 2015, 7 (32), 17874–17883.
(66) Tweedie, C. A.; Constantinides, G.; Lehman, K. E.; Brill, D. J.; Blackman, G. S.; Van Vliet,

K. J. Enhanced Stiffness of Amorphous Polymer Surfaces under Confinement of Localized Contact Loads. Adv. Mater. 2007, 19 (18), 2540–2546.

4. Impact of Metal Cations in Ionomer Thin Films

4.1. Introduction to Cations in Bulk Perfluorosulfonic Ionomers

Introduction of metal cations into electrochemical devices has three main pathways: (1) transition metal and lanthanoid cations are intentionally introduced into a membrane-electrode assembly (MEA) to improve overall performance and stability, (2) group I, group II and other metals are incorporated into the ionomer structure to alter mechanical and rheological behavior, and (3) cationic contaminants migrate into the ionomer from other components of the electrochemical device or operating environment. Discussion and exploration of the root cause underlying the effects of metal cations in electrochemical devices, and more specifically ionomers, started in the 1980s. Table 4-1 summarizes the types of metal cations found in different components, introduction route, and characterization techniques used. As discussed in Chapter 1, innovative electrocatalyst designs in fuel cells alloying platinum(Pt) metal with transition metal (such as Pd, Fe, V, Co, Ni, Cu, Cr, and Ti) have demonstrated oxygen-reduction kinetics improvements from 3 to 22 fold.[1–5] These alloys, however, cause stability and durability concerns as Pt-metal electrodes suffer from higher performance degradation rate compared to classical Pt electrodes,[1,6] exhibit supporting metal loss and relocation from electrode into membrane during cycling,[7–9] and lack long-term stability and retention of geometry in the highly acidic environment present in PEFCs.[10] A consequence of Pt-metal electrode degradation is the relocation of metal cations in the thin film ionomer binder in the electrode and ionomer electrolyte separator due to the high affinity of M^{z+} for sulfonate groups (SO_3^-) end groups over H^+.

Table 4-1: Introduction and final location of cationic contaminants and characterization techniques utilized

Metallic and Cationic Contaminants	Location	Characterization Method	Ref.
Ca^{2+} Co^{2+}, Pd^{2+}, Pt^{2+}, Ni^{2+}	Membrane Electrode Assembly (MEA) from co-alloy metals, and gas and coolant supply	Electrochemical Impedance spectroscopy (EIS), scanning electron microscope (SEM), energy dispersive X-ray spectroscopy (EDX), micro-computed tomography, Synchrotron micro-X-ray fluorescence (μ-XRF), accelerated stress tests (ASTs), in-operando anomalous small angle x-ray scattering (ASAXS), X-ray absorption spectroscopy, Inductive Coupled Plasma Optical Mass spectroscopy (ICPMS),Transmission electron microscopy (TEM), Atomic-level chemical mapping enabled by STEM-EELS, Electron probe microanalysis (EPMA), High-Resolution Electron Microscopy (HREM), Rotating Disk Electrode	[1,3–8,11–15]
Li^{+}, Na^{+}, K^{+}, Cs^{+}, Ru^{+} Mg^{2+}, Ca^{2+}, Sr^{2+}, Ba^{2+} Sc^{3+}, Y^{3+}, Fe^{2+}, Fe^{3+}, Ni^{2+}, Cu^{2+}, Zn^{2+}, Cr^{z+}, Ag^{+} Al^{3+}, Sn^{2+} Eu^{3+}, La^{3+}, Ce^{4+}	Polymer Electrolyte membrane (Ionomer Separator) From bipolar plates, fabrication method, piping tubes, humidification and coolant reagent, gas supply.	Ultraviolet-Visible Spectroscopy (UV-Vis), Dynamic Scanning Calorimetry (DSC), Dynamic Mechanical Analysis (DMA), Dynamic Thermogravimetric Analysis (DTG), Small Angle X-ray scattering (SAXS), Wide Angle X-ray Scattering (WAXS), Small angle neutron scattering (SANS), Nuclear Magnetic Resonance (NMR), Spectrophotometer, Fourier transform infrared spectroscopy (FTIR), XRD, Mechanical Testing, Dielectric Spectroscopy, Viscometer	[16–49]
Ni^{2+}, Co^{2+}, Ce^{4+}	Ionomer thin films (<10μm)	XRF, EIS, Microelectrode, Inductive Coupled Plasma Optical Emission Spectroscopy (ICP-OES)	[50,51]

Introduction of metal cations into ionomer can occur during electrode preparation and PEFC operation. Ionomers can be contaminated by foreign cationic ions (such as K^{+}, Na^{+}, Al^{3+}, Fe^{3+}, Ca^{2+}, Ba^{2+}) originating from pollutants in gas supply and coolant reagent, during fabrication of the fuel cell, and as a result of corrosion of bipolar plates and leaching form other sources.[7,12,23,40,52] Such contaminants are revealed through electrochemical impedance spectroscopy, accelerated stress tests and post-mortem analysis. Even at low ppm levels, metal cation contaminants with lower mobility have been shown to replace protonic sites, reduce transference number of conductive species, lower ionomer/membrane conductivity,[21,38,40] hinder oxygen-reduction reaction kinetics,[50,53,54] reduce membrane water retention, and promote peroxy radical formation resulting in chemical degradation, rise in cell temperature, enhanced pinhole formation and cell death.[55] Mitigating these negative impacts is critical for meeting durability and lifetime requirements for increased commercialization and marketability of PEFCs.[56,57]

Due to direct cation's impact on electrostatic interactions with the fixed anionic groups in ionomers, intentional introduction of distinct cations in the ionomer can provide an alternative means of changing ionomer properties. By varying the cation-ionomer interaction, modulation in ionomer behavior can be accomplished without requiring synthesis of new materials. Ionomer

properties can be controlled by key factors like local interaction of cation with polymer matrix, concentration of cations, nature of cation, ionomer backbone and side-chain nature and length, etc.[36,58,59] These factors have been used to modify properties of various other ionomers outside of PFSAs such as sulfonated polystyrene, polyurethane, and poly (ethylene-co-acrylic acid). These alternative ionomers are utilized as battery separators/electrolytes, where tethered metal-ion mobility and thermo-mechanical properties are highly coupled with ionomer aggregation structure that is influenced by counterion type, neutralization level, and cation-anion spacer length. [60] In bulk PFSA ionomers, metal cations impact thermostability, water sorption, conductivity, gas-transport coefficients, density, mechanical properties, relaxation dynamics, and morphological structure.[21–26,30–32,34–37,61–65] As a result, it is expected that metal cations can also impact ionomer thin films in the electrode. Impact of group I monovalent cations on ionomer thin film thermal relaxation has already been discussed in Chapter 3. This chapter uses monovalent cations as a jump-off point towards a comprehensive understanding of impact of metal cations on confined ionomer thin film properties. Water uptake, structure, and mechanical properties of group-I, some group-II and transition-metal cation-exchanged thin film ionomers of varied thickness are explored in this chapter. However, prior to discussing ionomer thin films, it is worthwhile to examine key cation factors responsible for determining ionomer behavior.

Discussion on the impact of metal cations on bulk PFSA ionomer in the literature has largely focused on group I and group II metals; discussion on the impact of transition metals like Al and Zn are few and primarily focused on electrode performance. Metal neutralized or exchanged ionomers are impacted by ionic charge-to-size ratio. Eisenberg et. al. first demonstrated ionic-potential-controlling coulombic attraction between cation and anion as a parameter controlling inter-chain spacing (d-spacing) and storage modulus of styrene-based ionomers, especially for monovalent group-I metal cations.[66] This finding has been supported by various studies that came after examining thermal stability and water uptake of PFSA ionomers.[21,31,49] In an aqueous environment, the implication of these findings is that ions with the lowest surface charge density are preferentially absorbed into ionomer structure with greater affinity.[67] In a dry or humidified environment, Lewis-acid strength (LAS) appears to be the more structure-function defining parameter compared to ionic radius. LAS quantifies the affinity of cation with anion (sulfonate anion attached to the ionomer side-chain). Critical transition for properties like the temperature window of degradation and solvation of water in ionomer has been observed to be around LAS of 0.27, which is equivalent to the approximated Lewis-base strength of sulfonate anion.[35] Ionomers neutralized by cations with LAS < 0.2 showed strong cation/sulfonate anion interaction resulting of improved side-chain stability and thermal stability whereas cations with LAS > 0.3 showed reduced stability due to increased polarizing effects.[23,68] Location of solvating water molecule in cation-exchanged ionomer is also impacted by LAS, increasing and decreasing LAS above or below a critical value, results in cation-anion interaction that is disrupted by water molecules instead of water molecule enveloped cation-anion pair.[21,35] The extent of this disruption is a result of additional factors including cation covalent nature, hydration energy, size, and valence.

Strong cations with large charge-to-size ratios and high hydration energies are found in the more aqueous ionic domains, whereas weaker cations like Cs^+ are commonly located near the polymer matrix wall charges with weaker hydrogen bonds with water.[67] This observation agrees with the separation of ionomer morphology into nonpolar fluorocarbon backbone, ionic cluster region, and interfacial side-chain-rich regions.[36] Such localization of cations depends on the covalent nature of the cation; this trend is more evident when observing trends across the periodic

table row than down the column. Visser and coworkers observed cation-dependent ionic aggregates in the order of Cd^{2+}< Ni^{2+} < Na^{+} < Sr^{2+}< Ca^{2+} cations in sulfonated polyurethane ionomers.[58,69] Within the same column, the size of aggregate decreased with decrease in cation radius, while within the same row and charge, more covalent metals like Ni^{2+} and Cd^{2+} had larger size than Ca^{2+}. The local area near the transition-metal cation becomes more ordered, inducing ionic aggregates that result in physical crosslinks and stiff ionomer chains.[58,69] Expanding on this finding, Pan et. al demonstrated oxygen/transition metal coordination distances in hydrated and dry ionomers to be similar to transition metal(Ni—Ni) crystal distances.[41] Such cation-ionomer coordination can result in cation dependent electrostatic networks, aggregation size, chain mobility, all impacting transport properties. Findings from Goswami and coworkers corroborate the relationship between ionic aggregation and transport as they report an inverse relationship between polymer volume fraction and self-diffusion coefficient of monovalent and divalent ions in Nafion.[17,36] More explicitly, cation-metal-dependent morphology has been shown experimentally via relaxation studies[39,70] and computationally by Bolintineanu et. al.,[59] Li et. al.,[26] and Daly et. al.[71]

This chapter extends the fundamental insights from bulk PFSA membranes to thin film ionomers coating the electrocatalyst. Although both thin film ionomers and bulk membranes are sourced from the same polymer, confinement and finite size effects in thin films point towards deviation of thin film ionomer behavior from bulk membrane, as discussed in Chapter 1. As such, local impacts of co-alloy leaching and cation contamination in thin ionomer films requires additional attention. Impact of cations on thin film ionomers so far remains unexplored with few studies[50,51] so far focused on impact of transition-metal cations limiting fundamental understanding to specific metals alone. In this work, water uptake and morphology of ionomer thin films of thickness 20-200 nm are investigated as a function of different cation doping. Monovalent cations (Li^{+}, Na^{+} and Cs^{+}) are explored as baseline cations to contrast proton form (non-doped, baseline ionomer) to elucidate impact of ionic size and ionic crosslinking on water uptake and ionomer nanostructure. Relaxation dynamics of Li^{+}, Na^{+} and Cs^{+} exchanged ionomer thin films of thickness 50 to 300nm explored in Chapter 3 revealed similar expansion dynamics as bulk ionomer due to dominating strong ionic interactions over confinement. Similarities and deviations from this expected outcome are discussed. In addition, impact of divalent and transition metal cations (Mg^{2+}, Co^{2+} and Ni^{2+}) on ionomer thin film water-uptake capacity and relaxation dynamics are also explored in section 4.4.

4.2. Materials and Experimental Methods

4.2.1. Substrate Preparation

Substrates used in this study were Silicon (Si 100 n-type). Wafers were cut into 1/2-inch squares before cleaning. Gold (Au)-coated quartz crystal substrates were also used for select water-uptake measurements. The square wafers and Au crystals were rinsed with water, and then rinsed twice with isopropyl alcohol (IPA) with nitrogen drying after each rinse. For improved film adhesion and removal of additional organic contaminants, rinsed substrates were treated with a benchtop ultraviolet ozone cleaner for 15 min (Novascan).

4.2.2. Ionomer Thin Film Preparation

Commercially available Nafion resin (5 wt%) from Ion Power was used as a stock solution and diluted to 0.4 to 2.95 wt.% ionomer in isopropyl alcohol (Sigma Aldrich) to result in desired film thickness (20 to 200 nm, respectively). Diluted solutions were filtered (Millex-SV 2-5.0µm, EMD Millipore Corporation) to remove contaminants and large aggregates, sonicated for 20 min (5510 Branson Ultrasonic) to ensure thorough dispersion, and allowed to equilibrate for at least 24 hours prior to casting for consistent film formation. Solutions were spun cast on clean Si substrates at variable speeds of 1000 to 3000 rpm for 1 minute (Laurell WS-650-23B model) to obtain the desired film thickness. The resultant spun-cast thin films were annealed in vacuum oven at 150ºC for 1 hour (Binder) to remove residual, trapped solvent and immediately removed into ambient lab environment.

4.2.3. Cation (M^+) Exchange of Ionomer Thin Films

To ion-exchange Nafion thin films, spun-cast samples were immersed in 0.5 M aqueous solution of their respective sulfate salts (Li_2SO_4, Na_2SO_4, Cs_2SO_4, $MgSO_4$, $NiSO_4$, $CoSO_4$) for 5 hrs. Exchanged samples (except Ni^+ and Co^+ form) were then removed from the exchange-salt solutions, thoroughly rinsed with deionized water (18MΩ-cm, Milli-Q), and heat treated at 100ºC for 1 hour (Binder) to remove surface water and dry the samples. This was done for equivalent comparison against un-exchanged (H^+ form) ionomer thin film samples and bulk membrane literature data (where bulk samples were dried in a similar manner[21]). Impact of post-exchange heat treatment on Ni^+ and Co^+ form ionomer thin films will be discussed later in this chapter (Section 4.4)

4.2.4. Water-Uptake Measurement via Quartz Microbalance and Ellipsometry

Relative humidity induced changes in thickness and sorbed water mass of Si/SiO_2 and Au supported Nafion thin films were captured by tracking changes in polarized light via in-situ spectroscopic ellipsometry (J. A. Woollam) and quartz-crystal microbalance (QCM). Clean and bare Au-coated quartz crystals were placed into the QCM holder to obtain baseline bare crystal reading for 2 hr. Thin film samples were then spun cast and annealed on the Au crystal as described above. Samples were then loaded in QCM holder exposed to dry and humidified gas N_2 in a sealed chamber (See Appendix B for discussion on QCM) While mass uptake is being tracked by QCM, change in thickness is simultaneously tracked by spectroscopic ellipsometry (See Appendix A for spectroscopic ellipsometry).

All samples used a leak-proof environmental cell; the cell was provided by J. A. Woollam for spectroscopic ellipsometry only measurements while combined QCM-ellipsometry measurements used in-house made custom environmental cell. N_2 was used as humidifying gas at a flowrate of 500 sccm for all set points. To minimize sample-to-sample variability and to create a consistent water history, all measurements were preceded with 30 min of dry (0%) and saturated (100%) relative-humidity (RH) exposure, followed by 30 min hold step from 0% to 100% at 25% RH intervals; total in-situ tracking time was 3.5 hrs. In spectral range of 400 to 1000 nm at single incident angles of 70º, ionomer thin film thickness supported on Si wafer was accurately modeled using a two-layer model (Si, native SiO_2, and Cauchy material). The optical model shows presence of SiO_2 layers of 0.2 to 4 nm in thickness. For Au-coated quartz crystals, thin film thickness was accurately modeled using a two-layer model (Au substrate and Cauchy material). Mean-squared error for samples was in the range of $1\text{-}4\times10^{-3}$. Equilibrated thin film thickness at a given RH, L_{RH},

is the average thickness from the last 2 to 5 min of the selected humidity step. The change in swelling is calculated relative to the dry thickness taken as the average thickness of the second 0% RH step (L_o),

$$Swelling\ Fraction(\%) = \frac{\Delta L}{L_o} \times 100 = \frac{L_{RH} - L_o}{L_o} \times 100 \quad (1)$$

Fractional swelling associated with one-dimensional swelling in these thin film ionomers can be converted to local water content, λ, quantifying number of water molecules per sulfonic acid group (mol H_2O/ mol SO_3^-) via

$$\lambda = \frac{\Delta L}{L_o} \times \frac{EW_{Nafion}}{M_W \cdot \rho_{Nafion}} \quad (2)$$

where EW_{Nafion} is equivalent weight of Nafion (1100 $g_{polymer}/mol_{SO3-}$), M_w is molar mass of water (18 g/mol) and ρ_{Nafion} is Nafion polymer density. Properties pertaining to cations, and ionomer exchanged cations are given in Table 4-2.

Table 4-2: Properties of Cations and Cation exchanged Nafion.

	H_3O^+	Li^+	Na^+	Cs^+	Mg^{2+}	Ni^{2+}	Co^{2+}
Cationic radius(r_c, pm)[21,72]	60	90	116	181	86	72	74
Ionic potential (q^2/ r_c, nm^{-1})	16.7	11.1	8.62	5.5	46.5	55.6	54.1
Hydration radius (pm)[73]		382	360	329	470	404	
Primary Hydration Number[74]	10	5	5	2[a]	14	13.5	13.3
Ionic Mobility (D_{M+}, $\times 10^5 cm^2/s$)[c]	9.31	1.03	1.33		0.71		
Hydration energy (kJ/mol)[75]	1091	513	409	264	1921	2105	1996
Ionomer Dry Density(g/cm^3) [26,64,76,77]	2.075	2.078	2.113	2.304	2.2 [b]		
LAS[23,35]	0.33	0.22	0.16	0.08	0.36	0.50	0.40

[a] Solvation number from Table 2.7 ref. [74]
[b] Estimated Density
[c] D_{M+} are at infinite dilution in water at 25 °C[78]

4.2.5. M^+ Thin Film Ionomer Structure via Grazing Incidence Small Angle X-ray Scattering (GISAXS)

The GISAXS experiments were carried out in beamline 7.3.3 of the Advanced Light Source (ALS) at Lawrence Berkeley National Laboratory (LBNL). Si/SiO_2 supported Nafion thin films were placed into an in-house built environmental chamber with X-ray transparent Kapton windows as described in ref .[79] The sample was equilibrated in humidified N_2 gas at room temperature and GISAXS patterns were collected in-situ. GISAXS patterns were recorded at varying incidence angles (α_i) above the critical angle (α_c) for Nafion film (~0.18) but below that for Si/SiO_2 substrate (~ 0.2°). Sample-to-detector distance was approximately 1.8 m. Exposure time for the collected images was 20 sec. The X-ray energy used was 10 keV, with a monochromator energy resolution E/dE of 100. Patterns shown were acquired with a 2D Dectris Pilatus 2M CCD detector (172 µm × 172 µm pixel size).

4.2.6. Thin film Ionomer Mechanical Property Measurement

For mechanical-property measurement[2], cation-exchanged Nafion thin films were prepared on a thin Si cantilever wafer (105 μm thickness by approximately 0.5 cm x 4 cm). The sample was clamped in an environmental cell that allowed for humidified gas feeds. Constrained swelling caused by the presence of the substrate results in a compressive force, which bends the thin Si cantilever. Using a laser array reflected off the backside of the sample, the change in curvature of the substrate is measured. Using Stoney's thin film equation the stress-thickness $\sigma_f t_f$ is calculated via

$$\Delta F_c = \frac{E_s h_s^2 \Delta\kappa}{6(1-\nu_s)} = \sigma_f t_f \quad (3)$$

where E_s, ν_s, $\Delta\kappa$ and h_s are the Young's modulus, Poisson's ratio, change in curvature, and thickness of the substrate, respectively [80]. The measured cantilever force (ΔF_c) is equal to the average biaxial stress of the Nafion film (σ_f) multiplied by its thickness (t_f). A full description of the method can be found in ref.[19] Ellipsometry gives the strain (equation 1) under the same conditions. From these two experiments, stress-strain curves are generated. Integrating the area under the stress-swelling strain curve gives an estimate for mechanical energy associated with deformation of the sample during swelling. Although quantification of thin film deformation is not trivial, results from this test still provide valuable insight for obtaining qualitative trends and comparison between different samples.

4.3. Impact of Monovalent Cations on Sorption Property of Ionomer Thin Films

4.3.1. Impact on Structure and Aggregation of Ionomer Thin Films

Figure 4-1 shows GISAXS morphological patterns in thin film ionomers in H^+, Li^+, Na^+, and Cs^+ form. Figure 4-1a shows strongly phase separated ionomer peak halo in H^+ and Li^+ form thin film under saturation, while Na^+ form shows only faint peak and Cs^+ form displays no discernable peak in the 2D GISAXS spectra. Cations with large radius induce lower hydration energy as water molecules surrounding the cation preferably interact with each other instead of strongly associating with the counterion.[23,81] As a result, cations with large ionic radii, like Cs^+, allow greater coordination geometry and large aggregation and reduced phase separation.[59] This is reflected in the Figure 4-1b in-plane line-cut intensity profiles where minimal structural features are observed for Cs^+ form thin film followed by a broadening but growing ionomer peak in Na^+, Li^+ and H^+ form around q = 1.7 nm^{-1}, indicative of a wider domain size-distribution. Cs^+ cation, due to its much larger size, appears to cause a notable change in structure. Here, it is important to note that, X-ray scatting patters of Cs^+-exchanged ionomers are weak and have broad peaks with large background scattering. This is a consequence of the cation's large size, electron density and polarizability and results in reduced certainty around structural implications for Cs^+ ionomer. Figure 4-1c reflects this degree of phase separation via the full-width at half-maximum (FWHM) analysis of the observed ionomer peak. The lower the FWHM, the narrower the distribution of

[2] Mechanical property measurements were conducted in collaboration with Peter J. Dudenas (PhD candidate, Chemical and Biomolecular Engineering, University of California, Berkeley)

ionomer hydrophilic domains, indicating stronger nanophase separation upon hydration. FWHM increases with cation ionic radius similar to bulk membranes,[21] signifying similarly, locally, phase-separated morphology both in bulk and in thin film ionomers. The takeaway in these findings is that cation-induced structural changes are present in thin films as well as in bulk ionomers; as such, bulk to thin film property deviation reflects the additional roles of confinement and substrate effects.

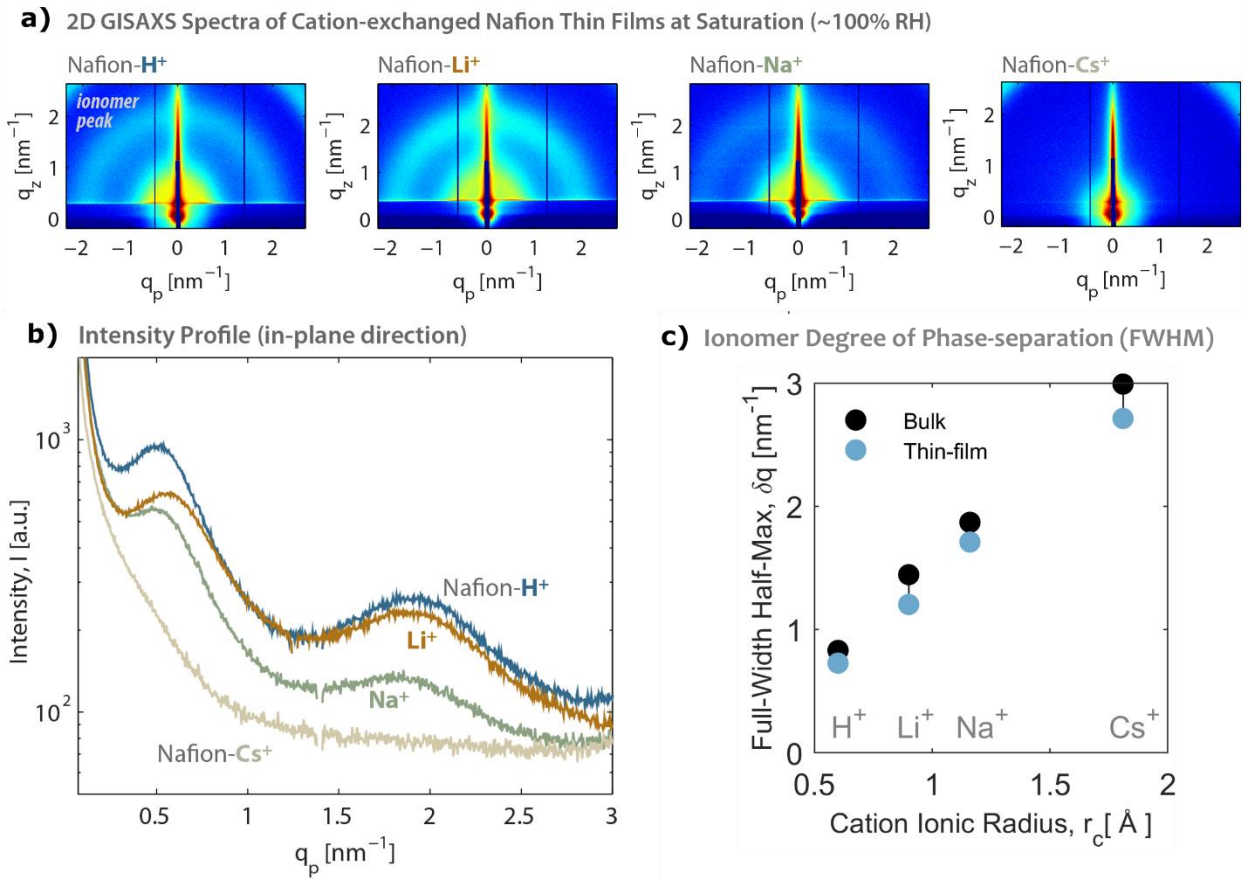

Figure 4-1: (a) GISAXS 2D spectra (b) scattering profiles, and (c) corresponding full-width half-max (FWHM) of ionomer peak as a function of cation ionic radius of Nafion thin films of different monovalent cation forms in saturated conditions.

4.3.2. Coupled Impact of Substrate and Confinement on Water Sorption Dynamics

Water-sorption isotherm of bulk Nafion membrane and thin film ionomer (~100nm) in acid (H^+), monovalent (Li^+, Na^+ and Cs^+) and divalent (Mg^{2+}, Co^{2+} and Ni^{2+}) metal cation forms are shown in Figure 4-2. Water contents for bulk Nafion (N212, thickness = 50.8 μm) are reprinted from Shi et al. [21] in H^+, Li^+, Na^+, Cs^+, and Mg^{2+} form. Water-uptake data on bulk Nafion in Co^{2+} and Ni^{2+} form does not exist in the literature. Therefore, water-sorption isotherms of bulk Nafion in Zn^{2+} and Fe^{2+} forms are used as analogous comparison; Zn^{2+} and Fe^{2+} have similar properties (ionic radius, hydration energy, LAS) to Co^{2+} and Ni^{2+}. Bulk membrane sorption isotherms are plotted without residual water for a more equivalent comparison with water content in ionomer thin films. Residual water refers to remaining water content in membrane at 0% relative humidity.

PFSA ionomers are highly hygroscopic and, depending on the cation form retain strongly bound water molecules up to 2λ (H_2O molecule/sulfonic acid site, SO_3^-) in the primary hydration shell even in dry conditions.[76] Confined ionomer thin films spin cast on substrate show no bound water content, perhaps due to the significantly restricted and strained state of ionomer chains. Therefore, water-content isotherm in ionomer thin films are compared with bulk sorption dynamics that excludes residual water. Monovalent cation exchanged thin film sorption shows decreasing water content with increase in cation size and decrease in LAS. Water uptake in divalent-cation exchanged ionomers does not show significant variability despite an increase in LAS. This tracks well with transition LAS value of ~0.27 as discussed above. Divalent cations compared here are also variable in nature. Although, they all have comparable cation size, hydration number and energy, transition metals Ni^{2+} and Co^{2+} have a more covalent nature.

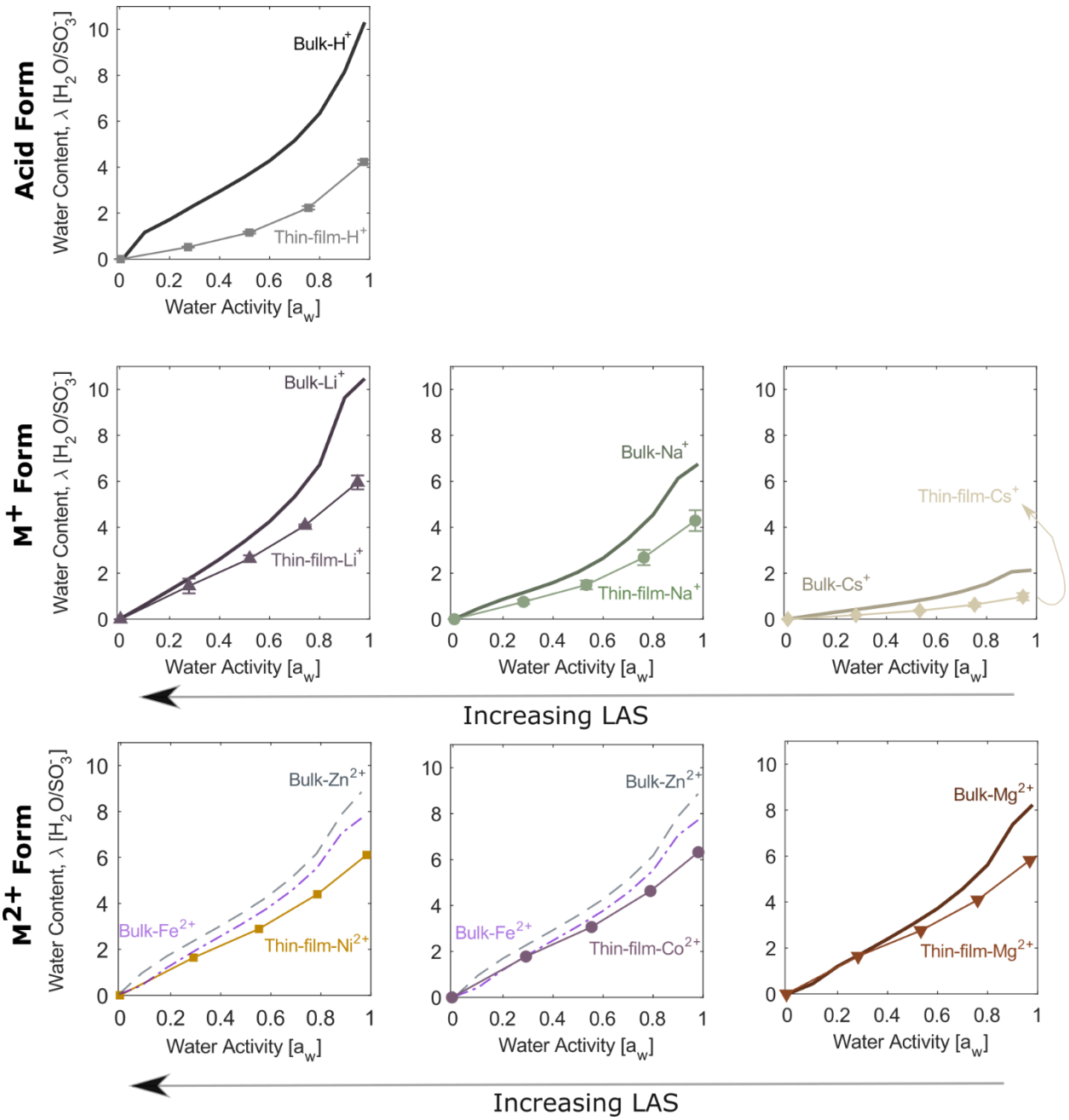

Figure 4-2. Comparative water sorption isotherm of Nafion (Bulk) from Ref.[21] compared to thin film ionomer(100nm) on Si/SiO_2 support at 25ºC in different cation exchanged form. Sorption isotherm of bulk membrane precludes residual water.

Consistent with Chapter 1 and literature for Nafion-H^+,[82–84] all thin films demonstrate a reduction in water-uptake capacity compared to their bulk membrane analogues. Figure 4-3 plots the overall reduction in water content between bulk and 100nm thin film ionomer at 100% RH as a function of LAS. The largest loss in water content is observed for the low charge density metal cation (Cs^+), while the lowest water-content loss is seen for the transition metals. Water-content reduction percentage decreased with increasing LAS, signifying strong affinity for anion (high LAS) improves water retention, while weak affinity (low LAS) results in the significant loss in

water content upon confinement. Interestingly, total amount of water loss in thin film form relative to bulk ($\lambda_{Bulk,M+}$ - $\lambda_{Thin\ Film,M+}$) shows increase in amount of water molecules lost from hydrophilic phase, peaking around LAS ~ 0.24. This reiterates the trends discussed above around critical LAS and the impact of the coordination of cation to the structure of the ionomer as well as location of water molecule around the cation/anion pair. Findings here indicate that water molecules surrounding the cation/sulfonate anion pair are easier to remove than water molecules found disrupting the cation/sulfonate direct coordination.

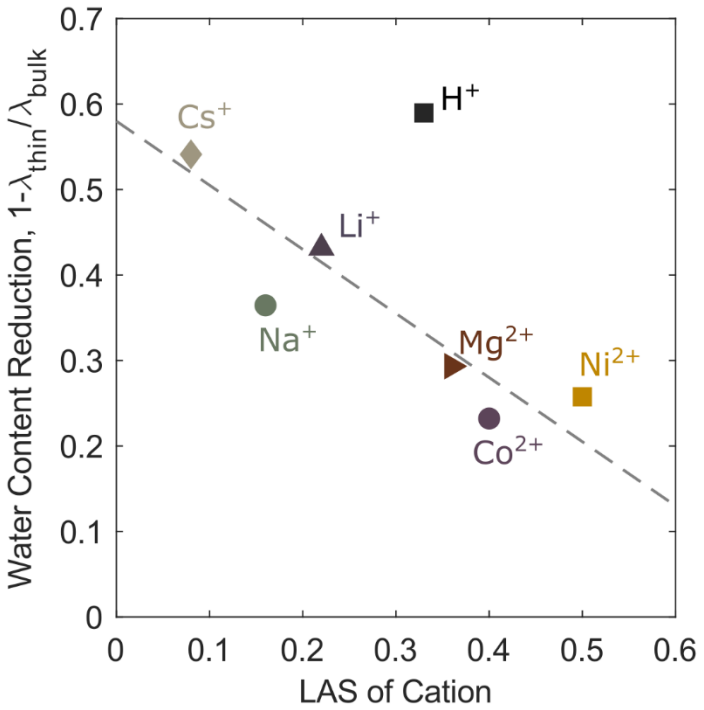

Figure 4-3: Fractional water content loss in ionomer thin film(100nm) in different metal cation forms as compared to bulk PFSA at saturated conditions (~95%RH); there is an inverse linear relationship as a function of Lewis acid strength of cations (LAS).

Figure 4-4 shows saturated swelling behavior of Li^+, Na^+, and Cs^+ exchanged bulk PFSA, and thin (160 nm) through ultra-thin film (26 nm) ionomers. Results demonstrate the impact of confinement on decreasing water content, in agreement with literature reports of acid form.[82–84] However, thickness of Li^+, Na^+, and Cs^+ exchanged thin films show minimal effect of thin film thickness (within the range explored) on water uptake except for the 26 nm case. It has previously been reported that hydration of Na^+-exchanged ionomer thin films (610 to 70 nm) exhibit minimal thickness dependence; however, no literature data exists for other monovalent cations in thin film form.[84] In a mainly hydrogen-bonded polymer matrix of Nafion-H^+, impact of substrate interaction exacerbates finite-size effects in thin films. Crothers et. al has shown that solvation in bulk PFSA is controlled by balancing forces of electrostatic attraction between the cation/sulfonate anion and solvation energy of cation.[85] However in thin film ionomers, the additional local constraints placed by the mechanical strain exerted on ionomer chains has to be accounted for. The presence of an interacting substrate interface could reduce the degrees of freedom of ionomer chains, imposing mechanical constraints against reorganization that results in reduced equilibrium water content, as

shown in Figure 4-4. This phenomenon is consistent with the confinement-driven stiffening in thin films, the moduli of which were shown to be 3 times higher than that of a bulk membrane.[86] With the introduction of cations, specifically monovalent cations, factors such as cation size, hydration energy as well as electron density play dominant roles before surface effects become prominent. This was also true for thermal relaxation dynamics observed for monovalent cation exchanged relative to acid form thin films as discussed in Chapter 3. The finding here is further corroborated by the sorption measurements conducted on gold (Au) in Figure 4-5. Literature on water uptake of ionomer thin films on Au supports is highly scattered and overall shows increase in water content with decrease in thickness which is inconsistent with the findings here. However, ionomer thin film preparation technique in the literature is wide-ranging and many have yet to address the root of this variability.[76] Within our set of experiments, Na^+ and Cs^+ exchanged ionomers exhibit minimal differences in water uptake in Si/SiO_2 and Au substrates indicating a minimal substrate effect. However, for the 26 nm ultra-thin films, water uptake on Au displays the similar disparity reflected in H+ form ionomer thin films. Factors impacting cation-exchanged ionomer water uptake also affects ionomer morphology, as discussed in the next section.

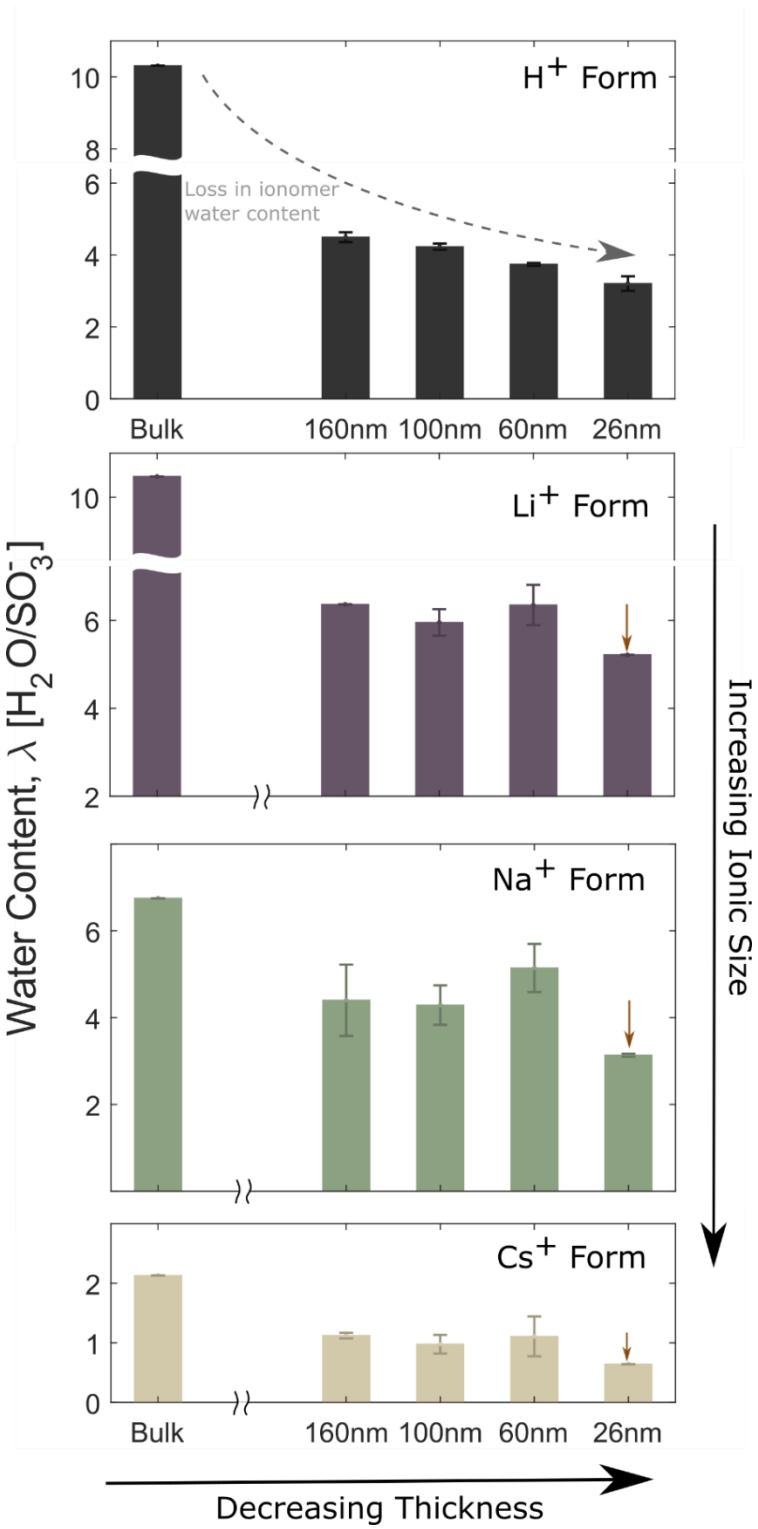

Figure 4-4: Maximum water uptake content of Nafion in bulk membrane[21] and Nafion thin films supported on Si//SiO_2. Li^+, Na^+, and Cs^+ exchanged monovalent cations are compared to H^+ form at ~95% relative humidity and 25ºC.

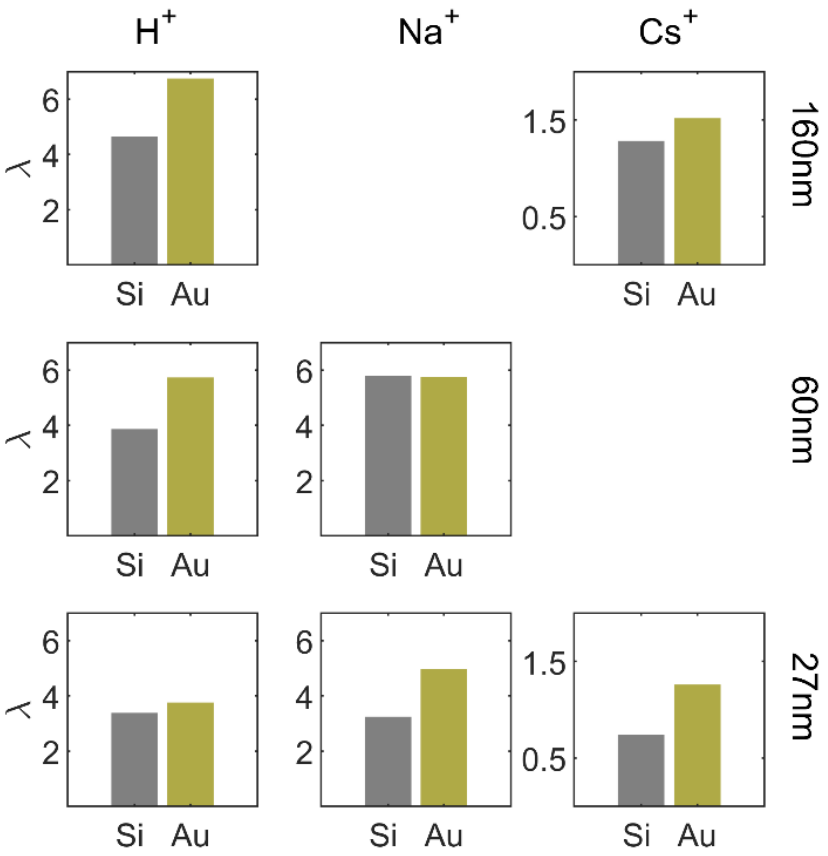

Figure 4-5: Maximum water content, λ (mol H_2O/SO_3^- group) of Nafion thin films in H^+, Na^+, and Cs^+ form supported on Au and $Si//SiO_2$.

4.3.3. Role of Cations in Inducing Mechanical Property

The sections above demonstrated that monovalent cation-exchanged Si/SiO_2-supported ionomer thin films exhibit a reduction in water uptake that tracks with reduction in the degree of phase separation, LAS and monovalent cation size. It has also been shown that the impact of thickness and confinement effects are significantly diminished for Li^+, Na^+ and Cs^+ ionomer thin films with the exception of ultra-thin film (26nm). Finding here is consistent with prior work that demonstrated that the water content of monovalent cation-exchanged bulk ionomer also decreases with increases with increase in ionic radius and LAS.[21] Hydration in PFSA ionomers is a balance between the chemical energy of solvation and the mechanical deformation forces related to stretching of the ionomer chains.[76] As such, altering stored mechanical energy by subjecting ionomers to confinement, shear strain(during spin-coating), and addition of cations can ultimately tip this balance impacting effective solvation. The impact of monovalent cations in increasing chain strain and restricting mobility discussed in Chapter 3 also results in mechanical strains that increase resistance to local deformation required for swelling and incorporation of water molecules in the ionomer matrix. Shi et al. have shown this to be the case by measuring dry storage modulus and water content in bulk PFSA; they observed an inverse linear relationship. Figure 4-6 shows dry storage modulus of bulk PFSA,[21] H^+ form thin film modulus from Page et al.[86] along with the measured ionomer thin-film moduli via the cantilever bending-beam method. Figure 4-6 shows the introduction of confinement effects induces a nonlinear relationship that increases H^+ form thin

film ionomer modulus (~800MPa) with decrease in thickness resulting in low water content. The same nonlinear trend is observed for the different cationic forms. By looking at the full spectrum of dry modulus and water content for various thicknesses, for acid form(H^+) and monovalent metal cation forms (Li^+, Na^+, Cs^+) two trends emerge. H+ form ionomer shows an increase in stiffness and dry modulus driven via confinement results in reduction in water content. Water-content-loss trend is observed for all monovalent metal cations, where increase in ionic size, reduction in LAS raises dry modulus of the membrane that initially dictates water content reduction but is then additionally strained by confinement resulting in similar trend in water content loss as in H^+.

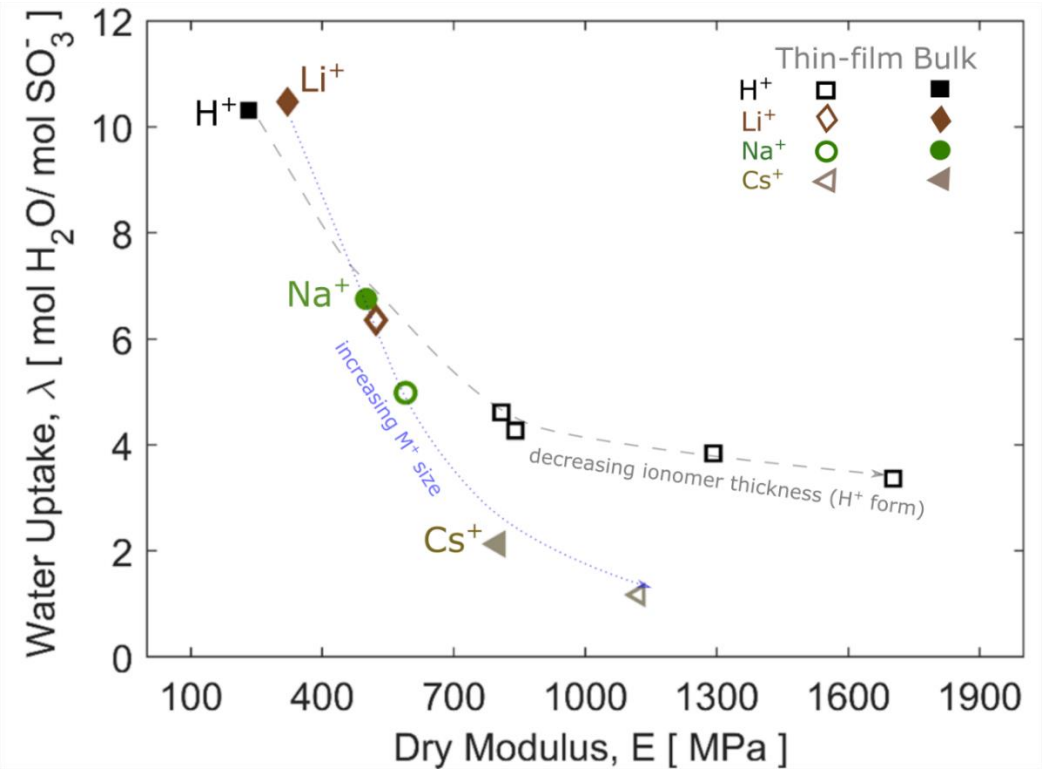

Figure 4-6:Relationship between modulus and water content in bulk membrane and thin film ionomers in baseline acid form (H^+) and in different cationic exchanged forms (Li^+, Na^+, Cs^+). Bulk modulus values reproduced here from ref.[21] and thin film H^+ form are reproduced here from ref.[86]

4.4. Impact of Transition Metal Cation-Exchanged Thin Film Ionomer

The growing interest in Pt-Co and Pt-Ni alloys as cathode catalyst nanoparticles, due to their increased kinetics, is countered with co-alloy particle loss and dissolution into the cell that reduces activity/performance and accelerates MEA degradation. Therefore, there is need to understand the impact of dissolved transition metals ($Ni^{2+}$and Co^{2+}) on the ionomer thin film. Using the model system of Si/SiO_2-supported, transition-metal-exchanged ionomer thin films, water-uptake behavior can reveal thermodynamically driven structure-function relationships that can explain ionomer thin film performance within the transition-metal loaded supported MEAs. To understanding these phenomena, transition metal exchanged ionomer are subjected to variety of heat treatments. This is done for two reasons: to reveal the nature of cation-exchanged ionomer after exposure to liquid salt solutions, and to mimic temperature effect during MEA fabrication.

During MEA fabrication, ink containing electro-catalytic material and ionomer are initially in solution. After being casted via variety of ways (blade coating, ink jet, slot die, etc.), electrode-membrane assembly are heat treated at variety of temperatures (70-140 ^{o}C). Figure 4-7 shows the change in swelling fraction of thin films exchanged with varying external concentrations of Co^{2+} and dried at different post ion-exchange heat treatments in a vacuum oven. Samples were monitored for 1 hr hold in dry N_2 gas, followed by water saturation at 95 % RH for 1 hr. Figure 4-7a shows that water content is impacted by exposure to Co^{2+} even at the lowest concentration studied (0.001 M). This is indicative of lack of concentration dependence in the range explored. Nasef et al. examined heavy metal ion adsorption using spectrophotometer and reported that Co(II) and Ni(II) adsorption into Nafion 117 membrane cease to depend on cation external concentration at concentrations as low as 1.5 mg/L (~2.5×10^{-5} mol of transition metal per liter (M)) within 1 hr of exposure.[32]

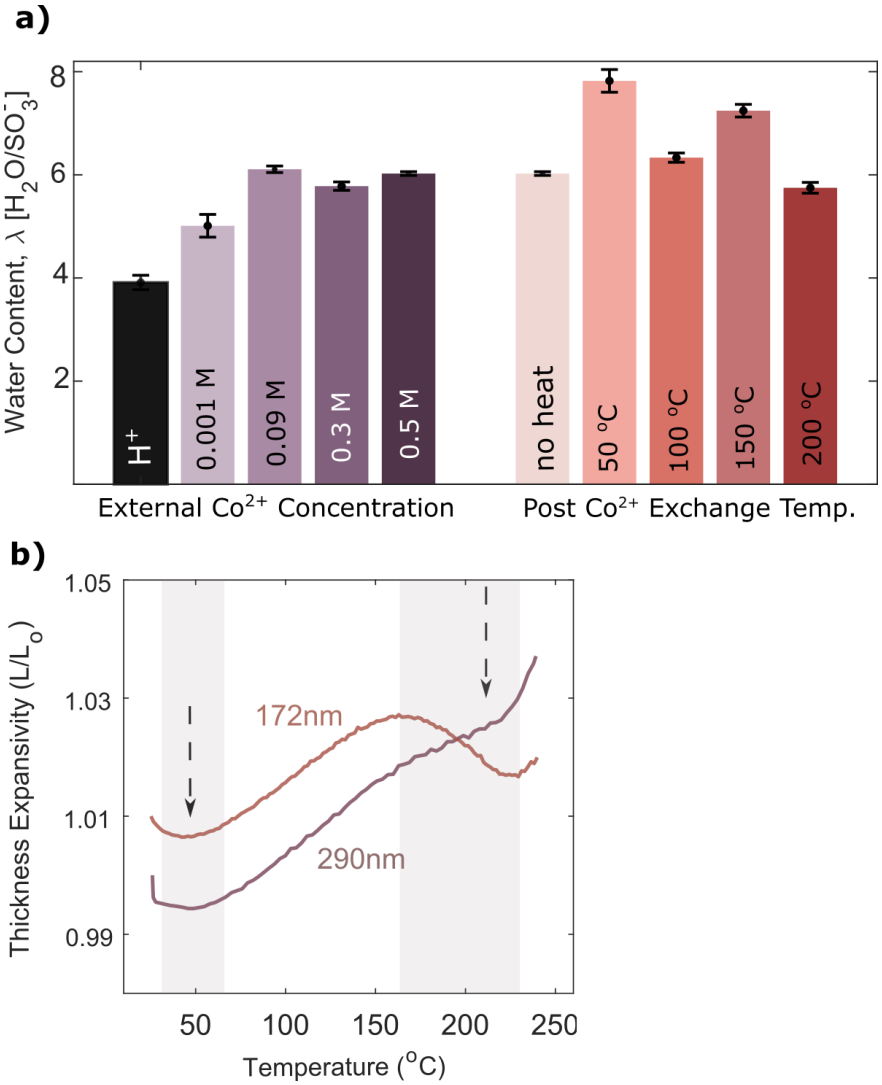

Figure 4-7:(a) Impact of concentration and post exchange heat treatment (0.5 M) on water uptake of Co^{2+} exchanged thin film ionomers (170 nm) compared to H^{+} form. (b) In-situ tracking of Co^{2+} exchanged (0.5M) ionomer thin film expansion during heating. Expansivity lines are shifted to increase visibility.

An interesting trend is observed for exchanged thin films subject to varying post-exchange heat treatment. Figure 4-7a compares maximum swelling of 170 nm thin films in H^+ form, Co^{2+} form with no post-exchange heat treatment, followed by 4 different post Co^{2+}-exchange heat treatment ranging from 50 to 200ºC. Trends display an increase in swelling fraction in Co^{2+} form up to 50ºC, followed by a decrease in uptake at 100ºC and an increase at 150ºC and finally lowest uptake observed in Co^{2+} form at 200ºC. Unexpectedly, Co^{2+}-exchanged ionomer thin films show an increase in dimensional swelling fraction by a factor of 2 to 2.5 (up to 50% increase in water content) relative to the H^+-form thin films. In-situ monitoring of impact of heat on Co^{2+}-exchanged ionomer thin films was done via heated-cell ellipsometry. Here, it is critical to note the fact that the transition metals studied are divalent cations, and at fully exchanged level their concentration is half of the concentration of H^+ and other monovalent forms discussed above (per electroneutrality). However, transition metals show 1.5x or more the water content of H^+ ionomer. Given the fact that there are half the cationic sites in the ionomer after exchange, the increase in water content is not expected. Additionally, conversion to water content, λ, uses EW of H^+ for conversation to equivalent water molecules per cation. However, EW of ionomer could be altered by the presence of Co^{2+} now associating with two sulfonic acid sites rather than one in H^+ form, or non-uniformities in the ionomer exchanged could result in some protonic locations un-exchanged but still containing $CoSO_4$ in the thin film. Proper visualization technique with spectroscopic capabilities or post measurement exact ion content evaluation is needed to clarify this observation. The most likely reason for the unexpected rise in water uptake is that the hydration energy of H_3O^+ is ~4 times that of Co^{2+}.[87] However, this water content is disrupted by an increase in applied heat energy. Heat could be removing weakly bound water or change ionomer thin film density. The latter requires further work and measurement of density using QCM to validate this hypothesis. The former could be associated with the water-field stabilization energy, which is a unique feature of transition-metal ions upon hydration.[74] Water-field stabilization energy arises from interaction of coordinated water molecules around a transition metal cation. Lone pairs electrons of the oxygen atom from the water molecules exert a repulsive force on the d-orbital valence electrons of the transition-metal ion creating a high hydration energy orbital and lower hydration energy d-orbital. This results in water molecules stabilized ion with lower energy, and leads to a more negative heat of hydration. Given this fact and trends in Figure 4-7a, the two lowest swelling fractions observed at ~100ºC and ~200 ºC could indicate water removal from the lower energy water bonds and then from the higher energy water bonds, respectively. This increase and decrease in thickness with heat treatment has also been observed via in-situ thickness tracking in upon heating in dry environment (Figure 4-7b). Increase in swelling fraction at 50ºC and 150ºC could then be associated with film expansivity prior to first water removal, and then thermal breakage of ionic crosslinks around the possible transition temperature (likely to be around 220 to 340 ºC), respectively.

To compare with other cations, post-exchange heat treatment of 100 ºC was used (similar to previous monovalent cations). Figure 4-8 shows water uptake as function of thickness in different transition metals. Uptake is compared against Mg^{2+} exchanged ionomers as a reference for more equivalent comparison. Water content in Co^{2+} and Ni^{2+} exchanged ionomer thin films show no discernable thickness dependence. Mg^{2+} cations exhibit higher water content similar to transition metals. Some unexpected ionomer thickness dependence is observed but further work is necessary to validate this trend. Overall increase in water content is observed for divalent cations over H^+ form. This is likely due to the high hydration number of these cations. Additionally, infrared studies from Falk et al., evaluating types of water stretching bonds has also demonstrated

that the high LAS and nature of Mg^{2+}, Co^{2+} and Ni^{2+} cations results in strong coordination with SO_3^- groups that causes similar amount of water molecules to locate near cation(near SO_3) as well as between cation and SO_3 (fluorocarbon facing).[24,35]

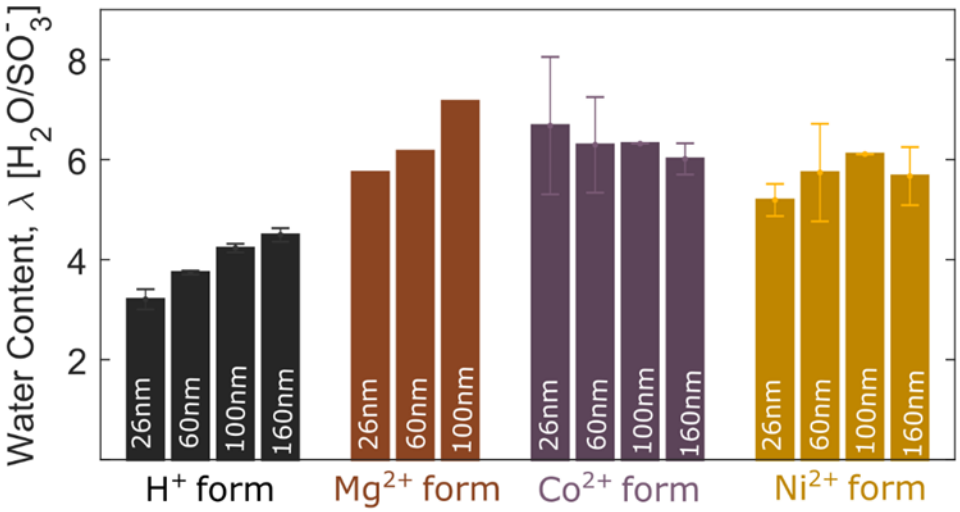

Figure 4-8:Water content of divalent cation (Mg^{2+}) and transition metal cations (Co^{2+} and Ni^{2+}) as a function of thickness.

4.5. Summary

Understanding the impact of presence of cations in ion-conducting polymer (ionomer) thin film holds the key to predicting stability and function of electrolyte thin film binders utilized in fuel cell and other solid-state energy-conversion device electrodes. Mitigating the impact of cationic contamination and co-alloy leaching requires closer investigation into the cation-induced thermodynamic and morphological changes in thin film properties and underlying structure-function relationship. In this chapter, affinity for anion (LAS), nature of cation, cation interaction range, coordination with structure, hydration size, cation induced morphological aggregation of ionomer chains and mechanical property of these ionomer chains have been identified and discussed as possible explanations for observed property changes. Figure 4-9 outlines these factors and their order of influence for the set of cations explored. From the figure, it is easy to see that while monovalent cations follow a somewhat consistent cation-size and LAS dependent trend, divalent cations, especially transition metals, exhibit various irregularities that limit extrapolation toward cohesive trends. These factors have already been shown to influence critically the functionality of bulk PFSA. However, the existence of additional finite-size effects and surface-specific interactions endemic to thin films compounds interpretation. In this study, monovalent cation containing ionomer thin films (H^+, Li^+, Na^+ and Cs^+) exhibit reduced water uptake and weaker phase-separation in their nanostructure, compared to bulk. Counter to the trends observed for H^+ form ionomer thin films, Li^+, Na^+ and Cs^+ thin films had minimal substrate and thickness dependence, with the exception of 26 nm thickness, indicating dominating influence of ionic networks with-in ionomer over substrate/ionomer interaction. This finding is consistent with lessons learned from thermal relaxation of monovalent cation exchanged thin films in Chapter 3. The overall reduction in water-uptake capacity upon confinement from bulk is the unavoidable reduction of swelling dimension in the presence of a substrate interface (i.e., confinement).

Additional reduction in water uptake in H^+ ionomer thin films can be due to strong hydrogen bonding to the substrate upon film formation, resulting in a stiffer ionomer matrix with minimal flexibility for accommodating more water molecules. This was shown to be consistent with the increase in modulus observed with decreasing thickness. Initial exploration into divalent cations (Mg^{2+}, Ni^{2+}, Co^{2+}) indicate significantly higher uptake than H^+ form, owing to high hydration number and more negative hydration energy. Results here could provide insight into effect of cations on ionomer performance in fuel-cell catalysts which has implications for MEA manufacturing and processing, an area of great interest for further exploration. Findings also aid in providing tunable levers that alter ionomer thin film's mechanical property, ion transport (via cation doping and altering water content) and likely gas transport properties as well as they alter chain stiffness, accessible free volume and relaxation dynamics. Altering cation-ionomer relationship via controls like LAS, hydration shell, and coordination in ionomer structure can provide an alternative route to ionomer design without new material synthesis.

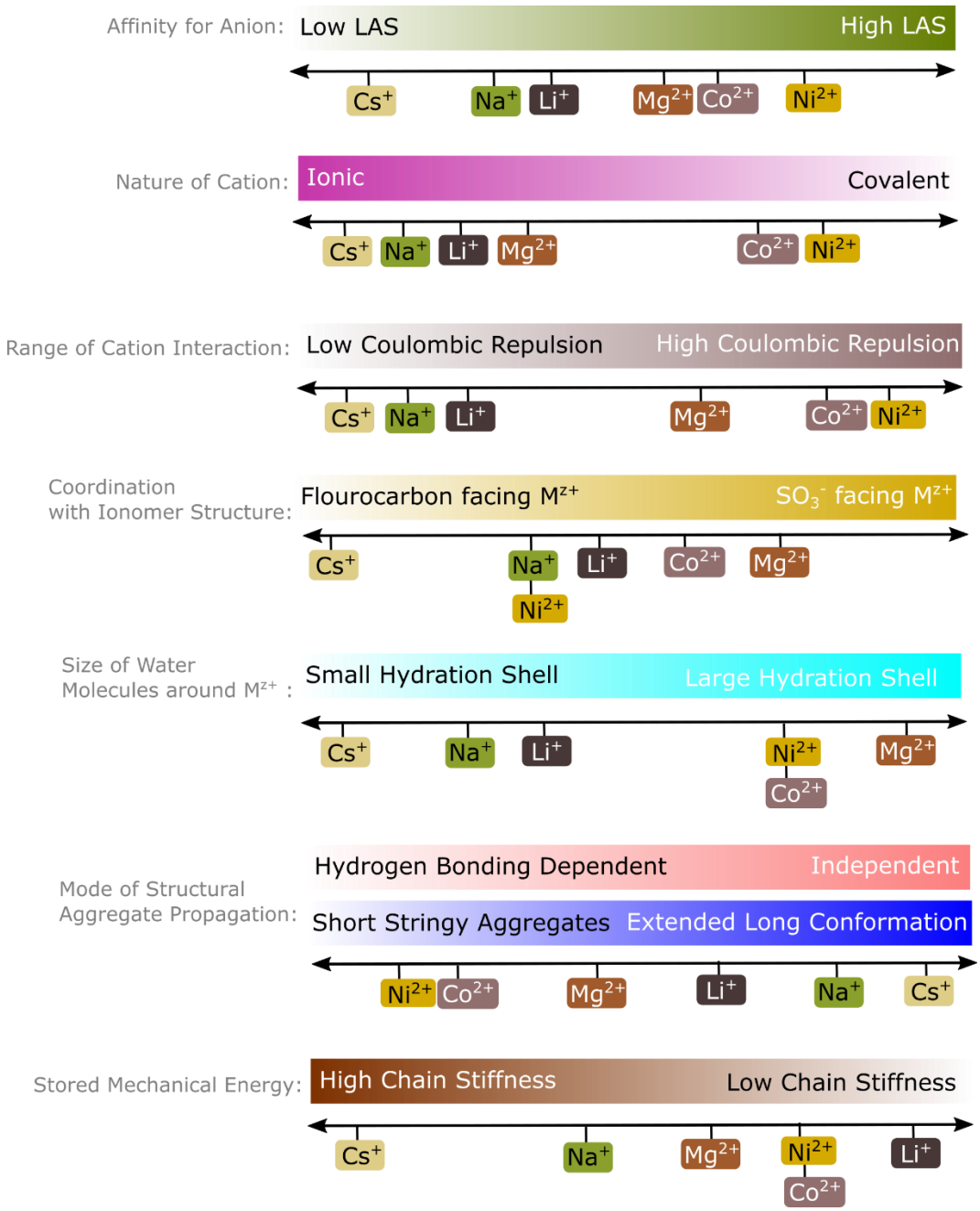

Figure 4-9:Critical factors impacting cation exchange ionomer property. Extent(order) of impact and influence on ionomer property varies for monovalent and divalent cations.

4.6. References

(1) Mathias, M. F.; Makharia, R.; Gasteiger, H. a.; Conley, J. J.; Fuller, T. J.; Gittleman, C. J.; Kocha, S. S.; Miller, D. P.; Mittelsteadt, C. K.; Xie, T.; et al. Two Fuel Cell Cars in Every Garage? Electrochem. Soc. Interface 2005, 14, 24–35.

(2) Kongkanand, A.; Mathias, M. F. The Priority and Challenge of High-Power Performance of Low- Platinum Proton-Exchange Membrane Fuel Cells. J. Phys. Chem. Lett. 2016, 7,

1127–1137.
(3) Gröger, O.; Gasteiger, H. A.; Suchsland, J.-P. Review—Electromobility: Batteries or Fuel Cells? J. Electrochem. Soc. 2015, 162 (14), A2605–A2622.
(4) Gasteiger, H. A.; Kocha, S. S.; Sompalli, B.; Wagner, F. T. Activity Benchmarks and Requirements for Pt, Pt-Alloy, and Non-Pt Oxygen Reduction Catalysts for PEMFCs. Appl. Catal. B Environ. 2005, 56, 9–35.
(5) Paulus, U. A.; Wokaun, A.; Scherer, G. G.; Institut, P. S.; Psi, C.-V. Oxygen Reduction on Carbon-Supported Pt - Ni and Pt - Co Alloy Catalysts. 2002, No. 41, 4181–4191.
(6) Gilbert, J. A.; Kropf, A. J.; Kariuki, N. N.; DeCrane, S.; Wang, X.; Rasouli, S.; Yu, K.; Ferreira, P. J.; Morgan, D.; Myers, D. J. In-Operando Anomalous Small-Angle X-Ray Scattering Investigation of Pt 3 Co Catalyst Degradation in Aqueous and Fuel Cell Environments. J. Electrochem. Soc. 2015, 162 (14), F1487–F1497.
(7) Cai, Y.; Ziegelbauer, J. M.; Baker, A. M.; Gu, W.; Kukreja, R. S.; Kongkanand, A.; Mathias, M. F.; Mukundan, R.; Borup, R. L. Electrode Edge Cobalt Cation Migration in an Operating Fuel Cell: An In Situ Micro-X-Ray Fluorescence Study. J. Electrochem. Soc. 2018, 165 (6), F3132–F3138.
(8) Kongkanand, A.; Subramanian, N. P.; Yu, Y.; Liu, Z.; Igarashi, H.; Muller, D. A. Achieving High-Power PEM Fuel Cell Performance with an Ultralow-Pt-Content Core-Shell Catalyst. ACS Catal. 2016, 6 (3), 1578–1583.
(9) Wu, J.; Yuan, X. Z.; Martin, J. J.; Wang, H.; Zhang, J.; Shen, J.; Wu, S.; Merida, W. A Review of PEM Fuel Cell Durability: Degradation Mechanisms and Mitigation Strategies. J. Power Sources 2008, 184 (1), 104–119.
(10) Chen, S.; Gasteiger, H. A.; Hayakawa, K.; Tada, T.; Shao-Horn, Y. Platinum-Alloy Cathode Catalyst Degradation in Proton Exchange Membrane Fuel Cells: Nanometer-Scale Compositional and Morphological Changes. J. Electrochem. Soc. 2010, 157 (1), A82.
(11) Antolini, E.; Salgado, J. R. C.; Gonzalez, E. R. The Stability of Pt – M (M = First Row Transition Metal) Alloy Catalysts and Its Effect on the Activity in Low Temperature Fuel Cells and Its Effect on the Activity in Low Temperature Fuel Cells. J. Power Sources 2006, 160, 957–968.
(12) Uddin, A.; Qi, J.; Wang, X.; Pasaogullari, U. Distributed Cation Contamination from Cathode to Anode Direction in Polymer Electrolyte Fuel Cells. Int. J. Hydrogen Energy 2015, 40, 13099–13105.
(13) Auer, E.; Freund, A.; Pietsch, J.; Tacke, T. Carbons as Supports for Industrial Precious Metal Catalysts. Appl. Catal. A Gen. 1998, 173 (2), 259–271.
(14) Yu, X.; Ye, S. Recent Advances in Activity and Durability Enhancement of Pt/C Catalytic Cathode in PEMFC. Part I. Physico-Chemical and Electronic Interaction between Pt and Carbon Support, and Activity Enhancement of Pt/C Catalyst. J. Power Sources 2007, 172 (1), 133–144.
(15) Debe, M. K. Electrocatalyst Approaches and Challenges for Automotive Fuel Cells. Nature 2012, 486 (7401), 43–51.
(16) Zhai, X.; Weiss, R. A. Wetting / Dewetting Behavior of Lightly Sulfonated Polystyrene Ionomers on Solid Surfaces. Langmuir 2008, 24 (22), 12928–12935.
(17) Goswami, A. K.; Acharya, A.; Pandey, A. K. Study of Self-Diffusion of Monovalent and Divalent Cations in Nafion-117 Ion-Exchange Membrane. J. Phys. Chem. B 2001, 105 (38), 9196–9201.
(18) Ogumi, Z.; Kuroe, T.; Takehara, Z. Gas Permeation in SPE Method. J. Electrochem Soc.

1985, 132 (11), 2601–2605.
(19) Page, K. A.; Shin, J. W.; Eastman, S. A.; Rowe, B. W.; Kim, S.; Kusoglu, A.; Yager, K. G.; Stafford, G. R. In Situ Method for Measuring the Mechanical Properties of Nafion Thin Films during Hydration Cycles. ACS Appl. Mater. Interfaces 2015, 7 (32), 17874–17883.
(20) Serincan, M. F.; Pasaogullari, U.; Molter, T. Modeling the Cation Transport in an Operating Polymer Electrolyte Fuel Cell (PEFC). Int. J. Hydrogen Energy 2010, 35 (11), 5539–5551.
(21) Shi, S.; Weber, A. Z.; Kusoglu, A. Structure-Transport Relationship of Perfluorosulfonic-Acid Membranes in Different Cationic Forms. Electrochim. Acta 2016, 220, 517–528.
(22) Lage, L. G.; Delgado, P. G.; Kawano, Y. Thermal Stability and Decomposition of Nafion Membrane with Different Cations Using High-Resolution Thermogravimetry. J. Therm. Anal. Calorim. 2004, 75, 521–530.
(23) Albe, N. D.; Bas, C.; Reymond, L.; Dane, A.; Rossinot, E.; Flandin, L. Key Counter Ion Parameters Governing Polluted Nafion Membrane Properties. J. Polym. Sci. Part B Polym. Phys. 2009, 47 (14), 1381–1392.
(24) Falk, M. An Infrared Study of Water in Perfluorosulfonate (Nafion) Membranes. Can. J. Chem. 1980, 58 (14), 1495–1501.
(25) Page, K. A.; Cable, K. M.; Moore, R. B. Molecular Origins of the Thermal Transitions and Dynamic Mechanical Relaxations in Perfluorosulfonate Ionomers. Macromolecules 2005, 38 (15), 6472–6484.
(26) Li, J. Y.; Nemat-nasser, S. Micromechanical Analysis of Ionic Clustering in Na®on Per¯uorinated Membrane. Science (80-.). 2000, 32.
(27) Almeida, S. H. De; Kawano, Y. Ultraviolet-Visible Spectra Membrane of Nafion. Europe 1997, 33 (8), 1307–1311.
(28) Lambard, Jacques; Gebel, G. Small-Angle Scattering Study of Water-Swollen Perfluorinated Ionomer Membranes. Macromolecules 1997, 30, 7914–7920.
(29) Szentirmay, M. N.; Martin, C. R. Ion-Exchange Selectivity of Nafion Films on Electrode Surfaces. Anal. Chem. 1984, 56 (11), 1898–1902.
(30) Pellegrino, J.; Wang, D.; Rabago, R.; Noble, R.; Koval, C. Gas Transport Properties of Solution-Cast Perfluorosulfonic Acid Ionomer Films Containing Ionic Surfactants. J. Memb. Sci. 1993, 84 (1–2), 161–169.
(31) Boakye, E. E.; Yeager, H. L. Water Sorption and Ionic Diffusion in Short Side Chain Perfluorosulfonate Ionomer Membranes. J. Memb. Sci. 1992, 69 (1–2), 155–167.
(32) Nasef, M. M.; Yahaya, A. H. Adsorption of Some Heavy Metal Ions from Aqueous Solutions on Nafion 117 Membrane. Desalination 2009, 249 (2), 677–681.
(33) Okada, T. Ion and Water Transport Characteristics in Membranes for Polymer Electrolyte Fuel Cells Containing H[Sup +] and Ca[Sup 2+] Cations. J. Electrochem. Soc. 1997, 144 (8), 2744.
(34) Okada, T.; Ayato, Y.; Yuasa, M.; Sekine, I. The Effect of Impurity Cations on the Transport Characteristics of Perfluorosulfonated Ionomer Membranes. J. Phys. Chem. B 1999, 103 (17), 3315–3322.
(35) Quezado, S.; Kwak, J. C. .; Falk, M. An Infrared Study of Water-Ion Interactions in Perfluorosulfonate. Can. J. Chem. 1984, 62 (229), 958–966.
(36) Yeager, H. L.; Steck, A. Cation and Water Diffusion in Nafion Ion Exchange Membranes: Influence of Polymer Structure. J. Electrochem. Soc. 1981, 128 (9), 1880.
(37) Jalani, N. H.; Datta, R. The Effect of Equivalent Weight, Temperature, Cationic Forms, Sorbates, and Nanoinorganic Additives on the Sorption Behavior of Nafion®. J. Memb. Sci.

2005, 264 (1–2), 167–175.
(38) Hongsirikarn, K.; Goodwin, J. G.; Greenway, S.; Creager, S. Effect of Cations (Na + , Ca 2 + , Fe 3 +) on the Conductivity of a Nafion Membrane. J. Power Sources 2010, 195 (21), 7213–7220.
(39) Matos, B. R.; Dresch, M. A.; Santiago, E. I.; Linardi, M.; de Florio, D. Z.; Fonseca, F. C. Nafion -Relaxation Dependence on Temperature and Relative Humidity Studied by Dielectric Spectroscopy. J. Electrochem. Soc. 2012, 160 (1), F43–F48.
(40) Qi, J.; Wang, X.; Ozdemir, M. O.; Uddin, A.; Bonville, L.; Pasaogullari, U.; Molter, T. Effect of Cationic Contaminants on Polymer Electrolyte Fuel Cell Performance. J. Power Sources 2015, 286, 18–24.
(41) Pan, H. K.; Yarusso, D. J.; Knapp, G. S.; Cooper, S. L. EXAFS Studies of Nickel Nafion Ionomers. J. Polym. Sci. 1983, 21, 1389–1401.
(42) Pan, H. K.; Yarusso, D. J.; Knapp, G. S.; Pineri, M.; Meagher, A.; Coey, J. M. D.; Cooper, S. L. EXAFS and Mössbauer Studies of Iron Neutralized Nafion Ionomers. J. Chem. Phys. 1983, 79 (10), 4736–4745.
(43) Chaudhury, S.; Agarwal, C.; Goswami, A. Transport Properties of Multivalent Cations in Nafion-117 Membrane with Mixed Ionic Composition. J. Phys. Chem. B 2015, 119 (33), 10566–10572.
(44) Godino, M. P.; Barragán, V. M.; Villaluenga, J. P. G.; Ruiz-Bauzá, C.; Seoane, B. Water and Methanol Transport in Nafion Membranes with Different Cationic Forms. 1. Alkali Monovalent Cations. J. Power Sources 2006, 160 (1), 181–186.
(45) Osborn, S. J. Morphological and Mechanical Properties of Dispersion-Cast and Extruded Nafion Membranes Subjected to Thermal and Chemical Treatments. Macromol. Sci. Eng. 2009, 314.
(46) Pellegrino, J.; Kang, Y. S. CO2CH4 Transport in Polyperfluorosulfonate Ionomers: Effects of Polar Solvents on Permeation and Solubility. J. Memb. Sci. 1995, 99 (2), 163–174.
(47) Yeo, S. C.; Eisenberg, A. Physical Properties and Supermolecular Structure of Perfluorinated Ion-containing (Nafion) Polymers. J. Appl. Polym. Sci. 1977, 21 (4), 875–898.
(48) Hensley, J. E.; Way, J. D.; Dec, S. F.; Abney, K. D. The Effects of Thermal Annealing on Commercial Nafion Membranes. J. Memb. Sci. 2007, 298, 190–201.
(49) Feldheim, D. L. .; Lawson, D. R. .; Martin, C. R. . Influence of the Sulfonate Countercation on the Thermal Stability of Nafion @ Perfluorosulfonate Membranes. J. Polym. Sci. Part B Polym. Phys. 1993, 31, 953–957.
(50) Dumont, J. H.; Baker, A. M.; Maurya, S.; Kim, Y. S.; Mukundan, R.; Borup, R. L. Effect of Cerium, Cobalt and Nickel Contaminants in the CL Ionomer on the Oxygen Reduction Reaction Oxygen at Platinum Microelectrodes. ECS Trans. 2017, 80 (8), 861–867.
(51) Braaten, J. ; Kongkanand, A.; Lister, S. Oxygen Transport Effects of Cobalt Cation Contamination of Ionomer Thin Films in Proton Exchange Membrane Fuel Cells. ECS Trans. 2017, 80 (8), 283–290.
(52) Zamel, N.; Li, X. Effect of Contaminants on Polymer Electrolyte Membrane Fuel Cells. Prog. Energy Combust. Sci. 2011, 37, 292–329.
(53) Okada, T.; Ayato, Y.; Satou, H.; Yuasa, M.; Sekine, I. The Effect of Impurity Cations on the Oxygen Reduction Kinetics at Platinum Electrodes Covered with Perfluorinated Ionomer. J. Phys. Chem. B 2001, 105 (29), 6980–6986.
(54) Li, H.; Tsay, K.; Wang, H.; Shen, J.; Wu, S.; Zhang, J.; Jia, N.; Wessel, S.; Abouatallah, R.;

Joos, N.; et al. Durability of PEM Fuel Cell Cathode in the Presence of Fe3+and Al3+. J. Power Sources 2010, 195 (24), 8089–8093.
(55) Li, H.; Tsay, K.; Wang, H.; Shen, J.; Wu, S.; Zhang, J.; Jia, N.; Wessel, S.; Abouatallah, R.; Joos, N.; et al. Durability of PEM Fuel Cell Cathode in the Presence of Fe3+and Al3+. J. Power Sources 2010, 195 (24), 8089–8093.
(56) Curtin, S.; Gangi, J. State of the States: Fuel Cells in America 2016. U.S. Dep. Energy 2016, No. November, 1–46.
(57) Curtin, S.; Gangi, J. Fuel Cell Technologies Market Report 2015; Washington, D.C., 2015.
(58) Visser, S. A.; Cooper, S. L. Effect of Neutralizing Cation Type on the Morphology and Properties of Model Polyurethane Ionomers. Polymer (Guildf). 1991, 33 (5).
(59) Bolintineanu, D. S.; Stevens, M. J.; Frischknecht, A. L. Influence of Cation Type on Ionic Aggregates in Precise Ionomers. Macromolecules 2013, 46 (13), 5381–5392.
(60) Eisenberg, A. .; Kim, J. S. . Introduction to Ionomers; Wiley-Interscience: New York, 1998.
(61) Okada, T.; Satou, H.; Okuno, M.; Yuasa, M. Ion and Water Transport Characteristics of Perfluorosulfonated Ionomer Membranes with H+and Alkali Metal Cations. J. Phys. Chem. B 2002, 106 (6), 1267–1273.
(62) Nemat-Nasser, S.; Wu, Y. Comparative Experimental Study of Ionic Polymer-Metal Composites with Different Backbone Ionomers and in Various Cation Forms. J. Appl. Phys. 2003, 93 (9), 5255–5267.
(63) Osborn, S. J.; Hassan, M. K.; Divoux, G. M.; Rhoades, D. W.; Mauritz, K. a.; Moore, R. B. Glass Transition Temperature of Perfluorosulfonic Acid Ionomers. Macromolecules 2007, 40 (10), 3886–3890.
(64) Gierke, T. D.; Munn, G. E.; Wilson, F. C. The Morphology in Nafion Perfluorinated Membrane Products, as Determined by Wide- and Small-Angle x-Ray Studies. J. Polym. Sci. Polym. Phys. Ed. 1981, 19 (11), 1687–1704.
(65) Kyu, T.; Hashiyama, M.; Eisenberg, A. Dynamic Mechanical Studies of Partially Ionized and Neutralized Nafion Polymers. Can. J. Chem. 1983, 61, 680–687.
(66) Eisenberg, A.; Navratil, M. Ion Clustering and Viscoelastic Relaxation in Styrene-Based Ionomers. IV. X-Ray and Dynamic Mechanical Studies. Macromolecules 1974, 7 (1), 90–94.
(67) Tandon, R.; Pintauro, P. N. Divalent / Monovalent Cation Uptake Selectivity in a Nation Cation-Exchange Membrane: Experimental and Modeling Studies. J. Memb. Sci. 1997, 136, 207–219.
(68) Moukheiber, E.; Bas, C.; Alberola, N. D.; Flandin, L. Infrared and Thermal Behaviour of Proton Exchange Membrane (PEM) after Cationic Contamination. J. Memb. Sci. 2013, 431, 105–112.
(69) Visser, S. A.; Cooper, S. L. Extended X-Ray Absorption Fine Structure Spectroscopic Analysis of Cation Local Environment in Model Polyurethane Ionomers. Polymer (Guildf). 1992, 33 (5), 930–937.
(70) Page, K. A.; Landis, F. A.; Phillips, A. K.; Moore, R. B. SAXS Analysis of the Thermal Relaxation of Anisotropic Morphologies in Oriented Nafion Membranes. Macromolecules 2006, 39 (11), 3939–3946.
(71) Daly, K. B.; Panagiotopoulos, A. Z.; Debenedetti, P. G.; Benziger, J. B. Viscosity of Nafion Oligomers as a Function of Hydration and Counterion Type: A Molecular Dynamics Study. J. Phys. Chem. B 2014, 118 (48), 13981–13991.
(72) Yavuz, Ö.; Altunkaynak, Y.; Güzel, F. Removal of Copper, Nickel, Cobalt and Manganese

from Aqueous Solution by Kaolinite. Water Res. 2003, 37 (4), 948–952.
(73) Tansel, B. Significance of Thermodynamic and Physical Characteristics on Permeation of Ions during Membrane Separation: Hydrated Radius, Hydration Free Energy and Viscous Effects. Sep. Purif. Technol. 2012, 86 (August 2006), 119–126.
(74) Bockris, J. O.; Reddy, A. K. N.; Gamboa-Aldeco, M.; Gamboa-Aldeco, M. E. Modern Electrochemistry 2B: Electrodics in Chemistry, Engineering, Biology and Environmental Science; Springer Science & Business Media, 1998; Vol. 2.
(75) Smith, D. W. Ionic Hydration Enthalpies. J. Chem. Educ. 1977, 54 (9), 540.
(76) Kusoglu, A.; Weber, A. Z. New Insights into Perfluorinated Sulfonic-Acid Ionomers. Chem. Rev. 2017, 117, 987–1104.
(77) Takamatsu, T.; Eisenberg, a. Density and Expansion Coefficients of Nafion. J. App. Poly. Sci. 1979, 24, 2221–2235.
(78) Newman, J.; Thomas-Alyea, K. Electrochemical Systems; 2004.
(79) Kusoglu, A.; Kushner, D.; Paul, D. K.; Karan, K.; Hickner, M. a.; Weber, A. Z. Impact of Substrate and Processing on Confi Nement of Nafi on Thin Films. Adv. Funct. Mater. 2014, 24 (30), 4763–4774.
(80) Stoney, G. G. The Tension of Metallic Films Deposited by Electrolysis Author (s): G . Gerald Stoney Source : Proceedings of the Royal Society of London . Series A , Containing Papers of a Published by : Royal Society Stable URL : Http://Www.Jstor.Org/Stable/92886 Acc. In Proceedings of the Royal Society of London series A, Containing Papers of a Mathematical and Physical Character; 1909; Vol. 82, pp 172–175.
(81) Kwasny, M. T.; Zhu, L.; Hickner, M. A.; Tew, G. N. Thermodynamics of Counterion Release Is Critical for Anion Exchange Membrane Conductivity. J. Am. Chem. Soc. 2018, 140, 7961–7969.
(82) Kusoglu, A.; Dursch, T. J.; Weber, A. Z. Nanostructure/Swelling Relationships of Bulk and Thin film PFSA Ionomers. Adv. Funct. Mater. 2016, 26, 4961–4975.
(83) Kusoglu, A. Ionomer Thin Films in PEM Fuel Cells. In Encyclopedia of Sustainability Science and Technology; Meyers, R., Ed.; Springer, New York, NY, 2018.
(84) Dishari, S. K.; Hickner, M. A. Con Fi Nement and Proton Transfer in NAFION Thin Films. 2013.
(85) Crothers, A. R.; Radke, C. J.; Weber, A. Z. Impact of Nano- and Mesoscales on Macroscopic Cation Conductivity in Perfluorinated-Sulfonic-Acid Membranes. J. Phys. Chem. C 2017, 121 (51), 28262–28274.
(86) Page, K. A. .; Kusoglu, A.; Stafford, C. M. .; Kim, S.; Kline, R. J.; Weber, A. Z. . Confinement-Driven Increase in Ionomer Thin film Modulus. Nano Lett. 2014, 14, 2299–2304.
(87) Mejías, J. A.; Lago, S. Calculation of the Absolute Hydration Enthalpy and Free Energy of H+and OH-. J. Chem. Phys. 2000, 113 (17), 7306–7316.

5. Understanding Gas Transport in Ionomer Thin Films

5.1. Gas Transport in Ionomers in Catalyst Layers

The performance of fuel cells and many other electrochemical devices depends strongly on the durable, selective, gas-impermeable solid-electrolyte separator. Use of these low-gas permeability separators impacts fuel efficiency (by minimizing reactant gas crossover), fuel utilization (by reducing leaks of fuel and balance gases) and overall cell durability (by decreasing harmful peroxide radical formation).[1,2] The minimal gas permeability requirement ideal for performance as a separator electrolyte, is counter to the desired high gas transport rates required for optimal activity of ionomer thin film binder used catalyst-layer. Historically, ionomer thin film binder was incorporated into polymer-electrolyte fuel-cell (PEFC) electrode structure to circumvent anionic adsorption issues brought about by liquid electrolytes.[3,4] However, addition of ionomer in the electrode provides significant unexpected advantages. Ionomer thin film binder (1) increases the three-dimensional electrochemically active surface area, (2) reduces in electrode thickness (due to improved interfacial area) with subsequent improvement in exchange current densities, (3) supplies highly acidic protons due to the superacid nature of PFSA especially upon hydration, and (4) increases the solubility of oxygen relative to traditional liquid electrolytes and alternative solid electrolytes.[3–7] The ability of ionomers to be cast (and recast) into very thin(nanometers thick) film is an additional advantage that minimizes ohmic losses inside the electrode.[5] Despite their benefits, ionomers (2 to 70 nm) in the catalyst layer(CL) are reportedly responsible for the high transport resistance observed in electrodes with low Pt loadings or minimal catalytic sites, especially at high current densities,[8–13] one of the most significant problems facing fuel-cell commercialization today. So far, reported transport resistances cannot be explained fully by transport properties observed in bulk ionomers. This fact has borne a need for quantification of gas permeability of ionomer thin films. In doing so, it is critical to contextualize the transport properties of ionomer thin films observed mainly from in-situ catalyst layer electrochemical measurements with bulk (micrometer thick) ionomer membranes used as electrolytes. Therefore, this chapter discusses gas permeability of bulk ionomers, parameters that control their properties, and extends the main insights gained to methods aimed at capturing ionomer thin film gas transport parameters.

Gas transport through dense polymeric materials involves dissolution of the gas at the membrane's surface, followed by a transport process driven by a pressure or concentration gradient through the membrane, and finally desorption at the opposite surface.[14] Therefore, gas permeation through polymers is a cumulative effect of solubility and diffusivity. Gas transport measurements of bulk (25 to 180 μm thickness) perfluorosulfonic acid (PFSA) membranes have commonly been carried out via three different methods: ex-situ measurements involving pressure cells,[15–21] electrochemical methods involving the use of microelectrodes,[3,22–27] and electrochemical monitoring cells[1,28–32] to capture transport parameters like diffusivity and solubility. Pressure cells commonly involve imposing pressure gradients across the ionomer and flux detection via pressure sensors in dry conditions or use of gas chromatograph/mass spectroscopy in hydrated conditions. Use of pressure cell is discussed in this chapter in section 5.2. Electrochemical monitoring cells can apply similar pressure gradients as pressure cells under humidified conditions. However, the flux across the membrane is measured via current detected by electrodes positioned downstream of the pressure gradient. The last method of gas transport parameter measurement involves use of microelectrodes which was initially developed to understand local electrode kinetics and surface interactions impacting electrochemical performance via very small (μm in diameters), well-

defined electrode surfaces. Microelectrodes are now more widely utilized to understand both kinetics and transport behavior of ionomers including capturing interfacial dynamics and resistances near electrode surfaces as well. As a result of their electrochemical nature, measurements are commonly utilized under hydrated conditions and require electrochemical techniques to isolate gas-transport related currents. Despite their growing use, the sensitivity of microelectrodes to various interactions makes them susceptible to inaccuracy, over interpretation, and uncertainty. Microelectrodes are discussed later in section 5.3.2. of this chapter. Operando techniques like hydrogen crossover measurements have also been used to measure gas permeation of PFSAs.[33] To a lesser extent, other additional methods like positron annihilation lifetime[34] and molecular simulation[35] have also been used to study transport parameters such as free volume, adsorption dynamics, and self-diffusion coefficient of bulk ionomers in dry and hydrated states.

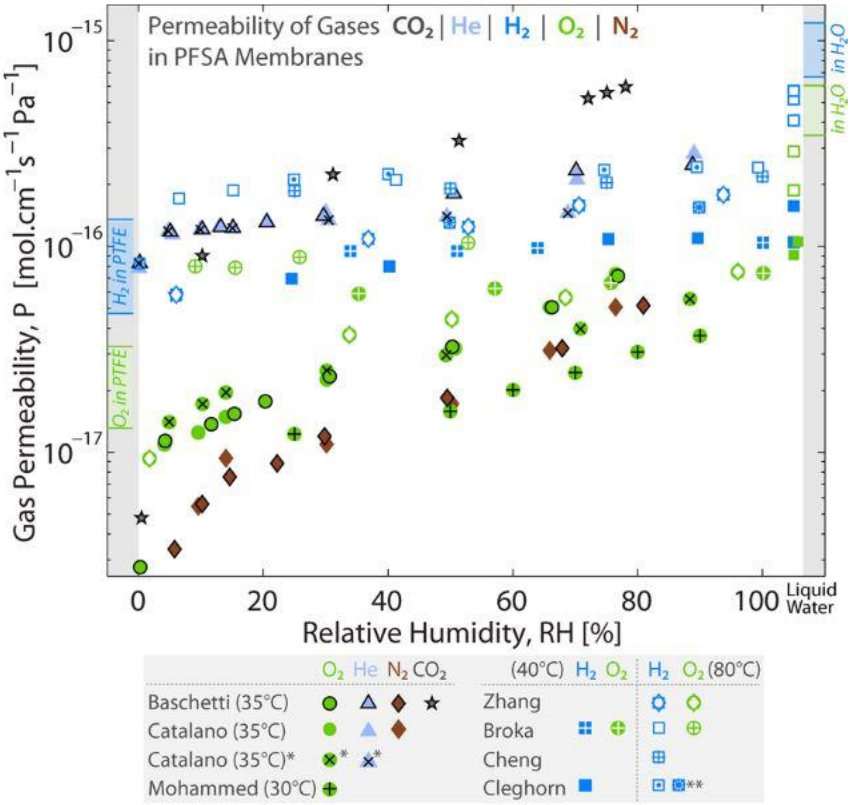

Figure 5-1: Gas permeability of bulk PFSA(Nafion) membranes from select literature sources using pressure cell method,[15,16,18,19] positron annihilation lifetime,[34] electrochemical monitoring cell technique,[36] and gas-crossover method.[33] Image adapted with permission from Kusoglu and Weber,[37] Copyright 2017 American Chemical Society.

Figure 5-1 shows select gas permeability of various gases as a function of humidity measured via different techniques discussed above from recent review paper of PFSAs.[37] As a semi-crystalline polymer, PFSA ionomer gas transport is influenced by segmental motion in the polymer chains, size of penetrant gas, and type of interaction of penetrant with the polymer matrix and moieties. As a result, limited transport is expected in the crystalline backbone, while an intermediate region containing flexible polar side-chains, amorphous backbone, and the hydrophilic-domain regions with sulfonic-acid end groups can provide diffusion pathways for

transport.[16,32,38] Domain swelling due to water uptake into the intermediate and hydrophilic region and higher diffusivity in water results in an increase in permeability with increase in humidity and in liquid water as shown in Figure 5-1. Figure 5-1 also shows variability in the literature data set even within bulk membranes of similar fabrication.[28,39] Sources of this variations could be lack of consistency among various methods, variability in estimation of critical parameters like electroactive area, employing varying membrane pre-treatment protocols, and unreliability around the exact amount of membrane water content. Variability in the data also affects permeability selectivity that is critical for understanding effective anode/cathode gas separation and losses associated with gas crossover through the membrane. Figure 5-2 shows H_2/O_2 selectivity as a function of temperature and humidity from select references. Although selectivity overall decreases with rise in humidity and temperature, the trend is inconsistent and variable across methods. Such variability is the motivation behind employing a single technique of measurement across nanometer to micrometer ionomer thicknesses, which will be discussed later. Selectivity is, however, related to the effect of temperature and humidity on gas adsorption, solubility, and diffusivity. Adsorption of gas in Nafion has been demonstrated to have low coverage especially for nonpolar gases like O_2 and H_2.[35] As a result, solubility of O_2 and H_2 is proportional to concentration and follows Henry's law. With the introduction of water, phase segregation of the ionomer results in fewer gas molecules dissolved in the hydrophilic, water-phase resulting in lower solubility with rise in water content. Reduction in solubility is also seen with increase in temperature due to increase in entropy. However, enlarged hydrophilic phase and high temperature enhance diffusivity, resulting in dominant transport of gases through water-phase and reducing overall selectivity. Such a trend with temperature and humidity is also expected for nanometer thin ionomer coating the electrode.

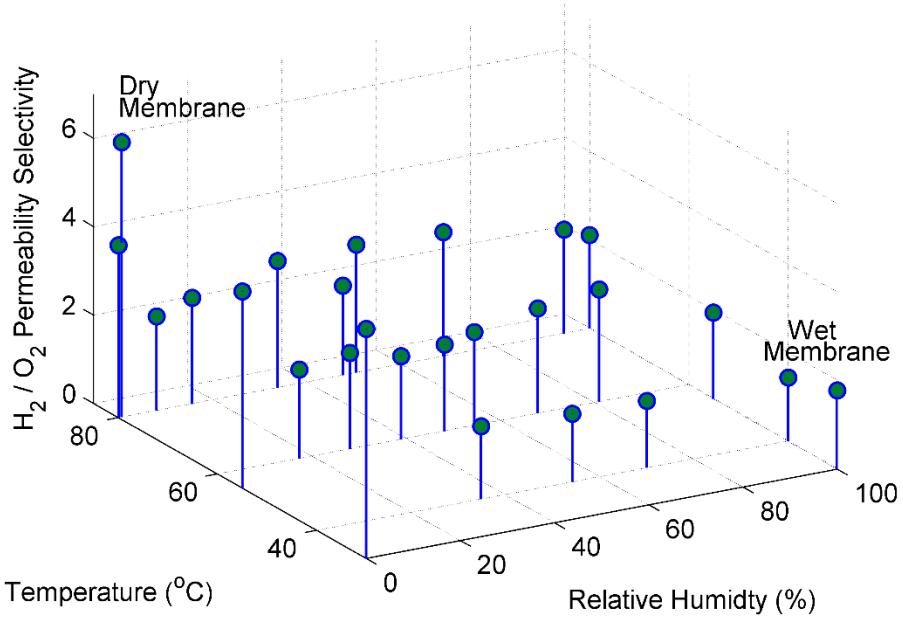

Figure 5-2: H_2/O_2 selectivity of gases in Nafion as a function of humidity and temperature from literature sources.[1,15,16,29]

Thus far, measurement of ionomer thin film gas transport involved several in-situ measurements using limiting current in conjunction with hydrogen/oxygen pump to measure

overall catalyst layer (CL) resistance,[40–48] and microelectrode methods[6,23,24,49–51] with the exception of a single electrochemical monitoring cell.[39] (See Chapter 1- Section 2.1 for details). Due to the heterogeneous nature of the CL and the varying distribution of ionomer thin film binder coating in the electrode, in-situ measurements of gas transport are usually extracted using various experimental controls (varying pressure, thickness of electrode, Pt loading, etc.) and employing mathematical models. Variability in the ionomer thickness is inferred from experimentally varying ionomer to carbon ratio and Pt loading. Upon using these parameters as a proxy to ionomer thickness and isolating ionomer transport resistance by decoupling it from other resistances in the cell, researchers unanimously report a pressure independent resistance that increases with decrease in effective ionomer thickness (decrease in platinum loading and increase in ionomer to carbon ratio).[52] Figure 5-3 summarizes O_2 (and H_2) gas permeability as a function of ionomer thickness from various literature sources at 80ºC and 90% relative humidity (RH).[1,15,23,24,43–45,47,48,51,53] Permeability in the ionomer was calculated from reported pressure independent transport resistances corrected for variability in roughness factor (electroactive surface area) provided in the reference publications. It is important to note that some transport measurements reported do not separate interfacial transport resistance from resistance through the ionomer. Therefore, the gas permeability values in Figure 5-3 are reported as min and max value and an ionomer thickness of ~5nm was assumed to obtain permeability values. Real CLs could be coated with ionomer thickness of 2 to 70nm in thickness with variations in accessibility and distribution (As discussed in Chapter 2). Therefore, the permeability reported in Figure 5-3 is an extracted representation of permeability in the ionomer thin films in the CL rather than actual value. Permeability reported as ionomer thin film in Figure 5-3 are sourced from planar and disk microelectrode studies that measured permeability by varying the thickness of cast membranes coating the microelectrode. Membrane permeabilities in Figure 5-3 were derived from pressure-cell and electrochemical monitoring methods of gas-permeability measurements discussed in previous paragraph.

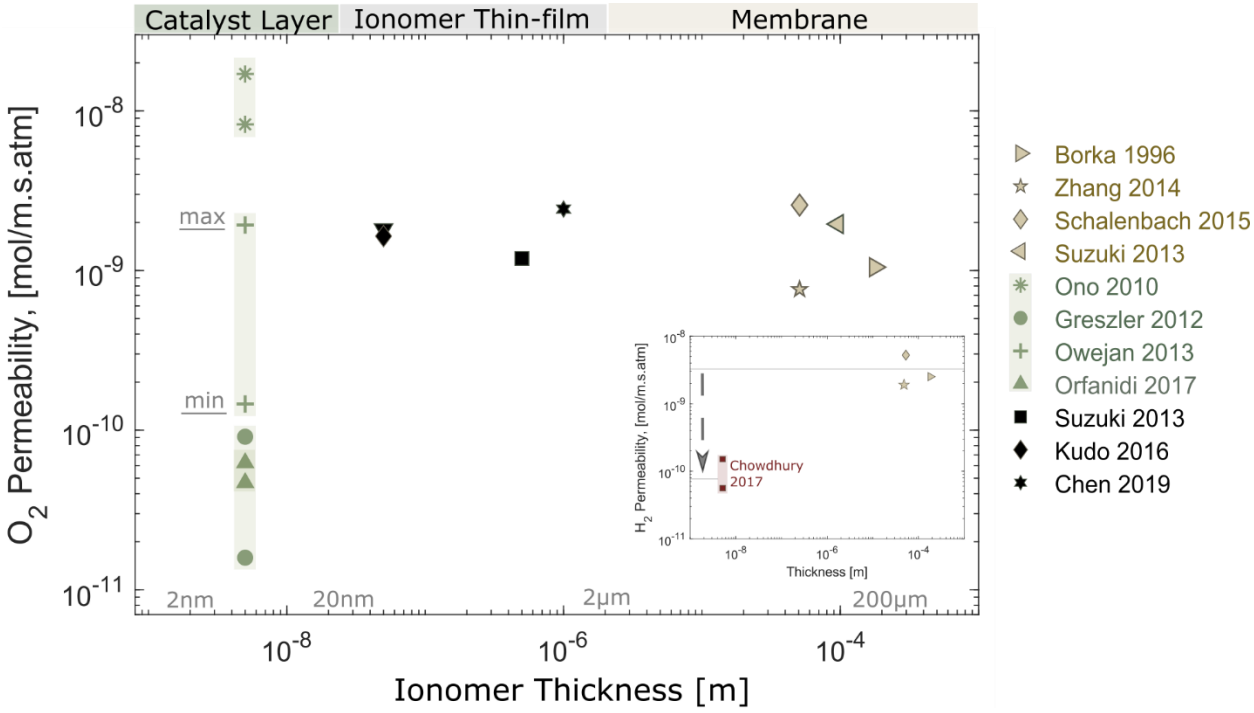

Figure 5-3: O_2 permeability through ionomer as a function of thickness. Data reported from various literature sources. Permeability from catalyst layer was extracted using roughness factor and assumed constant 5nm ionomer thickness.[1,15,23,24,43–45,47,48,51,53] (Inset) H_2 permeability as a function of thickness . All data points are for Nafion ionomer at 80ºC and 90-100% relative humidity for all samples except Greszler et. al (62%).

Overall Figure 5-3 shows that gas permeability remains somewhat unchanged until ~100nm, and demonstrates decreases with decrease in thickness with some scatter in the CL data. This supports the unexplained but unanimously reported ionomer mass transport resistance in the CL at high current densities.[8,10] As discussed in Chapter 1, this reduction in gas permeability has been correlated with three main possibilities. First is confinement driven changes associated with finite size effects. At nanometers in thickness, ionomers approach the length scales of the polymer coils, and are therefore highly sensitive to interfaces.[54] Loss of crystallinity in spin-cast thin film ionomers and localization of crystallites near the substrate interface during thermal annealing can also alter diffusion pathways.[11,55,56] Similarly, changes in ionomer thin film structural-relaxation dynamics (as discussed in Chapter 3) can impact free-volume accessibility and chain stiffness impacting gas transport. Additionally, confinement driven acceleration in physical ageing rate could result in loss in desired transport property in the ionomer thin film.[57,58]

The second possible reason is associated with interfacial-transport resistance at the Pt/ionomer and the gas/ionomer interface. Interfacial interactions and water distribution can result in gas transport resistance at the Pt/ionomer and gas/ionomer interfaces. Interaction at the Pt/ionomer interface can result in adsorption of sulfonate acid groups altering available Pt active area and morphology of ionomer thin film.[11,56] Ionomer thin films on Pt substrate have been shown to have strong interaction with sulfonic acid moieties.[59,60] This could result in increased backbone alignment parallel to the substrate that selectively lowers in-plane proton conductivity and increases tortuosity for transport.[61,62] At the gas/ionomer interface changes in wettability can impact diffusive pathway distribution through the ionomer especially at low humidity.[22,63] Kudo

et. al, Suzuki et. al. and Chen coworkers all utilized planar and disk microelectrode studies to measure micrometer and nanometer-thick ionomers.[23,24,51] However, all came to varying conclusions. Kudo and coworkers concluded that the largest transport resistance contribution is the Pt/ionomer interface, and, as a result, authors observed very little thickness dependence between thin film ionomers (20 to 100nm) and bulk PFSA.[23] This conclusion was similar to Liu and coworkers, who found minimal dependence on thickness using an electrochemical-monitoring cell technique.[39] Contradictorily, recent work by Chen et. al. demonstrates an increase in transport coefficient with decrease in thickness, despite observing conductivity loss in ionomer with thickness reduction.[51] Few works in literature have bridged this discrepancy by using a single technique to measure both bulk and ionomer thin film gas permeability. Therefore, prior work quantifying ionomer gas transport parameters remains inconclusive on the effect of thickness on ionomer transport parameters. Regardless, confinement and surface interactions remain critical influencers of thin and ultra-thin film polymers and for ionomers as discussed in the last three chapters. Additionally, data for thicknesses < 100 nm is largely lacking missing or remain irreproducible, highlighting the need for quantifying thickness-dependent gas permeability in that range.

Similar to bulk PFSA, transport in ionomer thin films strongly depends on humidity and temperature. Additionally, proximity to interfaces and local electro-activity makes performance of ionomer thin films dependent on operating potential as well. Therefore, a methodology of transport interrogation that enables measurement under all variable conditions is critical. As noted above, it is ideal to utilize a single method of gas permeability measurement across a wide range of thicknesses. In this chapter, three methods are evaluated for measurement of thickness-dependent gas transport. A pressure cell method of constant-volume variable-pressure technique is employed to evaluate gas permeability of both bulk PFSA and thin film ionomer. This technique is ideal for capturing intrinsic gas-transport coefficients of low gas-permeability polymers under dry conditions and variable temperatures. The second method for measuring gas transport in ionomer thin films is microelectrode method. As discussed above, microelectrodes provide significant advantages in directly capturing local gas transport using well-defined electrode surfaces under all expected operating conditions (i.e. humidity, temperature, and potential). The third method utilizes an optical method to correlate change in luminescent intensity to transient oxygen transport through the ionomer. Unique to this method is the capability of obtaining valuable parameters in similar ionomer-on-substrate model systems utilized thus far. This allows for direct extrapolation and correlation of our understanding from pervious chapters to transport phenomena. However, it is only ideal for dry and humidified gas transport measurements at ambient temperature.

Thin-film Ionomer Gas Permeation Measurement Method	Variable Conditions			
	Dry	Humidity	Temperature	Potential
Constant Volume Variable Pressure	✓		✓	
Ionomer Coated Microelectrode		✓	✓	✓
Luminescence Quenching	✓	✓		

Figure 5-4: Methods considered for capturing gas permeability of thin film ionomers under various conditions.

5.2. Gas Transport in Bulk PFSA Ionomer

5.2.1. Materials and Sample Preparation

Bulk ionomer materials studied in this work comprised of extruded membranes (Nafion 117 and 112), cast membranes (Nafion 212), Nafion 1500EW from DuPont, 3M ionomers from 3M and Aquivion ionomer produced by Solvay Plastics. The chemical formulae, range of thicknesses, equivalent weights, and physical properties of these materials are summarized in Table 5-1. Sample thickness characterization was done with a micrometer (Mitutoyo Corporation) with a resolution of 1 µm. Membrane density was measured using helium gas pycnometry (AccuPyc II 1340, Micromeritics, Norcross, GA). Membranes were cut into small pieces and placed in the pycnometer sample cup (1 cm^3 total volume). Each sample was degassed 50 times to remove trapped air inside the sample cup; the occupied volume was measured with 30 repeats/sample. The measurement was repeated 3 times, and the density is measured to be is reflected in Table 5-1. Characteristic transition temperature (T_α) was measured via dynamic mechanical analyzer (DMA) (DMA-Tritec 2000). The sample was tested in tension mode with a frequency of 1 Hz. Temperature sweep tests were performed within the range of 25 to 200ºC with a heating rate of 5 ºC/min. Peak tan δ (ratio of storage and loss modulus) from the stress-temperature data were defined as T_α. The membrane crystallinity of ionomers explored here are is taken from wide angle x-ray scattering (WAXS) or x-ray diffraction (XRD) data reported in Kusoglu et al.[37] Scattering peaks arising from amorphous and crystalline phases (originating from TFE backbone) of PFSA were deconvoluted to obtain relative degrees of the crystallinity. PFSA samples were placed in the permeation assembly, backed by a filter paper, and sandwiched between two flat aluminum supports. The aluminum supports allow for transport through a defined active area but do not alter the measured permeability.

Table 5-1: Chemical structure and bulk properties of polymers used in this study

Polymer		Thickness (μm)	Density (g/cm^3)	T_α (^oC)[37]	Degree of Crystallinity (ϕ_c,%)[37]
Nafion	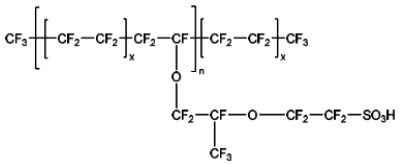				
N212		50.3	2.11	108	19
N117		180.8	2.04	111	11
N112		52.8	2.04	112	
N1500		28.8	-	121	31
3M Ionomer					
3M725		20.0	2.07	124	0
3M825	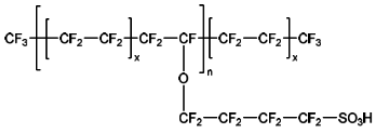	83.5	2.12	125	11
		70			
		50			
		20			
		15			
		10			
		7.5			
		5			
3M1000		20.0	2.16	130	23
Aquivion	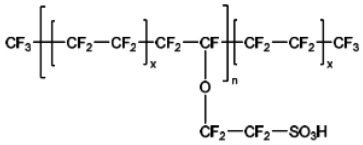				
Aquivion 870		49.6	2.05	138	11
Aquivion 980		52.2	2.09	144	17
PDMS	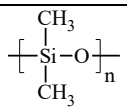	-	0.965[58]	-123	

5.2.2. Constant-Volume Variable-Pressure Method

Ionomer gas permeability was measured by an in-house-built constant-volume gas-permeator. This setup is ideal for low permeability membranes. It is also a completely dry system and, therefore, is well suited for capturing intrinsic gas properties of hygroscopic materials like PFSA. This setup can be used for both bulk and thin film (<1 μm) gas permeability measurements as discussed later in the chapter. Gas permeability is the steady-state gas flux (J) through membrane l due to a partial pressure difference ($p_1 - p_2$) across the membrane. Permeability (P_m) is the defining physical property for gas transport and a given polymer/gas pair.

$$P_m = \frac{J.l}{p_1 - p_2} \quad (1)$$

At steady state, the gas flux is given by Fick's first law as,[14]

$$J = \frac{-D_{loc}}{1-w}\frac{dc}{dx} \quad (2)$$

where D_{loc} is the binary diffusion coefficient of the gas in the polymer and w is the gas mass fraction in the polymer. Integrating equation (2) across the membrane thickness yields

$$J = \frac{1}{l}\int_{c_1}^{c_2} \frac{D_{loc}}{1-w} dc \tag{3}$$

where c_2 and c_1 are the penetrant concentrations in the polymer at the upstream and the downstream faces of the membrane in equilibrium with external pressures p_2 and p_1, respectively. Integration of equation (3) and combining with (1) results in

$$J = \frac{c_2 - c_1}{l} D_{app} \tag{4}$$

$$P_m = \frac{J.l}{p_2 - p_1} = \frac{c_2 - c_1}{p_2 - p_1} D_{app} \tag{5}$$

where D_{app} is the concentration-dependent effective diffusivity and S_{app} is effective solubility. For high gradient across the membrane, $c_2 >> c_1$ and $p_2 >> p_1$, equation (5) can be simplified,

$$P_m = \frac{c_2}{p_2} D_{app} \tag{6}$$

$$P_m = S_{app} D_{app} \tag{7}$$

A constant-volume variable-pressure system measures permeate flux through the well-defined active area (A) by monitoring the pressure increase of collected permeate gas in a closed volume (V) using a pressure transducer,

$$P_m = \frac{Vl}{\Delta p A\, RT}\left(\frac{dp_1}{dt}_{SS} - \frac{dp_1}{dt}_{leak}\right) \tag{8}$$

Figure 5-5a shows simplified schematic of the gas-permeation system. A sample assembled in the manner given in Figure 5-5b is placed in a tightly sealed stainless-steel cross-flow cell between the downstream and upstream pressure transducers. An active area diameter of $D_a \leq 0.25$ in. was used for films < 10 µm and $D_a \geq 0.4$ in. was used for films of thickness > 10µm. The system is exposed to vacuum prior to beginning a measurement to purge the system of diffusing species. For all of the bulk ionomer films, the system was purged for 5 to 12 hours prior to any measurement Initially, the downstream valve connecting the permeation cell to the vacuum pump is closed, and slow pressure rise in the downstream volume is observed to monitor leak rate. The maximum leak rate obtained was for low diffusing gases like N_2; leak rate was maintained below 10% of the flux. Next, the feed gas was introduced to the upstream side of the membrane, and the pressure rise in the downstream volume was recorded as a function of time. For effectively constant pressure difference across membrane, the downstream pressure was kept at 0.013 atm or less while the upstream pressure was maintained at 1 atm or above. The temperature of the system was controlled using a constant-temperature water bath with a heater. All permeation experiments are performed at 35 ºC unless noted. Membrane samples in this study were exposed to dry H_2, N_2, or O_2 gas (99.9% pure, Praxair, Danbury, CT) at the pressure of interest on the upstream side. Pressure range used in this study is 1 to 12 atm.

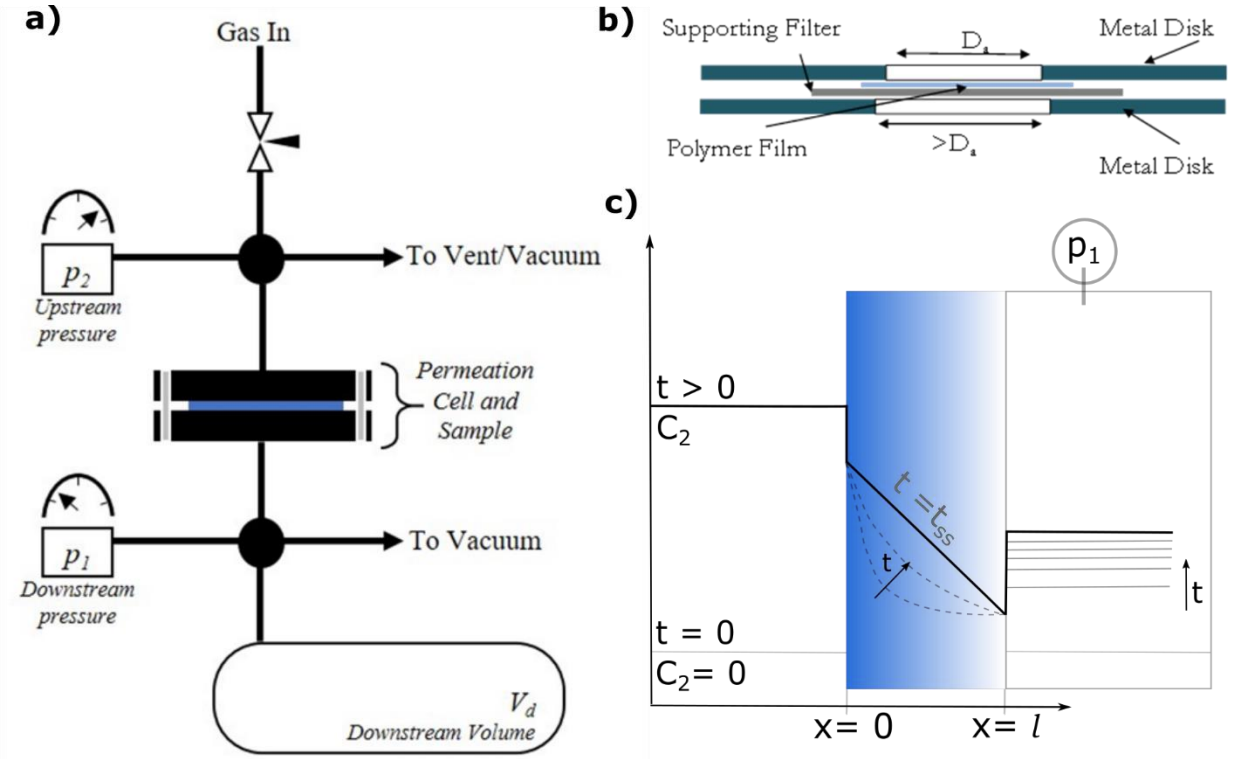

Figure 5-5: a) Schematic of experimental set up for constant volume variable pressure system built in-house. (b) Permeation sample assembly for transport through a defined active area (D_a). Indicated metal is aluminum foil. (c) Concentration profile across the membrane with time. Pressure rise in an enclosed volume downstream is used to capture steady state permeation.

5.2.3. Results and Discussion on Bulk Ionomer Gas Permeability

Nafion's ideal structure and performance have inspired development of similar, but shorter side-chain containing, PFSA ionomers such as 3M Ionomer and the even shorter side-chain Aquivion. Keeping the phase-separated structure of PFSA while tuning side-chain length has been employed to optimize ionomer's properties as discussed in Chapter 1. Gas permeability of bulk Nafion has been measured using different ex-situ and in-situ methods. However, literature data for shorter side-chain membranes like Aquivion and 3M ionomer are limited.[18,19,31] Dry gas permeability was measured for H_2, O_2, and N_2 as shown in Figure 5-6. Measurements indicated that for these gases, gas permeability was independent of pressure gradient, indicating that sorption in bulk ionomer follows a Henry's (linear) sorption isotherm as already discussed in the introduction section. Data in Figure 5-6 agrees well with Nafion literature studies for this type of measurement.[17,28,64]

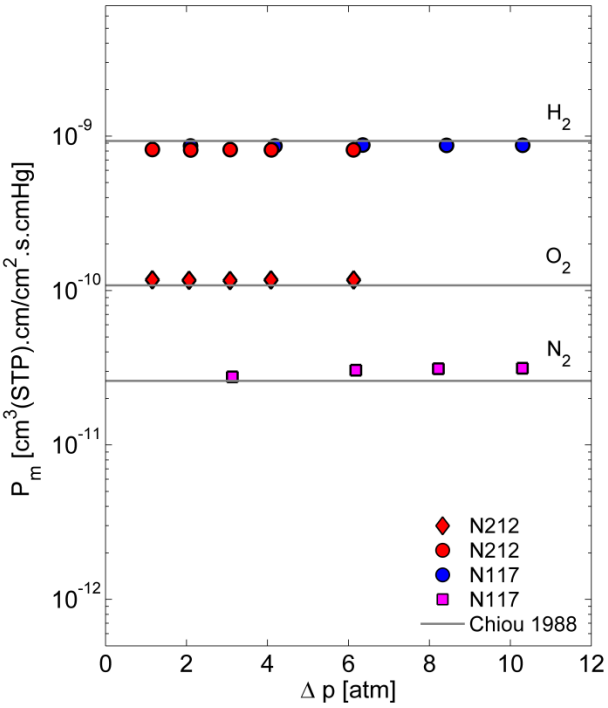

Figure 5-6: Gas permeability at T = 35°C as a function of different pressure gradients compared against Chiou and Paul using similar set up[17]. 1 Barrer = 10^{-10} cm^3(STP) cm/(cm^2 s cmHg)

Figure 5-7 shows the gas permeability of both H_2 and O_2 for three types of PFSA ionomers with varying equivalent weight (EW, ion-exchange capacity (IEC) of the ionomer). Given PFSA's TFE backbone, permeability of PTFE is also provided in the figure as a reference for the backbone gas permeability. With an increase in EW, Figure 5-7 shows an increase in gas permeability. Permeability depends on both a thermodynamic term (S_{app}) and a kinetic or mobility term (D_{app}) as given by equation (7). The gas solubility is influenced by penetrant/polymer interaction, temperature, pressure, and Lennard-Jones force constants.[14] Diffusion is mainly influenced by penetrant size, available free volume, and temperature. Figure 5-7 encompasses both the effect of reduction in side-chain length (Nafion> 3M> Aquivion) and EW. Varying the PFSA chemistry in such a way can impact crystallinity, available free volume, and penetrant-polymer interaction collectively impacting diffusivity and solubility to varying extent. Decrease in the side-chain length decreases the polar connector groups of –O– and –CF_2– bonds that both facilitate torsional movement and increase solubility. Increased stiffness of the decreased short side-chain ionomers is also seen in their higher T_α. In addition, the interaction between backbone and side-chain is enhanced with a decrease in side-chain length, resulting in a more compact packing and decreased accessibility to surface areas for adsorption and solubility. Additionally, increase in EW, increases the number of linear –CF_2-CF_2- backbone unit and length between side-chains resulting in increased crystallinity.[37] Short side-chain PFSA can also possess greater crystallinity due to improved ease of packing. Gas diffusivity is directly correlated with amorphous volume (ϕ_{am} = 100 - $\phi_{c,}$ %, given in Table 5-1); therefore, diffusivity is hindered with increase in EW. Solubility on the other hand experiences the reverse. With an increase in EW, the polar interaction between backbone and sulfonate group is decreased, results in a greater fraction of non-polar ionomer that can facilitate dissolution of gas in the polymer matrix. Therefore, gas permeability can be modified and normalized by amorphous volume (ϕ_{am}) of ionomer via P_m/ ϕ_{am}^2. Figure 5-7 shows gas permeability normalized by amorphous volume. Trends in Figure 5-7 display greater slope of

permeability for O_2 than H_2, demonstrating that the increase in amount of polymer per sulfonic group favors the strongly interacting and more soluble gas.[65] The compensative behavior of the multiple factors at play here on diffusivity and solubility result in peak permeability at certain EWs. Similar findings were observed for other alternative ionomers. [31,66]

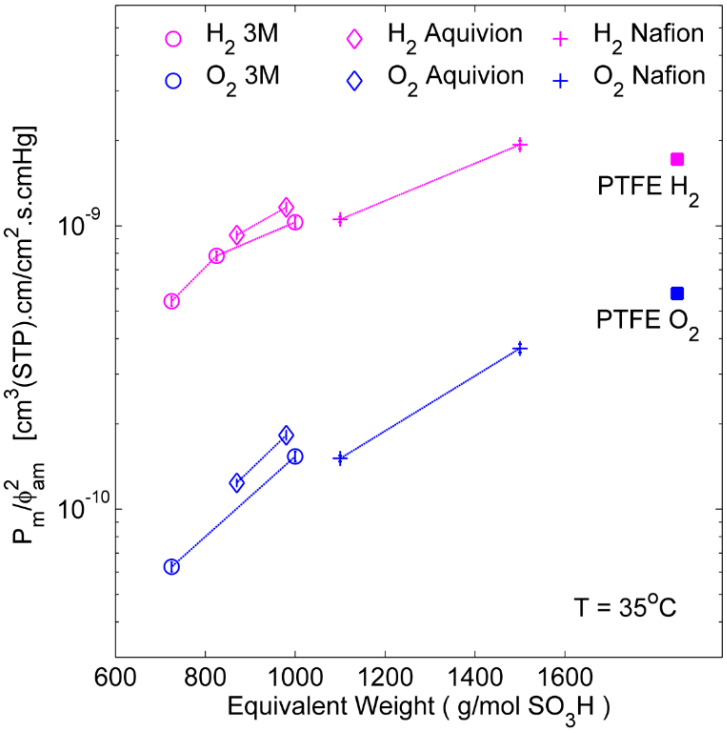

Figure 5-7: H_2 and O_2 gas permeability normalized by amorphous volume fraction as a function of equivalent weight of various PFSA. 1 Barrer = 10^{-10} cm^3(STP) cm/(cm^2 s cm_{Hg})

Having a grasp over the influence of EW and side-chain, gas permeability of bulk PFSA of varying thickness was explored. All samples discussed in this section were provided by manufacturer and cast in a similar manner. Figure 5-8 shows gas permeability of bulk 3M (825 g/mol, 1.21 IEC) as function of thickness. Overall, gas permeability appears to remain unchanged within the standard deviation of samples measured. Wide variability observed in some samples could be due to sample to sample cleanliness variability or physical aging effects that were not controlled. Ionomers used in this measurement were used untreated and as received. Findings here verify that gas permeability of ionomer does not show any significant size or confinement effects down to 5 μm in thickness.

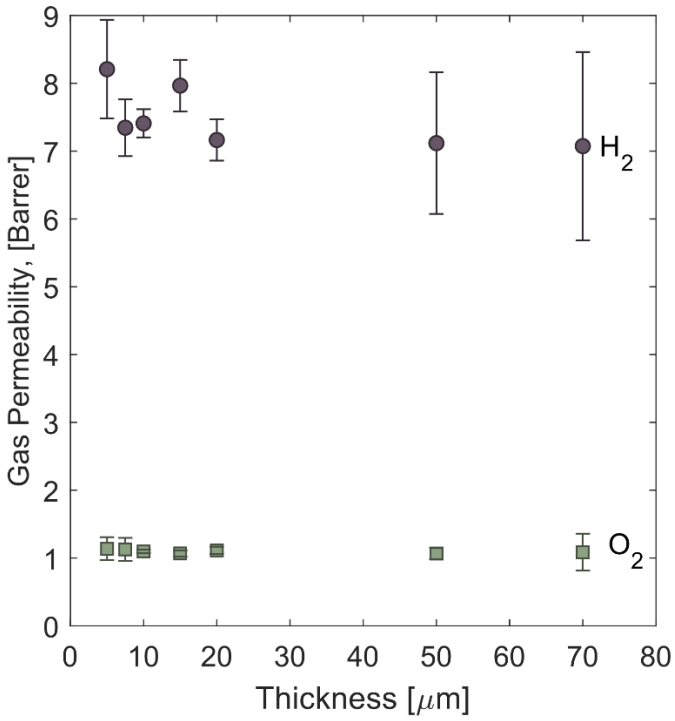

Figure 5-8: H_2 and O_2 gas permeability of 3M (825 g/mol, 1.21 IEC) PFSA as a function of thickness. 1 Barrer = 10^{-10} cm^3(STP) cm/ (cm^2 s cm_{Hg})

5.3. Quantifying Gas Transport in Thin Film Ionomers

In this section, three separate methods are evaluated for the purpose of establishing a good technique that can capture ionomer gas permeability in a reproducible manner under conditions useful for understanding performance in real catalyst layers and the constraints of handling delicate nanometer-thin ionomers.

5.3.1. Composite Polymer Method (PDMS and Nafion)

Composite polymer, where a polymeric layer of interest is supported by another polymer or a microporous support, is a method that has been utilized by the gas-separation industry.[67–70] Commonly, composite membranes are made from a combination of rubbery polymers (with high flexibility, high-moderate permeability, low selectivity) and rigid glassy polymers (low-moderate permeability, with high selectivity). Varying the thickness and nature of each component of the composite allows for engineering optimal selectivity and permeability for a desired application with a specific mechanical integrity and cost. In this work, a composite polymer composed of thin film ionomer and polydimethylsiloxane (PDMS) is used to quantify ionomer gas permeability while possessing the mechanical integrity and support of the highly permeable rubbery PDMS. Steady-state permeation through an ionomer/PDMS composite is modeled as resistors in series. Since the flux across the membrane is the same for each section, the unknown ionomer permeability can be calculated from known PDMS permeability values and the thickness of each layer by

$$\frac{J \cdot l_{composite}}{P_{composite}} = \frac{J \cdot l_{ionomer}}{P_{ionomer}} + \frac{J \cdot l_{PDMS}}{P_{PDMS}} \tag{9}$$

$$P_{ionomer} = l_{ionomer}\left(\frac{l_{compsite}}{P_{composite}} - \frac{l_{PDMS}}{P_{PDMS}}\right)^{-1} \tag{10}$$

5.3.1.1. Materials and Ionomer/PDMS Composite Polymer Preparation

Cast bulk and thin film ionomers of < 2 µm thickness were spin-casted onto silicon substrates (Si) from dilute solutions of 5 and 20 wt % Nafion (EW=1100) polymer resins obtained from Sigma Aldrich. Diluted solutions were sonicated for 5 min, allowed to equilibrate for at least 24 hours, and filtered prior to casting. Solutions were spun cast on Si substrates at variable speeds of 500 to 3000 rpm for 1 to 3 minutes to obtain the desired film thickness. The resultant thin film was annealed for 3 minutes at ~100 ºC to remove residual solvent. For thin films of thicknesses < 600 nm, a PDMS coating of thickness 5 to 7 µm was applied. Properties of PDMS are given in Table 5-1.Thin film support layer Dehesive 944 was diluted in cyclohexane to give 20 wt% PDMS solution and stirred for 24 hrs. A 400 µl cross linker and 200 µl catalyst OL were mixed slowly with 20 g of a PDMS solution in an ice bath for two hours. The solution was then filtered to remove any contaminants or coagulates that may have formed during the process. After degassing in a sonication bath for 20 minutes, the solution was spin cast at 1000 rpm for 90 s. The film was then annealed on a hot plate at ~110 ºC for 15 minutes to crosslink the PDMS and to remove residual solvent (thickness can range between 5 to 7 µm). The ionomer/PDMS composite film casted on a large wafer of diameter 4 to 6 inches is carefully cut into small pieces of square dimensions of 1 to 1.5 inches wide. Water is then used to lift these pieces of composite films off the substrate. The-now free-standing films are then finally lifted out of the water by the use of a copper wire to support only the edges. Lifted films are dried under N_2 gas for 5 minutes at 150 to 160 ºC, to remove residual water and erase thermal history. For the permeation measurement, thin films supported with PDMS are assembled in the same manner as bulk film as shown in Figure 5-5b.

5.3.1.2. Ionomer Thin films and Composite Polymer Characterization

In this study, a variable angle spectroscopic ellipsometer (VASE) M-2000D model from J. A. Woollam was used to characterize thin ionomer films with thickness ranges 100 to 1000 nm. Ellipsometry measures changes in polarized light as it is reflected from the substrate-supported sample. Ionomer thin films supported on silicon substrates were scanned over the spectral range of 400 to 1000 nm in the depolarization mode at single incident angles of 70°. A three-layer model (Si, Native SiO_2, and Cauchy material) is used determine film thickness. Thickness variation on 4- and 6-inch wafers was captured by implementing a 45-point square scan pattern, measuring thickness at 1.5 to 2 cm length intervals. (Expanded details on Spectroscopic Ellipsometry are given in Appendix A)

The thickness of thin film ionomer-PDMS composites on Si wafers was measured with a profilometer (Dektak 150 surface profiler from Vecco Instrument). A diamond stylus with a vertical range of 6.5 or 65 µm was used to scanned the sample surface with a low-inertia sensor tracking force of 1 mg along a 10 mm path over 100 seconds. Vertical resolution of the profilometer at this setting is 0.3 µm. At least 3 different measurements on each side of the edges were taken to determine the average thickness. Visual defects and interface between PDMS and Nafion were examined via JOEL scanning electron microscope (SEM) at the Molecular Foundry, Lawrence Berkeley National Laboratory.

5.3.1.3. Gas Permeation in Ionomer/PDMS Composite Polymer Films

To prove the structure of ionomer/PDMS composite membrane supported on Si, a sample was cut under liquid nitrogen and imaged via SEM as shown in Figure 5-9a. The image shows two separate layers stacked over each other as expected. Chemical characterization of the cross-section was done with Energy-dispersive X-ray spectroscopy (EDS) as shown in Figure 5-9b. Key elemental markers in the two separate films were Si in PDMS layer and F in Nafion. Figure 5-9 b shows the two layers explicitly. The Si markers in the Nafion layer and F markers in PDMS are artifacts or contaminants during SEM sample preparation.

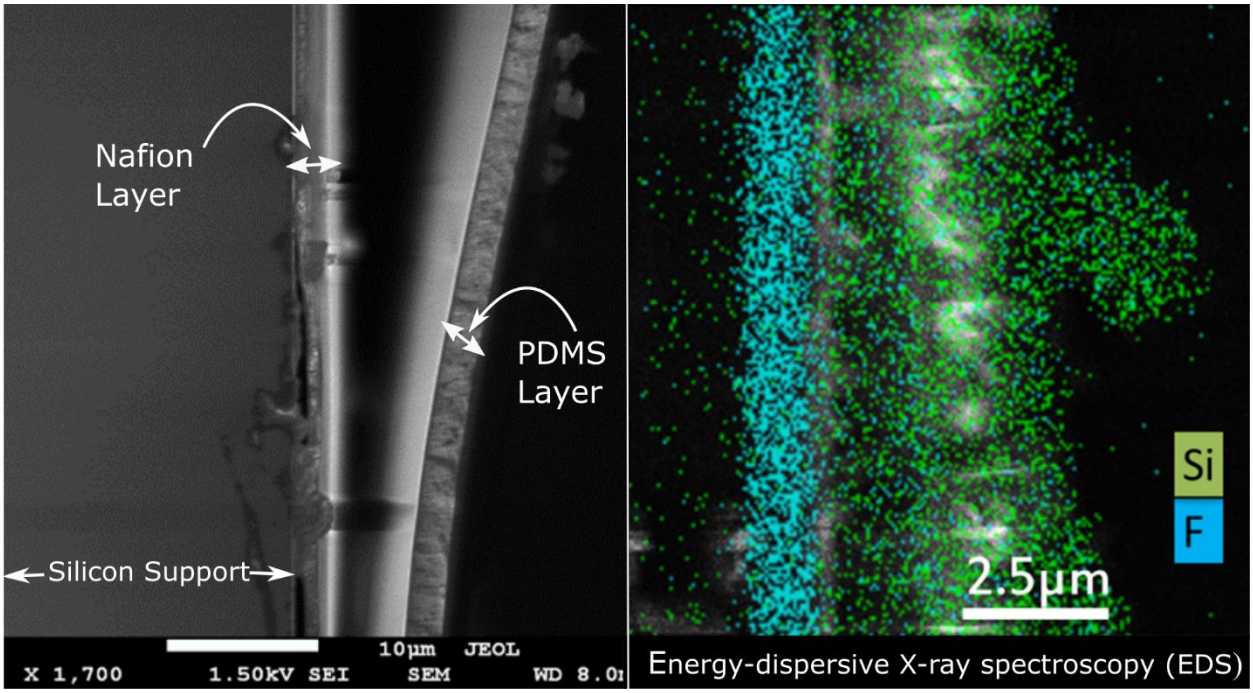

Figure 5-9: (a) Cross-sectional SEM Image of ~5µm composite film. (b) Energy-dispersive X-ray spectroscopy (EDS) chemical analysis of cross section of the composite film.

Supporting ionomer films with a highly permeable PDMS layer can provide the mechanical stability of a bulk film, while reflecting the resistance of the selective ionomer layer. To verify no interfacial resistance at the ionomer/PDMS interface is lumped with the ionomer resistance, samples were fabricated with constant ionomer-film thickness with variable PDMS layer thicknesses. Figure 5-10 shows composite film resistance of unsupported Nafion with those supported with varying PDMS thickness, indicating that reflected ionomer resistance is not influenced by interfacial resistance between the two layers.

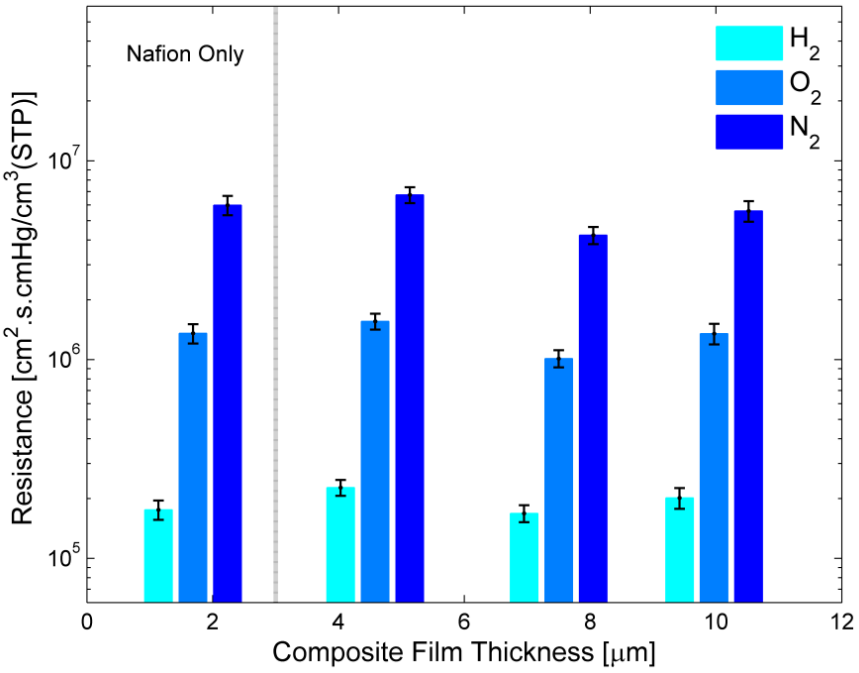

Figure 5-10: Composite film transport resistance as a function of thickness measured at T = 35°C and Δp = 2 atm. Nafion ionomer was held at 2μm with varying PDMS thickness coating.

Figure 5-11 shows gas permeability of H_2 and O_2 as a function of thickness of free-standing Nafion thin films and PDMS supported Nafion thin- and ultra-thin films in the composite polymer structure. Results from free-standing films demonstrate overall higher values than bulk ionomer gas permeability with scatter. Rise in oxygen permeability of some free-standing films displays 100% increase over bulk; while maximum rise in hydrogen permeability is 50%. PDMS supported ionomers also displayed inconsistencies. Although hydrogen permeability remained consistent with minor scatter, oxygen permeability appeared to increase with decrease in thickness. Disproportional rise in permeability H_2 and O_2 results in reduction in selectivity. Bulk Nafion gas selectivity (α_{H_2/O_2}) from section 5.2.3 and various literature sources is 6 to 7.5, while free-standing and PDMS supported ionomer thin films displayed variable lower selectivity as low as 4.5.[71] Simply based on the molecular weight and diameter of these two gases, selectivity in primarily Knudsen or molecular diffusion transport is 4 and 5.7, respectively. The reduction in selectivity in a Knudsen and molecular transport regime is intuitive as neither of these modes of gas diffusion involve solution diffusion process that occurs in dense glassy membranes. Therefore, the most probable explanation for observed permeability and variability in Figure 5-11 is the presence of surface defects or intrusions of PDMS into the Nafion thin film layer in the composite film, thereby artificially inflating the gas permeability of the ionomer and decreasing selectivity (i.e., approaching that of PDMS, $\propto_{H_2/O_2}$~1.4).[72] Using a one-dimensional resistance in parallel analysis for the composite, and accounting for the presence of micro surface defects(pores), the selectivity can be related to surface porosity as described by Lopez, et al. and Henis, et al.[73,74] Surface porosity is described as the ratio of total area of pores or defects in the ionomer to total non-defective area. At the resultant selectivity, surface porosity of ranges 10^{-7} to 10^{-3} can explain the possible increase in gas permeability (see Appendix D for calculations).

Preparation of composite polymer films for measurement involves removal from the casting surface (Silicon substrate) using water as a liquid agent separating surface from polymer. This is a highly sensitive process prone to mechanical stretch, tear and deformation. Ionomer/substrate interactions need to be broken by water tension, for the composite polymer film to float off supporting substrate. Even after film removal from the substrate, continued exposure of the hygroscopic ionomer thin film to water can affect its mechanical integrity. Lifting process used to remove the composite polymer film out of water can also add tension, adding yet another vulnerability and potential for sample damage. In addition, significant difficulty is experienced when exposing delicate composite films under large pressure gradient as is necessary for constant-volume variable-pressure method as discussed in section 5.2.2. The culmination of these experimental hurdles makes ionomer thin film gas transport measurement via composite polymer method highly challenging and unreliable.

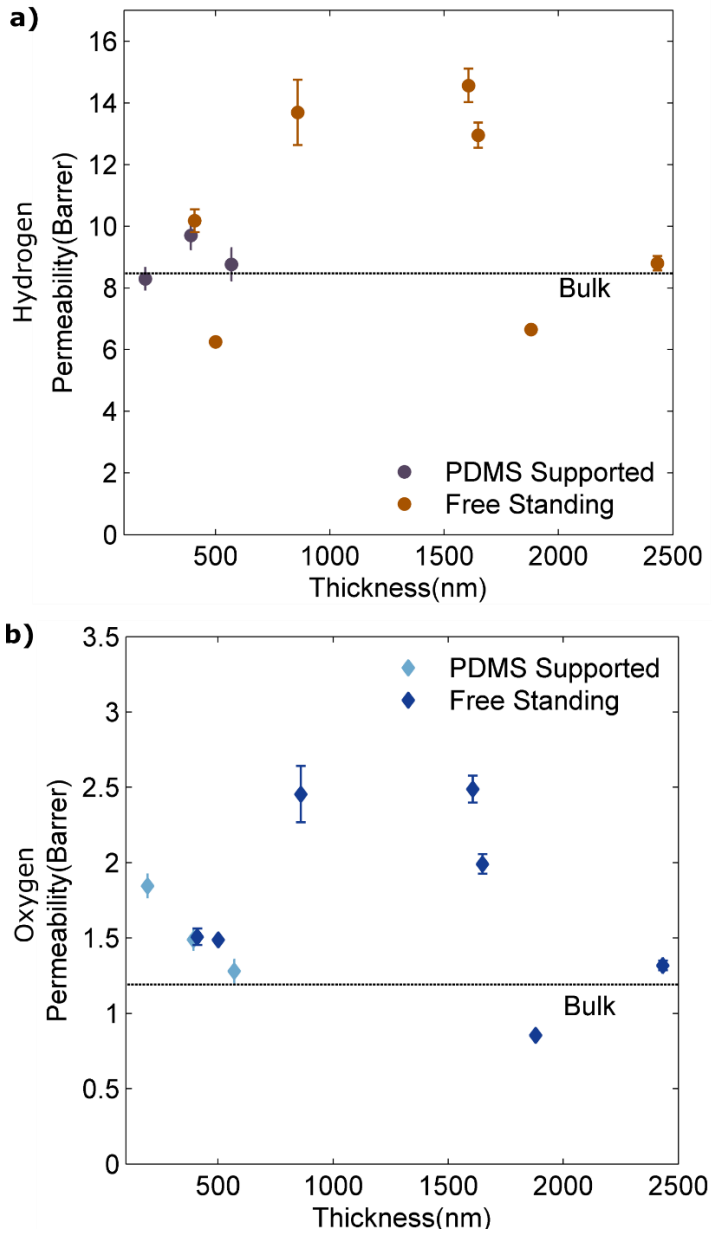

Figure 5-11: Thin film ionomer (a) H_2 and (b) O_2 gas permeability as a function of ionomer thickness measured via composite ionomer/PDMS polymer method. 1 Barrer = 10^{-10} cm^3(STP) cm/ (cm^2 s cm_{Hg})

5.3.2. Ionomer on Microelectrode Electrochemical Method

5.3.2.1. Ultra-microelectrode (UME) Electrochemical Set-Up Components

Potential-dependent, in-situ gas-permeability measurement was conducted using a 3-electrode microelectrode shown in Figure 5-12. Platinized platinum(Pt) mesh (from Alfa Aesar) coated with a layer of ionomer (5 wt% EW1100 Nafion solution from Sigma-Aldrich) for electrolyte contact was used as counter electrode (CE). Ionomer coating on the CE was applied until visible coverage of Pt surface with ionomer was established for good ionomer adherence. The ionomer coated CE was air dried first, and dried in vacuum oven at 120 ºC for 1 hr. The CE is designed to facilitate the balancing reaction to the working electrode (WE). It is essential for CE's

electroactive surface area to be significantly larger than that of the WE to ensure resistances and losses associated with the CE are minimal. Reference electrode (RE) is the Hydro-flex dynamic hydrogen electrode (DHE, Gasketel) with a Pt/Pd wire facilitating hydrogen oxidation and reduction from its own hydrogen cartridge as shown in Figure 5-12. Such RE permits an isolated source of gas, separate from and uncontaminated by external or test gas. DHE also allows for pH-sensitive reference 0 V to be established, ensuring more accurate account of local proton concentration in the electrolyte and proton bridge. DHE is also coated with layer of ionomer to ensure ionomer connectivity for proton shuttle between all moving components of the microelectrode setup. Ionomer (20 wt% EW1100 Nafion solution from Sigma-Aldrich) was drop casted on the DHE surface and dried at room temperature until completely dry and fully covered thin film is visible. The coated DHE was then annealed at 120 ºC for 1 hr. The proton bridge establishes connectivity between the CE/WE and the RE, and is composed of bulk Nafion (N211, 25.4µm) ionomer. It selectively conducts protons while forcing electron current induced by the reaction at the WE and CE to be captured by a potentiostat (SP-150 Potentiostat from Bio-Logic Instruments). Planar Pt ultra-microelectrode (UME) of 10 to 50 µm in diameter were used as the WE. The WE electrode facilitates the oxygen reduction reaction (ORR) similar to Pt nanoparticle in the cathode catalyst layer. The CE facilitates the complementary reaction of oxygen evolution reaction (OER) from water. Thin films of varying thickness of interest were cast onto the UME (BASi Analytical Instruments) as in Kudo et. al and as discussed below.[23]

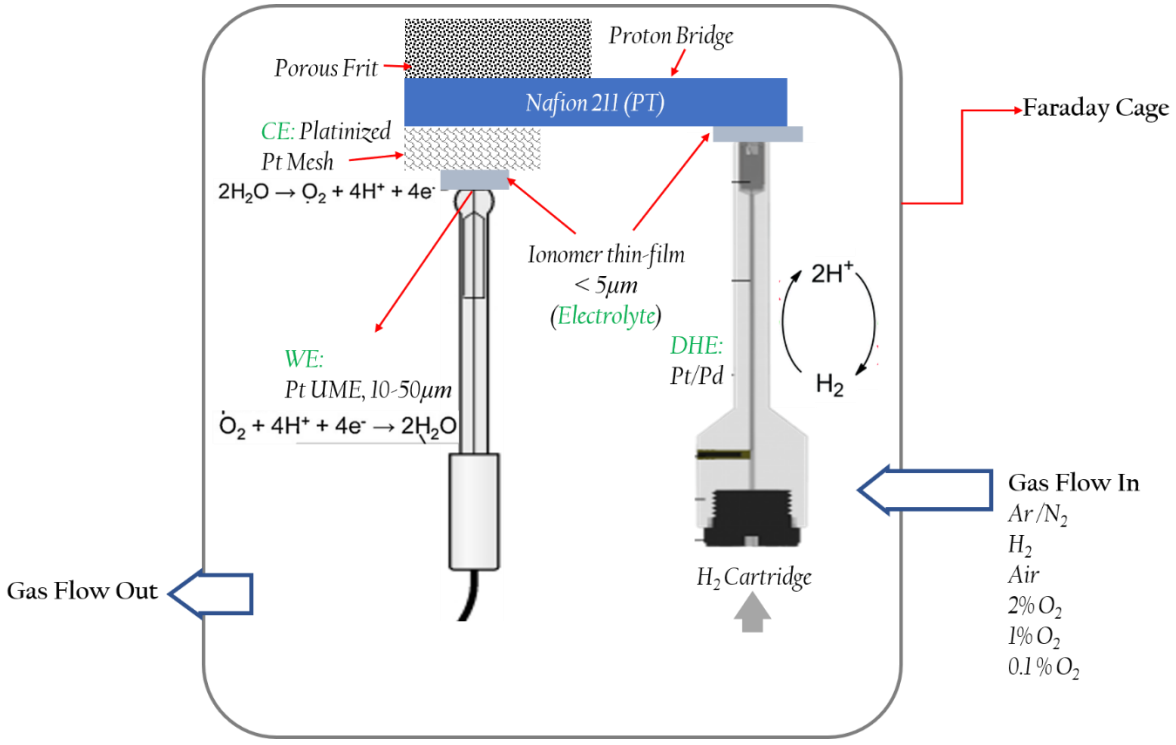

Figure 5-12: Microelectrode experimental set-up used for measurement of thin film in-situ gas permeability. CE= Platinum mesh counter electrode, DHE = Dynamic Hydrogen electrode reference electrode (RE), WE= ultra-microelectrode (UME) working electrode coated with ionomer thin film of interest. The porous frit provides a flow pathway for gas to the electrode surface. The setup is protected with a faraday cage for isolation from external signals.

5.3.2.2. Preparation and Characterization of Microelectrode Working Electrode

Prior to experiment, the Pt disk UME is cleaned in a wet cell to ensure optimal performance of UME and results. Glassware (including 3-port wet cell) components are soaked in highly concentrated sulfuric acid (alternatively nitric acid and sulfuric acid mixture can also be used) for over 12 hr to remove organic components. Glassware is then rinsed and boiled in DI water for 3 to 4 hr. At this point, glassware is isolated to minimize re-contamination. In addition to polishing, as recommended by providers, the UME is rinsed a few times in the cleaning concentrated-acid solution, rinsed with methanol, DI water, and dried with a N_2 gun. The UME is then placed in a 3-electrode wet cell containing 0.5 M sulfuric acid, Ag/AgCl reference electrode, and Pt mesh counter electrode with a N_2 bubbler. The three-electrode cell is placed in a custom-made Faraday cage (made out of aluminum foil) to minimize noise and disturbances from nearby activities. Given the small area and very low current output of UME, the Faraday cage is essential for good data collection. At this point, WE (UME) is cycled via cyclic voltammetry, sweeping from -0.2 to 1.2 V at 50 or 100 mV/s multiple times until performance stabilized to display critical peaks indicative of good performance. One of the critical peaks is hydrogen underpotential deposition which is associated with adsorption of H_2 on a Pt surface (HUPD, shown in green in Figure 5-13), which is used to determine the electroactive surface area and roughness of the UME.

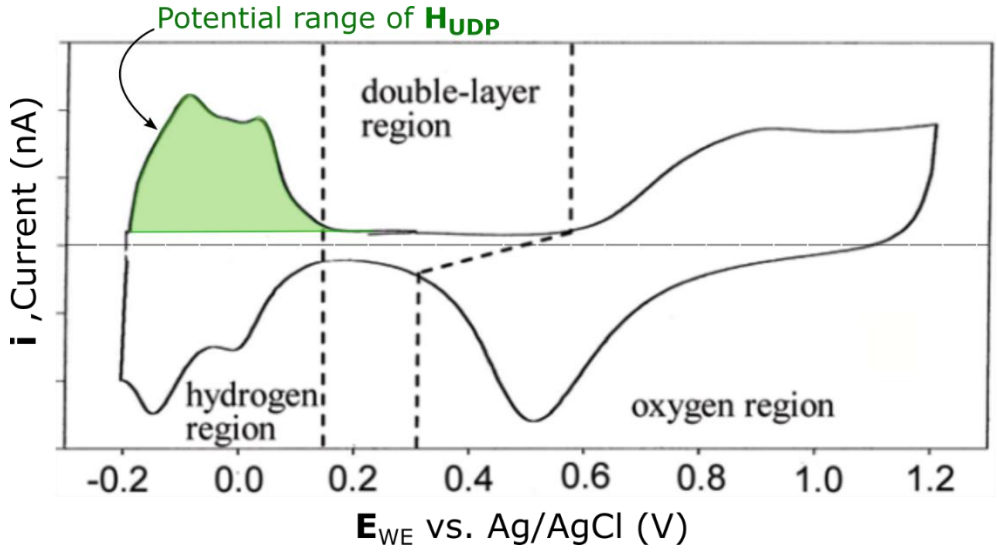

Figure 5-13: Cyclic voltammetry of platinum(Pt) microelectrode in wet 3-electrode in 0.5M H_2SO_4 electrolyte against Ag/AgCl reference electrode. Potential range and current associated with hydrogen adsorption on Pt surface are shown in green. Image reprinted and adapted from ref.[75] with permission from Journal of the American Chemical Society. Copyright 2009 American Chemical Society.

UME electroactive surface area is significantly enhanced compared to idealized smooth planar Pt electrode. The enhanced electroactive surface area is captured by roughness factor, R_f, and is directly correlated to the charge passed during the single atom adsorption of hydrogen during oxidation sweep ($H^+ + e^- \rightarrow H_{ad}$). (Equation (11) and (12)) Charge passed through HUDP (Q_{HUDP}) is the time(t) integral of current passed during adsorption (I_{HUDP}) with the capacitive process current associated with the double-layer (DL) region removed (I_{DL}). Charge density of UME is given by normalized charge during HUDP by geometric electrode area ($A_{geo.UME}$). Charge density of UME is compared to that of monolayer of adsorbed hydrogen on a perfectly smooth platinum is known to be 210 μC/cm^2.[76,77]

$$roughness\ factor = R_f = \frac{Surface\ Area\ Pt\ UME}{planar\ smooth\ Pt\ area} \quad (11)$$

$$R_f = \frac{\frac{Q_{HUDP}}{A_{geo.UME}}}{210\mu C/cm^2} = \frac{\int (I_{HUDP} - I_{DL}) \cdot dt}{A_{geo.UME} \cdot 210\mu C/cm^2} \quad (12)$$

5.3.2.3. Enhancing UME Electrode Activity via Platinization

Initial work reveals very small current responses even in the cleanest UME. To increase electroactive area and enhance signal-to-noise ratio that occurs due to contamination during operation, the Pt UME was platinized by depositing Pt nanoparticles from a solution source.[78] The clean Pt electrode from the wet cell was platinized using chloroplatinic acid (H_2PtCl_6). A two-electrode platinization setup, where the WE (UME) to be treated is placed with Pt mesh in the electrolyte of H_2PtCl_6 (5g/L). Hydrochloric acid is used as supporting electrolyte (1M) and the solution is bubbled with nitrogen. The whole setup is maintained in a water bath at 60 to 65ºC. A 2 V DC voltage was applied at low current for 5 min to obtain Pt deposits. The platinized UME was then rinsed to remove weakly adhered nanoparticles. The electrode was then annealed at 100ºC under vacuum for 1 hr to ensure lasting nanoparticle adherence on UME. A cyclic voltammogram of the newly platinized UME was performed until stable performance is recorded. Electroactive surface area and roughness factor was then measured via HUPD.[76,77]

5.3.2.4. Preparation of Ionomer Thin Film on Microelectrode

To coat the UME with an ionomer thin film, a 5 wt-% solution of EW 1100 Nafion was diluted to a 0.1 to 1 wt-% solution in isopropyl alcohol (IPA). 5 µL of this diluted solution was then drop cast over the tip of the microelectrode, which had a surface area of ~0.5 cm^2. The film is then left to dry for 1 hour in air at room temperature. The coated UME is then annealed in an oven at 60 ºC for 1 hr. To capture film thickness accurately, quartz windows of similar microelectrode surface size were used to drop cast ionomer thin films in similar manner as UME. After using similar procedure to dry films, thickness was measured via spectroscopic ellipsometry. Given the large area of the glass support relative to the active area platinum surface in the UME, glass windows will likely reflect accurate thickness.

5.3.2.5. Preliminary Evaluation of Thin Film Permeability via Electrochemical Methods

Two electrochemical methods can be used to capture the mass-transport-limited flux and extract gas-transport parameters of thin film ionomers. These two methods are used to obtain the same transport limited current in probed in two different ways.

(a) Chronoamperometric Potential-Step Measurements involves the application of a potential step to capture current response where the oxygen reduction reaction(ORR) is under mass-transport-limited control. To capture this voltage window accurately, sampled current voltammograms (SCV) can be applied. SCV involves application of series of waveform potential steps starting at a potential where no Faradaic process occurs.[79] Current-time-response curves at each potential step was recorded. At high overpotential, high current is drawn, reactant concentration at the Pt UME electrode surface is nearly zero, and electroactivity is limited by the concentration reaching the surface. Kinetics of ORR have no influence on the current response

observed. In the mass-transport-limited potential window, current-time responses from a SCV reflect current plateaus that are observed during forward and reverse SCV scans. After assembling the ionomer coating the UME equilibrated under humidified conditions (90%, N_2) for at least 12 hr. Cyclic voltammetry of the UME is carried out under inert conditions (N_2 or Ar) by sweeping from 0 to 1.4V versus RE (Pt mesh under 2% H_2 gas, in this single instance) at 100 mV/s until stable performance is observed. Prior to SCV, system is equilibrated at the given humidity (90%) in varying oxygen atmosphere of 1 or 2% O_2 in N_2 balance for 1 to 3 hr. The transport limited current density is determined by sweeping the potential from 0 to 1.4 V vs. RE in given O_2 environment at 10mV/s. After establishing the appropriate potential range using SCV, individual chronoamperometic potential-step measurements are performed. Figure 5-14 shows current-time responses of chronoamperometric potentials step applied by holding the potential of the cell at 0.1 V for 400 s. A similar method has been employed in studies employing microelectrodes for bulk PFSA and related ionomers.[80,81]

It is critical to identify the accurate potential step for mass-transport-limited current for a given electrochemical system; depending on electrode configuration structure, surface adsorption kinetics, type and state of reference electrode steady-state current could change. Using known concentration in bulk external environment (oxygen concentration) and almost zero species at the electrode surface, flux of gas through ionomer is related to the limiting current using Faraday's constant and the number of electrons participating in ORR (n = 4). Simultaneous evaluation of solubility and diffusivity (permeation) of gas through ionomer on a disk UME can be evaluated via modified Cotrell equation (equation 13) known as the Shoup and Szabo equation (equation 14), which provides a single empirical relationship accounting for wide range of dimensionless time $\tau = 4Dt/r^2$.

$$i = \frac{4nFADC_0}{\pi r} f(\tau) \tag{13}$$

$$f(\tau) = 0.7854 + 0.8862\tau^{-\frac{1}{2}} + 0.2146e^{-0.7823\tau^{-\frac{1}{2}}} \tag{14}$$

D is diffusion constant of O_2 gas, r is the diameter of microelectrode, t is time, F is Faraday's constant, n is number of electrons involved in reaction of interest (ORR), electroactive surface A is area which can be calculated from HUPD, and C_0 is the constant O_2 concentration far from the electroactive interface.

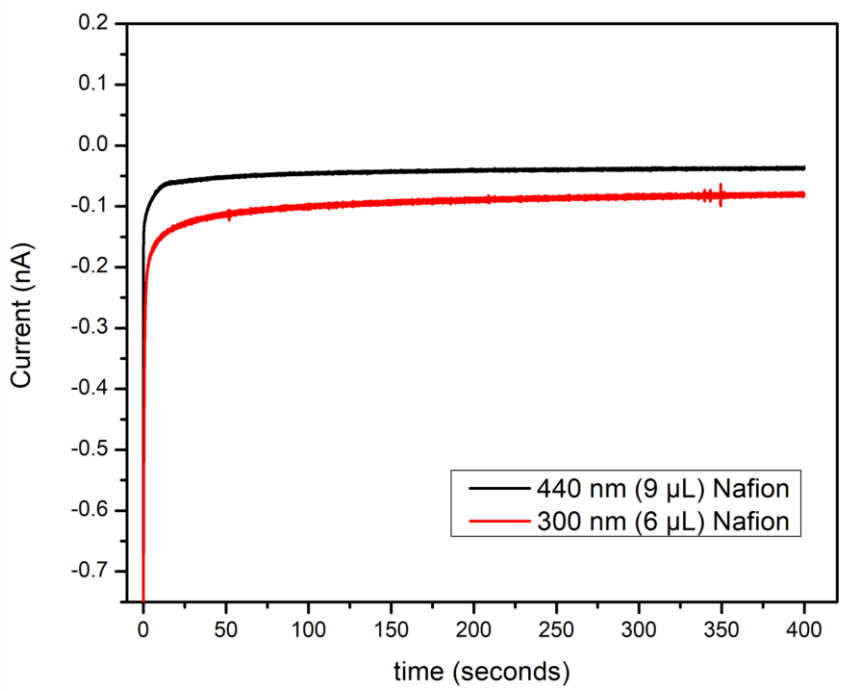

Figure 5-14. Raw data points from current-time response of chronoamperometric potential step applied to UME at 0.1V at 90% relative humidity at 26ºC. Ionomer coating thickness varied with drop cast volume.

Diffusivity, solubility, and permeability values calculated from chronoamperometric potential method are shown in Table 5-2. Ionomer permeation values show gas permeability parameters very close to bulk value of reference study.[80] No discernable trend is observed with reduction in thickness.

Table 5-2: Diffusivity, solubility and permeability values for varying ionomer film thicknesses measured via chronoamperometric potential step

Thickness	Diffusivity (D) (cm^2/s)	Solubility (C_0) (mol/cm^3)	Permeability (DC_0) ($mol/(cm*s)$)
26.5 µm (Ref.[80])	4.5×10^{-8}	7.6×10^{-6}	3.0×10^{-13}
440 nm	5.9×10^{-9}	9.2×10^{-6}	5.4×10^{-14}
300 nm	6.8×10^{-9}	1.8×10^{-5}	1.2×10^{-13}

(b) Extracted Limiting-Current Density: In a slightly different manner, limiting-current density can be extracted from the voltammogram responses under different concentrations of gas. In the mass-transport-limited regime, contribution from kinetic losses is minimal. That is, all gas of interest reaching the Pt active interface is immediately reacted and time scale for transport is assumed to be the major contributor to resistance. However, transport through the ionomer involves interfacial resistance at the gas/ionomer interface, diffusive transport through ionomer and interfacial resistance at the Pt interface. (See Figure 5-15) Therefore limiting current (i_d) is proportional to the total transport resistance which includes resistances at the Pt and gas interface

(k_{Pt}, $k_{ionomer}$) as well as resistance due to diffusion through ionomer (D). Flux through the ionomer is, therefore, linearly dependent on thickness as shown in equation (15):

$$R_{total} = \frac{nFAC_{ext}}{i_d} = \frac{1}{RTD.H} L_{ionomer} + \frac{1}{RTH}\left(\frac{1}{k_{ionomer}} + \frac{1}{k_{Pt}}\right) \quad (15)$$

where R is universal gas constant, T is temperature, D is diffusion coefficient of gas, H is solubility coefficient and $L_{ionomer}$ is ionomer thickness. Upon varying ionomer thickness, slope reflects resistance associated with transport through ionomer, and intercept reflects resistance at the interface.[23,24,49]

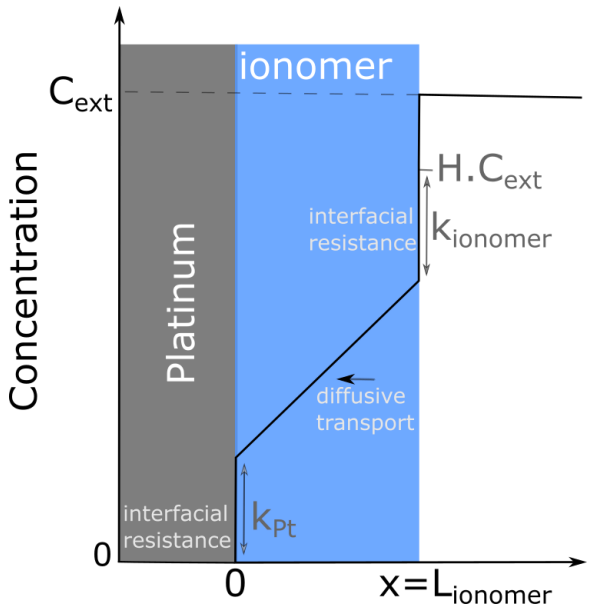

Figure 5-15: Gas concentration profile through ionomer thin films in microelectrode set-up.

Figure 5-16 shows the current response of potential sweep from 0 to 1.4V vs. DHE under varying H_2 concentrations of 0.3, 0.5, and 2% (N_2 balance) at 26ºC and 90% relative humidity, as an example. Current associated with hydrogen oxidation reaction (HOR) are of interest here. As a result of HOR, positive currents are observed rather than the negative(reduction) currents commonly observed during ORR; same method can be used with varying concentration of O_2.[22] Current associated with HOR due to varying H_2 concentration can be isolated by subtracting current under balance gas (i.e. $i_d = i_{\%H2} - i_{Ar}$). Limiting current associated with HOR increase when the electrode potential is increased from 0 V and reached a maximum around 0.2 V right before onset of ohmic losses, which are minimal (See Figure 5-16). Transport resistance calculated from HOR in figure below were significantly high due to overestimation of electroactive surface area.

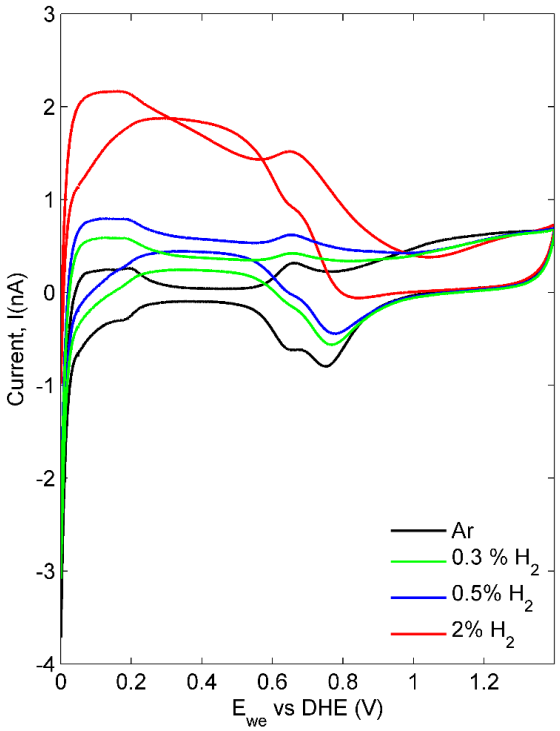

Figure 5-16 : Cyclic voltammograms of the Pt UME coated with ionomer thin film under Argon(black), 0.3% H_2 (green), 0.5% H_2 (blue) and 2% H_2 (red) in Argon at 26ºC and 90% relative humidity.

Given the preliminary nature of the data, more work is required to verify findings and to capture values for thinner ionomer films. Although advantages of microelectrode method were discussed above, significant challenges also exist with this method. First challenge is the variability of microelectrode setups in the literature. Few researchers have utilized microelectrodes to evaluate kinetic and transport parameters in proton exchange and anion exchange ionomers. However, each research group has developed different setup and optimized for their parameter of interest, consequently validating their measurement protocol only for their given experimental set-up. This variance would be of minimal effect if detailed protocol and result sharing was commonplace. The second challenge in utilizing UME is contamination of electroactive area with various contaminants in the experimental cell. Introduction of organic and other contaminants has resulted in several erroneous cyclic voltammograms that do not reflect expected signature peaks. The sources of the contaminants could be gas flow lines, UME cell itself, ionomer coating procedure, ionomer contaminant, dissolved Pt from counter electrode, etc. This issue is exacerbated by evolution of peaks due to different surface adsorption dynamics like sulfonate adsorption on Pt.[59,60] These contaminants and adsorbents are likely to cause shift in current or minimize electrode area, resulting in inaccurate results. Third challenge to UME setup is the non-uniformity of ionomer film. Drop casting ionomer on very small area creates issues of non-uniformity and edge effects that makes it difficult to have uniform coverage over electroactive area causing erroneous reading of thickness of ionomer coating on UME. Mitigation of these challenges will require defined procedure, rigorous cleaning protocols, and verification of results with reproducibility to increase confidence in data obtained.

5.3.3. Oxygen Luminescence Quenching Method

One method of circumventing pinholes in an ex-situ gas-transport measurement is to employ a solid-state structure that does not require free-standing films or high-pressure gradients. This section discusses initial work employing luminescence quenching of an oxygen-sensitive dye probe to quantify gas-transport through ionomer while still accomplishing the goal of developing a method that can evaluate permeability over a range of thickness. When certain dye molecules are excited by light, electrons from the ground state are propelled to a higher energy excited state; return to the ground state emits light at longer wavelength, is referred to luminescence.[82] If the emission lifetime is short lived (10^{-9}-10^{-7} s) from the singlet state with electrons spin-paired, it is considered fluorescence.[82,83] If a change in electron spin and an intersystem transition from excited singlet state to triplet state occurs, the decay back to ground state is referred to as phosphorescence (See Figure 5-17). The reduction in florescence and phosphorescence intensity of dye molecules (fluorophore) by an external quencher molecule (O_2 in this case) is referred to as luminescence quenching. Quenching is non-random occurrence due to various reasons including excited-state reactions, molecular rearrangements, energy transfer, ground-state complex formation, or collisional quenching between the fluorophore and the quencher.[82–84] As one of the most notable quenchers, O_2 provides a technique with localized oxygen sensing capability. Phosphorescence, having a longer emission lifetime (10^{-5} to 10s), is more sensitive to fluorophore-quencher interaction than florescence.

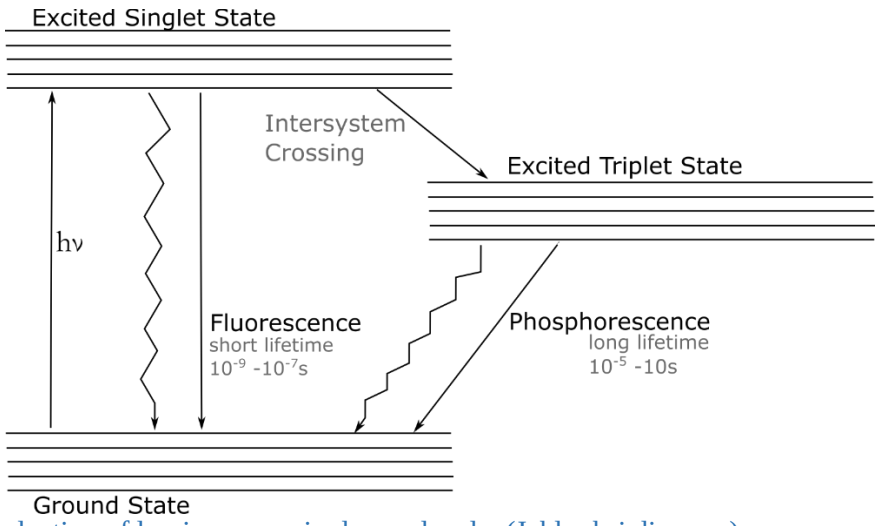

Figure 5-17: Production of luminescence in dye molecule. (Jablonksi diagram)

Metal phosphorescence complexes like 5,10,15,20-Tetrakis(pentafluorophenyl)porphyrin platinum (II) (PtTFPP) are uniquely structured to be quenched by the presence of O_2 via collisional quenching. O_2 sensing porphyrin dyes are commonly dispersed in host materials like polymers or biological samples.[85–89] Observation of intensity, fluorescence lifetime and differing dependence on temperature and viscosity of host material delineates the differing types of quenching.[84] For example, ground-state complexation does not result in emission of photons: fluorophore-quencher complex absorbs light and immediately returns to ground state. On the other hand, collisional quenching results in intensity response that is linearly proportional to concentration of dye, quencher, and at a rate that increases with temperature. This relationship guarantees that the quenching of the photo-excited triplet state is entirely diffusional.[90] The dynamic response during

collisional quenching results in changes in intensity that can be time resolved and correlated to transport coefficients like diffusion and permeation. The additional advantage of this method's reliance on spectroscopic technique is the ability to evaluate parameters like diffusivity with greater sensitivity and resolution even at short time scales. Photoluminescent molecules (like PtTFPP) are employed in various applications for their ability to be integrated into an existing structure, response to host molecule chemical nature, stability, time resolved response, and unique signature emission wavelengths. Systems utilizing dye probes have been applied in solar-energy conversion, electroluminescent systems, optical data storage, biochemical indicators and in gas barrier material as air pressure sensors.[83,84,90–94] Utilizing O_2 sensitivity of these unique molecules, a layered structure composed of fluorophore layer and ionomer layer is used to measure O_2 permeability in ionomer thin films as discussed below.

5.3.3.1. Materials and Preparation of Dye/Ionomer Composite Layer

Porphyrin molecules can also be dissolved in traditional polymer casting solvents making sample preparation and dispersion in a polymer host easy. In this method, due to the large structure of PtTFPP molecule (structure shown in Figure 5-18b) and possible interaction of Pt with ionomer structure, a film-on-sensor model was selected. A thin layer of polystyrene containing porphyrin is prepared separately, and the ionomer layer of interest is coated on top (Figure 5-18a). PtTFPP dye molecules (~5×10^{-4} mol/L, Frontier Scientific, Inc., Logan, UT, USA) are dispersed in the host polystyrene polymer (Sigma-Aldrich, Milwaukee, WI, USA, average Mw 280,000) dissolved in toluene (3 wt.%). Substrates used in this study were Silicon (Si, 100 n-type). Wafers were cut up into 1cm wide x 5 cm long rectangles before cleaning; the size was selected to fit the spectrometer sample cell width and length. Substrates were rinsed by distilled water and then washed twice with isopropyl alcohol (IPA) with a nitrogen drying step after each rinse. A solution containing polystyrene and dye is then coated onto the clean Silicon substrate. Porphyrin-doped polystyrene (dye layer) has been explored by various researchers and provides ideal homogenous structure critical for good optical response.[83,85,87,90,95,96] In addition to the structural integrity of a supported structure, ease of incorporating an ionomer layer of varying thickness (via spin-casting) to the same dye-layer system is a prime advantage for evaluating ionomer O_2 diffusivity as a function of thickness. A thin film ionomer layer is coated using similar methods discussed in previous chapters. Thickness of dye layer and ionomer layer was measured via spectroscopic ellipsometry (J. A. Woollam). Thickness variability was captured by a multi-point measurement over the area covering the substrate. Fluorescence intensity was monitored in the kinetics mode using the Spectrophotometer. Figure 5-18c shows experimental enclosure allowing alternating N_2 and air gas to flow in and out of spectrophotometer chamber. Figure 5-18d & e demonstrate excitation wavelength at 400 and 540 nm and emission at 650 nm as previously reported.[85,96] Samples were also excited continuously for up to 30 min to monitor photo bleaching or photo decay overtime. No significant amount of decay was observed.

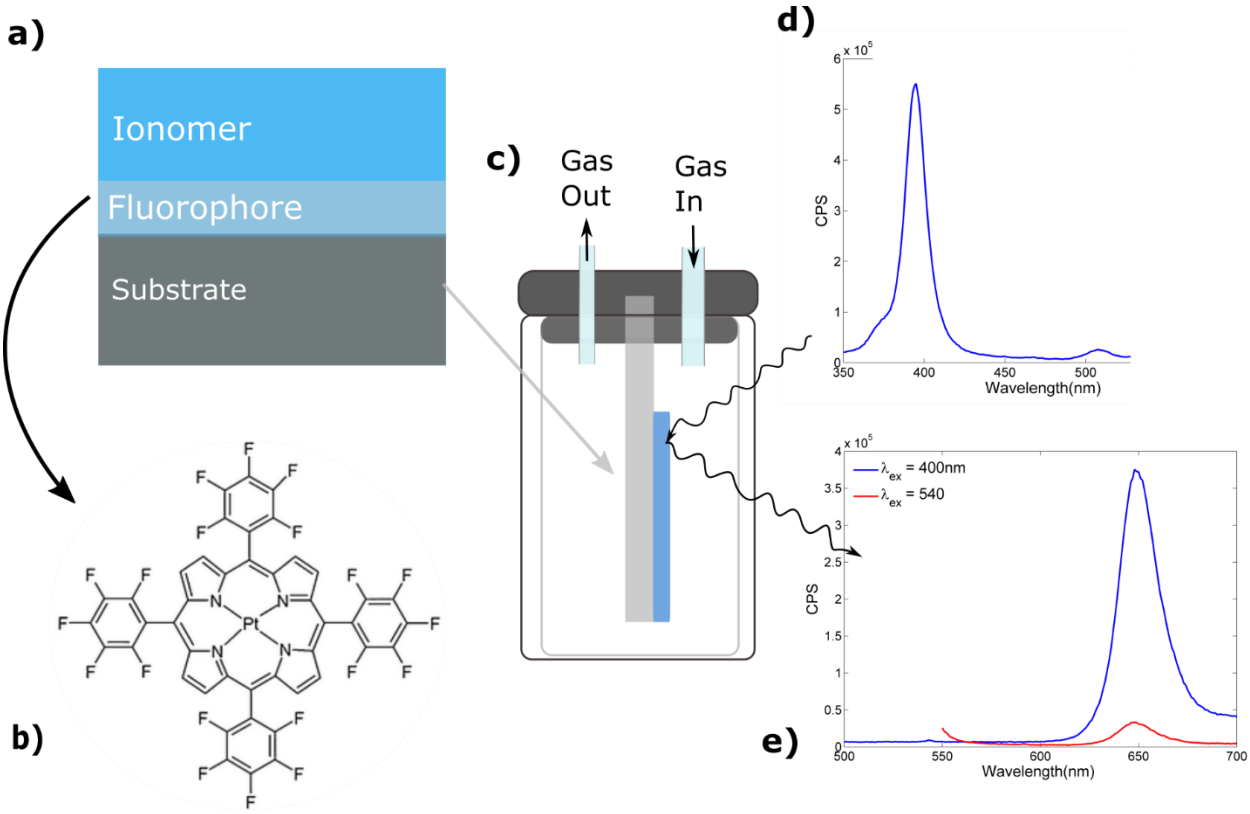

Figure 5-18: Experimental components and working principle of dye layered ionomer oxygen permeation measurement system. (a) structure of substrate supported solid state fluorophore and ionomer two layer set up. (b) Chemical structure of Pt phosphorescence complex, 5,10,15,20 -Tetrakis(pentafluorophenyl) porphyrin platinum (II) (PtTFPP) (c) Experimental enclosure exposing fluorophore to quenching (O_2) and non-quenching gas (N_2). (d) Absorption peaks (~400nm, 540nm) and (e) emission peak(650nm) of dye layer measured via spectroscopy. Y-axis (d, e) is arbitrary units of count per second (CPS).

5.3.3.2. Analytical Model and Intensity Analysis

The linear relationship between concentration of quenching molecule and luminescence quenching is commonly described by the Stern-Volmer relationship (Equation 16).

$$\frac{I_o}{I} = 1 + K_{sv}Q \tag{16}$$

I and I_o are luminescence intensities in the presence and absence of quencher respectively. Q is the concentration of the quencher(oxygen) inside fluorophore immobilized molecule. K_{sv} is Stern-Volmer constant accounting for the quenching rate, lifetime of unquenched luminescence, probability of quenching causing collision, radius of interaction between donor (dye molecule), and acceptor(oxygen) and their diffusion coefficients.[83,84] For a given immobilized probe system with a defined quencher, K_{sv} is a constant. The Stern-Volmer relationship assumes an equally accessible single class of fluorophores. Deviation from this relationship may indicate more complicated dynamics. Most fluorophores exhibit a linear relationship with quencher at low-to-medium concentrations.[83] Deviation from the linear relationship is expected at high concentrations for two possible reasons. First is the existence of additional static quenching processes that result in dissociation of weakly bound quencher-fluorophore complexes at higher temperatures.[84,85] The

second possible reason is differences in the dye-occupied sites and variability in accessibility by oxygen.[85] Previous studies utilizing PtTFPP have confirmed the Stern-Volmer relationship in the oxygen-concentration range utilized in this study (0-21%). [86,95,96]

The relationship between transient luminescence quenching of PtTFPP molecules and oxygen transport coefficients is established by combining Fick's law and the Stern-Volmer equation. Oxygen gas diffusion through ionomer and dye layer is described with respect to position and time, Q (x, t)

$$\mathbf{0} \leq \boldsymbol{x} \leq \boldsymbol{L_{dye}}, \qquad \frac{\partial \boldsymbol{Q}(\boldsymbol{t},\boldsymbol{x})}{\partial \boldsymbol{t}} = \boldsymbol{D_{dye,O_2}} \cdot \frac{\partial^2 \boldsymbol{Q}}{\partial \boldsymbol{x}^2} \tag{17}$$

$$\boldsymbol{L_{dye}} \leq \boldsymbol{x} \leq \boldsymbol{L_{ionomer}}, \qquad \frac{\partial \boldsymbol{Q}(\boldsymbol{t},\boldsymbol{x})}{\partial \boldsymbol{t}} = \boldsymbol{D_{ionomer,O_2}} \cdot \frac{\partial^2 \boldsymbol{Q}}{\partial \boldsymbol{x}^2} \tag{18}$$

Luminescence intensity response for the dye layer in the absence and presence of oxygen can be defined under nitrogen flow (I_{N2}) and air flow((I_{air}) conditions and the stern Stern-Volmer equation.

$$\frac{\boldsymbol{I_o}}{\boldsymbol{I}} - \mathbf{1} = \frac{\boldsymbol{I_{N_2}}}{\boldsymbol{I}} - \mathbf{1} = \boldsymbol{K_{sV}}\boldsymbol{Q}(\mathrm{t}) \tag{19}$$

Boundary conditions are,

$$\boldsymbol{t} = \mathbf{0}, \qquad \boldsymbol{Q_{O_2}} = \mathbf{0}\ (\boldsymbol{N_2}) \tag{20}$$

$$\boldsymbol{t} > \mathbf{0},\ \boldsymbol{x} = \mathbf{0}\ (\boldsymbol{substrate\ face}), \qquad \frac{\partial \boldsymbol{Q_{ioinomer}}(\boldsymbol{t},\boldsymbol{x})}{\partial \boldsymbol{x}} = \mathbf{0} \tag{21}$$

$$\boldsymbol{t} > \mathbf{0},\ \boldsymbol{x} = \boldsymbol{L_{dye}}, \qquad \boldsymbol{J_{dye,O_2}} = -\boldsymbol{J_{ionomer,O_2}} = \boldsymbol{D_{dye,O_2}}\frac{\partial \boldsymbol{Q}}{\partial \boldsymbol{x}} = -\boldsymbol{D_{ionomer,O_2}} \cdot \frac{\partial \boldsymbol{Q}}{\partial \boldsymbol{x}} \tag{22}$$

$$\boldsymbol{t} > \mathbf{0}, \quad \boldsymbol{x} = \boldsymbol{L_{ionomer}}(\boldsymbol{ionomer\ face}), \quad \boldsymbol{Q} = \boldsymbol{Q_{air}} = \boldsymbol{S_{ionomer,O_2}}\boldsymbol{p_{air}} \tag{23}$$

Oxygen concentration in the film is given by,

$$\frac{\boldsymbol{Q}(\boldsymbol{x},\boldsymbol{t}) - \boldsymbol{Q}(\mathbf{0},\mathbf{0})}{\boldsymbol{Q}(\boldsymbol{L},\boldsymbol{t}_\infty) - \boldsymbol{Q}(\mathbf{0},\mathbf{0})} = \frac{\boldsymbol{Q}(\boldsymbol{L},\boldsymbol{t})}{\boldsymbol{Q_{air}}} = \mathbf{1} - \frac{\mathbf{4}}{\boldsymbol{\pi}} \sum \frac{(-\mathbf{1})^{\boldsymbol{n}}}{(\mathbf{2}\boldsymbol{n}+\mathbf{1})} \boldsymbol{exp}\left(\frac{-\boldsymbol{D}(\mathbf{2}\boldsymbol{n}+\mathbf{1})^2\boldsymbol{\pi}^2\boldsymbol{t}}{\mathbf{4}\boldsymbol{L}^2}\right) \tag{24}$$

$$\frac{\boldsymbol{I_{N_2}}}{\boldsymbol{I}(\boldsymbol{t})} - \mathbf{1} = \left(\frac{\boldsymbol{I_{N_2}}}{\boldsymbol{I_{air}}} - \mathbf{1}\right)\left(\mathbf{1} - \frac{\mathbf{4}}{\boldsymbol{\pi}} \sum \frac{(-\mathbf{1})^{\boldsymbol{n}}}{(\mathbf{2}\boldsymbol{n}+\mathbf{1})} \boldsymbol{exp}\left(\frac{-\boldsymbol{D}(\mathbf{2}\boldsymbol{n}+\mathbf{1})^2\boldsymbol{\pi}^2\boldsymbol{t}}{\mathbf{4}\boldsymbol{L}^2}\right)\right) \tag{25}$$

When the sample is only coated with dye layer containing luminophore and polystyrene host, $D = D_{dye,O_2}$, $L = L_{dye}$. When evaluating ionomer on dye layer geometry additional equation decoupling diffusion through ionomer and polystyrene is required,

$$\frac{L}{D} = \frac{L_{dye}}{D_{dye,O_2}} + \frac{L_{ionomer}}{D_{ionomer,O_2}}, \; L = L_{dye} + L_{ionomer} \tag{26}$$

As concentration of oxygen changes with the switch from nitrogen to air at the inlet, the emission intensity, I(t), changes with time. First intensity response of dye layer is evaluated and diffusion coefficient of dye layer is fit to equation 26. Diffusion coefficient evaluated from dye layer is used in the ionomer and dye composite layer which is fit in a similar manner with additional equation 27 to determine diffusion coefficient of oxygen in ionomer as a function of thickness.

5.3.3.3. Preliminary Thin Film O2 Permeability Results via Luminescent Quenching

Samples exhibit a reduction in intensity upon exposure to oxygen (introduction of air) as expected. Figure 5-19 shows an example of intensity response with gas switching. Ratio of intensity (I_{N2}/I_{air}) is commonly evaluated as a metric of photostability and sensitivity of the porphyrin in the host polymer to O_2. The ratio of intensity in this system is 2.2 to 2.8 and is within the ratio of 1.9 to 3 reported in the literature.[83,90,96]

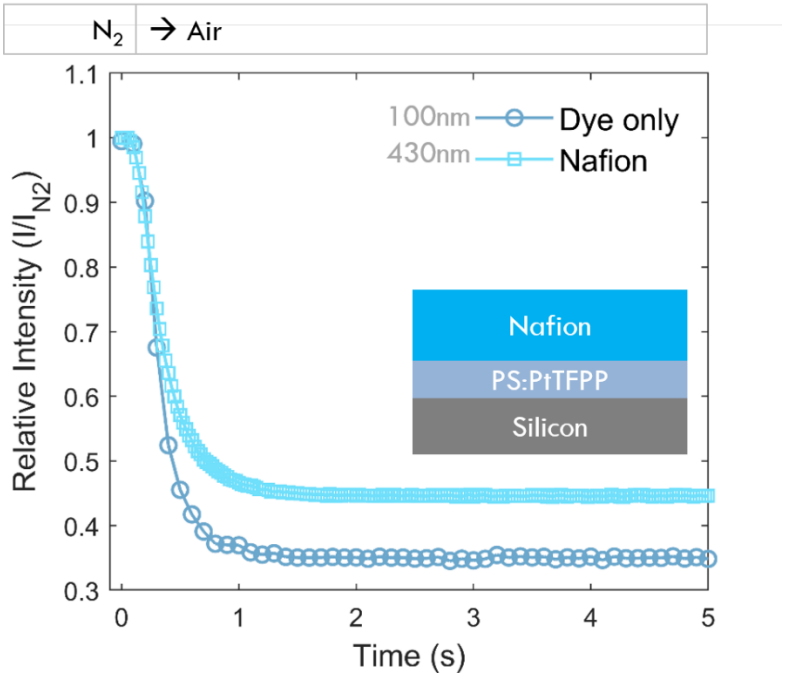

Figure 5-19: Time dependent intensity response to exposure to oxygen of intensity. Phosphorescence intensity response of dye layer containing porphyrin PtTFPP in polystyrene (PS:PtTFPP) and response of ionomer on dye two layer composite structure supported on Silicon substrate.

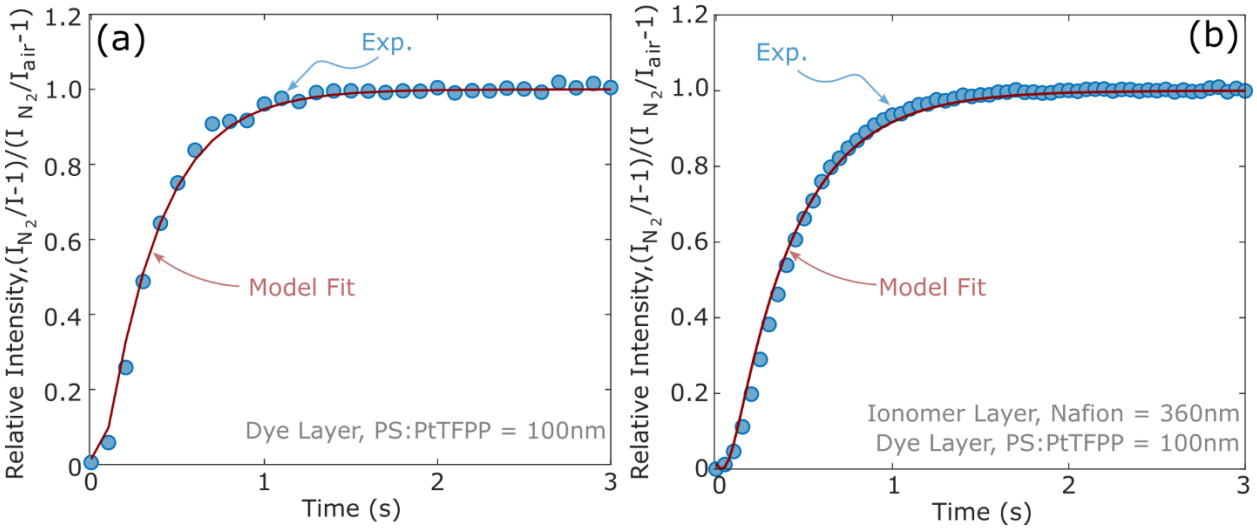

Figure 5-20: Example of phosphorescence time scan of (a)dye layer containing PtTFPP embeded in Polystyrene and (b) dye layer coated with Nafion ionomer of 360nm thickness. Experimental data (points) and model (line).

Figure 5-20 shows example transient phosphoresce intensity data fitted to the model discussed above. Model fit of diffusion coefficient of O_2 in dye layer and ionomer layer were for good agreement with experimental data. Diffusion coefficient of dye layer was captured prior to ionomer layer coating and dye/ionomer composite layer measurment. Diffusion of O_2 in PS:PtTFPP is $\Theta(10^{-10})$, which is 3 orders of magnitude lower than reported literature diffusion coefficient for polystyrene.[87,96] The reason for this could be over concentration of dye molecule in the polystyrene thin layer. High concentration of dye molecule may be localizing dye to the substrate/polystyrene interface, effectively increasing diffusion path length and reducing diffusion coefficient of polystyrene. Despite the discrepancy with dye layer diffusion coefficient, the diffusion coefficient of O_2 in the ionomer layer was an order of magnitude lower than literature data for bulk ionomer; as this is a dry system values are compared to dry bulk ionomer diffusion coefficient values (See Table 5-3).

Similar to the microelectrode method, this technique is still in preliminary stages of development. Therefore, more work is required to optimize experimental variables and determine sensitivity and reproducibility. One example of an unoptimized experimental component is the distance between switch gas and spectrophotometer cell. Additionally, pressure variability due to the switch gas is unknown. That is, it is not clear if pressure gradient between diffusing out nitrogen gas and diffusing in oxygen gas causes variability in luminescent intensity response. Overall though, the experimental advantages of using solid state structure of dye layer with ionomer to measure gas diffusion with minimal moving parts makes this method ideal for ionomer thin films and is the focus of ongoing work.

Table 5-3: Diffusion coefficient values calculated from time dependent luminescence quenching response.

Nafion	Dry Diffusivity (D) (cm^2/s) at 25ºC, dry conditions	
Bulk (178µm)	8.8×10^{-8}	Ref.[17]
360nm	8.98×10^{-9}	This Work
230nm	4.16×10^{-9}	This Work

5.4. References

(1) Schalenbach, M.; Hoefner, T.; Paciok, P.; Carmo, M.; Lueke, W.; Stolten, D. Gas Permeation through Nafion. Part 1: Measurements. J. Phys. Chem. C 2015, 119, 25145–25155.

(2) Kim, Y. S.; Lee, K.-S. Fuel Cell Membrane Characterizations. Polym. Rev. 2015, 55 (2), 330–370.

(3) Parthasarathy, A.; Martin, C. R. .; Srinivasan, S. Investigations of the O2 Reduction Reaction at the Platinum/Nafion® Interface Using a Solid-State Electrochemical Cell. J. Electrochem. Soc. 1991, 138 (4), 916.

(4) Parthasarathy, A.; Srinivasan, S.; Appleby, A. J.; Martin, C. R. . Temperature Dependence of the Electrode Kinetics of Oxygen Reduction at the Platinum/Nafion® Interface—A Microelectrode Investigation. J. Electrochem. Soc. 1992, 139 (9), 2530.

(5) Parthasarthy, A.; Srinivasan, S.; Appleby, A. J.; Martin, C. R. Electrode-Kinetics of Oxygen Reduction at Carbon-Supported and Unsupported Platinum Microcrystallite Nafion(R) Interfaces. J. Electroanal. Chem. 1992, 339, 101–121.

(6) Uribe, F. A. .; Springer, T. E. .; Gottesfeld, S. A Microelectrode Study of Oxygen Reduction at the Platinum/Recast-Nafion Film Interface. J. Electrochem. Soc. 1992, 139 (3), 765.

(7) Wilson, M. S. Membrane Catalyst Layer for Fuel Cells. US 5234777, 1993.

(8) Weber, A. Z.; Kusoglu, A. Unexplained Transport Resistances for Low-Loaded Fuel-Cell Catalyst Layers. J. Mater. Chem. A 2014, 2 (c), 17207–17211.

(9) Kongkanand, A.; Mathias, M. F. The Priority and Challenge of High-Power Performance of Low- Platinum Proton-Exchange Membrane Fuel Cells. J. Phys. Chem. Lett. 2016, 7, 1127–1137.

(10) Kongkanand, A.; Gu, W.; Mathias, M. F. Proton-Exchange Membrane Fuel Cells with Low-Pt Content. In Encyclopedia of Sustainability Science and Technology; 2018.

(11) Kusoglu, A. Ionomer Thin Films in PEM Fuel Cells. In Encyclopedia of Sustainability Science and Technology; Meyers, R., Ed.; Springer, New York, NY, 2018.

(12) Karan, K. PEFC Catalyst Layer: Recent Advances in Materials, Microstructural Characterization, and Modeling. Curr. Opin. Electrochem. 2017, 5 (1), 27–35.

(13) Cetinbas, F. C.; Ahluwalia, R. K.; Kariuki, N.; De Andrade, V.; Fongalland, D.; Smith, L.; Sharman, J.; Ferreira, P.; Rasouli, S.; Myers, D. J. Hybrid Approach Combining Multiple Characterization Techniques and Simulations for Microstructural Analysis of Proton Exchange Membrane Fuel Cell Electrodes. J. Power Sources 2017, 344, 62–73.

(14) Yampolskii, Y.; Pinnau, I.; Freeman, B. D. Materials Science of Membranes for Gas and Vapor Separation; 2006.

(15) Borka, K.; Ekdunge, P. Oxygen and Hydrogen Permeation in Bulk and Recast Films. J. Appl. Electrochem. 1997, 27, 117–123.

(16) Zhang, Z.; Chattot, R.; Bonorand, L.; Jetsrisuparb, K.; Buchmüller, Y.; Wokaun, A.; Gubler, L. Mass Spectrometry to Quantify and Compare the Gas Barrier Properties of Radiation Grafted Membranes and Nafion®. J. Memb. Sci. 2014, 472, 55–66.
(17) Chiou, J. S.; Paul, D. R. Gas Permeation in a Dry Nafion Membrane. 1988, No. Figure 5, 2161–2164.
(18) Catalano, J.; Myezwa, T.; De Angelis, M. G.; Baschetti, M. G.; Sarti, G. C. The Effect of Relative Humidity on the Gas Permeability and Swelling in PFSI Membranes. Int. J. Hydrogen Energy 2012, 37 (7), 6308–6316.
(19) Giacinti Baschetti, M.; Minelli, M.; Catalano, J.; Sarti, G. C. Gas Permeation in Perflurosulfonated Membranes: Influence of Temperature and Relative Humidity. Int. J. Hydrogen Energy 2013, 38 (27), 11973–11982.
(20) Ansaloni, L.; Minelli, M.; Giacinti Baschetti, M.; Sarti, G. C. Effect of Relative Humidity and Temperature on Gas Transport in Matrimid®: Experimental Study and Modeling. J. Memb. Sci. 2014, 471, 392–401.
(21) Sakai, T. Gas Permeation Properties of Solid Polymer Electrolyte (SPE) Membranes. J. Electrochem. Soc. 1985, 132 (6), 1328.
(22) Novitski, D.; Holdcroft, S. Determination of O2 Mass Transport at the Pt | PFSA Ionomer Interface under Reduced Relative Humidity. ACS Appl. Mater. Interfaces 2015, 7, 27314–27323.
(23) Kudo, K.; Jinnouchi, R.; Morimoto, Y. Humidity and Temperature Dependences of Oxygen Transport Resistance of Nafion Thin Film on Platinum Electrode. Electrochim. Acta 2016, 209, 682–690.
(24) Suzuki, T.; Kudo, K.; Morimoto, Y. Model for Investigation of Oxygen Transport Limitation in a Polymer Electrolyte Fuel Cell. J. Power Sources 2013, 222, 379–389.
(25) Buchi, F. N.; Wakizoe, M.; Srinivasan, S. Microelectrocle Investigation of Oxygen Permeation in Perfluorinatecl Proton Exchange Membranes with Different Equivalent Weights. J. Electrochem Soc. 1996, 143 (3), 927–932.
(26) Beattie, P. D.; Basura, V. I.; Holdcroft, S. Temperature and Pressure Dependence of O 2 Reduction at Pt Nafion ® 117 and Pt BAM ® 407 Interfaces. J. Electroanal. Chem. 1999, 468, 180–192.
(27) Basura, V. I.; Beattie, P. D.; Holdcroft, S. Solid-State Electrochemical Oxygen Reduction at Pt Nafion ® 117 and Pt BAM3G ™ 407 Interfaces. J. Electroanal. Chem. 1998, 458, 1–5.
(28) Sethuraman, V. a.; Khan, S.; Jur, J. S.; Haug, A. T.; Weidner, J. W. Measuring Oxygen, Carbon Monoxide and Hydrogen Sulfide Diffusion Coefficient and Solubility in Nafion Membranes. Electrochim. Acta 2009, 54 (27), 6850–6860.
(29) Gode, P.; Lindbergh, G.; Sundholm, G. In-Situ Measurements of Gas Permeability in Fuel Cell Membranes Using a Cylindrical Microelectrode. J. Electroanal. Chem. 2002, 518 (2), 115–122.
(30) Haug, A. T.; White, R. E. Oxygen Diffusion Coefficient and Solubility in a New Proton Exchange Membrane. J. Electrochem. Soc. 2000, 147 (3), 980–983.
(31) Tsou, Yu-Min; Kimble, M. C.; White, R. E. . Hydrogen Diffusion, Solubility and Water Uptake in SSC and Perflorocarbon Membra. J. Electrochem Soc. 1992, 139 (7), 1913–1917.
(32) Ogumi, Z.; Kuroe, T.; Takehara, Z. Gas Permeation in SPE Method. J. Electrochem Soc. 1985, 132 (11), 2601–2605.
(33) Cheng, X., Zhang, J., Tang, Y., Song, C., Shen, J., Song, D., & Zhang, J. Hydrogen

Crossover in High-Temperature PEM Fuel Cells. J. Power Sources 2007, 167 (1), 25–31.
(34) Mohamed, H. F. M.; Kobayashi, Y.; Kuroda, C. S.; Ohira, A. Free Volume and Gas Permeation in Ion-Exchanged Forms of the Nafion® Membrane. J. Phys. Conf. Ser. 2010, 225, 1–8.
(35) Ban, S.; Huang, C.; Yuan, X.-Z.; Wang, H. Molecular Simulation of Gas Adsorption, Diffusion, and Permeation in Hydrated Nafion Membranes. J. Phys. Chem. B 2011, 115 (39), 11352–11358.
(36) Cleghorn, S.; Kolde, J.; Liu, W. Advances in Electrocatalysis, Materials, Diagnostics and Durability. In Handbook of Fuel Cells: Fundamentals Technology and Applications; Wolf, V., Arnold, L., Hubert, G., Ed.; John Wiley & Sons, Ltd, 2003.
(37) Kusoglu, A.; Weber, A. Z. New Insights into Perfluorinated Sulfonic-Acid Ionomers. Chem. Rev. 2017, 117, 987–1104.
(38) Yeager, H. L.; Steck, A. Cation and Water Diffusion in Nafion Ion Exchange Membranes: Influence of Polymer Structure. J. Electrochem. Soc. 1981, 128 (9), 1880.
(39) Liu, H.; Epting, W. K.; Litster, S. Gas Transport Resistance in Polymer Electrolyte Thin Films on Oxygen Reduction Reaction Catalysts. Langmuir 2015, 31, 9853–9858.
(40) Nonoyama, N.; Okazaki, S.; Weber, A. Z.; Ikogi, Y.; Yoshida, T. Analysis of Oxygen-Transport Diffusion Resistance in Proton-Exchange-Membrane Fuel Cells. J. Electrochem. Soc. 2011, 158 (4), B416–B423.
(41) Mashio, T.; Ohma, A.; Yamamoto, S.; Shinohara, K. Analysis of Reactant Gas Transport in a Catalyst Layer. ECS Trans. 2007, 11 (1), 529–540.
(42) Mashio, T.; Iden, H.; Ohma, A.; Shinohara, K. Local Gas Transport in Catalyst Layers of PEM Fuel Cell. J. Electroanal. Chem. 2017, 790.
(43) Orfanidi, A.; Madkikar, P.; El-Sayed, H. A.; Harzer, G. S.; Kratky, T.; Gasteiger, H. A. The Key to High Performance Low Pt Loaded Electrodes. J. Electrochem. Soc. 2017, 164 (4), F418–F426.
(44) Owejan, J. P.; Owejan, J. E.; Gu, W. Impact of Platinum Loading and Catalyst Layer Structure on PEMFC Performance. J. Electrochem. Soc. 2013, 160 (8), 824–833.
(45) Ono;, Y.; Mashio, T.; Takaichi, S.; Ohma, A.; Kanesaka, H.; Shinohara, K. The Analysis of Performance Loss with Low Platinum Loaded Cathode Catalyst Layers. Electrochim. Acta 2010, 28 (27), 69–78.
(46) Sakai, K.; Sato, K. ; Mashio, T.; Ohma, A.; Yamaguchi, K.; Shinohara, K. Analysis of Reactant Gas Transport in Catalyst Layers ; Effect of Pt-Loadings. Trans. E C S Soc. Electrochem. 2009, 25 (1), 1193–1201.
(47) Chowdhury, A.; Radke, C. J.; Weber, A. Z. Transport Resistances in Fuel-Cell Catalyst Layers. ECS Trans. 2017, 80 (8), 321–333.
(48) Greszler, T. a.; Caulk, D.; Sinha, P. The Impact of Platinum Loading on Oxygen Transport Resistance. J. Electrochem. Soc. 2012, 159 (12), F831–F840.
(49) Kudo, K.; Morimoto, Y. Analysis of Oxygen Transport Resistance of Nafion Thin Film on Pt Electrode. ECS Trans. 2013, 50 (2), 1487–1494.
(50) Parthasarthy, A.; Srinivasan, S.; Appleby, A. J.; Martin, C. R. Electrode-Kinetics of Oxygen Reduction at Carbon-Supported and Unsupported Platinum Microcrystallite Nafion(R) Interfaces. J. Electroanal. Chem. 1992, 339 (1–2), 101–121.
(51) Chen, D.; Kongkanand, A.; Jorne, J. Proton Conduction and Oxygen Diffusion in Ultra-Thin Nafion Films in PEM Fuel Cell: How Thin? J. Electrochem. Soc. 2019, 166 (2), F24–F33.

(52) Darling, R. A Comparison of Models for Transport Resistance in Fuel-Cell Catalyst Layers. J. ofThe Electrochem. Soc. 2018, 165.
(53) Zhang, S.; Yuan, X.; Wang, H.; Me, W.; Zhu, H.; Shen, J.; Wu, S.; Zhang, J.; Merida, W.; Zhu, H.; et al. A Review of Accelerated Stress Tests of MEA Durability in PEM Fuel Cells. Int. J. Hydrogen Energy 2009, 34 (1), 388–404.
(54) Frank, B.; Gast, A. P.; Russell, T. P.; Brown, H. R.; Hawker, C. Polymer Mobility in Thin Films. Macromolecules 1996, 29 (20), 6531–6534.
(55) Modestino, M. A.; Paul, D. K.; Dishari, S.; Petrina, S. A.; Allen, F. I.; Hickner, M. A.; Karan, K.; Segalman, R. A.; Weber, A. Z. Self-Assembly and Transport Limitations in Con Fi Ned Na Fi on Films. Macromolecules 2013, 46, 867−873.
(56) Kusoglu, A.; Dursch, T. J.; Weber, A. Z. Nanostructure/Swelling Relationships of Bulk and Thin film PFSA Ionomers. Adv. Funct. Mater. 2016, 26, 4961–4975.
(57) Murphy, T. M.; Freeman, B. D.; Paul, D. R. Physical Aging of Polystyrene Films Tracked by Gas Permeability. Polym. (United Kingdom) 2013, 54 (2), 873–880.
(58) Huang, Y.; Paul, D. R. Effect of Film Thickness on the Gas-Permeation Characteristics of Glassy Polymer Membranes. Ind. Eng. Chem. Res. 2007, 46 (8), 2342–2347.
(59) Kodama, K.; Motobayashi, K.; Shinohara, A.; Hasegawa, N.; Kudo, K.; Jinnouchi, R.; Osawa, M.; Morimoto, Y. Effect of the Side-Chain Structure of Perfluoro-Sulfonic Acid Ionomers on the Oxygen Reduction Reaction on the Surface of Pt. ACS Catal. 2018, 8, 694–700.
(60) Masuda, T.; Sonsudin, F.; Singh, P. R.; Naohara, H.; Uosaki, K. Potential-Dependent Adsorption and Desorption of Perfluorosulfonated Ionomer on a Platinum Electrode Surface Probed by Electrochemical Quartz Crystal Microbalance and Atomic Force Microscopy. J. Phys. Chem. C 2013, 117 (30), 15704–15709.
(61) Nagao, Y. Proton-Conductivity Enhancement in Polymer Thin Films. Langmuir 2017, 33, 12547–12558.
(62) Ono, Y.; Nagao, Y. Interfacial Structure and Proton Conductivity of Nafion at the Pt-Deposited Surface. Langmuir 2016, 32, 352–358.
(63) Ohira, A.; Kuroda, S.; Mohamed, H. F. M.; Tavernier, B. Effect of Interface on Surface Morphology and Proton Conduction of Polymer Electrolyte Thin Films. Phys. Chem. Chem. Phys. 2013, 15 (27), 11494.
(64) Mann, R. F.; Amphlett, J. C.; Peppley, B. a.; Thurgood, C. P. Henry's Law and the Solubilities of Reactant Gases in the Modelling of PEM Fuel Cells. J. Power Sources 2006, 161 (2), 768–774.
(65) Merkel, T. C.; Pinnau, I. .; Prabhakar, R. .; Freeman, B. D. . Gas and Vapor Transport Properties of Perfuoropolymers. In Materials Science of Membranes for Gas and Vapor Separation; 2006; pp 251–270.
(66) Shimizu, R.; Park, Y.-C.; Kakinuma, K.; Iiyama, A.; Uchida, M. Effects of Both Oxygen Permeability and Ion Exchange Capacity for Cathode Ionomers on the Performance and Durability of Polymer Electrolyte Fuel Cells. J. Electrochem. Soc. 2018, 165 (6), F3063–F3071.
(67) Kimmerle, K.; Hofmann, T.; Strathmann, H. Analysis of Gas Permeation through Composite Membranes. J. Memb. Sci. 1991, 61, 1–17.
(68) Lai, Juin-yih; Yamada, Sumito; Kamide, Kenji; Manabe, Sei-ichi; Kawai, T. Gas Permeability of Composite Membranes. J. Appl. Polym. Sci. 1986, 32, 4625–4637.
(69) Pinnau, I.; Wijmans, J. G.; Blume, I.; Kuroda, T.; Peinemann, K.-V. . Gas Permeation

through Composite Membranes. J. Memb. Sci. 1991, 61 (C), 1–17.
(70) Sadrzadeh, M.; Amirilargani, M.; Shahidi, K.; Mohammadi, T. Gas Permeation through a Synthesized Composite PDMS/PES Membrane. J. Memb. Sci. 2009, 342 (1–2), 236–250.
(71) Merkel, T. C.; Bondar, V. I.; Nagai, K.; Freeman, B. D.; Pinnau, I. Gas Sorption, Diffusion, and Permeation in Poly (Dimethylsiloxane). J. Polym. Sci. Part B Polym. Phys. 2000, 38 (3), 415–434.
(72) Hägg, M.-B. Membrane Purification of Cl 2 Gas I. Permeabilities as a Function of Temperature for Cl 2 , O 2 , N 2 , H 2 in Two Types of PDMS Membranes. J. Memb. Sci. 2000, 170, 173–190.
(73) Lopez, J. L. .; Matson, S. L. .; Marchese, J. .; Quinn, J. A. . Diffusion Through Composite Membranes: A Two-Dimensional Analysis. J. Memb. Sci. 1986, 27.
(74) Henis, J. M. S.; Tripodi, M. K. Composite Hollow Fiber Membranes for Gas Separation: The Resistance Model Approach. J. Memb. Sci. 1981, 8 (3), 233–246.
(75) Dongping, Z.; Velmurugan, J.; Mirkin, M. V. Adsorption/Desorption of Hydrogen on Pt Nanoelectrodes: Evidence of Surface Diffusion and Spillover. J. Am. Chem. Soc. 2009, 131 (41), 14756–14760.
(76) Doña Rodríguez, J. M.; Herrera Melián, J. A.; Pérez Peña, J. Determination of the Real Surface Area of Pt Electrodes by Hydrogen Adsorption Using Cyclic Voltammetry. J. Chem. Educ. 2000, 77 (9), 1195.
(77) Zhan, D.; Velmurugan, J.; Mirkin, M. V. Adsorption / Desorption of Hydrogen on Pt Nanoelectrodes : Evidence of Surface Diffusion and Spillover. 2009, No. 9.
(78) Rao, C. R. K.; Trivedi, D. C. Chemical and Electrochemical Depositions of Platinum Group Metals and Their Applications. Coord. Chem. Rev. 2005, 249 (5–6), 613–631.
(79) Bard, F. Electrochemical Methods : Fundamentals and Applications; 2000; Vol. 30.
(80) Chlistunoff, J. Oxygen Permeability of Cast Ionomer Films from Chronoamperometry on Microelectrodes. J. Power Sources 2014, 245, 203–207.
(81) Lee, K.; Ishihara, A.; Mitsushima, S.; Kamiya, N.; Ota, K. Effect of Recast Temperature on Diffusion and Dissolution of Oxygen and Morphological Properties in Recast Nafion. J. Electrochem. Soc. 2004, 151 (4), A639.
(82) Williams, A. R. Introduction to Fluorescence Spectroscopy; 2000.
(83) Amao, Y. Probes and Polymers for Optical Sensing of Oxygen. Microchim. Acta 2003, 143, 1–12.
(84) Lakowicz, J. R. Quenching of Fluorescence. Princ. Fluoresc. Spectrosc. 2006, 3rd Editio, 277–330.
(85) Lee, S.-K.; Okura, I. Photoluminescent Determination of Oxygen Using Metalloporphyrin-Polymer Sensing Systems. Spectrochim. Acta, Part A Mol. Biomol. Spectrosc. 1998, 54A (1), 91–100.
(86) Köse, M. E.; Carroll, B. F.; Schanze, K. S. Preparation and Spectroscopic Properties of Multiluminophore Luminescent Oxygen and Temperature Sensor Films. Langmuir 2005, 21 (20), 9121–9129.
(87) Rharbi, Y.; Yekta, A.; Winnik, M. A. A Method for Measuring Oxygen Diffusion and Oxygen Permeation in Polymer Films Based on Fluorescence Quenching. Anal. Chem. 1999, 71 (22), 5045–5053.
(88) Yekta, A.; Masoumi, Z.; Winnik, M. A. Luminescence Measurements of Oxygen Permeation and Oxygen Diffusion in Thin Polymer Films. Can. J. Chem. 1995, 73 (11), 2021–2029.

(89) Wolfbeis, O.; Orellana, G.; Moreno-Bondi, M. C. Frontiers in Chemical Sensors: Novel Principles and Techniques; 2010.
(90) Amao, Y.; Okura, I. Optical Oxygen Sensor Devices Using Metalloporphyrins. ChemInform 2009, 13, 1111–1122.
(91) Xu, W.; Schmidt, R.; Whaley, M.; Demas, J. N.; DeGraff, B. A.; Karikari, E. K.; Farmer, B. L. Oxygen Sensors Based on Luminescence Quenching: Interactions of Pyrene with the Polymer Supports. Anal. Chem. 1994, 66, 4133–4141.
(92) Gregory, P. Industrial Applications of Phthalocyanines. J. Porphyr. Phthalocyanines 2000, 4, 432–437.
(93) Henning Tschiersch, Gregor Liebsch, A. S.; Rolletschek, L. B. and H. R. Planar Oxygen Sensors for Non Invasive Imaging in Experimental Biology. In Microsensors; 2011.
(94) Wolfbeis, O.; Orellana, G.; Moreno-Bondi, M. C. Frontiers in Chemical Sensors: Novel Principles and Techniques; 2010.
(95) Chowdhury, S.; Bhethanabotla, V. R.; Sen, R. Measurement of Oxygen Diffusivity and Permeability in Polymers Using Fluorescence Microscopy. Microsc. Microanal. 2010, 16 (6), 725–734.
(96) Lee, S.-K.; Okura, I. Photostable Optical Oxygen Sensing Material: Platinum Tetrakis(Pentafluorophenyl)Porphyrin Immobilized in Polystyrene. Anal. Commun. 1997, 34 (June), 185–188.

6. Summary and Future Directions

The current electrode interface structure in polymer electrolyte fuel cell (PEFC) is unable to meet low cost and long lifetime requirements necessary for high volume transportation application and widespread commercialization. Electrodes in PEFC are challenged with large kinetic over potentials that significantly hamper energy output, ohmic resistivity in separator electrolyte membrane and other components, and ion and gas transport losses that persist in the electrode at high current densities.[1] These challenges are also closely associated with electrode durability concerns that limit longevity of PEFC devices. Future research directions for the field has to therefore trend towards:

- Development of new electro catalyst with high activity performance in the membrane electrode assembly (MEA) improvement. Currently explored structures are showing 3 – 20x activity improvements in the lab but struggle to be sustainable once implemented in an electrode structure.[2]
- Improvement of chemical and structural stability of electrocatalyst with and minimal degradation issues and sustained activity. Current lifetime hours for PEFCs for automotive applications are < 4000h need to be raised significantly to ensure affordable stretch target of $30/kW.[1] Efforts tackling carbon support corrosion, platinum particle growth and dissolution are also critical to increase electrode utilization and achieve increased technology adoption.
- Enhancement in conductivity for existing micrometers thick, bulk ionomer, electrolyte separator perflourosulfonic acid (PFSA) in low humidity conditions (20-50% humidity) and during start/stop events.[3] Minimization of thermo-chemical-mechanical degradation in PFSA, without losing dimensional swellability or conductivity.
- Advancement of synthesis and characterization of more ordered alternative ionomer membranes with structures that are directly correlated with function (proton conductivity and gas transport).[4] Increased research effort to improve chemical and mechanical stability of these alternative electrolytes over a wide range of temperature is also necessary for high temperature operation and thermo-stability.
- When it comes to the nanometer-thin ionomers utilized in the electrode, new and alternative chemistries and structures are needed to improve ion conductivity while increasing gas permeability. More oriented structures with large backbone structures have been postulated as the ideal ionomer thin film to improve in-plane conductivity and through plane permeation to active platinum (Pt) sites.[5]
- Increase in fundamental understanding of interface at the ionomer thin film/Pt active site and link between ex-situ studies to operation relevant conditions (humidity, gas, temperature and potential) is necessary for elucidating factors necessary for alleviation of transport losses. [1,6]
- Modeling aided improvement to MEA structure visualization techniques and increase in in-situ and ex-situ quantification methods for ionomer, carbon (C), Pt distribution and accessibility can better inform electrode utilization and offer design parameters for improved structure.[7]
- The research direction above can also inform ionomer and ink processing technique for more systematic correlations between electrode structure and performance metrics.[8]
- Hurdles also exist outside of the technological barriers of the PEFC device including lacking fuel supply structure, non-robust component supply base, fluctuating and volatile nature of source of precious metal group, high cost of membranes, lacking local manufacturing

infrastructure and significant policy and market structures that can only be shifted through economies of scale.[9,10]

In this dissertation work, an attempt has been made to tackle some of the fundamental research needs laid above. Work focused significantly focused on addressing insights needed to improve gas transport performance of electrode, especially at the ionomer/electrode interface. This work is predominantly accomplished by employing an ex-situ methodology utilizing a model system of ionomer supported on substrate (electrode). The central approach applied in this work was the process-structure-property scheme; utilized to elucidate underlying ionomer physics and phenomenon and in order to understand the cyclic relationship between these three aspects. (See Figure 6-1) Experiments were designed to alter processing aspects of ionomer like it's chemistry, thickness, supporting substrate, heat treatment to mimic the state or condition at which ionomer thin film may exist in the electrode. As a result of these processing changes, structure responds with intrinsic markers that captures the morphology of the ionomer (like degree of phase separation, domain spacing, chain stiffness, etc.). This structure is the direct influencer of the critical functions and properties required for performance. This seemingly linear path is actually cyclic. Processing factors necessary for required property may not necessarily derive from the same specific structural origin. For instance, Chapter 4 showed that both the addition of monovalent cations into ionomer thin film and the reduction of ionomer to a confined thickness of ~20nm resulted increase stored mechanical energy (modulus). However, the structural origins of the observed property are slightly different; the former is driven by loss in phase separation and increase in chain stiffness with increase in cation size while the latter is driven by lack of phase separation due to confinement and increased interaction with substrate. These three aspects (process-structure-property) are also present in real electrodes. Electrode functions dictated by C, Pt and ionomer distribution, ionomer binder adhesion and orientation is dependent on processing conditions like nature of ink solvent, ionomer/C/Pt loading content and coating technique which results in different ionomer aggregation structures in solution form and variability in ionomer structure ultimately formed.[8,11,12] The negotiation between process, structure and property dictates the resultant structural state and functional prospects of the material under consideration (ionomer thin film in this case).

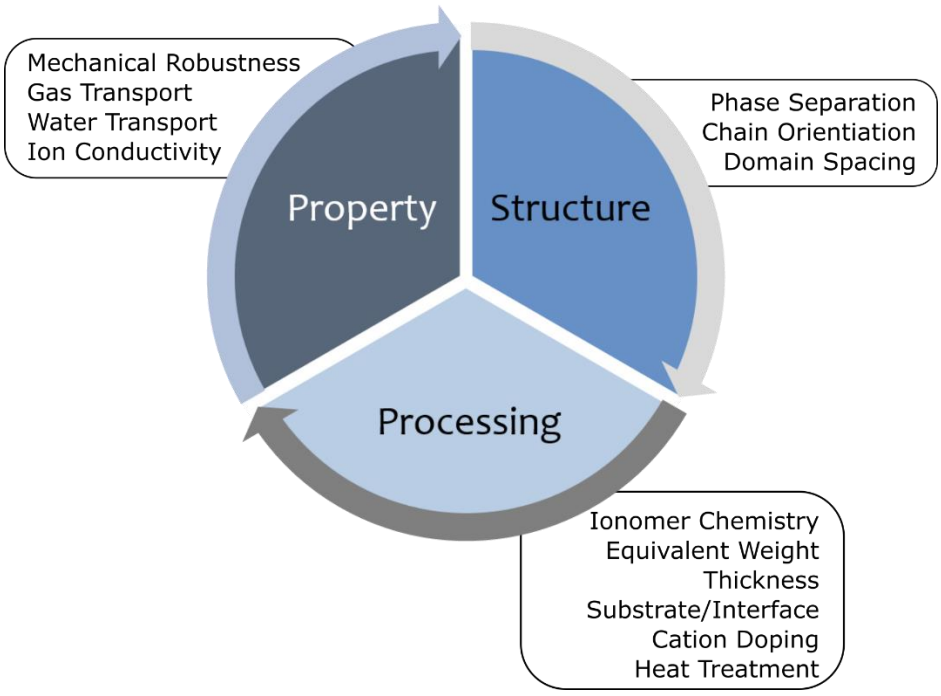

Figure 6-1: Processing-Structure-Property relationship in ionomer thin film employed in electrodes of fuel cells and other electrochemical devices.

6.1. Summary of Findings

Thin film polymers are critical and versatile components utilized in a wide range of applications including PEFCs. The underlying drivers behind the properties of these thin ionomer films was of interest in this work. Ionomers of thickness < 100 nm are used in catalyst layers of PEFCs serving to bind the catalytic Pt on C nanoparticles. Unfortunately, thin film ionomers contribute between 60 to 80% of the total observed mass-transport losses attributed to the catalyst layer, which is associated with reactant gas transport resistance at the Pt/ionomer interface, transport loss through the ionomer thin film, and at the ionomer/gas interface.[1] In addition, these resistances have been shown to increase with decrease in Pt loading in the catalyst layer, which limits PEFC cost reduction.[1] This work aimed to understand source of this transport resistance by exploring the impact of confinement on ionomer thin film property. The four main chapters in this dissertation examined substrate effect, relaxation dynamics, cation effect and ultimately quantified ionomer thin film gas transport via multiple methods. Confinement induced deviation of polymer thin film behavior from that of bulk can be one possible reason for increased resistance of ionomers thin films in the catalyst layer. Combining these chapters new understanding of effect of confinement on performance can be gained.

Examination of the impact of interfaces by using ionomers supported on different substrates, was first. Substrate-ionomer interaction was tuned via reducing and oxidizing environment mimicking anodic and cathodic environment at the electrode interface. Swelling behavior of ionomer thin films (~50nm) spin coated onto the Pt support were exposed to both H_2 and Air.[13] Findings indicate lower uptake, increased densification of ionomer matrix, and increased rate in relative humidity induced aging in a reducing environment as compared to oxidizing and inert environment. Underlying Pt surface interaction with reducing environment causes water phase and

ionomer to segregate, reducing effective water retention. However, in oxidizing environment, polar interaction at the Pt interface allows long range coordination with hydronium ions and sulfate end groups to allow strong water networks to percolate further into ionomer phase.

Next, impact of cooperative motion and chain dynamics was explored via thermal expansion study of nano-confined ionomers. Change in thermal transition temperature is key marker of stiffness and polymer chain mobility and has direct implications on ease of gas transport through polymer films. To explore this phenomenon, thermal transition temperature in ionomers supported on silicon substrate were evaluated as a function of thickness.[14] Increase in thermal transition temperature in ionomers is observed with decrease in thickness. In addition, alteration of intermolecular forces in acid form ionomer was conducted via exchange with metal cations. In the later scenario thermal transition temperature remained constant as a function of thickness. Findings here point to the balanced effect of increased chain mobility at free surface and hindered motion at the positively interacting substrate interface which results in reduced chain mobility required for ease of gas transport through ionomer matrix. This balance is additionally impacted by intermolecular forces within ionomer as the trade-off between high degree of hydrogen bonding freedom at the interfaces is dominated by strong ionic network with the addition of cations into the ionomer matrix.

Cations in ionomer thin films are considered in Chapter 3 as yet another parameter of processing that can be tuned to alter ionomer thin film property. For monovalent cations with varying cation size and Lewis acid strength, water content showed inverse relationship with the former and direct relationship with the later. Hydration is reduced by the increase in mechanical strength upon cation exchange, which is a result of solvation and thermodynamic energy equilibrium in the ionomer matrix. Findings laid a strong baseline for further exploration into impact of divalent contaminant and additive cations in PEFC. Monovalent cations follow a somewhat consistent cation-size and LAS dependent trend, however, divalent cations, especially transition metals, exhibit various non-single parameter dependencies that limit extrapolation toward few single parameters. The culmination of the surface, confinement and cation type dependent trends need to be validated with explicitly quantified gas transport resistance metric. Quantification of ionomer gas transport property is carried out in three separate methods that account for variable pertinent conditions for operation (temperature, humidity and potential). Methods under exploration show great promise and reflect an order of magnitude reduction in gas permeability for thin films of thickness relative to the bulk ionomer membrane counterparts. In depth work is currently underway as it is essential for clarifying gas and ion transport in PEFC.

6.2. Future Work

To address the remaining goals of establishing relationship between ionomer thin film structure and property for improving material and catalyst-layer design, few directions are already underway and some are envisioned as described below.

6.2.1. Substrate Dependent Relaxation Dynamics of Ionomer Thin Films

Chapter 3 examined confinement induced impediments to relaxation on silicon substrate. There is a clear impact of substrate on mechanical property, long-range polymer-chain motion and gas permeability. However, other pertinent substrates (Pt, C) have not been explored. A recent study by Chi and coworkers indicated negative expansion of Nafion ionomer on metal substrates and enhanced positive expansion on carbon supports.[15] Study of ionomers cast on Pt and C support

will be conducted to ensure if similar behaviors are also observed. If interaction with Pt and C substrate is the main driver for observed relaxation dynamics, dependence on sidechain concentration (i.e. equivalent weight, EW) should be significantly more pronounced. Therefore, thermal expansion of ionomer thin film of various side-chain length and EW will be studied on model systems of flat Pt and C substrate via heated cell ellipsometry.

6.2.2. Continued Work on Impact of Cation on Ionomer Thin Film Properties

Chapter 4 was predominantly focused on the impact of monovalent cation effect on ionomer thin film structure, water uptake and mechanical property. Although from a fundamental point of view understanding of size and Lewis acid strength dependent behavior of monovalent cations on ionomer thin film is useful, introduction of cations from leached electrocatalysts (Co^{2+}, Ni^{2+}) and additives were not fully considered to the same extent. Initial exploration into co-alloy leaching indicated significantly higher uptake than H^{+}, owing to more negative hydration energy. Results can provide insight into effect of leached co-alloy cations on ionomer performance in fuel cell catalysts and has implications for MEA manufacturing and processing, an area of great interest for further exploration.

6.2.3. Continued Work on Gas Permeation through Ionomer Thin Film

Chapter 5 discussed various methodologies currently employed to measure ionomer thin film gas permeability. Three different methodologies have been established in this work, with the first being the constant volume variable pressure gas permeability. This method used a composite layer methodology where the resistive thin film ionomer is supported by highly permeable supporting layer. Findings reflect that accurately capturing dry gas permeability of thin and ultra-thin film ionomers is a delicate and challenging effort. However, microelectrode technique and oxygen luminescent quenching method do not share the same vulnerabilities and will continue to be employed. Together the techniques will capture potential dependent and potential independent intrinsic permeability which is critical for capturing ionomer thin film transport resistance under operation relevant conditions. Ionomers are highly hygroscopic and sorption of water increases gas permeability. Water in ionomer membranes can coordinate around the sulfonic-acid groups increasing the size of the ionic region and connecting hydrophilic domains, thereby providing additional transport channels through the membrane. In addition, water plasticizes ionomers to relax polymer chains and increase free volume. Although, preliminary work discussed in Chapter 5 was only focused on dry gas permeation and fully saturated permeation for microelectrode, gas transport as a function of humidity and temperature is work underway.

6.2.4. Relationship between Processing Conditions and Ionomer Thin Film Properties

The impact of processing method, storing condition, and operating environment on thin PFSA ionomer coatings used in electrodes of electrochemical devices is unclear and not established. While some environmental conditions intrinsic to device operation (such as hydration) are necessary to maintain PFSA functionality, they can also permanently alter structure and subsequently functionality over time.[16–18] In this on-going work, exposure to elevated temperature and humidity (hygrothermal ageing) is used to alter the orientation of the ionomer's nano-domains parallel to the support. Current findings reflect strong inverse correlation between ageing-induced ionomer thin film domain orientation and water transport time constant evaluated via swelling kinetics. Results suggest prolonged exposure to high humidity and temperatures alter an ionomer's

nanostructure, its response to environmental stimuli, and its subsequent functionality in energy devices. This current work is under review for publication. Outside of the role of hygrothermal ageing, other conditions like solvent annealing are employed to access different nanostructures in di-block co-polymers.[19] Future, work will involve different processing conditions including employment of solvents that preferentially interact with hydrophilic phase of ionomer to induce and lock-in different morphological structures and correlate these structural parameters with properties like ion conductivity.

6.3. References

(1) Kongkanand, A.; Gu, W.; Mathias, M. F. Proton-Exchange Membrane Fuel Cells with Low-Pt Content. In Encyclopedia of Sustainability Science and Technology; 2018.

(2) Stamenkovic, V. R.; Strmcnik, D.; Lopes, P. P.; Markovic, N. M. Energy and Fuels from Electrochemical Interfaces. Nat. Mater. 2016, 16 (1), 57–69.

(3) Mathias, M. F.; Makharia, R.; Gasteiger, H. A.; Conley, J. J.; Fuller, T. J.; Gittleman, C. J.; Kocha, S. S.; Miller, D. P.; Mittelsteadt, C. K.; Xie, T.; et al. Two Fuel Cell Cars In Every Garage ? Electrochem. Soc. Interface 2005.

(4) Miller, A. D.; Gervais, M.; Krishnamurthy, J.; Dyers, L.; Zhu, X.; Potrekar, R.; Fei, X.; Weber, A.; Kerr, J. B. Polymer Materials for Charge Transfer in Energy Devices. ACS Symp. Ser. 2012, 1096, 165–174.

(5) Kongkanand, A.; Mathias, M. F. The Priority and Challenge of High-Power Performance of Low- Platinum Proton-Exchange Membrane Fuel Cells. J. Phys. Chem. Lett. 2016, 7, 1127–1137.

(6) Kusoglu, A. Ionomer Thin Films in PEM Fuel Cells. In Encyclopedia of Sustainability Science and Technology; Meyers, R., Ed.; Springer, New York, NY, 2018.

(7) Cetinbas, F. C.; Ahluwalia, R. K.; Kariuki, N.; De Andrade, V.; Fongalland, D.; Smith, L.; Sharman, J.; Ferreira, P.; Rasouli, S.; Myers, D. J. Hybrid Approach Combining Multiple Characterization Techniques and Simulations for Microstructural Analysis of Proton Exchange Membrane Fuel Cell Electrodes. J. Power Sources 2017, 344, 62–73.

(8) Hatzell, K. B.; Dixit, M. B.; Berlinger, S. A.; Weber, A. Z. Understanding Inks for Porous-Electrode Formation. J. Mater. Chem. A 2017, 5 (39), 20527–20533.

(9) Satyapal, S. Hydrogen & Fuel Cells Program Overview. In DOE Annual Merit Review; 2011.

(10) Staffell, I.; Scamman, D.; Abad, A. V.; Balcombe, P.; Dodds, P. E.; Ekins, P.; Shah, N.; Ward, K. R. The Role and Status of Hydrogen and Fuel Cells across the Global Energy System. Energy Environ. Sci. 2019.

(11) Doo, G.; Lee, J. H.; Yuk, S.; Choi, S.; Lee, D. H.; Lee, D. W.; Kim, H. G.; Kwon, S. H.; Lee, S. G.; Kim, H. T. Tuning the Ionomer Distribution in the Fuel Cell Catalyst Layer with Scaling the Ionomer Aggregate Size in Dispersion. ACS Appl. Mater. Interfaces 2018, 10 (21), 17835–17841.

(12) Kim, Y. S.; Welch, C. F.; Mack, N. H.; Hjelm, R. P.; Orler, E. B.; Hawley, M. E.; Lee, K. S.; Yim, S.-D.; Johnston, C. M. Highly Durable Fuel Cell Electrodes Based on Ionomers Dispersed in Glycerol. Phys. Chem. Chem. Phys. 2014, 16 (13), 5927–5932.

(13) Tesfaye, M.; MacDonald, A. N.; Dudenas, P. J.; Kusoglu, A.; Weber, A. Z. Exploring Substrate/Ionomer Interaction under Oxidizing and Reducing Environments. Electrochem. commun. 2018, 87, 86–90.

(14) Tesfaye, M.; Kushner, D. I.; McCloskey, B. D.; Weber, A. Z.; Kusoglu, A. Thermal Transitions in Perfluorosulfonated Ionomer Thin films. ACS Macro Lett. 2018, 1237–1242.
(15) Zhang, C.; Davies, M.; Karan, K. Probing Interfacial Interactions of Nafion Ionomer: Thermal Expansion of Nafion Thin Films on Substrates of Different Hydrophilicity/Hydrophobicity. J. Polym. Sci. Part B Polym. Phys. 2019, 57 (6), 343–352.
(16) Naudy, S.; Collette, F.; Thominette, F.; Gebel, G.; Espuche, E. Influence of Hygrothermal Aging on the Gas and Water Transport Properties of Nafions Membranes. J. Memb. Sci. 2014, 451, 293–304.
(17) Shi, S.; Dursch, T. J.; Blake, C.; Mukundan, R.; Borup, R. L.; Weber, A. Z.; Kusoglu, A. Impact of Hygrothermal Aging on Structure/Function Relationship of Perfluorosulfonic-Acid Membrane. J. Polym. Sci. Part B Polym. Phys. 2016, 54, 570–581.
(18) Shi, S.; Chen, G.; Wang, Z.; Chen, X. Mechanical Properties of Nafion 212 Proton Exchange Membrane Subjected to Hygrothermal Aging. J. Power Sources 2013, 238, 318–323.
(19) Jung, Y. S.; Ross, C. A. Solvent-Vapor-Induced Tunability of Self-Assembled Block Copolymer Patterns. Adv. Mater. 2009, 21 (24), 2540–2545.

A. Appendix: Spectroscopic Ellipsometry Expanded

1. Methodology and Background:

Ellipsometer is an optical method that utilizes change in elliptically polarized light to evaluate parameters like thickness, index of refraction, absorbance, etc. of planar materials. The concept of utilizing elliptically polarized light dates back around the 1800s but the extent of utilization of ellipsometer as a technique peaked with semi-conductor industry over the last 70-80 years. Ellipsometer is one of the most well-known optical methods that is non-destructive, versatile in its concurrent combination with various experimental set-ups, storage conditions and measurement environments. Principle of operation of spectroscopic ellipsometry involves a light source followed by a polarized light generator sending elliptically polarized with well-known coordinates light to object of interest (See Fig A-1a). Light from the source is linearly polarized in two orthogonal planes (p,s). The s-direction stands thereby perpendicularly to the plane of incidence while p-plane is parallel to it (Fig A-1 b). This polarized light can be reflected, transmitted, scattered and diffused as it travels through the object. In the rotating analyzer configuration mode, which is a common configuration, reflected and transmitted light from sample is elliptically polarized as it travels through a rotating polarization state analyzer and reaches the detector where the light, converted to electronic signal, is recorded as a function of the rotation angle (α) as shown in Fig. A-1a. Assuming polarization of incident light is retained, input polarization leaving the source is compared with output polarization received by detector to determine polarization change and extract intrinsic parameters.

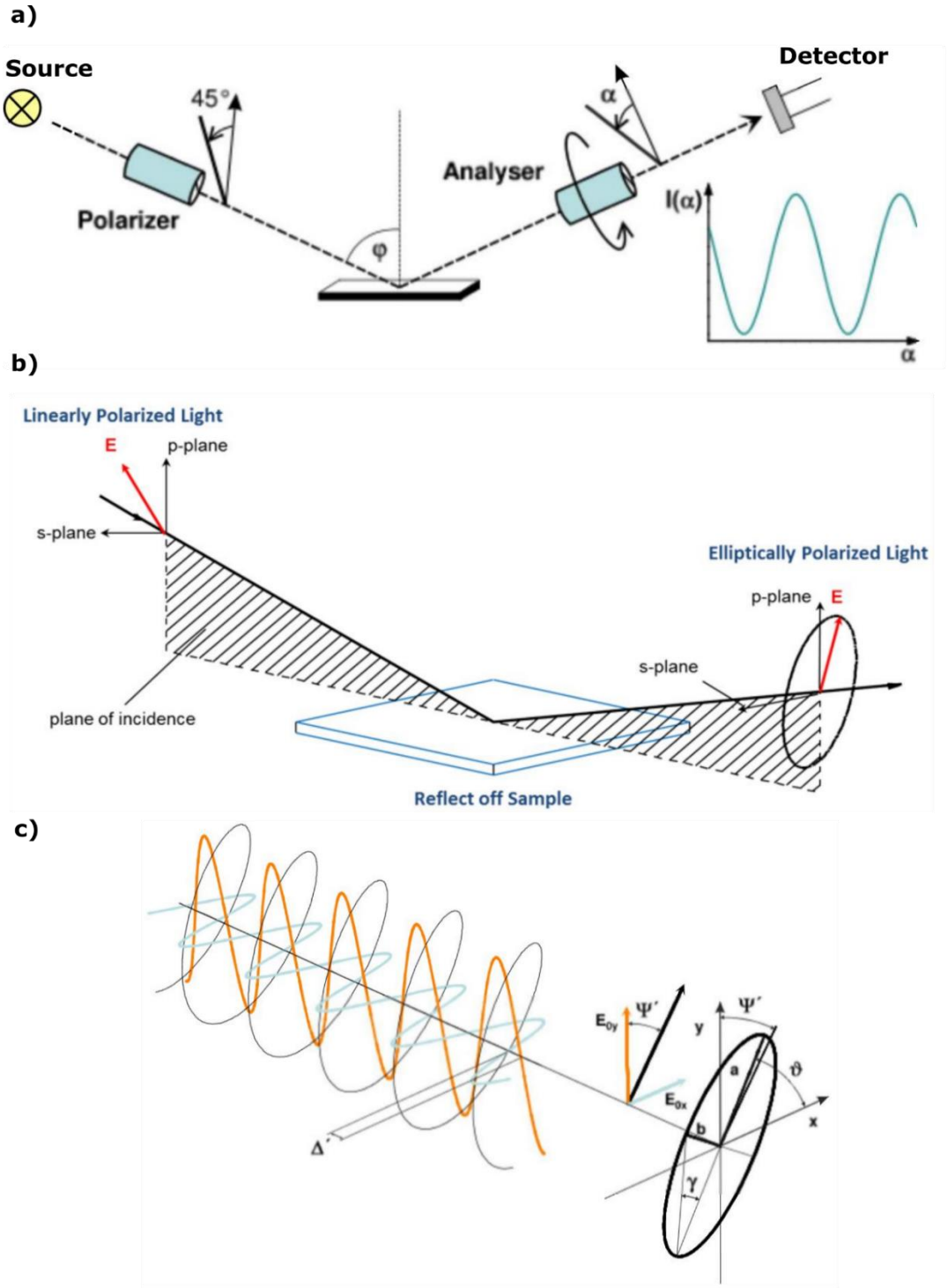

Figure A-1 (a) Principal of a rotating analyzer ellipsometer. (b) The incident light is linear with both p- and s- components. The reflected light has undergone amplitude and phase changes for both p- and s- polarized light, and ellipsometry measures their changes. (c)Elliptically polarized light and the projected polarization ellipse.

2. Data Fitting Using Model

A few assumptions are a given in this method: (1) since incident light is linearly polarized, optical effects are addressed separately at each wavelength(λ) in a monochromatic or quasi-monochromatic approximation, (2) due to much larger distances between source and receiver, objects are assumed to be interacting with light independently and propagating in forward direction, effects due interaction and coherence of light are neglected, (3)surrounding medium of propagation is assumed to be homogenous and isotropic.

In ellipsometry, orthogonally polarized light can be described mathematically using wave vectors in x and y cartesian coordinates**.** Figure A-1c shows general case of an elliptical polarization where E_{0x} and E_{0y} are amplitudes of wave vectors whose relative ratio gives Ψ the phase angle difference of the x and y component of the wave vector provide the other term Δ**.** The oscillations of Ψ and Δ are a result of the constructive interference of light within the sample as it undergoes multiple reflections. As illustrated, Fig A2 shows measured change in amplitude of polarized reflected and incident beam **(**Ψ) and their phase difference Δ**.** Ψ and Δ responses measured by rotating analyzer are related to the index of refraction and thickness via Fresnel reflection coefficients and Snell's law. Ratio of complex Fresnel internal reflection coefficients r_p and r_s are related to Ψ and Δ using the relationship (1). r_p and r_s are related to index of refraction of the sample(n_1) and index of refraction of medium (n_0) and angle of incidence of incident beam($\emptyset_0$) and angle of propagation of transmitted beam($\emptyset_1$) as given in (2) and (3). Index of refraction of the sample (n_1) and index of refraction of medium (n_0) are correlated by Snell's law in equation (4). At a given wavelength (λ) and angle of incidence, imaginary part of reflection coefficient is related to optical thickness or phase thickness (β) given by equation (5). Initial guess of film thickness and refractive index is used to calculate phase thickness and reflection coefficient and iterated until an adequate model found. Optical dispersion and index of refraction is a function of wavelength. For transparent thin films, relationship between wavelength and index of refraction in the sample is given by Cauchy equation in equation (6) where A, B and C are model fitting constants. Model fit given in Fig 2 showed a good fit of mean squared error (MSE) of 1.73 with this model.

$$\frac{r_p}{r_s} = tan\,\Psi\ e^{-i\Delta} \tag{1}$$

$$r_s = \frac{n_0 cos\,\emptyset_0 - n_1 cos\,\emptyset_1}{n_0 cos\,\emptyset_0 + n_1\,cos\,\emptyset_1} \tag{2}$$

$$r_p = \frac{n_1 cos\,\emptyset_0 - n_0 cos\,\emptyset_1}{n_1 cos\,\emptyset_0 + n_0\,cos\,\emptyset_1} \tag{3}$$

$$n_0\,sin\,\emptyset_0 = n_1\,sin\,\emptyset_1 \tag{4}$$

$$\beta = 2\pi\,\frac{l}{\lambda}\sqrt{{n_1}^2 - {n_0}^2\,sin^2\,\emptyset_0} \tag{5}$$

$$n_1\,(\lambda) = A + \frac{B}{\lambda^2} + \frac{C}{\lambda^4} \tag{6}$$

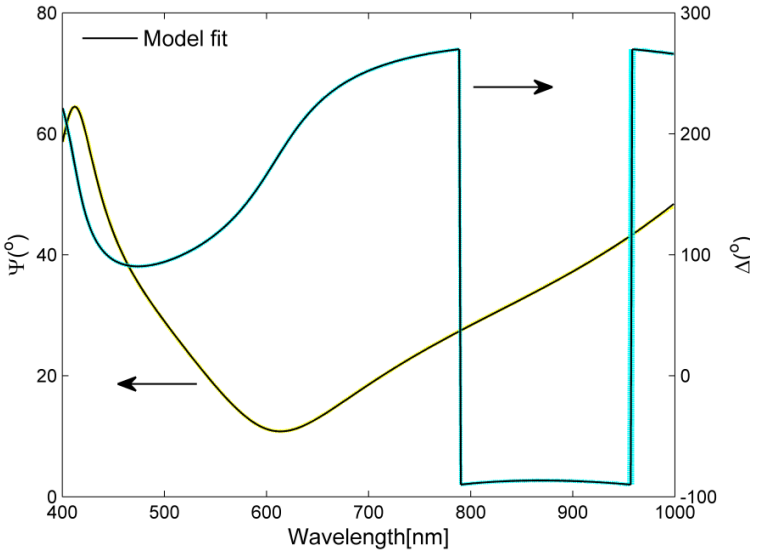

Figure A-2: An example of data fitting using Cauchy model for l = 310.68nm with a 3.7nm SiO2 layer and MSE =1.73.

B. Appendix: Quartz Crystal Microbalance Expanded

Mass uptake measurements in this thesis were all conducted by using Inficon's research quartz crystal microbalance (QCM). QCM is piezoelectric based ultrasensitive device that detects change is mass. It consists of a thin disk (usually 1" in diameter) single crystal quartz, a metal sensing electrode and contact electrode deposited on each side of the disk. Electrodes are commonly coated with gold, but can also be coated with platinum, silver, aluminum and titanium. Quartz crystal is made out a slab of crystal of quartz and that creates acoustic wave perpendicular to the surface of the crystal as a result of an applied electrical potential. Therefore, QCM, once powered, electrodes generate the electrical energy necessary to oscillate the quartz crystal, the resultant oscillation frequency is recorded by frequency counter that uses digital conversion to monitor frequency in real time.

Each type of QCM crystal has a resonant oscillation frequency of the fundamental mode. Resonant frequency includes the oscillation of the crystal, electric and mechanical oscillations. Resonant frequency depends on the thickness, chemical structure shape and mass of the quartz crystal. When crystal is used with no loading, resonance frequency is also dependent on density, shear modulus and shear modulus of the media. Up on detection of mass resonant frequency of loaded crystal is measured. The change in frequency (Δf) is proportional to the mass detected on the surface of the crystal. QCM can measure mass changes between ng/cm^2 to 100μg/cm^2. Mass detected can be given by the saurberry equation which assumes that any additional film deposited on the crystal has same acousto-elastic properties as the quartz. This assumption has been shown to be sufficient for uniform, rigid, thin film deposits.

$$\Delta m = -\frac{\Delta f}{C_f} \tag{1}$$

$$\Delta f = f_q - f \tag{2}$$

$$C_f = \frac{2n \times f^2}{\sqrt{\rho_q \times \mu_q}} \tag{3}$$

Where μ_q effective piezoelectrically stiffened shar modulus of quartz crystal, n is number of the harmonic at which the crystal is driven, and ρ_q, density of quartz.

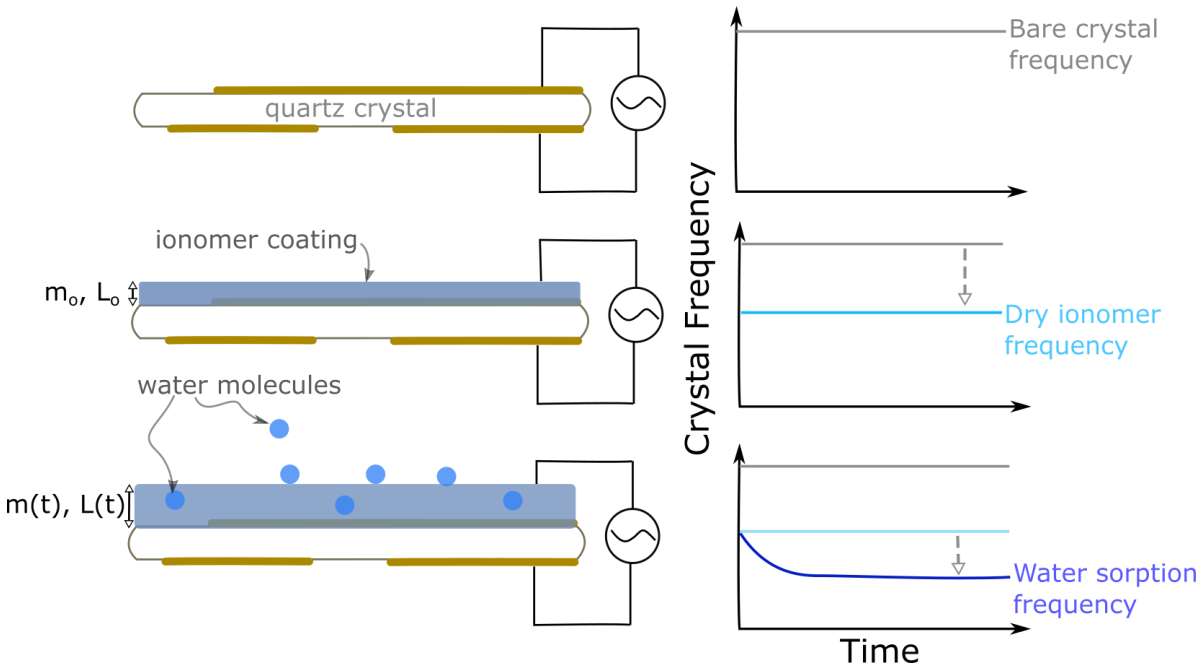

Figure B-1: Schematic of operational QCM bare crystal, crystal with ionomer loading and during water sorption.

In this work Au coated and Pt coated QCM have been utilized. Uniform coating of ionomer is achieved via spin-coating. To measure the mass associated with water taken up by ionomer, damped resonant frequency associated with ionomer coating has to be separated from depression in frequency associated with water uptake. As a result, mass of water sorbed has is referenced from both unloaded bare crystal frequency as well as dry ionomer coated frequency. Amout of water taken up by ionomer can be calculated via:

$$\text{Mass Uptake (\%)} = \frac{m_{uptake} - m_{dry}}{m_{dry}} \times 100 = \frac{\Delta f_{RH,ionomer} - \Delta f_{dry\ ionomer}}{\Delta f_{dry\ ionomer}} \times 100 \quad (4)$$

C. Appendix: Bulk PFSA Gas Permeability

Table C-1: Summary of measured membranes and their activation energy including literature values

Type of Membrane		EW (g/mol SO_3)	IEC (meq/g)	Permeability (Barrer)[+,++]			Activation Energy (kJ/mol)			Ref.
				H_2	O_2	N_2	H_2	O_2	N_2	
Nafion	N112[*]	1100	0.91	8.47 ± 0.37	1.19 ± 0.05	0.29 ± 0.01				This Work
				8.14	1.23					[1]
	N117[*]	1100	0.91	9.48 ± 0.32	-	0.30 ± 0.01				This Work
				9.30	1.08	0.26		24.60	28.2	[2,3]
	N212	1100	0.91	8.16 ± 0.18	1.17 ± 0.03	0.26 ± 0.01	34.77	33.44		This Work
				10.7	1.2		20.40	30.50		[4]
	N1500	1500	0.67	9.48 ± 0.32	1.81 ± 0.06	-				This Work
3M Ionomer	3M 725	725	1.38	5.21 ± 0.20	0.60 ± 0.02	-	23.03	29.02		This Work
	3M 825	825	1.21	6.55 ± 0.25	-	-	23.65	-		This Work
	3M 1000	1000	1.00	6.60 ± 0.27	0.98 ± 0.04	-	24.23	-		This Work
Aquivion	Aquivion 870	870	1.15	7.35 ± 0.23	0.98 ± 0.03	-	23.01	-		This Work
		860	1.16					34.5	41.7	[5]
	Aquivion 980	980	1.02	8.02 ± 0.31	1.26 ± 0.05	-		-		This Work
	PTFE	-	-	13	4.5	1.9	21.34	19.04	24.3	[6]
	PDMS	-	-	890	800	400	-	-	-	[7]

[+] Permeability values reported at T = 35°C. [++] 1 Barrer = 10^{-10} cm^3(STP) cm/(cm^2 s cmHg)

[*] Extruded Membranes

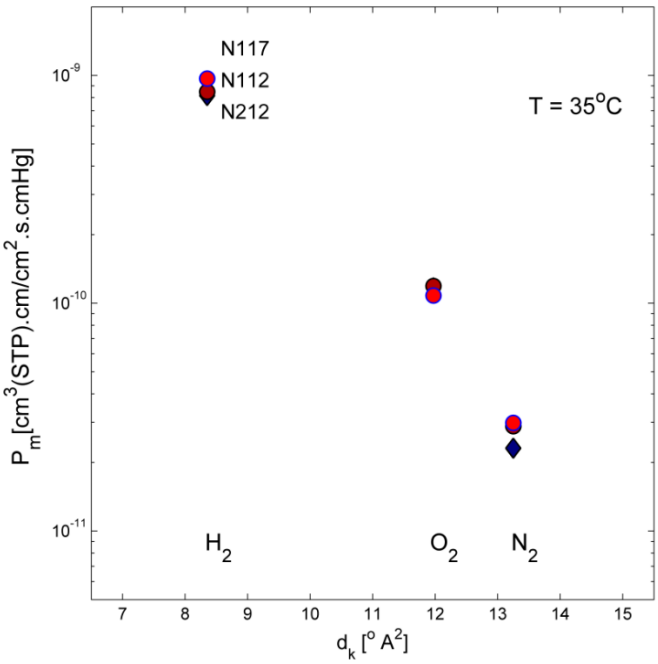

Figure C-1: H_2, O_2, N_2 permeability of Nafion inversely correlated with kinetic diameter of gas, d_k (Cast: N212 (50.4µm) Extruded: N112 (50.4µm) N117 (180µm))

D. Appendix: Influence of Surface Defect on PDMS/Ionomer Composite Gas Permeability

Composite permeability can be obtained from modeling the transport as transport in parallel. Sum of resistance through PDMS layer (Region I in Figure D-1) and through non-defective layer as well as defected pore (Region II and Region III respectively) is given by equation (1). Here, surface porosity is defined as $\epsilon = \frac{a^2}{b^2}$ and f is fraction of pore that is filled with PDMS.

$$\frac{P_{comp}}{(l+d)} = \left(\frac{l}{P_1} + \frac{d}{P_2(1-\epsilon)+\epsilon P_3}\right)^{-1} \quad (1)$$

Permeability in region 3 (P_3) is sum of permeability of filled and unfilled pore adjusted by the respective fraction f. Unfilled pore could be estimated to have all types of flow; viscous, Knudsen and bulk-diffusive flow. Effective permeability is sum of all three types of transport modeled as resistance in series with filled pore having transport properties of PDMS. Given vales for P_1 and P_2 are bulk values listed in Table C-1**.** A 560nm thin film (d) with a 7 µm PDMS layer support(l) with a 5nm pore size (a) was assumed for this calculation. Permeability through pore (P_v) is given by equation (9) where D_K is Knudsen diffusivity, M_i is molecular weight of select gas, µ is viscosity, m is mass of gas per molecule, k_B is Boltzmann constant and r is molecular radius of gas and p is average pressure through pore. [Look at ref. [8,9] for complete derivation] Values calculated for each gas are compared using selectivity given by equation (7).

$$P_3 = \frac{P_1}{f+(1-f)P_1/P_v} \quad (2)$$

$$P_v = P_{viscous-flow} + P_{knuden-diffusion} + P_{diffusivity} \quad (3)$$

$$P_{viscous-flow} = \frac{N}{\frac{dp}{dx}} = \frac{a^2 p}{8\mu RT} \quad (4)$$

$$P_{knuden-diffusion} = \frac{D_K}{RT} = \frac{2a}{3RT}\sqrt{\left(\frac{8RT}{\pi M_i}\right)} \quad (5)$$

$$P_{diffusivity} = \frac{D}{RT} = \frac{1}{12RT\pi^{3/2}} \frac{(k_B T)^{3/2}}{pm^{1/2}r^2} \quad (6)$$

$$\alpha_{H_2/O_2} = \frac{P_{comp\ H_2}}{P_{comp\ O_2}} \quad (7)$$

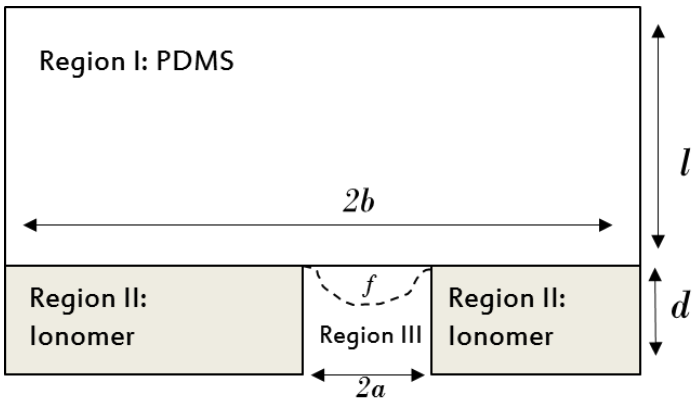

Figure D-1: Composite film with ionomer film thickness of d and PDMS thickness of l. Pore, or defect is of size 2a. f is fraction of pore defect in ionomer that is all or in part filled with PDMS

Figure D-2 shows the two extremes of surface porosity for unfilled and fully filled pore plotted against selectivity. Plot can give a good estimate of total pore size. However, imaging techniques need to be used to identify the distribution of pores.

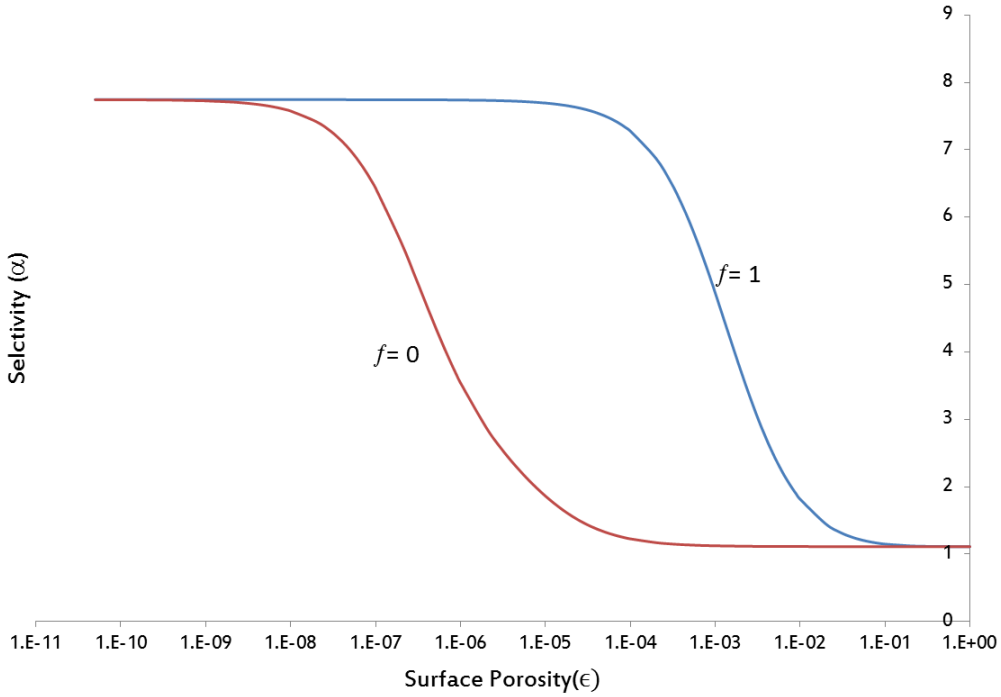

Figure D-2: Relationship between surface porosity and selectivity for unfilled pore (f = 0) and filled pore (f=1)

E. Appendix: Funding Acknowledgements

Work in this dissertation made use of facilities at the Joint Center for Artificial Photosynthesis supported through the Office of Science of the U.S. Department of Energy under Award Number DE- SC0004993. This work also made use of facilities at the Advanced Light Source beamline 7.3.3, supported by the Office of Science, Office of Basic Energy Sciences, of the U.S. Department of Energy (Contract No. DE-AC02- 05CH11231). Luminescent quenching work was conducted at the Molecular Foundry was supported by the Office of Science, Office of Basic Energy Sciences, of the U.S. Department of Energy under Contract No. DE-AC02-05CH11231.

Project funding also came from Fuel Cell Performance and Durability Consortium (FC- PAD), by the Fuel Cell Technologies Office (FCTO), Office of Energy Efficiency and Renewable Energy (EERE), of the U.S. Department of Energy under Contract Number DE-AC02-05CH11231.

Graduate student funding was supplied in part by the National Science Foundation (Grant No. DGE 1106400) and the University of California Berkeley Graduate Chancellor Fellowship.

F. Appendix: Work Cited

(1) James, C. W.; Roy, A.; McGrath, J. E.; Marand, E. Determination of the Effect of Temperature and Humidity on the O2 Sorption in Sulfonated Poly(Arylene Ether Sulfone) Membranes. J. Memb. Sci. **2008**, 309 (1–2), 141–145.

(2) Chiou, J. S.; Paul, D. R. Gas Permeation in a Dry Nafion Membrane. **1988**, No. Figure 5, 2161–2164.

(3) Sakai, T. Gas Permeation Properties of Solid Polymer Electrolyte (SPE) Membranes. J. Electrochem. Soc. **1985**, 132 (6), 1328.

(4) Mohamed, H. F. M.; Ito, K.; Kobayashi, Y.; Takimoto, N.; Takeoka, Y.; Ohira, A. Free Volume and Permeabilities of O2 and H2 in Nafion Membranes for Polymer Electrolyte Fuel Cells. Polymer (Guildf). **2008**, 49 (13–14), 3091–3097.

(5) Catalano, J.; Myezwa, T.; De Angelis, M. G.; Baschetti, M. G.; Sarti, G. C. The Effect of Relative Humidity on the Gas Permeability and Swelling in PFSI Membranes. Int. J. Hydrogen Energy **2012**, 37 (7), 6308–6316.

(6) Pasternak, R. a.; Christensen, M. V.; Heller, J. Diffusion and Permeation of Oxygen, Nitrogen, Carbon Dioxide, and Nitrogen Dioxide through Polytetrafluoroethylene. Macromolecules **1970**, 3 (3), 366–371.

(7) Merkel, T. C.; Bondar, V. I.; Nagai, K.; Freeman, B. D.; Pinnau, I. Gas Sorption, Diffusion, and Permeation in Poly (Dimethylsiloxane). J. Polym. Sci. Part B Polym. Phys. **2000**, 38 (3), 415–434.

(8) Lopez, J. L. .; Matson, S. L. .; Marchese, J. .; Quinn, J. A. . Diffusion Through Composite Membranes: A Two-Dimensional Analysis. J. Memb. Sci. **1986**, 27.

(9) Henis, J. M. S.; Tripodi, M. K. Composite Hollow Fiber Membranes for Gas Separation: The Resistance Model Approach. J. Memb. Sci. **1981**, 8 (3), 233–246.